Beyond the standard cosmological paradigm with weak gravitational lensing

Catherine Danielle Bartlett Leonard
Worcester College
University of Oxford

A thesis submitted for the degree of
Doctor of Philosophy

Trinity 2016

Beyond the standard cosmological paradigm with weak gravitational lensing

Catherine Danielle Bartlett Leonard
Worcester College
Submitted for the degree of Doctor of Philosophy
Trinity Term 2016

Abstract

Next-generation cosmological surveys will demand an unprecedented understanding of the interplay between theoretical and observational aspects of weak gravitational lensing. This thesis presents a study of the parameter degeneracies and theoretical uncertainties which will affect weak lensing tests of cosmology beyond the standard paradigm. In particular, tests of alternative theories of gravity and of spatial curvature are considered.

First, by considering linear-order departures from the standard gravitational theory of general relativity, a novel expression is derived for the weak lensing convergence power spectrum under alternative theories of gravity. Using this expression, degeneracies between gravitational parameters in weak lensing observations are explored, first with a focus on scale-independent parameterisations of gravity, then considering new physical scales introduced by alternative theories. The degeneracy-breaking offered by the combination of weak lensing and redshift-space distortions is shown to be robust to the time-dependence of the functions parameterising modified gravity.

Next, the gravity-testing statistic E_G is investigated, and a new theoretical expression for its observationally-motivated definition is presented. The theoretical uncertainty of E_G is compared to forecast statistical errors, and found to be significant in the case of a more futuristic measurement. Predictions are then computed for E_G under deviations from general relativity, and the ongoing utility of E_G as a probe of gravity is discussed.

Finally, an investigation is made of the potential for measuring or constraining the spatial curvature using weak lensing and complementary observables. The predicted constraint on Ω_K is forecast for a suite of upcoming surveys, and the effect of including parameters which may be degenerate with the spatial curvature is explored. It is found that upcoming observations are likely to constrain Ω_K at a 10^{-3} level, but not to reach the best-case constraint of $\sim 10^{-4}$.

Acknowledgements

First and crucially, I thank my supervisor Pedro Ferreira. His astounding patience has been indispensable over the past four years. He has been as engaged and as supportive a supervisor as anyone could ask for, and I am extremely grateful to have had the privilege of being his student.

The cosmology group at Oxford has been a welcoming and friendly environment, and I thank everyone who has made it that way. In particular, thanks to my second supervisor Lance Miller, to friends and collaborators Phil, Tessa, and Rupert, and to Thibaut, for keeping my French in practice. Thanks also to Catherine Heymans, at Edinburgh, with whom collaborating has been a pleasure.

Elsewhere in the Astrophysics Sub-department, thanks first to Ashling, for answering every question. Thanks to the various occupants of the Tower over the past four years, and in particular to Sarah, Luke, Alfie, Tessa, Alex, Ruth, and, of course, to David. Thanks as well to Holly, for putting up with me at home over this final year, and to Dominic, who has done it for three.

I will forever be grateful to my undergraduate supervisor Robert Mann. His mentorship and support have been essential in allowing me to reach this point. Thanks to Robb and to the students of his who made Waterloo my second home, especially to Paul, Sean, Eric, Melanie, Miok, Marius, and, of course, to Wilson. Thanks as well to Eleanor, who made sure that we occasionally talked about something other than physics.

The funding for my DPhil has been provided by the Rhodes Trust and by the Natural Sciences and Engineering Research Council of Canada. I am truly grateful to both of these organisations.

Thanks to the friends and family in Newfoundland who have been there for me over the past four years and long before that. Thanks to Alycia, who has been coaching me through moments of crisis since she learned to talk. Finally, and most importantly, thanks to my parents, who have always encouraged and supported me in everything I have done. Thanks to Mom, who has probably learned far more about physics than she ever wanted, and to Dad, whose love of the subject is what put me on this path in the first place.

Statement of publications

This thesis is based in part upon the following published papers:

1. *Exploring degeneracies in modified gravity with weak lensing.* C. Danielle Leonard, Tessa Baker, and Pedro G. Ferreira. Physical Review D, 91, 083504. arXiv: 1501.03509.

2. *New gravitational scales in cosmological surveys.* Tessa Baker, Pedro G. Ferreira, C. Danielle Leonard, and Mariele Motta. Physical Review D, 90, 124030. arXiv: 1409.8284.

3. *Testing gravity with E_G: mapping theory onto observations.* C. Danielle Leonard, Pedro G. Ferreira, and Catherine Heymans. Journal of Cosmology and Astroparticle Physics, 12(2015), 051. arXiv: 1510.04287.

4. *Spatial curvature endgame: Reaching the limit of curvature determination.* C. Danielle Leonard, Philip Bull, and Rupert Allison. Physical Review D, 94, 023502. arXiv: 1604.01410.

The work presented in this thesis is my own, with the following clarifications:

- Chapter 2 is based on Paper 1, the work for which I led. The text of Paper 1 was written by me, incorporating input from co-authors and the referee.

- Chapter 3 is based on aspects of Paper 2. The text of this chapter was written by me. The code which was used to produce the main results of this chapter was written by me, with some modifications by Tessa Baker. I did not contribute heavily to the derivation which I review in Section 3.2.1.

- Chapter 4 is based on Paper 3, the work for which I led. The text of Paper 3 was written by me, incorporating input from co-authors and the referee.

- Chapter 5 is based on Paper 4, of which I was the lead author. The text of Paper 4 was written by myself and Philip Bull, with some edits by Rupert Allison, but the text of this chapter was written by me. The weak lensing forecasting code was written by me. The primary CMB forecasting code was written by Rupert Allison and modified by me. BAO Fisher matrices were computed by Philip Bull.

Contents

List of Figures

List of Tables

Chapter 1

Introduction

Observational cosmology is in the midst of an era unlike any other in the history of the subject. In recent years, exquisite measurements of cosmological observables have permitted unprecedented precision in cosmological parameter constraints. With the upcoming generation of cosmological surveys, the capabilities of these observables will only increase. Surveys such as Euclid [1] and the Large Synoptic Survey Telescope [2] promise to vastly enhance the available datasets for weak gravitational lensing and galaxy clustering observations. This presents the possibility of improved constraints not only on standard cosmological parameters, but also on cosmological physics beyond the standard paradigm. However, with this great expansion in available data will come also the necessity for a radically improved understanding of theoretical issues. The objective of this thesis is to explore parameter degeneracies and theoretical uncertainties of relevance to upcoming tests of cosmology beyond the standard paradigm.

The main observable of interest in this work will be weak gravitational lensing. Originally detected in 2000 [3], weak lensing is a remarkably potent cosmological probe with incredible potential. Ongoing and next-generation surveys will represent a significant step forward in its statistical power. The study of theoretical uncertainties and parameter degeneracies which may affect weak lensing tests of gravity and of spatial curvature is the main focus of this thesis.

In this introductory chapter, a review is first provided in Section 1.1 of the standard cosmological paradigm, with extensions discussed in Section 1.2. These extensions include alternative theories of gravity, dynamical dark energy models, and a spatially curved Universe. In Section 1.3, an introduction to weak gravitational lensing and relevant complementary observables is provided, and the method of Fisher forecasting, which will be employed to explore degeneracies, is reviewed. A description is also made of current and planned surveys of interest. Finally, in Section 1.4, an outline of the remainder of the thesis is presented.

1.1 The standard cosmological paradigm

Before discussing possible extensions to the standard cosmological model, the crucial building blocks of modern cosmology will be reviewed. Section 1.1.1 introduces the gravitational theory of general relativity, while Section 1.1.2 discusses the Friedmann-Robertson-Walker (FRW) metric and scalar perturbations thereof. The inflationary paradigm is then reviewed in Section 1.1.3, followed by a description of cold dark matter in Section 1.1.4. Finally, the standard cosmological model of ΛCDM is introduced in Section 1.1.5.

1.1.1 General relativity

In 1916, Einstein proposed general relativity (GR) [4], a revolutionary theory which suggested that gravity is intrinsically linked to geometry. Crucial to GR is the interpretation of spatial and temporal dimensions as part of the same underlying manifold, called spacetime. A core insight of the theory is the link between matter (and energy), and the geometry of this manifold. Within the context of general relativity, the presence of mass or energy corresponds to the curvature of spacetime, which manifests as gravity.

A key quantity in GR is the metric. This is a rank 2 tensor, which arises from the notion that one can write an infinitesimal spacetime displacement ds as:

$$ds^2 = g_{\mu\nu} dx^\mu dx^\nu \, , \tag{1.1}$$

where the Einstein summation convention is followed in summing over indices. g, the metric, has dimensions $D \times D$, where D is the total number of spatial and temporal dimensions of the spacetime (typically four in cosmological applications, but not always). The metric of flat space, for example, can be written in Cartesian coordinates as

$$g = \begin{bmatrix} -c^2 & 0 & 0 & 0 \\ 0 & 1 & 0 & 0 \\ 0 & 0 & 1 & 0 \\ 0 & 0 & 0 & 1 \end{bmatrix}$$

or in line-element form as

$$ds^2 = -c^2 dt^2 + dx^2 + dy^2 + dz^2. \tag{1.2}$$

In the more realistic case in which the spacetime has curvature, the metric gains complexity. Notice that a metric signature has been introduced: the temporal dimension is given a negative sign, to distinguish it from the spatial dimensions. The $(-,+,+,+)$ signature will be employed throughout this thesis.

Operating on a generally non-Euclidean manifold implies that the usual flat-space notion in which a vector can be trivially transported no longer applies. A quantity called the affine connection is needed to encode information which allows different parts of the manifold to be connected. The affine connection which is generally employed in GR is known as the metric connection:

$$\Gamma^{\sigma}_{\lambda\mu} = \frac{1}{2} g^{\nu\sigma} \left(g_{\mu\nu,\lambda} + g_{\lambda\nu,\mu} - g_{\mu\lambda,\nu} \right) . \tag{1.3}$$

Although it is always possible within general relativity to interpret the local geometry as flat, a source of mass or energy leads to global curvature. This curvature can be written as a function of the metric connection, since the latter specifies how quantities can be transported globally around the spacetime. The curvature is encoded in the *Riemann tensor*:

$$R^{\lambda}_{\mu\nu\kappa} = \Gamma^{\lambda}_{\mu\nu,\kappa} - \Gamma^{\lambda}_{\mu\kappa,\nu} + \Gamma^{\eta}_{\mu\nu}\Gamma^{\lambda}_{\kappa\eta} - \Gamma^{\eta}_{\mu\kappa}\Gamma^{\lambda}_{\nu\eta} \, , \tag{1.4}$$

where contractions of this quantity are known as the *Ricci tensor*:

$$R_{\mu\kappa} = R^{\lambda}_{\mu\lambda\kappa} \, , \tag{1.5}$$

and the *Ricci scalar*:

$$R = g^{\mu\kappa} R_{\mu\kappa} \,. \tag{1.6}$$

Given these quantities which describe global curvature, the action for general relativity can be introduced. Requiring that the field equations to be derived from this action are second order (and thus free of instabilities) leaves only one choice of action:

$$S = \int d^4x \sqrt{-g}(R + 2\Lambda) \,, \tag{1.7}$$

where g here is the determinant of the metric, and Λ is an integration constant which is often assumed to be zero (although it is the geometric equivalent of a constant vacuum energy).

Varying the action of equation 1.7 with respect to the metric leads to the field equations of general relativity. These are given by

$$R_{\mu\nu} - \frac{1}{2} g_{\mu\nu} R + \Lambda g_{\mu\nu} = -8\pi G T_{\mu\nu} \,, \tag{1.8}$$

where $T_{\mu\nu}$ is the energy-momentum tensor, which captures information about the matter and energy content of the spacetime. From this, one can explicitly see the link between gravity and geometry: energy and matter source curvature. Equation 1.8 is a set of ten independent coupled partial differential equations. Given the energy-momentum tensor, one can in principle solve for the metric.

General relativity was tested shortly after its proposal, notably via gravitational lensing. Einstein's theory predicted that the angle through which a strongly lensed image would be displaced via gravitational lensing would be twice that predicted in Newtonian gravity. Observations of the lensing of stars by the sun at the occasion of a solar eclipse were consistent with the general relativistic prediction [5]. Further tests of gravity using gravitational lensing and gravitational redshift continued throughout the following decades, sometimes making use of the parameterised post-Newtonian formalism (see, for example, [6]). As evidence accumulated, it became clear that GR was an excellent description of gravity on scales within the solar system.

In the years following its publication, GR would suffer setbacks at smaller distance scales. Quantum mechanics and quantum field theory would produce impeccable predictions at very small scales, but exhibited incompatibility with GR. This discrepancy has led to a still-ongoing research programme examining the possibilities for a quantum theory of gravity, the products of which have included string theory and loop quantum gravity. However, on scales relevant to astrophysics, general relativity has long been accepted as a standard component of the physical paradigm.

1.1.2 The FRW metric and scalar perturbations

General relativity employs the metric to encode information about spacetime manifolds. In cosmology, the spacetime of interest is often the Universe as a whole. This subsection will discuss the standard metric which describes the unperturbed Universe, as well as that which includes the scalar perturbations which source the growth of structure.

To begin, consider a smooth, unperturbed Universe. Deducing the appropriate metric for this scenario relies on the assumption that the Universe is spatially homogeneous (the same everywhere) and isotropic (the same in every direction). This is a statement of the cosmological principle: that is, that the Earth is not in a special location, and that special locations do not exist. The cosmological principle leads to the inevitable conclusion that the background evolution of the Universe is described by the Friedmann-Robertson-Walker (FRW) metric (see, for example, [7]). Allowing for the possibility of a spacetime with spatial sections which are not globally flat, this is given by

$$ds^2 = -c^2 dt^2 + a(t)^2 \left[\frac{dr^2}{1 - kr^2} + r^2 (d\theta^2 + \sin^2(\theta) d\phi^2) \right] , \tag{1.9}$$

where k is a constant describing the spatial curvature of the Universe (negative for an open Universe, zero for a flat Universe, and positive for a closed Universe). $a(t)$ is known as the *scale factor*, which describes the expansion of the spatial dimensions as a function of time. The cosmological redshift, z, is then defined by $a = \frac{1}{1+z}$.

Inserting this metric into the Einstein field equations provides two key relations which govern the evolution of the smooth Universe. These are found by assuming that matter and energy can be described as a perfect fluid, which allows the energy-momentum tensor to be written as

$$T_{\mu\nu} = P g_{\mu\nu} + (\rho + P) U_\mu U_\nu \,, \tag{1.10}$$

where P is the pressure of the fluid, ρ is its density, and U_μ is its four-velocity. Inserting this and equation 1.9 into equation 1.8, it can be found that:

$$\frac{\dot{a}}{a} = \frac{8\pi G}{3}\rho - \frac{kc^2}{a^2} \,, \tag{1.11}$$

and

$$3\frac{\ddot{a}}{a} = -4\pi G \left(\rho c^2 + 3P\right) . \tag{1.12}$$

Note that the possibility of a constant vacuum energy is included here via ρ, along with all other types of energy and matter. The former of these two equations is known as the Friedmann equation, and the latter as the Raychaudhuri equation. Imposing the conservation of the energy-momentum tensor provides another useful equation:

$$\dot{\rho} + 3(1+w)\frac{\dot{a}}{a}\rho = 0 \,, \tag{1.13}$$

where w is the equation of state, $\frac{P}{\rho c^2}$.

It will be useful to employ a notation whereby the fractional energy density of each matter or energy component x is given by $\Omega_{\mathrm{x}}(a) = \frac{\rho_{\mathrm{x}}(a)}{\rho_{\mathrm{c}}(a)}$. $\rho_{\mathrm{c}}(a)$ is the critical density: the density required for the spatial sections of the Universe to be flat. It is given by $\rho_{\mathrm{c}}(a) = \frac{3H(a)^2}{8\pi G}$ where $H(a) = \frac{\dot{a}}{a}$ is the Hubble parameter (denoted H_0 at $a = 1$). Additionally, an effective fractional energy density is defined for the curvature, given by: $\Omega_{\mathrm{K}}(a) = \frac{-kc^2}{a^2 H^2}$. Introducing this notation allows the Friedmann equation to be rewritten as:

$$1 = \Omega_{\mathrm{M}}(a) + \Omega_{\mathrm{R}}(a) + \Omega_{\mathrm{K}}(a) + \Omega_{\Lambda}(a) \,, \tag{1.14}$$

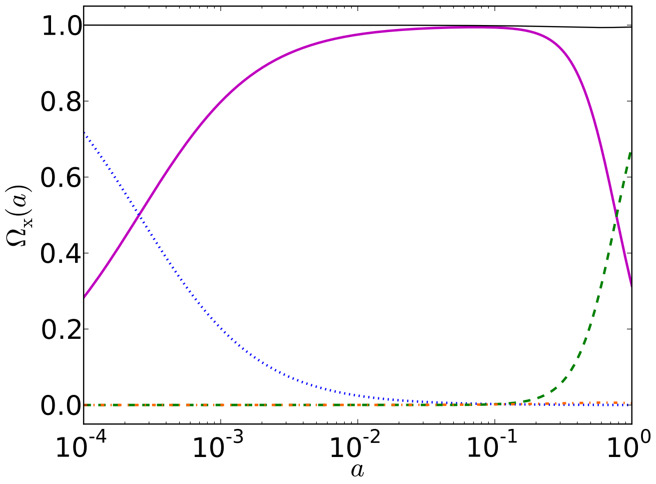

Figure 1.1: The evolution of the fractional energy densities $\Omega_{\mathrm{x}}(a)$. The values of the fractional energy densities today are taken from the *Planck* 2015 release [8], with that of $\Omega_{\mathrm{K}}(a = 1)$ being set to the 2σ upper bound. Blue, dotted: $\Omega_{\mathrm{R}}(a)$; green, dashed: $\Omega_{\Lambda}(a)$; purple, solid: $\Omega_{\mathrm{M}}(a)$; orange, dot-dashed: $\Omega_{\mathrm{K}}(a)$; black, solid: $\Omega_0(a) = \Omega_{\mathrm{M}}(a) + \Omega_{\mathrm{R}}(a) + \Omega_{\Lambda}(a)$.

where $\Omega_{\mathrm{M}}(a)$ is the fractional energy density of matter, $\Omega_{\mathrm{R}}(a)$ is that of radiation, and $\Omega_{\Lambda}(a)$ is that of a constant vacuum energy. The evolution of these fractional energy densities with respect to the scale factor are plotted in Figure 1.1.

The unperturbed FRW metric is an essential description of the smooth Universe on large scales. However, the Universe is clearly not perfectly homogeneous and isotropic on all scales of cosmological importance. Perturbations to the FRW metric must be considered in order to describe structure formation. There exist three possible types of perturbation: scalar, vector, and tensor. Vector perturbations are unimportant within the standard cosmological model [9], while tensor perturbations source gravitational waves. Scalar perturbations produce density perturbations and hence the growth of structure. The decomposition theorem leads to the fortunate conclusion that these three types of perturbation can be considered independently, and so only scalar perturbations will be discussed here.

Within this illustrative discussion of the scalar-perturbed metric, it will be assumed for the sake of simplicity that the Universe is flat. However, extensions to the curved case are possible (see, for example, [10]), and are employed in the calculation of observables in Chapter 5. The FRW metric under scalar perturbations in a flat Universe is given as [11]:

$$ds^2 = a(\eta)^2 \Big[-(1+2\Psi) d\eta^2 - 2(\vec{\nabla}_i \epsilon) d\eta \, dx^i + (1-2\Phi)\, \gamma_{ij} \, dx^i dx^j + (D_{ij}\nu)\; dx^i dx^j \Big] \,, \tag{1.15}$$

where $D_{ij} = \vec{\nabla}_i \vec{\nabla}_j - \frac{1}{3}\delta_{ij} \vec{\nabla}_k \vec{\nabla}^k$ and γ_{ij} is the flat-space metric presented in Section 1.1.1. The scale factor has been pulled out of the metric via the introduction of conformal time η, with $d\eta = a(\eta) dt$.

Equation 1.15 represents the scalar-perturbed metric prior to gauge fixing. Choosing the conformal Newtonian gauge, and hence setting $\epsilon = \nu = 0$, results in:

$$ds^2 = a(\eta)^2 \Big[-(1+2\Psi) d\eta^2 + (1-2\Phi)\, \gamma_{ij} \, dx^i dx^j \Big] . \tag{1.16}$$

What can equation 1.16 tell us about the growth of structure? Linear perturbation theory provides an excellent description of the Universe on those scales which have recently entered the cosmic horizon. Considering this regime and inserting equation 1.16 into the field equations of GR leads to the following (in Fourier space) [11]:

$$\begin{aligned}
& k^2\Phi + 3\frac{\dot{a}}{a}\left(\dot{\phi} + \frac{\dot{a}}{a}\Psi\right) = 4\pi G a^2 \delta T^0_{\;0} \,, \\
& k^2 \left(\dot{\Phi} + \frac{\dot{a}}{a}\Psi\right) = 4\pi G a^2 (\bar{\rho} + \bar{P})\theta \,, \\
& \ddot{\Phi} + \frac{\dot{a}}{a}\left(\dot{\Psi} + 2\dot{\Phi}\right) + \left(2\frac{\ddot{a}}{a} - \left(\frac{\dot{a}}{a}\right)^2\right)\Psi + \frac{k^2}{3}(\Phi - \Psi) = \frac{4\pi G}{3} a^2 \delta T^i_{\;i} \,, \\
& k^2(\Phi - \Psi) = 12\pi G a^2 (\bar{\rho} + \bar{P})\sigma \,,
\end{aligned} \tag{1.17}$$

where θ is the velocity potential, σ is the anisotropic stress (non-zero only for radiation components), and a bar indicates a background quantity. Densities, pressures, the velocity potential, and the anisotropic stress should be assumed to be summed over all matter and energy species. $\delta T^i_{\;i}$ is the trace of the spatial part of the perturbed energy-momentum tensor.

In the case of non-relativistic fluid species, the energy-momentum tensor ${T^\mu}_\nu$ (the perturbed part of which is required in equation 1.17), is given by equation 1.10 via contraction with the metric. Invoking then conservation of ${T^\mu}_\nu$ produces [11]:

$$\begin{aligned}
\dot{\Delta} &= -(1+w)(\theta + 3\dot{\Phi}) - 3\frac{\dot{a}}{a}\left(\frac{\delta P}{\delta \rho} - w\right)\Delta \,, \\
\dot{\theta} &= -\frac{\dot{a}}{a}(1-3w)\theta - \frac{\dot{w}}{1+w}\theta + \frac{\delta P/\delta \rho}{1+w}k^2\Delta - k^2\sigma + k^2\Psi \,,
\end{aligned} \tag{1.18}$$

where $\delta\rho = \rho - \bar{\rho}$, $\delta P = P - \bar{P}$, and $\Delta = \frac{\delta\rho}{\bar{\rho}}$. Specifically, the variable Δ_{M} will be employed throughout this thesis to refer to the density contrast of the matter perturbation. Equation 1.18 is valid for components of the matter-energy budget which are both non-relativistic and uncoupled (for example, for cold dark matter, which will be introduced in Section 1.1.4).

In the case of relativistic species, such as photons, the full phase-space configuration must be considered in order to derive the equivalent of equation 1.18. This is accomplished via the Boltzmann equation:

$$\frac{df}{d\eta} = \left(\frac{\partial f}{\partial \eta}\right)_{\mathrm{C}} , \tag{1.19}$$

where f is the phase space distribution. The right-hand side of equation 1.19 captures effects from collision, with the exact form being related the species of particle under consideration. For example, in the case of photons, these terms account for Thomson scattering. The Boltzmann equation can be manipulated to obtain a set of coupled differential equations, which provide a relationship between phase-space quantities. Solving these equations results in the multipoles of the perturbation to, for example, photon temperature and polarization [11, 12].

Given equations 1.17, 1.18, and 1.19, as well as a description of relevant interactions between components, initial conditions, and the spectrum of primordial scalar perturbations (see equation 1.24, below), the evolution of temperature and polarization multipoles, of density perturbations, and of velocity perturbations can be found. Two-point functions for each matter or energy component can then be computed, in real- or Fourier-space. Several public codes exist for this purpose, including CAMB [10] and CLASS [13]. However, recall that power spectra computed in this way are only applicable for scales and times at which cosmic horizon entry was recent. On smaller scales and at later times, non-linear effects must be accounted for. A brief introduction to how this is accomplished for matter is presented in Section 1.1.4. Figure 1.2 displays the theoretical linear power spectrum of matter (including cold dark matter, baryons, and massive neutrinos), computed using the public code CAMB. It also displays the correction at high k (smaller scales) due to non-linear effects. It can be seen that non-linear effects are important above $k \approx 0.1$ Mpc/h.

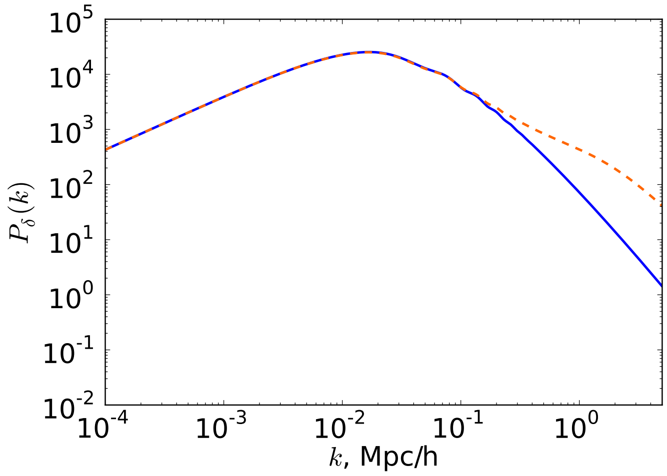

Figure 1.2: The theoretical matter power spectrum today, $P_\delta(k)$. The blue solid curve displays the power spectrum calculated using only linear effects, while the orange dashed curve accounts for non-linear effects using Halofit [14, 15]. Cosmological parameters values are from [8].

1.1.3 Inflation

Equations 1.17, 1.18, and 1.19 provide a means by which to solve for the linear growth of structure. But how are the initial conditions of these differential equations chosen? The answer lies in inflationary theory, the standard paradigm of very early Universe cosmology. Inflation was developed as a means of solving several major discrepancies in cosmological physics, including the flatness and horizon problems.

The flatness problem arises from the fact that the spatial curvature of the Universe is measured to be very near zero. As can be seen in equation 1.14, this is equivalent to the statement that the total fractional density, $\Omega_0 = \Omega_\mathrm{M} + \Omega_\mathrm{R} + \Omega_\Lambda$, is today very close to 1. The difficulty of this scenario can be seen by rewriting equation 1.14 as:

$$|\Omega_0(t) - 1| = \frac{|k|c^2}{a^2 H^2}. \tag{1.20}$$

In a Universe which is dominated by either matter or radiation, it can easily be shown that aH decreases with time, driving Ω_0 away from unity. Thus, for spatial curvature to be measured as very near zero today (i.e., Ω_0 to be very near unity), Ω_0 in the early Universe would have had to be even closer to unity, requiring an improbable degree of fine-tuning.

The horizon problem is best presented via the example of cosmic microwave background (CMB) observations (see Section 1.3.2.2 for an introduction to the CMB). An observer on or near Earth can observe the CMB in opposite directions (the directions for which the two locations of photon emission and the Earth all lie on a line). In these opposite directions, as well as in all observable parts of the sky, the mean temperature of CMB photons is the same. However, in each of these directions, light from the CMB has been travelling since the time of recombination. Because the fastest possible means of interaction is via the transmission of photons, the two regions of the last-scattering surface in question, as well as many other locations on the sky, are in principle causally disconnected now and at all earlier times. However, these regions appear to have mysteriously equilibrated with each other.

Inflation was proposed to solve the horizon and flatness problems, as well as certain other outstanding issues such as the fact that magnetic monopoles are not observed in the current Universe. First suggested in the early 1980s [16, 17], it is defined by a period of accelerated expansion in the early Universe such that $\ddot{a} > 0$. This provides a solution to the flatness problem, as it can be seen from equation 1.20 that if aH is rapidly increasing with time, Ω_0 is strongly driven towards unity. Inflation also resolves the horizon problem, by suggesting that regions which were causally connected at the beginning of the inflationary period could have expanded so rapidly as to take up the whole observable Universe today. They are thus causally disconnected now, but were previously able to achieve equilibrium.

How is this proposed period of inflation driven? In principle, by a type of matter or energy which, in the fluid description, has an equation of state of less than $-\frac{1}{3}$. According to equation 1.12, this will produce the required accelerated expansion. The matter or energy in question must also be able to decay in order to bring an end to the inflationary period, producing standard model particles (or particles which will decay to those of the standard model). However, there is currently no compelling particle physics candidate which can fulfil these requirements. The result is that a generic scalar field is typically assumed, known as the *inflaton.* The scalar field portion of the action is given by

$$S = \int d^4x\sqrt{-g}\left[\frac{1}{2}\left(\nabla\phi\right)^2 - V(\phi)\right] , \tag{1.21}$$

where $V(\phi)$ is the potential of the inflaton ϕ.

The initial proposal of inflation [16] suggested a model of *false-vacuum inflation*, in which the inflaton quantum-tunnels out of a local minimum in the potential and then rolls down to the global minimum. However, problems with this scenario were soon demonstrated [18, 19], in that the required quantum tunnelling was insufficiently frequent. For this reason, *slow-roll inflation* was proposed [17]. Slow-roll inflation is simply the case in which the inflaton rolls down its potential very slowly, such that, for example, the Hubble scale is nearly constant throughout the inflationary period. There are two standard parameters which quantify the 'slowness':

$$\begin{aligned} \epsilon &= -\frac{\dot{H}}{aH^2} , \\ \eta &= -\frac{1}{aH\dot{\phi}}\left[3aH\dot{\phi} + a^2\frac{dV}{d\phi}\right] , \end{aligned} \tag{1.22}$$

where ϕ here is the unperturbed value of the inflaton.

In addition to solving the horizon and flatness problems, inflation provides a natural mechanism for setting the initial conditions of the perturbations which propagate into CMB anisotropies and large-scale structure [20–22]. Recall first that in flat-space, quantum vacuum fluctuations lead to the production of pairs of particles and antiparticles, which annihilate rapidly, in agreement with the Heisenberg uncertainty principle. However, in inflation, space is quickly expanding as these vacuum fluctuations occur, and so paired particles may become causally disconnected prior to annihilation. They are hence 'frozen in' as classical perturbations, which will later enter the cosmic horizon and seed the growth of structure.

This type of quantum fluctuation creates tensor modes, which manifest as primordial gravitational waves, and scalar density perturbations [23]. The resulting expressions for perturbations to the density and to the metric depend on the Hubble scale:

$$\begin{aligned} \left(\frac{\delta\rho}{\rho}\right)_{k=aH} &= \frac{H^2}{4\pi^{\frac{3}{2}}\dot{\phi}}\,, \\ \left(h_{+,\times}\right)_{k=aH} &= \frac{H}{2\pi m_{\mathrm{Pl}}}\,, \end{aligned} \tag{1.23}$$

where $h_{+,\times}$ are the two components of the metric tensor perturbation and m_{Pl} is the Planck mass. These expressions can be obtained by considering the Einstein equations (equation 1.8) for tensor perturbations, and the conservation of the energy-momentum tensor for scalar perturbations.

Because H is almost constant during slow-roll inflation, equation 1.23 leads to nearly, but not exactly, scale-invariant spectra in scalar and tensor perturbations. These are normally parameterised as:

$$P_{\mathrm{s}}(k) = A_{\mathrm{s}}\left(\frac{k}{k_0}\right)^{n_{\mathrm{s}}-1}\,, \tag{1.24}$$

and

$$P_{\mathrm{T}}(k) = A_{\mathrm{T}}\left(\frac{k}{k_0}\right)^{n_{\mathrm{T}}}\,, \tag{1.25}$$

respectively, where k_0 is an arbitrarily chosen pivot scale. The parameters which are employed observationally to characterise these primordial spectra are n_{s}, A_{s}, and r, where r is the ratio of the tensor to scalar contributions to the CMB quadrupole.

Other than requiring that $V(\phi)$ permits slow-roll inflation, the particular form of the potential has not yet been addressed. The most commonly cited model is perhaps the potential of a free scalar field with mass m: $V(\phi) = m^2\phi^2/2$. However, there exist many possible models for $V(\phi)$ which have been proposed in the literature, including, for example, other polynomial forms and exponential forms. For a review of many models of current interest, see [24].

1.1.4 Cold dark matter

Cold dark matter (or CDM) is a non-relativistic matter constituent of the Universe. It notably interacts via electromagnetism either not at all or only very weakly, and therefore is not luminous at any wavelength. Within the standard model of cosmology, cold dark matter is currently measured to make up over 80% of the non-relativistic matter in the Universe [8].

Evidence for a non-luminous component of the matter budget of the Universe dates back several decades, with hints first detected in the 1930s [25, 26]. Throughout the 1970s, a series of observations reported galaxy rotation curves which were flat at much larger radii than predicted by the visible galaxy content [27–32]. Observations in the X-ray and the radio also suggested a non-luminous matter component, demonstrating galaxies within the Virgo cluster to have much more mass than expected [33]. Theoretical investigations of new kinds of non-luminous matter soon followed [34–37]. Further evidence for the existence of cold dark matter can be found from observations of the CMB, of weak gravitational lensing and other large-scale structure probes, and, recently, of the post-merger configuration of the Bullet cluster [38].

What exactly is cold dark matter? As yet, this remains unknown, but theoretical candidates do exist in the literature. These include Weakly Interacting Massive Particles (WIMPS) [39], axions (see, for example, [40]), sterile neutrinos [41], and various fermionic supersymmetric partner particles. Experimental work towards the possible detection of these candidates is underway, including attempts to produce WIMPS in colliders, and to directly detect astrophysical dark matter particles in the lab (for a review, see [42]). No convincing detections have been verified at this point.

Despite a lack of direct understanding of dark matter from a particle theory perspective, predictions can be made of dark matter-related cosmological quantities. The linear cold dark matter power spectrum, for example, can be computed using the techniques of linear perturbation theory described in Section 1.1.2. By incorporating basic assumptions about the behaviour of cold dark matter in equations 1.17 and 1.18, the theoretical time- and scale-dependent behaviour of $\Delta_{\rm CDM}$ can be obtained.

The *halo model* further facilitates the prediction of dark matter-related cosmological quantities, permitting the calculation of two-point functions of dark matter in the non-linear regime. It is a model for structure formation which is based on the assumption that all cold dark matter is bound in a halo of some size. Within this scenario, the non-linear two-point correlation function of cold dark matter, which describes the excess probability of finding overdensities of cold dark matter at separation r, is given by

$$\xi(r) = \xi_{\rm 1h}(r) + \xi_{\rm 2h}(r)\,. \tag{1.26}$$

Here, $\xi_{\rm 1h}(r)$ is the one-halo term, quantifying correlations between mass elements within the same halo, and $\xi_{\rm 2h}(r)$ is the two-halo term, serving the same role for mass elements within different halos. To compute these directly, one must specify the mass function, $\frac{dn(m)}{dm}$ (where n is the number of halos and m is the halo mass), the linear two-point function of dark matter, and $\lambda(\vec{x})$, the distribution of matter within a halo, normally given by a model such as the NFW profile [43]. The halo model can be extended to compute the non-linear matter power spectrum using scaling formulae derived from n-body simulations [14, 15, 44].

Several outstanding issues do exist with cold dark matter (other than its lack of confirmed particle physics origin). These include the core/cusp problem, in which observations suggest a constant density at the centre of galaxies whereas CDM simulations predict a cusp (see [45] for a review), and the missing satellite problem, in which less satellite galaxies are observed than are predicted [46]. Despite these issues, cold dark matter remains a crucial part of our current understanding of cosmology.

1.1.5 ΛCDM

So far, a review has been made of general relativity, the FRW metric, inflation, and cold dark matter. With these components of the standard paradigm in hand, the cosmological model of ΛCDM can be introduced.

ΛCDM is notable for its inclusion of both cold dark matter and a cosmological constant term Λ. Such a term can be incorporated within gravitational theory as suggested in equation 1.7, but is more usually interpreted as a constant vacuum energy with equation of state $w = -1$. With these two crucial components, the ΛCDM model describes the cosmological Universe with only six parameters (presuming spatial flatness):

- $\Omega_{\rm c}h^2$, characterising the fractional energy density of cold dark matter
- $\Omega_{\rm b}h^2$, characterising the fractional energy density of baryons
- $A_{\rm s}$, the amplitude of the spectrum of primordial scalar perturbations
- $n_{\rm s}$, the scale dependence of the spectrum of primordial scalar perturbations
- τ, the optical depth to reionisation, the period in cosmological history wherein the first luminous objects were formed (see, for example, [47])
- one of either h, Ω_Λ, or another observation-specific parameters such as $\theta_{\rm A}$ for the CMB, which quantifies the role of the cosmological constant

In this context, $h = H_0/100$. ΛCDM typically also assumes general relativity, an FRW metric, and a flat Universe, and makes the standard, particle-physics based assumptions about the number and mass of cosmological neutrinos. Using only these assumptions and the six parameters listed, ΛCDM provides beautiful fits to many cosmological observations, including notably CMB observations (see, for example, [8]).

Although cold dark matter was proposed in the 1980s, it was not until the Cosmic Background Explorer (COBE) satellite results (see, for example, [48]), in combination with complementary large-scale structure measurements (e.g. [49]), that serious consideration was given to models beyond a Universe containing only baryons, cold dark matter, and radiation. Several alternatives were considered at that time, including the possibility that some or all of dark matter was warm (relativistic) (see, for example, [41,50]), or the inclusion of a cosmological constant term [51]. The solidification of ΛCDM as the most likely cosmological model occurred in 1998, when two independent groups employed observations of Type 1a supernovae to demonstrate that not only was the Universe expanding (as had already been known) but that expansion was accelerating in the recent Universe [52,53]. This discovery of late-time acceleration was crucial to modern cosmological physics as we know it, and garnered the 2011 Nobel Prize in Physics. Over the years following these landmark papers, many other observations corroborated their conclusion. ΛCDM correctly predicted the location of the baryon acoustic oscillation (BAO) peak (see Section 1.3.2) [54], the weak gravitational lensing cosmic shear spectrum [3], and the polarization of the CMB (see, for example, [55]), to name a few. Its remarkable observational success has cemented ΛCDM as the standard model of cosmology.

Having now reviewed all relevant aspects of the standard cosmological paradigm, the next section will introduce and motivate a key subject of interest to this thesis: extensions of and modifications to standard cosmology.

1.2 Beyond the standard paradigm

The standard cosmological model fits cosmological observations remarkably well. However, compelling motivations do exist to consider cosmology beyond GR+ΛCDM. In this thesis, a focus will be placed upon two types of extensions to the standard paradigm: alternative explanations for accelerated expansion, and non-zero spatial curvature.

As discussed in Section 1.1.5, the now-standard explanation for the late-time acceleration of the Universe is the presence of a cosmological constant, often interpreted as a physical vacuum energy. Despite the observational successes of this model, some theoretical issues remain which have spurred the study of other possible explanations. One such complication is known as the cosmological constant problem (see, for example, [56]). Taking the vacuum energy of Λ to be equivalent to a zero-point energy in quantum field theory – that is, the energy of a spacetime devoid of particles – and computing the corresponding energy density leads to a value which is many orders of magnitude larger than that which is required to fit the accelerated expansion of the Universe. The result is that initial conditions must be heavily fine-tuned in order to reproduce observations. Another dilemma is sometimes called the coincidence problem (see, for example, [57]). It arises from the fact that within the current model, for the vast majority of the history of the Universe, the fractional energy densities Ω_Λ and Ω_M were of radically different orders. However, today, they are of the same order of magnitude. Why is this coincidentally the case at the time in the history of the Universe which corresponds with the existence of human life?

Several explanations have been proposed to resolve these issues, with the objective of providing a more physically natural paradigm. The proposed solution which will be principally discussed in this work is the replacement of GR with an alternative theory of gravity. Such a theory would match the successful behaviour of GR on solar system scales, but act differently on cosmological scales in order to reproduce the accelerated expansion of the Universe. Another very well-studied proposed solution is dynamical dark energy, in which a new scalar field, minimally coupled to gravity, evolves with time in order to produce today's observed acceleration in a natural way. While not directly studied in this thesis, dynamical dark energy will be indirectly considered via constraints on the expansion history, and is therefore sufficiently relevant that it is reviewed in this section. Both dynamical dark energy and alternative theories of gravity are current topics of intensive research and exploration, theoretically [57–68] and observationally [69–72]. Other possible alternatives to the cosmological constant which will not be considered in depth here also exist, such as, for example, the effects of an inhomogeneous cosmology [73].

Another, unrelated way in which the standard paradigm can be modified is via the presence of spatial curvature. Spatial curvature, parameterised by $\Omega_{\rm K}$, is not part of the basic ΛCDM model. In fact, as was mentioned above, inflation was developed in part to provide a scenario in which the spatial curvature of the Universe is naturally very small. When considering ΛCDM with the addition of a spatial curvature parameter, $\Omega_{\rm K}$ is currently constrained to be below 5×10^{-3} by cosmic microwave background and baryon acoustic oscillation data [8]. However, it is precisely because the standard paradigm predicts $\Omega_{\rm K}$ to be very near zero that any measurement of non-zero curvature, even well below the current level, can provide novel and exciting hints of non-standard cosmological physics (see, for example, [74, 75]).

An introduction is now provided to these three extensions to the standard cosmological paradigm.

1.2.1 Alternative theories of gravity

1.2.1.1 An introduction to alternative theories of gravity

General relativity is an important component of standard physical theory, and is remarkably well tested on lab and solar system scales. Despite this, there have been many attempts to modify GR over the century since its inception. Motivation for doing so has included unifying gravity with other fundamental forces in a single theoretical framework and explaining the late-time acceleration of the Universe.

The notion that gravity could explain the accelerating expansion of the Universe was first proposed in 2003 [76, 77]. At that time, it was postulated that a non-general relativistic theory of gravity could potentially reproduce late-time acceleration without requiring an unknown physical dark energy component. Most cosmologically interesting theories of gravity therefore reproduce the ΛCDM expansion history by construction (although this is by no means universal).

How do these alternative theories differ from general relativity? Lovelock's theorem [78] provides some guidance as to the types of modifications which are possible. The theorem states that the Einstein field equations of GR are the only Euler-Lagrange equations derived from a Lagrangian $\mathcal{L}(g_{\mu\nu}, \partial g_{\mu\nu})$ in four dimensions which:

- conserve the energy-momentum tensor,
- are second order in the metric derivatives,
- are local,
- are rank-2 tensor equations, and
- are symmetric under the exchange of indices.

Any alternative theory of gravity in four dimensions must break at least one of these conditions. (For completeness, note that Lovelock's theorem also allows for Lovelock gravity, a generalisation of GR which includes surface terms having no effect in four dimensions.)

One requirement for a healthy alternative theory of gravity is that it is stable. Perhaps the most commonly arising issue in this domain is known as Ostrogradski's instability. This is a phenomenon in which the presence of higher-than-second-order derivatives in the Lagrangian of a theory may cause the Hamiltonian to depend on the momenta in such a way that negative momenta can compensate for highly excited modes. The result is that these terms can 'run away' to arbitrarily high and low values. A related stability issue is that which is commonly referred to as a ghost. This arises when a kinetic energy term is present which has the opposite sign from what is normally expected, leading to a mode which has arbitrarily negative energy. The presence of either of these instability issues is generally considered to be the hallmark of a theory which is not viable.

Despite these seemingly strong restrictions, many alternative theories of gravity which are cosmologically interesting exist in the literature, and are actively studied. In order to provide a concrete example of a theory which extends GR, a particular theory, $f(R)$ gravity, will now be briefly introduced. For a more thorough review of $f(R)$ gravity, see [67].

$f(R)$ gravity: An example $f(R)$ gravity is obtained by replacing the Ricci scalar in the Einstein-Hilbert action with a function $f(R)$. The action becomes:

$$S = \int d^4x\sqrt{-g}f(R). \tag{1.27}$$

$f(R)$ gravity was first studied in 1970 [79]. Since the discovery of the late-time acceleration of the Universe and the resulting renewal of enthusiasm for alternative gravitational theories, it has been of considerable interest. As a result, it was found that $f(R)$ theories could be mapped to *scalar-tensor* theories, another set of alternative gravitational theories in which a new scalar field couples non-minimally to gravity [80, 81]. While $f(R)$ gravity itself does not produce field equations which are generically second-order, mapping $f(R)$ to scalar-tensor theory can recover this desirable characteristic. In Chapter 3 of this thesis, an expression for scale-dependence in alternative gravitational theories will be utilised which holds for theories with a single new spin-0 degrees of freedom; both $f(R)$ and scalar-tensor gravity are prime examples of this type of theory.

In examining the observational consequences of $f(R)$ gravity, via simulation or data analysis, the theory is often parameterised using the fact that $f_R = \frac{\partial f}{\partial R}$ can be thought of as a scalar field, called a scalaron. $f(R)$ gravity can then be considered in terms of the parameter [82, 83]:

$$B = \frac{f_{RR}}{1+f_R}R'\frac{H}{H'} \tag{1.28}$$

where a prime is a derivative with respect to $\ln(a)$ and f_{RR} is the second derivative of f with respect to R. The parameter B is the dimensionless Compton wavelength of the scalaron.

An interesting feature of $f(R)$ gravity is that there exist two formulations of the theory, corresponding to two possible ways in which the action can be varied to obtain the field equations. The action can be varied with respect to the metric alone (assuming the connection depends on the metric, as is typical in GR) or with respect to the metric and the connection independently. In GR, these approaches result in the same field equations. However, in $f(R)$, the first of these results in the metric variational formulation, while the latter results in the Pallitini formulation [84].

$f(R)$ theories in their scalar-tensor form are in fact a subset of a more general set of scalar-tensor theories. *Horndeski* gravity provides the most general scalar-tensor theory of gravity which results in second-order equations of motion [85,86]. Some stable beyond-Horndeski scalar-tensor theories have also recently been found, in which the equations of motion of propagating degrees of freedom are well-behaved and second-order [87, 88].

The theories mentioned here – $f(R)$, scalar-tensor, and Horndeski – are only a small fraction of the set of alternative theories of gravity which are of cosmological interest. Other examples include massive gravity [89], other types of bimetric gravity [90], and the related DGP gravity [66], as well as Tensor-Vector-Scalar gravity [91], and others.

1.2.1.2 Parameterising gravity and the quasistatic approach

As has been noted, there exist many cosmologically-motivated alternative theories of gravity (for a review, see [61]). In addition, the theoretical investigation of gravity beyond GR is an active area of study, with theories being developed or extended on a regular basis. With so many theories in play and no obvious forerunner presenting as the most natural alternative to GR, constraining each of these theories individually becomes a significant burden. Performing a full observational analysis to constrain individual theories is time-consuming, and often impractical due to the number of free parameters and the available data.

Given this, what is the optimal method to detect or constrain modifications to GR on cosmological scales? One common strategy is to take advantage of the structural similarities of many cosmologically-motivated theories in order to design parameterisations which encompass most or all viable candidates. There exist several such parameterisations in the literature. The parameterisation which will be employed frequently in this thesis is the quasistatic parameterisation.

The quasistatic parameterisation is so called because it makes use of the quasistatic approximation (see, for example, [92]), which states that on certain intermediate cosmological length scales, the time-derivatives of the scalar potentials Φ and Ψ (of equation 1.16) are negligible in comparison to spatial derivatives. Imposing the quasistatic approximation requires setting these terms, as well as all terms which go like the Hubble scale, to zero within the gravitational equations of motion. This approximation is valid within the range of linear scales relevant for current and near-future galaxy surveys. In the case of alternative theories, the quasistatic approximation requires also that the time-derivatives of any new degrees of freedom are set to zero.

Enforcing these assumptions within the gravitational field equations of alternative theories shows that the most significant effects of a sizeable class of modified theories can be captured by introducing two non-GR functions of time and scale within the linearised gravitational field equations. These functions play the role of a modified gravitational constant, and a non-unity (late-time) ratio of the two FRW scalar gravitational potentials:

$$\begin{aligned} 2\nabla^2\Phi(a,k) &= 8\pi G a^2 \mu(a,k)\bar{\rho}_{\mathrm{M}}\Delta_{\mathrm{M}}(a,k)\,, \\ \frac{\Phi(a,k)}{\Psi(a,k)} &= \gamma(a,k), \end{aligned} \tag{1.29}$$

In GR, both $\gamma(a,k)$ and $\mu(a,k)$ are equal to 1, and time-dependence has been shown to dominate over scale-dependence in the quasistatic regime [92–94]. Equation 1.29 is an effective description of the true, more complicated field equations [63, 87, 88, 94–101], valid only on certain scales. However, the validity of the quasistatic approximation has been numerically verified in many gravitational theories (notably those with one new degree of freedom) on distance scales relevant to current and near-future galaxy surveys [102–106]. The quasistatic parameterisation and the functions μ and γ (and linear combinations thereof) will be employed extensively throughout this thesis when considering observational constraints on gravitational theories.

The quasistatic parameterisation is only one choice of several formulations which parameterise alternative gravitational theories. For example, the Parameterised Post-Friedmann (PPF) formulation [63, 96] captures the linear-scale effects of theories of gravity which introduce new spin-0 degrees of freedom. The PPF formulation's more general nature includes allowing for twenty-two free functions of times, although for many theories of interest the number of free functions is in effect greatly reduced. Another well-known parameterisation of gravity is the EFT parameterisation, based on an effective field theory formulation of gravity [99, 107–109]. The EFT parameterisation, which also captures linear-scale effects, is the basis of the public data analysis and forecasting codes EFTCamb and EFTCosmoMC [110]. These choices of parameterisation framework are more complicated, but could be of use for the analysis of more futuristics datasets which may include near-Hubble scales, such as those from the LSST and the Square Kilometer Array (SKA) [111] .

1.2.1.3 Current observational constraints

With the upcoming generation of cosmological surveys, and especially with the related increase in large-scale structure data, constraints on gravity are expected to become possible at an unprecedented level. However, some preliminary attempts have already been made to constrain gravity using cosmological observations.

Testing gravity generally requires the use of observables which are sensitive to the formation of large-scale structure. Gravitational theories also have the capacity to alter the background expansion rate, as has been discussed above. However, probing only the expansion rate results in total degeneracy with dynamical models of dark energy, as described in Section 1.2.2. To break this degeneracy, probes which measure structure formation are required. Weak gravitational lensing has been put forward as a highly promising observable for this task [112–119], but as will be discussed extensively in this work, combining observables is necessary to achieve optimal constraints.

One method of testing gravity involves the combination of observables via standard Bayesian likelihood methods, in order to constrain a parameterisation of gravity. The most up-to-date constraint of this nature combines *Planck* CMB measurements, lensing observations from CFHTLenS, and BAO observations from BOSS. These are reported in [72], while the original CFHTLenS analysis with older complementary datasets was presented in [69]. The resulting constraints on gravity from [72] are shown in Figure 1.3. The apparent effect of including weak gravitational lensing observations is to pull the constraint contour away from the fiducial GR scenario. However, it remains unclear whether poorly understood weak gravitational lensing systematics or inadvertently-incorporated non-linear effects could be the cause of this, rather than modifications to GR.

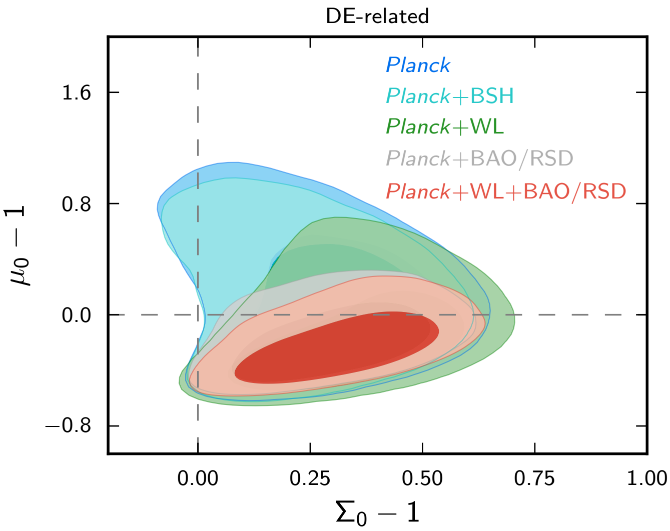

Figure 1.3: Source: Figure 15 of [72], by the *Planck* collaboration. Constraints on modifications to GR, at the 68.3% and 95.4% confidence levels. $(0, 0)$ represents the GR case, and the title 'DE-related' indicates that the parameterising functions of gravity take a time-dependent ansatz which scales like $\Omega_\Lambda(a)$. 'BSH' signifies the inclusion of BAO, supernovae, and Hubble parameter measurements. It can be seen that the inclusion of weak lensing observations (WL) appears to pull the constraint contours away from GR.

Another set of current observational constraints on gravity derive from the use of the statistic E_G [70, 116]. E_G, which will be discussed extensively in Chapter 4, combines lensing and galaxy clustering directly into a single observable with the intention of testing gravity. In its current incarnation, it aims primarily to check consistency with GR, rather than to place constraints on gravitational parameters. The first measurement of E_G was made in [70], which was found to be consistent with general relativity but also with $f(R)$ gravity (where only GR, $f(R)$ and Tensor-Vector-Scalar gravity were considered). E_G was later measured using lensing data from RCSLenS and CFHTLenS, as well as galaxy clustering data from BOSS [71]. Again, the measured value was found to be consistent with GR.

Finally, as has been discussed, it is often considered too arduous to place observational constraints on individual theories of gravity. However, in the case of certain well-studied theories, some work has been done towards constraining specific parameters (e.g. [120–125]). No significant signatures of deviation from GR have been discovered.

1.2.2 Dynamical dark energy

1.2.2.1 An introduction to dynamical dark energy

Like alternative theories of gravity, dynamical dark energy models attempt to explain late-time acceleration without the use of a cosmological constant. Dynamical dark energy is in some sense a more straightforward extension: instead of a constant vacuum energy, another source of exotic energy is introduced, which evolves with time. This is accomplished via the addition of a novel scalar field.

Within this thesis, a distinction will be drawn between alternative theories of gravity (in particular, scalar-tensor theories) and dark energy models by the fact that in dynamical dark energy models, the new scalar is minimally coupled to gravity. It is hence considered to form part of the matter-energy sector, while gravity is assumed to behave in the normal general relativistic manner. Therefore, dark energy models typically do not directly induce modifications to the formation of large-scale structure;

they do so only via changes to the expansion history of the Universe.

Prior to the 1998 discovery of the accelerating expansion of the Universe, some interest had already arisen in dynamical dark energy models (e.g., [126, 127]), as a result of measurements of $\Omega_{\mathrm{M}} \approx 0.3$ combined with a strong prior on a flat Universe from inflation. As the observational evidence for late-time acceleration became overwhelming, interest in reproducing the phenomenon with dynamical dark energy grew (see, for example, [57, 58, 128–130]). As has been discussed in Section 1.1.3 in the inflationary context, the condition for acceleration is that, assuming components of the matter-energy budget can be treated as perfect fluids, the Universe is dominated by a component with equation of state less than $-\frac{1}{3}$. The cosmological constant satisfies this, with $w = -1$.

As in Section 1.2.1 on alternative theories of gravity, a popular model is now briefly considered, in order to elucidate by example some of the features of dynamical dark energy.

Quintessence: An example Quintessence [126, 127] is arguably the simplest dynamical dark energy model in the literature. It involves a scalar field, minimally coupled to gravity, rolling down a potential. Its action is hence exactly the same as that of slow-roll inflation, introduced above in equation 1.21. Varying this with respect to the scalar field ϕ produces the equation of motion for ϕ:

$$\ddot{\phi} + 3H\dot{\phi} + \frac{dV}{d\phi} = 0. \tag{1.30}$$

Varying then with respect to the metric and assuming that the scalar field can be described as a perfect fluid allows for the calculation of the equation of state of ϕ:

$$w_\phi = \frac{\dot{\phi}^2 - 2V(\phi)}{\dot{\phi}^2 + 2V(\phi)}. \tag{1.31}$$

It can be seen that in the case in which potential energy dominates, $w_\phi = -1$.

Many different possible choices for $V(\phi)$ have been explored in the literature, including exponential forms [131] and power-law forms [126, 127]. A subset of these potentials are chosen such that they address the cosmological constant problem, by ensuring what is known as a *tracking solution* [57] to equation 1.30. This is a solution whereby the late-time behaviour of ϕ is insensitive to the choice of initial conditions on ϕ and $\dot{\phi}$, thereby eliminating the need for the extreme fine-tuning of initial conditions which is typically required in the cosmological constant case.

Quintessence is perhaps the most well-known example of dynamical dark energy, but many others have been proposed. These include, for example, K-essence [59], in which the kinetic energy associated with the scalar field is non-canonical, and phantom dark energy models [132] in which the equation of state of the scalar field is less than -1. For a review of proposed dark energy models, see [133].

1.2.2.2 Current observational constraints

Since the discovery of late-time acceleration, a great effort has been made towards testing and constraining dark energy models. This has been motivated both by an interest in stringently testing the validity of the cosmological constant scenario, and by a desire to explore the possibility of dynamical dark energy. Typically, cosmological probes of dark energy have included Type 1a supernovae, BAO, the CMB, and measurements of the Hubble parameter via the standard distance ladder. Observables such as weak lensing and redshift-space distortions are also able to indirectly probe the expansion history through its effect on the growth of structure.

In observational studies, dynamical dark energy models are often parameterised by the corresponding time-evolving equation of state $w(z)$. Specifically, a popular choice is to expand $w(z)$ about its constant value today, as proposed in [134, 135]:

$$w(z) = w_0 + w_a \left(1 - \frac{1}{1+z}\right). \tag{1.32}$$

This is known as the Chevallier-Polarski-Linder (CPL) parameterisation. It is often chosen as a means of enabling the detection of a time-evolving $w(z)$, regardless of whether the true underlying time-dependence follows equation 1.32. The $\{w_0, w_a\}$ parameterisation will be employed in Chapters 2 and 5 of this work. Another, simpler option is to consider a constant equation of state w, in the hopes that should the true w be time-dependent, a measurement of $w \neq -1$ would indicate the necessity for further investigation.

Up-to-date constraints on these dark energy parameters are given by the 2015 *Planck* release. Constraints on a constant w from the combination of CMB temperature, E-mode polarization, and lensing, as well as BAO observations, supernova data, and measurements of the Hubble parameter, resulted in $w = -1.019^{+0.075}_{-0.080}$ [8]. This analysis was then extended to consider the parameterisation of equation 1.32, as well as to incorporate additional weak lensing and redshift-space distortion data. The result is displayed in Figure 1.4 [72].

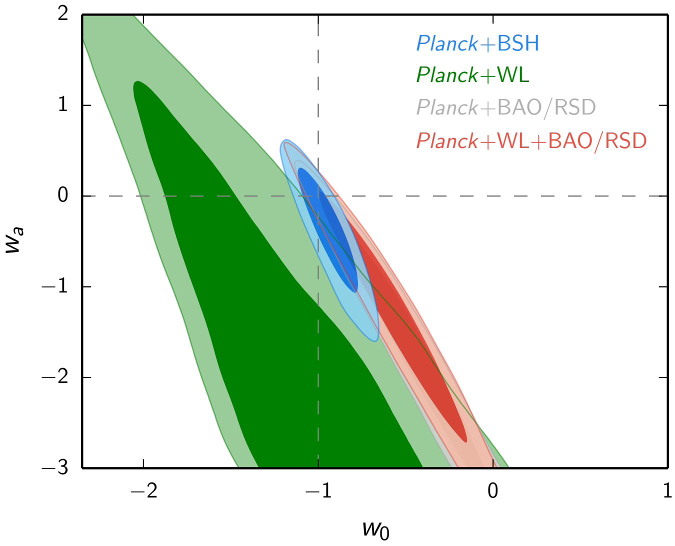

Figure 1.4: Source: Figure 4 (left) of [72], by the *Planck* collaboration. Constraints on the w_0 and w_a expansion history parameters (see equation 1.32), at the 68.3% and 95.4% confidence levels. $(-1, 0)$ represents the case of a cosmological constant, and 'BSH' signifies the inclusion of BAO, supernovae, and Hubble parameter measurements.

Many other attempts have been made in recent years to constrain dark energy, which have investigated both a general time-evolving $w(z)$ and specific dark energy models (see, for example, [136–142]). No compelling evidence has been found for a time-evolving equation of state of dark energy, however, more precise constraints will soon be possible with upcoming data.

1.2.3 Spatial curvature

1.2.3.1 Implications of non-zero spatial curvature

The spatial curvature of the Universe has been constrained to be very near zero [8]. Looking to equation 1.14, one can see that $\Omega_\mathrm{K} = 0$ implies that the total matter-energy density in the Universe is equal to the critical density. As described in Section 1.1.3, this requires that the total density in the early Universe was heavily fine-tuned, as anything else would result in significant divergences from the critical value today.

Inflation, as described in Section 1.1.3, was proposed in part to solve the flatness problem, by offering a natural mechanism by which to force the density to the required value at the end of the inflationary period [16, 17]. For this reason, a measurement of $\Omega_\mathrm{K} \neq 0$ today would rule out large swaths of inflationary model space, including the well-studied set of models known as eternal inflation [143]. Measuring or constraining Ω_K at a high precision would thus provide a strong test of early Universe physics.

The spatial curvature of the Universe can be observationally constrained by numerous cosmological observables, with the cosmic microwave background being a notably strong probe. Its sensitivity to Ω_K derives from the fact that features of known intrinsic size on curved surfaces exhibit different observed sizes than in the flat case. This means that an open or closed Universe would force structural features (peaks) in the CMB anisotropy power spectra to shift away from their expected flat-Universe location in multipole space.

However, taking again the CMB as an example, there also exist several biases and degeneracies which can affect constraints and measurements of spatial curvature. For example, the case in which an observer is within a large local inhomogeneity can induce a change in the inferred distance to the CMB, thus shifting the peaks in a similar manner as would spatial curvature [144]. The presence of dark energy can similarly shift the peaks of the CMB spectra, in an effect known as the geometric degeneracy [145–147]. Further such examples of biases and degeneracies which must be taken into account when constraining Ω_K are discussed in Chapter 5. The implication is that a measurement of, or constraint on, Ω_{K} at high precision is not merely a test of early Universe physics, but rather a probe of many assumptions within the standard cosmological paradigm. A measurement of non-zero spatial curvature would thus be indicative of some non-standard cosmological physics, and would provide a mandate to investigate further. This notion of Ω_{K} as a litmus test for precise and accurate cosmological constraints is discussed in Chapter 5.

1.2.3.2 Current observational constraints

Current best constraints on Ω_{K} from CMB and BAO data are given in the *Planck* 2015 parameters paper. Combining *Planck* temperature and lensing data, as well as BOSS BAO measurements, constrains $|\Omega_{\mathrm{K}}|$ to be less than 5×10^{-3} at a 95.4% confidence level. This constraint was achieved assuming a ΛCDM model with spatial curvature and no additional extensions. In Chapter 5, in which future constraints on Ω_{K} are considered, this value will be taken as a benchmark against which to compare forecast constraints.

Other observational works have examined the effect of varying additional non-ΛCDM parameters in combination with Ω_{K}, such as the number and mass of neutrinos [148, 149]. In these cases, comparable constraints were found to be achievable with the addition of other datasets such as supernovae and ground-based CMB observations.

1.3 Probing the standard paradigm with observations

With the theoretical background of the previous two sections in hand, it is now possible to consider whether and how cosmological observations can distinguish between the standard cosmological paradigm and the extensions which have been discussed.

A particular question of interest in this thesis is how weak gravitational lensing can constrain or detect signatures of beyond-standard cosmology. In this section, weak gravitational lensing is first reviewed, and other complementary cosmological probes are described. An introduction is then provided to the Fisher forecasting method, which will be employed in this thesis to obtain predicted parameter constraints from future observations and hence to explore degeneracies in multi-dimensional parameter space. Finally, a brief description is made of relevant cosmological surveys and experiments.

1.3.1 Gravitational lensing

The trajectories of photons traversing the Universe are affected by the gravity of intervening masses, causing observed images to appear distorted. This phenomenon is known as gravitational lensing.

There are two main regimes of observational gravitational lensing: strong and weak. Strong lensing is characterised by distinct features such as double images or arcs tangential to the lensing object. Weak lensing, on the other hand, is the case in which the distortion (usually of galaxy images) is too small to be detected for a single object. Instead, weak lensing analysis requires taking the statistical average over many lensed galaxies in order to detect a signal. Despite this more subtle effect, weak lensing is an extremely useful cosmological observable. It is employed to constrain standard cosmological parameters (e.g. [150, 151]), and is widely recognised as a promising probe of cosmology beyond the standard paradigm, especially in tests of gravity on cosmological scales [112–119].

1.3.1.1 An introduction to weak gravitational lensing

Weak lensing is by definition insufficiently strong to cause the multiple images or arcs which are associated with strong lensing systems. Instead, the weak lensing of a population of sources is quantified in two ways: convergence, which describes the size magnification, and shear, which represents the change in ellipticity (see, for example, [152]).

To understand how convergence, κ, and shear, γ, are defined, consider an image arising from a source at comoving distance χ. The position of any point of this image can be described by the coordinate system $\{\chi\theta_1, \chi\theta_2, \chi\}$ where $\vec{\theta} = \{\theta_1, \theta_2\}$ are the two-dimensional coordinates on the plane at χ orthogonal to the line of sight [9]. Let the underlying 'true' position (prior to lensing) be described by $\vec{\theta}_{\rm S}$, and let the position at which it is observed be $\vec{\theta}$. A Jacobian matrix is given by: $\mathcal{A}_{ij} = \frac{\partial\theta^i_{\rm S}}{\partial\theta_j}$. The convergence and the shear are then defined as follows (see, for example, [9, 152, 153]):

$$\mathcal{A} = \begin{bmatrix} 1-\kappa-\gamma_1 & -\gamma_2 \\ -\gamma_2 & 1-\kappa+\gamma_1 \end{bmatrix} .$$

The convergence describes magnification and can therefore can be represented by a scalar which varies with on-sky position. The shear, however, requires two numbers to encapsulate shape distortion in the on-sky plane. These two components are most conveniently presented as the complex number $\gamma = \gamma_1 + i\gamma_2$. γ transforms not as a vector, but as a polar (i.e., with the transformational properties of linear polarization).

In this scenario, γ_1 and γ_2 are defined with respect to a Cartesian coordinate system on the sky which can be arbitrarily chosen. However, at times, and especially when considering lensing by a particular foreground object or a stack thereof, it is preferable to employ a slightly more natural set of coordinates for the shear. The tangential shear, $\gamma_{\rm t}$ and the cross shear, $\gamma_\times$ fulfil this function. They are given as (see, for example, [153]):

$$\begin{aligned} \gamma_{\rm t} &= -{\rm Re}(e^{-2i\phi}\gamma) \\ \gamma_\times &= -{\rm Im}(e^{-2i\phi}\gamma) \end{aligned} \tag{1.33}$$

where ϕ is the angular polar coordinate describing the position of the galaxy image relative to the original Cartesian coordinate system in which γ is defined. $\gamma_{\rm t}$, the tangential shear, describes the radial mode of shear about the origin (often the position of a lensing object), whereas $\gamma_\times$ provides the cross component.

In practice, the shear rather than the convergence is the standard observable of weak gravitational lensing surveys. This is due to the fact that in order to extract a signal which can be attributed to gravitational lensing, the intrinsic average signal is required. For galaxy ellipticities, this can often be assumed to be zero for a sufficiently large population of galaxy images. However, convergence has no such convenient zero point. Although some recent work has examined the possibility of extracting convergence information from lensing surveys [154–156], shear remains the most common observable. Galaxy ellipticities obtained using shape measurement pipelines (e.g. [157]) are therefore a common data product of weak lensing surveys.

However, as has been seen, the two-component shear is more theoretically complicated than the scalar convergence. Therefore, ideally, observations would be reported in terms of shear while predictions would be made in terms of convergence. Fortunately, this is effectively possible, as shear and convergence can easily be related. In Fourier space, this relationship is given by (see, for example, [158]):

$$\gamma\left(\vec{l}\right) = \frac{\left(l_1 + i l_2\right)^2}{l^2} \kappa\left(\vec{l}\right) \tag{1.34}$$

where $\vec{l} = \{l_1, l_2\}$ is the two-dimensional on-sky Fourier-space variable, and l is its magnitude. The result is that the power spectrum of the shear is in general equal to that of the convergence.

Typically, weak gravitational lensing source images are of distant galaxies. Other potential sources do however exist, most notably the cosmic microwave background [159–161], the weak lensing of which will be considered in Chapter 5. In the case in which the source images are galaxies, convergence in this work will be labelled κ_{g}, while for CMB weak lensing, convergence will be denoted κ_{c}.

1.3.1.2 Cosmic shear

Cosmic shear is the name given to the weak lensing of galaxy images by the large-scale structure of the Universe. First detected in 2000 [3], it has since been measured by several surveys, including, for example, CFHTLenS [150, 151]. The Dark Energy Survey and the Kilo Degree Survey have also both recently produced cosmic shear measurements from their early data [162, 163].

The quantity of interest in the measurement of cosmic shear is the two-point function of the convergence or of the shear. Observational work usually reports cosmic shear measurements in terms of correlation functions in real-space, while theoretical predictions of cosmic shear are more likely to utilise the Fourier-space power spectrum. The power spectrum of the convergence (under the assumption of GR and ΛCDM) is given by:

$$C^{\ell}_{\kappa^i_{\rm g}\kappa^j_{\rm g}} = \frac{9}{16}\int_0^{\chi_\infty} d\chi \frac{g_i(\chi)g_j(\chi)}{f_K(\chi)^2c^4}\left(H(\chi)a(\chi)\right)^4\Omega_{\rm M}(\chi)^2 P_\delta\left(\frac{\ell}{f_K(\chi)},\chi\right), \tag{1.35}$$

where P_δ is used to refer to the matter power spectrum (shown in Figure 1.2). The lensing kernel g is

$$g_i(\chi) = 2f_K(\chi)\int_\chi^{\chi_H}\frac{f_K(\chi'-\chi)}{f_K(\chi')}W_i(\chi')d\chi', \tag{1.36}$$

and $W_i(\chi)$ is the distribution of source galaxies in comoving distance χ for redshift bin i. In recent cosmic shear analyses, it is typical to divide the source galaxy sample into several redshift bins and to consider both auto- and cross-correlations of these bins, in a technique known as tomographic weak lensing. The derivation of this power spectrum is reviewed and extended beyond GR in Chapter 2.

The validity of equation 1.35 depends upon the use of the Limber approximation [164, 165]. In order to briefly summarise the Limber approximation, recall first that the Limber equation is a general expression relating a two-dimensional two-point correlation to a three-dimensional two-point correlation via integration over a kernel function. This type of equation figures in the derivation of equation 1.35, as will be seen explicitly in Section 2.2. The Limber approximation, which can greatly simplify the integral expression in question, is the assumption that the kernel varies slowly over its argument. In the current context, the kernel is assumed to be slowly varying in the radial direction. A crucial aspect of the Limber approximation in this case is that it allows the three-dimensional Fourier space variable k to be set equal to $l/f_K(\chi)$, which becomes $\ell/f_K(\chi)$ at small angles (where ℓ labels an angular multipole). The trade-off for the considerable simplification offered is that the Limber approximation is not valid for the largest angular scales, and therefore equation 1.35 is applicable only for $\ell \geq 10$.

In addition to weak gravitational lensing, other physical effects can contribute to the observed correlation between galaxy ellipticities. These can engender an intrinsic contribution to the observed ellipiticity power spectrum, and hence to the inferred shear power spectrum if not taken into account. With these effects, referred to as intrinsic alignments, the observed power spectrum of galaxy ellipticity is given by

$$C^{\ell}_{\epsilon^i\epsilon^j} = C^{\ell}_{\kappa^i_{\rm g}\kappa^j_{\rm g}} + C^{\ell}_{\kappa^i_{\rm g}I^j} + C^{\ell}_{I^i\kappa^j_{\rm g}} + C^{\ell}_{I^iI^j} \, , \tag{1.37}$$

where I represents the intrinsic ellipticity. Intrinsic alignments have been measured within a number of galaxy lensing surveys (for example, [166, 167]).

It can be seen that there are two types of intrinsic alignment terms present in equation 1.37. The first type, exhibited in the second and third term on the right side of the equation, represents the case in which an overdensity at redshift z causes not only tangential shear in background galaxies, but also intrinsic radial alignment in nearby galaxies at z. The second type of intrinsic alignment, described by the final term of equation 1.37, represents the correlation between galaxies at the same redshift which are aligned radially about an overdensity (or tangentially about a void).

The power spectra representing these two types of intrinsic alignment correlations have been modelled in a number of different ways, with varying degrees of complexity (see, for example, [168, 169]). In Chapter 5 of this work, a linear intrinsic alignment model is employed in which it is assumed that the intrinsic alignment of galaxies is fixed early in their lifetime. Expressions for the final three terms on the right side of equation 1.37 are then given by (see, for example, [170, 171]):

$$\begin{aligned} C^{\ell}_{\kappa^i_{\rm g}I^j} &= -\frac{3C_1\rho_{\rm c}\Omega_{\rm M}(z=0)}{4}\int_0^{\chi_\infty} d\chi \frac{g_i(\chi)W_j(\chi)}{f_K(\chi)^2D(x)} f_{\rm red}(\chi)\Omega_{\rm M}(\chi) \\ &\qquad\qquad\qquad \times\sqrt{P^{\rm lin}_{\delta}\left(\frac{\ell}{f_k(\chi)}, z=0\right) P^{\rm NL}_{\delta}\left(\frac{\ell}{f_k(\chi)}, \chi\right)} \, , \\ C^{\ell}_{I^iI^j} &= (C_1\rho_{\rm c})^2\Omega_{\rm M}(z=0)^2 \int_0^{\chi_\infty} d\chi \frac{W_i(\chi)W_j(\chi)}{f_K(\chi)^2} f_{\rm red}(\chi)^2 P^{\rm lin}_{\delta}\left(\frac{\ell}{f_k(\chi)}, z=0\right) \, , \end{aligned} \tag{1.38}$$

where $D(x)$ is the linear growth factor, and $f_{\rm red}$ is the fraction of red galaxies. $C^{\ell}_{I^i\kappa^j_{\rm g}}$ is found simply by switching i and j in the expression for $C^{\ell}_{\kappa^i_{\rm g} I^j}$. Note that equation 1.38 makes use of the Limber approximation.

Figure 1.5 presents the theoretical angular power spectra (under GR) of $C^{\ell}_{\kappa_{\rm g}\kappa_{\rm g}}$, $C^{\ell}_{\kappa_{\rm g} I}$,and C^{ℓ}_{II}, for a $W(\chi)$ given below by equation 2.42 with a single redshift bin, and assuming a red galaxy fraction of $f_{\rm red} = 0.5$. As can be seen, the shear term dominates over intrinsic alignment correlations, but intrinsic alignments are not entirely insignificant.

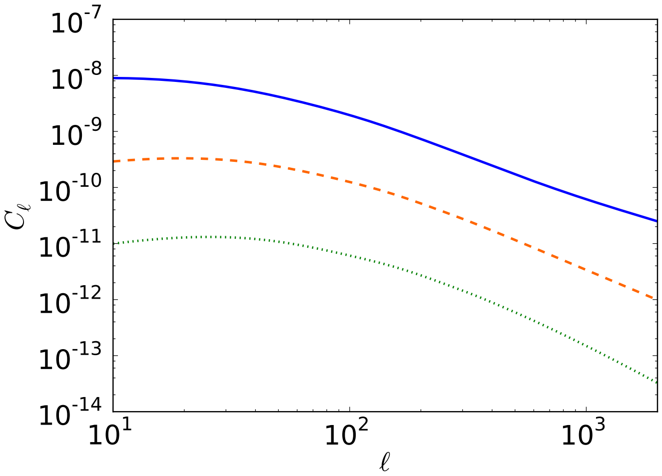

Figure 1.5: Angular power spectra of the cosmic shear $C^{\ell}_{\kappa_{\rm g}\kappa_{\rm g}}$ (equation 1.35, blue, solid), the 'intrinsic-intrinsic' intrinsic alignment correlation term, C^{ℓ}_{II} (equation 1.38, green, dotted), and the absolute value of the 'intrinsic-shear' intrinsic alignment term, $C^{\ell}_{\kappa_{\rm g} I}$ (equation 1.38, orange, dashed). In the latter case, the true spectrum is negative at all ℓ presented. The source window function is given by equation 2.42 (below) with a single redshift bin, and cosmological parameters values are from [8].

1.3.1.3 Galaxy-galaxy lensing

Galaxy-galaxy lensing is the case in which, instead of measuring the two-point correlation of the convergence or of the shear (e.g. $\langle \kappa_{\rm g}\kappa_{\rm g}\rangle$), a correlation is measured between weak lensing effects and galaxy positions ($\langle \kappa_{\rm g} g\rangle$). Galaxy-galaxy lensing has been measured using a number of datasets, including the Sloan Digital Sky Survey [172], CFHTLenS [173], and the Dark Energy Survey [174]. It has also been instrumental in testing alternative theories of gravity as part of the statistic E_G [70, 71, 116].

Similarly to cosmic shear, galaxy-galaxy lensing is preferentially measured in real-space. A key quantity of galaxy-galaxy lensing is $\Delta\Sigma_{gm}(R)$, which can be thought of as a projected correlation function between galaxy positions and matter (as traced by weak lensing). In order to measure $\Delta\Sigma_{gm}(R)$, pairs of lens and source galaxies are considered, and the ellipticities of source galaxies are summed in projected radial bins centred on lens galaxies. Lens galaxies, with related source galaxy lensing information, are then stacked in order to achieve a statistical measurement. $\Delta\Sigma_{gm}(R)$ will be discussed further in Chapter 4, in which the effect of measuring galaxy-galaxy lensing in real-space while comparing to predictions in Fourier-space is considered. $\Delta\Sigma_{gm}(R)$ can be written as:

$$\Delta\Sigma_{gm}(R) = \overline{\Sigma}_{gm}(R) - \Sigma_{gm}(R), \tag{1.39}$$

where $\Sigma_{gm}(R)$ is the projected surface mass density at R inferred from the weak lensing of source galaxies.

The Fourier-space cross-spectrum of the convergence with galaxy positions, which is qualitatively similar to the real-space $\Delta\Sigma_{gm}(R)$, is given by:

$$C^{\ell}_{\kappa^i_{\rm g} g^j} = \frac{3}{4}\int_0^{\chi_\infty} d\chi b(\ell,\chi)\frac{g_i(\chi)W_j(\chi)}{f_K(\chi)c^2}(H(\chi)a(\chi))^2\Omega_{\rm M}(\chi)P_\delta\left(\frac{\ell}{f_K(\chi)},\chi\right), \tag{1.40}$$

where b is the galaxy bias, as defined below in equation 1.41. This equation assumes the Limber approximation and so is valid only at $\ell \geq 10$.

Galaxy-galaxy lensing and cosmic shear are expected to be affected by different systematic errors [175]. This provides a useful opportunity to check for consistency in cosmological parameter constraints, and to ensure that systematic effects have been properly removed from the data. Additionally, intrinsic alignments are less problematic in the galaxy-galaxy lensing case, because lens-source pairs can be chosen such that the paired galaxies are likely to be removed from each other in redshift. This is not possible in the cosmic shear case, in which the lens is the large-scale structure along the line-of-sight.

1.3.2 Other cosmological probes

The focus of this thesis is the use of weak lensing as a test of cosmology beyond the standard paradigm. However, as will be seen, combinations of multiple cosmological observables are typically required to break degeneracies and achieve the best possible parameter constraints. Two other cosmological observables which will be considered in combination with weak lensing are now briefly introduced.

1.3.2.1 Galaxy clustering

Galaxy clustering refers to correlations between galaxy positions. These are most commonly quantified by the two-point galaxy correlation function and the galaxy power spectrum. The galaxy power spectrum is given in the simplest case by

$$P_{gg}(k,z) = b(k,z)^2 P_{\delta}(k,z)\,, \tag{1.41}$$

where b is the galaxy bias. The galaxy bias encapsulates the difference in amplitude between the distributions of matter and of galaxies. It can depend on scale and redshift, as denoted here, as well as on characteristics of the galaxy population. The galaxy bias represents an important potential source of degeneracy in galaxy-based tests of cosmology, as will be seen in Chapter 4.

The power spectrum P_{gg}, or equivalently the real-space correlation function, can in principle be measured directly and used to constrain cosmological parameters. An alternative observational strategy is to focus on particularly informative features of the two-point functions. Two such features which take a prominent place in the large-scale structure literature are redshift-space distortions and baryon acoustic oscillations.

Redshift-space distortions: The position of a galaxy along the line-of-sight is determined not directly in real-space but via a measurement of its redshift. In the case in which the redshift is sourced by only the Hubble flow, this can result in correctly recovering the galaxy's real-space position. However, when peculiar velocities are present, this method leads to features in the galaxy power spectrum known as redshift-space distortions.

One option for dealing with this discrepancy between real- and redshift-space is to consider the projected two-point function. In this case, the three-dimensional correlation function is integrated along the line-of-sight, a procedure which is expected to result in the cancellation of all redshift-space distortion effects. The projected two-point correlation function, which will be considered in Chapter 4, is defined as (see, for example, [176]):

$$w_{gg}(R) = \int_{-P}^{P} d\Delta\, \xi^s_{gg}\,(\Delta, R)\,, \tag{1.42}$$

where P is the line-of-sight distance over which the projection occurs, and ξ^s_{gg} is the redshift-space correlation function of galaxies.

However, it is not always desirable to eliminate the effects of peculiar velocities, as they may contain valuable information. Peculiar velocities are the result of the gravitational infall of galaxies towards overdense regions. This means that redshift-space distortions can act as a probe of large-scale structure. Specifically, the redshift-space power spectrum of galaxies in linear theory is given by [177]

$$P^s_{gg}(k_{||}, k_{\perp}, z) = (1 + \frac{f}{b}\mu^2)^2 b^2 P_{\delta}(k, z)\,, \tag{1.43}$$

where $\mu = \frac{k_{||}}{k}$, and $k = \sqrt{k_{||}^2 + k_{\perp}^2}$. For an example of the equivalent real-space two-point correlation function measured in [49], see Figure 1.6.

f is the observable of interest in equation 1.43: the linear growth rate of structure, defined as:

$$f(a) = \frac{d\ln\Delta_{\rm M}}{d\ln a}. \tag{1.44}$$

f is defined in the linear regime and on sub-horizon scales, such that in a GR context, it does not depend on k. It is not normally measured independently, because it is degenerate with the amplitude of the matter power spectrum. The related observable quantity is $f\sigma_8(a)$, where σ_8 is the amplitude of the matter power spectrum within spheres of radius 8 Mpc/h, and can be directly related to A_s. Redshift-space distortion

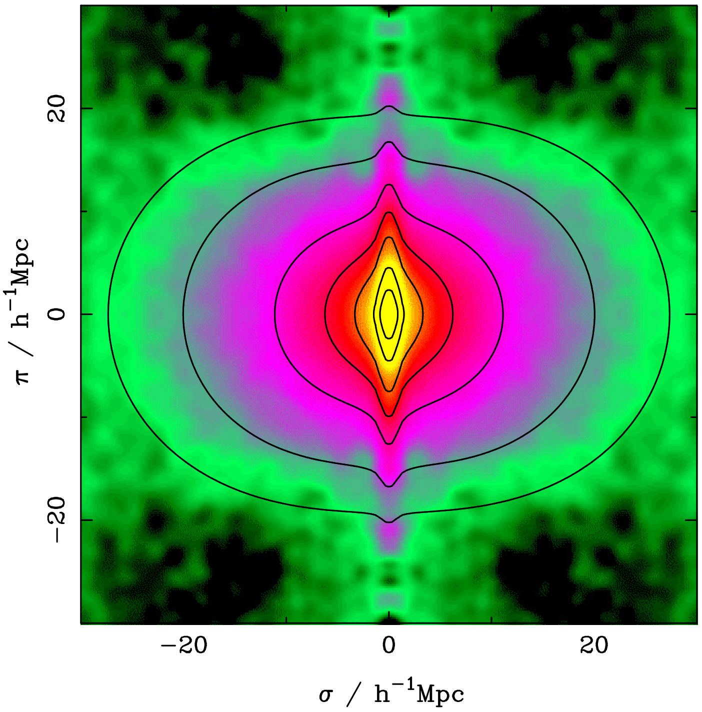

Figure 1.6: Source: Figure 2 of [49], by Peacock et al. The anisotropic redshift-space correlation function of galaxies, as measured by the 2dF Galaxy Redshift Survey. σ is separation transverse to the line-of-sight, while π is line-of-sight separation.

measurements of $f\sigma_8$ will be examined as a complementary probe to weak lensing in Chapters 2 and 3. The ratio f/b is also sometimes measured from redshift-space distortion observations. This quantity, usually called β, will be employed in Chapter 4.

Baryon acoustic oscillations Baryon acoustic oscillations (BAO) are a feature of galaxy clustering which was imprinted in the early Universe. At early times (post-inflation), photons and baryons were coupled in a single plasma. This plasma underwent oscillations as a result of the competing effects of the baryons' gravitational attraction to dark matter overdensities and the photons' radiation pressure.

Once the Universe had expanded and cooled such that baryons could recombine into atoms, the photons began to free-stream, forming the cosmic microwave background (see Section 1.3.2.2). The scale of oscillation at the time of decoupling was frozen into the baryon distribution, such that there exists an excess of galaxies at the corresponding characteristic scale in the large-scale structure distribution (see, for example, [178,179]). This can be observed as an excess in the real-space correlation function, or as an oscillatory feature in the Fourier-space power spectrum (see Figure 1.7). The BAO scale has been measured in numerous galaxy surveys (e.g. [180–182]).

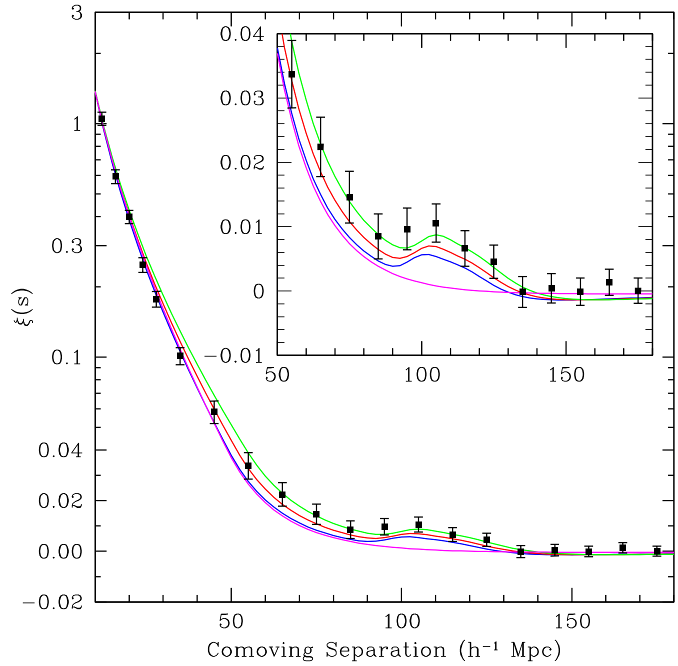

Figure 1.7: Source: Figure 2 of [54], by Eisenstein et al. The BAO peak in the real-space two-point correlation function, as measured in [54] using Sloan Digital Sky Survey luminous red galaxies. Coloured lines represent models with different fractions of cold dark matter, and the magenta line demonstrates the case without baryons (and hence with no peak).

Because baryon acoustic oscillations are a product of the early Universe, the scale at which they are measured at late times depends on the expansion history and hence $w(z)$. This feature will be utilised in Chapters 2 and 5.

1.3.2.2 The cosmic microwave background

The cosmic microwave background (CMB) consists of photons from the surface of last scattering, which have free-streamed since decoupling from the baryon-photon plasma. The CMB was first detected in 1964 [183], with more recent measurements placing the photon temperature at 2.7260 K [184]. However, the CMB offers far more information than a single temperature value.

Primordial perturbations from inflation seeded anisotropies in the CMB at the 10^{-5} level, the power spectra of which can be measured and used to constrain cosmological parameters to high precision (see Figure 1.8 for the temperature anisotropy power spectrum as measured by *Planck*). The fact that CMB anisotropies are present at this low level is one of the great advantages of CMB observations over other cosmological probes: issues arising from non-linear structure formation have negligible effect on primary CMB observables.

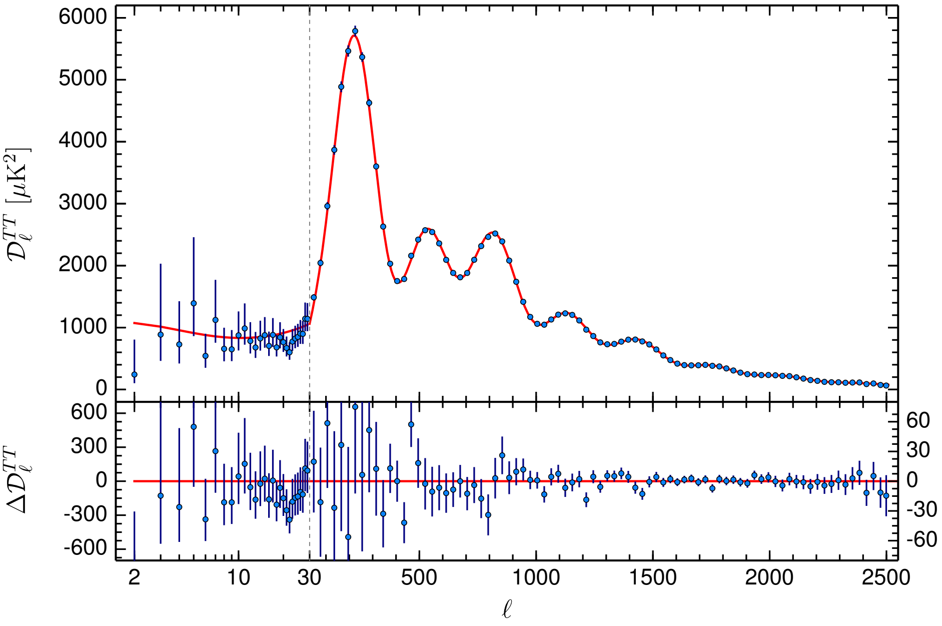

Figure 1.8: Source: Figure 11 of [185], by the *Planck* collaboration. The CMB temperature anisotropy power spectrum, as presented in the *Planck* 2015 release. The lower panel displays residual differences between model and data, for clarity.

Following the 1964 detection of the CMB, the COBE satellite of the 1990s was the first to detect the power spectrum of temperature anisotropies [48]. Soon after, the Wilkinson Microwave Anisotropy Probe (WMAP) [186] and later the *Planck* satellite [8] provided more precise measurements. Observations from *Planck* are essential to our current best cosmological parameter estimates. Additionally, ground-based CMB surveys such as, for example, the Atacama Cosmology Telescope [187, 188] and the South Pole Telescope [189], contribute important constraining power on smaller scales.

The major observables of CMB cosmology are the angular power spectra of the temperature, of E- and B-mode polarization, of the weak lensing of the CMB, and of relevant cross-correlations between these. The E- and B-mode components of CMB polarization represent a decomposition in which one mode, E, is curl-free, and the other, B, is divergence-free. B-mode polarization in particular has garnered interest in recent years as a probe of the primordial tensor to scalar ratio r [190, 191], a key quantity of inflationary theory. Significant work is currently underway to ensure that foreground contaminants affecting B-mode measurements can be effectively removed (see, for example, [192]).

In Chapter 5, CMB observations will be considered in combination with BAO and weak lensing in forecasting constraints on the spatial curvature of the Universe from future surveys.

1.3.3 Tests of the standard paradigm with future surveys

As has been discussed, in the coming years, a series of planned surveys and experiments will lend hugely increased statistical power to many cosmological observables. In particular, galaxy images suitable for weak gravitational lensing analysis will be obtained in unprecedented quantities. With this increase in data volume and corresponding decrease in statistical error bars comes a new set of challenges. It will become essential that parameter degeneracies and theoretical uncertainties be understood at a level which has never before been required. One way to investigate degeneracies which will affect upcoming observations is Fisher forecasting. This method will now be discussed, and a brief description will be provided of a number of current and upcoming surveys which are relevant to the work presented in this thesis.

1.3.3.1 Fisher forecasting

In the context of cosmological parameter estimation, forecasting is a procedure whereby given some knowledge of a future set of observations, expected parameter constraints can be predicted. The resulting information can determine the specifications required for a given survey design to achieve target parameter constraints. It can also offer insight into the more general interplay between theory and observation, as it provides not only predicted constraints on individual parameters, but also the anticipated structure of constraints in multi-dimensional parameter space. Given an observable and a set of parameters to be constrained, forecasting can establish the combination of parameters upon which bounds can realistically be placed. It can therefore also highlight the directions of parameter space in which other observables will be necessary to break degeneracies and pin down parameter values.

There are several methods of conducting forecasts. For example, one popular procedure makes using of Markov Chain Monte Carlo (MCMC) methods to build up an anticipated posterior probability distribution. By assuming a mock set of observations and invoking Bayes theorem, the posterior can be evaluated for a particular sample of cosmological parameters values. Doing this at many points in parameter space results in an anticipated posterior probability distribution. This forecasting procedure has the advantages of being practically similar to parameter estimation from real data, and allowing total freedom in the shape of the posterior probability distribution. However, it is computationally intensive and can be non-trivially complex to implement.

Another possible method is known as Fisher forecasting. While not as general as an MCMC-based approach, Fisher forecasting is computationally less intensive and in principle simpler to implement. For these reasons, Fisher forecasting will be the method of choice in this thesis to explore degeneracies and predict parameter constraints from future surveys.

The key quantity of Fisher forecasting is the Fisher information matrix [193]

$$\mathcal{F}_{ab} = -\left\langle \frac{\partial^2 \ln \mathcal{L}(\vec{d};\vec{p})}{\partial p_a \partial p_b} \right\rangle , \tag{1.45}$$

where $\vec{p}$ is a vector containing the relevant parameters p_i, and $\mathcal{L}(\vec{d};\vec{p})$ is the likelihood of the data $\vec{d}$ given the parameter values $\vec{p}$. Angle brackets here indicate an expectation value. In the case where the likelihood can be approximated as a multivariate Gaussian and priors are uninformative, the Fisher information matrix approximates the inverse covariance matrix and hence contains valuable information as to expected parameter constraints. To see intuitively how this is true, one can Taylor expand $\ln \mathcal{L}$ about a fiducial set of parameters $\vec{p}_*$, which is assumed to be the set of maximum likelihood values:

$$\ln \mathcal{L}(\vec{d};\vec{p}) \approx \ln \mathcal{L}(\vec{d};\vec{p}_*) + \frac{1}{2} \sum_a \sum_b \left. \frac{\partial^2 \ln \mathcal{L}(\vec{d};\vec{p})}{\partial p_a \partial p_b} \right|_{\vec{p}_*} (p_a - p_a^*)(p_b - p_b^*) + \dots \tag{1.46}$$

The first order term has vanished, because the first derivative of the likelihood is zero at the maximum likelihood parameter values. The second order term contains the second derivative of the logarithm of the likelihood, sometimes called the curvature matrix, the negative expectation value of which is the Fisher matrix. Qualitatively, it can be seen from equation 1.46 that the Fisher matrix provides a quantification of how sensitive the likelihood is to changes in the parameters near their maximum likelihood values.

More rigorously, the Cramér-Rao bound [194] can be invoked to show that the inverse of the Fisher matrix is, from a frequentist perspective, the best possible parameter covariance matrix. In the more relevant Bayesian sense, it can be shown that the Hessian matrix (the curvature matrix with opposite sign) is equal to the inverse covariance matrix in the case in which the likelihood is a multivariate Gaussian (see, for example, [195]).

Assuming then that the likelihood is a multivariate Gaussian, the Fisher matrix can be calculated as (see, for example, [196])

$$\mathcal{F}_{ab} = \frac{\partial\langle\vec{d}\rangle}{\partial p_a}\mathbf{C}^{-1}\frac{\partial\langle\vec{d}\rangle}{\partial p_b}\Bigg|_{\vec{p}_*} + \frac{1}{2}\mathrm{Tr}\left(\mathbf{C}^{-1}\frac{\partial\mathbf{C}}{\partial p_a}\mathbf{C}^{-1}\frac{\partial\mathbf{C}}{\partial p_a}\right)\Bigg|_{\vec{p}_*}, \tag{1.47}$$

where $\mathbf{C}$ is the covariance matrix of the data. In practice, often one term of this expression dominates heavily over the other. For example, in the case in which the covariance matrix is noise-dominated, the second term can be neglected. On the other hand, if the data $\vec{d}$ is chosen such that it has expectation value of zero, the first term is not required. The final form to which equation 1.47 evaluates is dependent on the choice of observable to be considered.

Finally, the Fisher matrix for weak lensing cosmic shear will be employed repeatedly throughout this thesis. For the case in which the corresponding observable is taken to be a map of galaxy ellipticities, equation 1.47 becomes [197]:

$$\mathcal{F}^{\mathrm{L}}_{ab} = \sum_{\ell}\frac{2\ell+1}{2}f_{\mathrm{sky}}\mathrm{Tr}\left[(\mathbf{C}(\ell))^{-1}\frac{\partial\mathbf{C}(\ell)}{\partial p_a}(\mathbf{C}(\ell))^{-1}\frac{\partial\mathbf{C}(\ell)}{\partial p_b}\right]. \tag{1.48}$$

where f_{sky} is the fraction of the sky covered by the survey area, and $\mathbf{C}(\ell)$ is an $N \times N$ matrix, where N is the number of tomographic redshift bins. The elements of $\mathbf{C}(\ell)$ are given by the observed angular power spectrum (including noise)

$$C^{i,j}(\ell) = C_{\ell}^{\kappa^i_{\mathrm{g}}\kappa^j_{\mathrm{g}}} + \frac{\langle\gamma^2_{\mathrm{int}}\rangle\delta_{ij}}{\bar{n}_i}, \tag{1.49}$$

where $C_{\ell}^{\kappa^i_{\mathrm{g}}\kappa^j_{\mathrm{g}}}$ was provided in equation 1.35, $\bar{n}_i$ is the number density of galaxies per steradian in bin i and $\langle\gamma^2_{\mathrm{int}}\rangle^{\frac{1}{2}}$ is the rms intrinsic shear.

Finally, an important feature of Fisher forecasting is that for a set of independent observables, combined Fisher matrices are found simply by adding individual Fisher matrices. Other Fisher matrices will be used in combination with that of the weak lensing cosmic shear throughout this thesis, and will be introduced when required.

1.3.3.2 Ongoing and upcoming cosmological surveys

As discussed, a principle objective of the work presented in this thesis is to explore the details of parameter degeneracies and theoretical uncertainties which may be important in future weak gravitational lensing tests of cosmology beyond the standard paradigm. In order to do this effectively, a number of current and upcoming surveys will be considered explicitly. A brief description of these is now provided, including weak gravitational lensing surveys as well as surveys which focus upon complementary observables such as those described in Section 1.3.2.

The Dark Energy Survey: The Dark Energy Survey, or DES [198], is an ongoing multinational project with the goal of understanding late-time acceleration. It employs the purpose-built Dark Energy Camera on the 4-metre Blanco telescope at the Cerra Tololo Inter-American Observatory, Chile. The DES wide-angle survey has an expected final observational area of 5000 square degrees over five years, with observations having begun in August 2013. The wide-angle survey focuses on observations of galaxy clusters, BAO, and weak gravitational lensing, with photometric galaxy redshifts expected over a range of $z \approx 0.2 - 1.3$. Recently, the DES collaboration released their first science papers using science-verification data (e.g. [162, 174, 199, 200]). DES additionally has a second survey which targets the observation of Type 1a supernovae, but this aspect is not considered here.

The Baryon Oscillation Spectroscopic Survey The Baryon Oscillation Spectroscopic Survey, or BOSS [201], is part of the now-complete third phase of the Sloan Digital Sky Survey (SDSS). Using the Sloan Foundation 2.5 metre telescope at the Apache Point Observatory, BOSS observed from 2009-2014 over approximately 10 000 square degrees. The objective of this survey was to measure the BAO scale at z= 0.32 and z=0.57, using spectroscopic redshifts and imaging of 1.5 million luminous red galaxies (LRGs) and 160 000 quasars.

The Dark Energy Spectroscopic Instrument The Dark Energy Spectroscopic Instrument, or DESI [202], is a spectrograph which will be mounted on the Mayall 4-metre telescope at the Kitt Peak National Observatory. The goal of the DESI survey is to provide spectroscopic redshifts, primarily for use in measurements such as of

BAO and redshift-space distortions. It is planned to run from 2018 to 2022, observing between 14 000 and 18 000 square degrees. It will observe three populations: 18 million emission-line galaxies, 4 million LRGs, and 3 million quasars. The LRG sample, which is considered in Chapter 4, is expected to have a redshift range of $z = 0.5 - 1$.

Euclid Euclid [1] is a satellite mission of the European Space Agency, planned for launch in 2020 with an expected lifetime of 6.5 years. Its primary science goals are the characterisation of dark energy, the investigation of possible deviations from GR, and the study of dark matter and large-scale structure. To achieve this, it will perform a galaxy survey over 15 000 square degrees with the objective of providing images suitable for weak gravitational lensing, BAO, and redshift-space distortion analysis. Euclid will measure spectroscopic redshifts for 50 million galaxies, and weak lensing shapes for 1.5 billion galaxies. A complementary ground-based component of the mission will enable photometric redshifts for weak lensing source galaxies. Note that at times in the following chapters, a survey will be considered which is referred to generically as a Dark Energy Task Force 4 (DETF4)-type survey. Euclid is one example of such a survey, and often the properties of the DETF4-type survey considered will be similar to those of Euclid

The Square Kilometre Array The Square Kilometre Array (SKA) [111] is a planned radio telescope to be constructed in South Africa and Australia. As the name suggests, the telescope, once complete, will have more than a square kilometre of collecting area. Its key science goals include the study of dark energy, reionisation, and galaxy evolution. The SKA will consist of two sub arrays: SKA LOW, a low-frequency aperture array to be constructed in Australia, and SKA MID, an array of mid-frequency dishes which will be located in South Africa and neighbouring countries. The SKA will be constructed in two phases: SKA1, which will begin construction in 2018 in the hopes of achieving early science by 2020, and SKA2, the full telescope, which is planned to be fully operational in 2030. The SKA is not designed as a single-survey instrument, but as a facility with which surveys can be performed. Currently, discussion is ongoing as to its potential use in performing an intensity mapping survey [203,204], in observing HI-emitting galaxies [205], and in measuring shapes of weak lensing sources in the radio [206,207].

The Large Synoptic Survey Telescope The Large Synoptic Survey Telescope (LSST) [2,208] is an optical telescope currently under construction, with science goals of understanding dark energy, dark matter, and transient events. Located on the Cerro Pachó ridge in Chile, it will employ an 8.4 metre mirror to image the whole sky every three nights. Its principle wide survey aims to image 18 000 square degrees of the sky, with 20 billion galaxies anticipated to be observed in total over ten years from 2023. Its main cosmological observables will be weak lensing, BAO, and supernovae. Redshifts of LSST galaxies will be obtained via photometry.

Planck *Planck* is a European Space Agency mission which has finished taking data [185]. It is a satellite mission with the goal of measuring CMB temperature and polarization anisotropies, as well as CMB lensing, on large scales. It provided unprecedented constraints on the ΛCDM cosmological parameters [8] as well as a convincing detection of the lensing of the CMB by large-scale structure [159,160]. After launching in 2009, *Planck* was fully functional for thirty months, with one of the two instruments (the Low Frequency Instrument) operating for more than four years.

The Advanced Atacama Cosmology Telescope Polarization Survey The Atacama Cosmology Telescope (ACT) is a 6-metre telescope in the Atacama dessert, Chile [187,188]. Its purpose is the observation of CMB temperature, polarization and lensing on relatively small scales, with a goal of constraining parameters which describe the early Universe as well as detecting galaxy clusters. The ACT collaboration has performed several stages of CMB surveys. Originally, the ACT survey measured temperature anisotropies and galaxy clusters (via the tSZ effect), with the first CMB power spectra published in 2010 [209]. Following this, the ACT camera was upgraded [210] to detect polarization, and used to undertake a new set of observations called ACTPol, from 2013 to 2015. Finally, further upgrades have permitted the current round of observations, Advanced ACTPol, sometimes abbreviated to Advanced ACT [211].

A Stage IV CMB survey A Stage IV CMB survey [212], sometimes abbreviated CMB-S4, is a proposed CMB survey which would combine the use of various current ground-based CMB telescopes (e.g., ACT, the South Pole Telescope [189]) with some additions and upgrades to improve small-scale measurements of the CMB, particularly in polarization. This survey would assist in placing limits on primordial gravitational waves, as well as in reconstructing the CMB lensing potential.

1.4 Thesis Outline

As has been stated, the objective of the research presented in this thesis is to investigate the parameter degeneracies and theoretical uncertainties which may affect weak gravitational lensing tests of cosmology beyond the standard paradigm. In this final introductory section, an outline of the remainder of the thesis is presented.

First, in Chapter 2, a new expression for the power spectrum of cosmic shear under small modifications to GR+ΛCDM is derived. This expression is employed to examine the degeneracy direction of weak lensing in the plane of the parameters of the quasistatic parameterisation functions μ and γ. Fisher forecasts are performed for a DETF4-type survey including weak lensing, redshift-space distortions, and BAO observations, with a focus on investigating degeneracies within a scale-independent ansatz for μ and γ. In Chapter 3, the same expression for the cosmic shear spectrum is employed, in combination with a generic formulation of the scale-dependence of μ and γ, to explore possibilities of constraining scale-dependent aspects of modifications to GR. Fisher forecasts are performed, and the resultant predicted constraints are presented in the planes of the parameter pairs which capture both scale-independence and scale-dependence in alternative theories of gravity.

Following this, Chapter 4 explores the theoretical uncertainty associated with the observational definition of the statistic $E_G(R)$. A new theoretical expression is derived from the observational definition of this gravity-testing statistic. It is then employed to explore the effect of varying auxiliary parameters on predictions of $E_G(R)$, and to evaluate the utility of the statistic in testing gravity with upcoming lensing and galaxy clustering surveys.

In Chapter 5, the ability of weak gravitational lensing combined with CMB and BAO observations to constrain spatial curvature is evaluated. A suite of current and upcoming cosmological surveys is considered, and a variety of beyond-ΛCDM parameters are incorporated, including parameters describing biases and systematic effects. Forecast constraints on spatial curvature are compared to the 'floor' value of $\Omega_{\rm K} \approx 10^{-4}$, below which it is not expected that flat and curved models of the Universe will be distinguishable.

Finally, conclusions are drawn in Chapter 6, where the potential of weak lensing as a probe of beyond-standard cosmology is discussed, and possibilities for future work are proposed.

Chapter 2

Exploring degeneracies in weak lensing tests of gravity with the linear response approach

2.1 Introduction

As has been discussed in Chapter 1, the upcoming generation of galaxy surveys represents a significant step forward for weak gravitational lensing as a cosmological observable. In particular, weak lensing is expected to serve as an excellent probe of gravity on cosmological scales [112–119]. In order to take full advantage of this situation, it is crucial to understand the degeneracies which may exist between the parameters to be constrained or measured. One way in which these degeneracies can be investigated is by developing novel theoretical tools which clarify the effect of modifications to GR on weak gravitational lensing. This is the goal of the work presented in this chapter.

In [213], an expression for the redshift-space distortion observable $f\sigma_8$ was derived in the case of linear deviations from the standard model of GR+ΛCDM. Here, a similar expression is constructed for $C_\ell^{\kappa_g\kappa_g}$, the angular power spectrum of the galaxy weak lensing convergence. The main advantage of this expression is that it clearly distinguishes the physical source of all modified gravity effects on $C_\ell^{\kappa_g\kappa_g}$, which allows for a more thorough interpretation and understanding of these effects than previously possible. While the focus of this chapter is on $C_\ell^{\kappa_g\kappa_g}$, recall from equation 1.34 that the two main weak lensing observables, convergence and shear, can be interconverted [152].

Therefore, convergence is treated as a proxy for weak lensing more generally, and all expressions which are derived here could be equivalently formulated in terms of shear.

This chapter is structured as follows: in Section 2.2, the derivation of the aforementioned new expression for $C_\ell^{\kappa_g\kappa_g}$ is detailed. Section 2.3 discusses how weak lensing degeneracy directions between gravitational parameters can be understood with the help of this expression. Section 2.4 presents forecast constraints on signatures of modified gravity from a Dark Energy Task Force 4 (DETF4)-type survey, and interprets these constraints. Conclusions are drawn in Section 2.5.

2.2 Convergence in modified gravity: the linear response approach

As described in Section 1.2.1, a commonly-used parameterisation of cosmologically-motivated gravitational theories is that which makes use of the quasistatic approximation. The quasistatic parameterisation is employed in this chapter because it is valid for the majority of cosmologically viable gravity theories, and it is applicable within the scales accessible by near-future galaxy surveys. The corresponding functions which encapsulate the effects of modifying GR, μ and γ, were defined in equation 1.29.

The derivation of the power spectrum of the convergence in general relativity is now reviewed. Following this, the derivation is generalised to alternative theories of gravity. In this chapter, as well as in Chapter 3, the simplifying assumption is made that radiation can be neglected for all redshifts of interest. That is, $\Omega_{\rm M}^{\rm GR}(z) + \Omega_{\Lambda}^{\rm GR}(z) \approx 1$. Additionally, the scalar perturbed FRW metric in the conformal Newtonian gauge is assumed, with the form given by equation 1.16.

2.2.1 Calculating convergence: general relativity

The convergence describes the magnification of an image due to lensing. This image could be sourced by a variety of astrophysical objects or phenomena; here, it is sourced by a collection of distant galaxies, and thus will be referred to as $\kappa_{\rm g}$. A derivation of the power spectrum of $\kappa_{\rm g}$ in general relativity is now reviewed, following closely the methods of [9]. For this derivation, a set of spatial coordinates $\vec{x} = (\chi\theta^1, \chi\theta^2, \chi)$ will be employed. χ is the comoving radial distance, while θ^1 and θ^2 are two-dimensional coordinates on a plane perpendicular to line of sight.

The relevant starting point to derive the power spectrum of $\kappa_{\rm g}$ is the geodesic equation for the displacement of a photon transverse to the line of sight. In the cosmological weak lensing context of general relativity, this is given by:

$$\frac{d^2}{d\chi^2}\left(\chi\theta^b\right) = -2\frac{\partial\Phi}{\partial(\chi\theta^b)}\,, \tag{2.1}$$

where it has been assumed that the gravitational potential Φ and the magnitude of θ^1 and θ^2 are small.

Equation 2.1 can be twice-integrated to obtain the 'true' on-sky position of a single light source as a function of the gravitational potential:

$$\theta^b_{\rm S} = -\frac{2}{\chi_{\rm S}}\int_0^{\chi_{\rm S}} d\chi' \int_0^{\chi'} d\chi'' \frac{\partial\Phi(\vec{x}(\chi''))}{\partial(\chi''\theta^b)} + \theta^b_{\rm obs} \tag{2.2}$$

where $\theta^b_{\rm obs}$ is the observed value of θ^b, and $\chi_{\rm S}$ is the comoving distance to the light source, in this case to a galaxy. Changing the order of integration leads to a simpler expression:

$$\theta^b_{\rm S} = -2\int_0^{\chi_{\rm S}} d\chi \frac{(\chi_{\rm S}-\chi)}{\chi_{\rm S}}\frac{\partial\Phi(\vec{x}(\chi))}{\partial(\chi\theta^b)} + \theta^b_{\rm obs}. \tag{2.3}$$

The two primary observables of weak gravitational lensing, the convergence and the shear, are then defined via a distortion matrix ψ_{ij} [9]:

$$\psi = \frac{\partial\theta^i_{\rm S}}{\partial\theta^j} - \delta_{i,j} = \begin{bmatrix} -\kappa_{\rm g} - \gamma_1 & -\gamma_2 \\ -\gamma_2 & -\kappa_{\rm g} + \gamma_1 \end{bmatrix}. \tag{2.4}$$

This matrix is related to the Jacobian matrix $\mathcal{A}_{ij}$, described in Section 1.3.1.1, via $\psi_{ij} = \mathcal{A}_{ij} - \delta_{ij}$. It can then clearly be seen that $\kappa_{\rm g} = -\frac{1}{2}(\psi_{11} + \psi_{22})$.

By implementing this definition, and in particular by converting derivatives with respect to θ^j to derivatives with respect to $\chi\theta^j$, the following expression is obtained for the convergence of a single galaxy at comoving distance $\chi_{\rm S}$ within general relativity:

$$\kappa_{\rm g}^{\rm GR} = \int_0^{\chi_{\rm S}} d\chi \frac{\chi_{\rm S}-\chi}{\chi_{\rm S}}\chi\left(\frac{\partial^2}{\partial(\chi\theta^1)^2} + \frac{\partial^2}{\partial(\chi\theta^2)^2}\right)\Phi(\vec{x}(\chi)). \tag{2.5}$$

This expression can be extended to allow for a population of source galaxies. This is accomplished by integrating over $W(\chi)$, which describes the normalised distribution of source galaxies with respect to comoving distance. The result is:

$$\kappa_{\rm g}^{\rm GR}(\vec{\theta}) = \frac{1}{2}\int_0^{\chi_\infty} d\chi\, g(\chi)\left(\frac{\partial^2}{\partial(\chi\theta^1)^2} + \frac{\partial^2}{\partial(\chi\theta^2)^2}\right)\Phi(\vec{x}(\chi)). \tag{2.6}$$

where $g(\chi)$ is the lensing kernel, given in equation 1.36, which incorporates $W(\chi)$ as well as a geometric factor. In this chapter, as in Chapters 3 and 4, a flat Universe will be assumed such that $f_K(\chi) = \chi$.

The power spectrum of the convergence is then computed, again following closely the method laid out in [9]. In the small-angle approximation, it is straightforward to find:

$$P_{\kappa_{\rm g}^i\kappa_{\rm g}^j}(l) = \frac{1}{4}\int d^2\theta\, e^{-I\vec{l}\cdot\vec{\theta}}\int_0^{\chi_\infty} d\chi\, g_i(\chi)\int_0^{\chi_\infty} d\chi'\, g_j(\chi')\int\frac{d^3k}{(2\pi)^3}\, P_\Phi(k)k^4 e^{I\vec{k}\cdot[\vec{x}-\vec{x}']} \tag{2.7}$$

where $\vec{x} = (\chi\theta^1, \chi\theta^2, \chi)$ and $\vec{x}' = (0, 0, \chi')$. i and j label the source redshift bins to be considered. Note that to avoid confusion, I is used here to denote an imaginary number.

Performing the integrals over θ^1 and θ^2 and then over k_1 and k_2 gives:

$$P_{\kappa_{\rm g}^i\kappa_{\rm g}^j}(l) = \frac{1}{4}\int_0^{\chi_\infty} d\chi\,\frac{g_i(\chi)}{\chi^2}\int_0^{\chi_\infty} d\chi'\, g_j(\chi')\int\frac{dk_3}{2\pi}\, P_\Phi\left(\sqrt{k_3^2 + \frac{l^2}{\chi^2}}\right)k^4 e^{Ik_3\cdot[\chi-\chi']}. \tag{2.8}$$

Finally, the Limber approximation [164, 165], valid on $l \geq 10$ [112], is employed, such that $k_3 \ll l/\chi$, and therefore $k \approx l/\chi$. The small angle limit also means that $P_{\kappa_{\rm g}^i\kappa_{\rm g}^j}(l) \simeq C_\ell^{\kappa_{\rm g}^i\kappa_{\rm g}^j}$, where ℓ labels an angular multipole [214]. It is therefore found that:

$$C_\ell^{\kappa_{\rm g}^i\kappa_{\rm g}^j} = \frac{\ell^4}{4}\int_0^{\chi_\infty} d\chi\,\frac{g_i(\chi)g_j(\chi)}{\chi^6}\, P_\Phi\left(\frac{\ell}{\chi}, \chi\right). \tag{2.9}$$

2.2.2 Calculating convergence: modified gravity

As is evident in equation 1.29, generally in non-GR theories $\Phi \neq \Psi$. So, in modified gravity, equation 2.1 becomes:

$$\frac{d^2}{d\chi^2}\left(\chi\theta^b\right) = -\frac{\partial(\Phi + \Psi)}{\partial(\chi\theta^b)}. \tag{2.10}$$

The convergence then becomes:

$$\begin{aligned}\kappa_{\rm g}^{\rm MG} &= \frac{1}{4}\int_0^{\chi_\infty} d\chi\, g(\chi)\left(\frac{\partial^2}{\partial(\chi\theta^1)^2}+\frac{\partial^2}{\partial(\chi\theta^2)^2}\right)[\Phi(\vec{x}(\chi))+\Psi(\vec{x}(\chi)] \\ &= \frac{1}{4}\int_{-\infty}^{0} dx\, \frac{c}{\mathcal{H}(x)} g(\chi(x))\left(\frac{\partial^2}{\partial(\chi(x)\theta^1)^2}+\frac{\partial^2}{\partial(\chi(x)\theta^2)^2}\right)[\Phi(\vec{x}(\chi(x)))+\Psi(\vec{x}(\chi(x)))]\end{aligned} \tag{2.11}$$

where hereafter in this chapter $x = \ln(a)$ is used, and the integration measure has been converted to x using $d\chi = -c/\mathcal{H}\, dx$, where $\mathcal{H} = aH$ is the conformal Hubble factor. Note that x here is entirely distinct from the three-dimensional position variable $\vec{x}$.

To calculate the power spectrum of the convergence under modifications to GR, the field equations are perturbed about those of the GR+ΛCDM model. Current observations only permit theories which can match GR+ΛCDM predictions to leading order; the objective here is to determine next-to-leading order corrections that are still permitted. The perturbations of the quasistatic functions μ and γ about their GR values are defined as:

$$\begin{aligned}\mu(x,k) &= 1+\delta\mu(x,k) \\ \gamma(x,k) &= 1+\delta\gamma(x,k).\end{aligned} \tag{2.12}$$

In addition, a perturbation about the standard value of the effective equation of state of the non-matter sector, $w(x)$, is introduced:

$$w(x) = -1+\beta(x), \tag{2.13}$$

and a useful related quantity is defined:

$$u(x) = \int_0^x \beta(x')\, dx'. \tag{2.14}$$

Consider now how these linear perturbation variables propagate through to $\kappa_{\rm g}$ and hence to $C_\ell^{\kappa_{\rm g}^i\kappa_{\rm g}^j}$. First, from equation 1.29:

$$\begin{aligned}\Phi(x,k)+\Psi(x,k) &= \left(1+\frac{1}{\gamma(x,k)}\right)\Phi(x,k) \\ &\approx (2-\delta\gamma(x,k))\,\Phi(x,k).\end{aligned} \tag{2.15}$$

In order to express results as corrections to GR+ΛCDM, $\Phi(x,k)$ must be related to $\Phi_{\rm GR}(x,k)$. There are two effects to be accounted for. First, the relationship between $\Phi(x,k)$ and matter density perturbations can be altered. Second, if the field equations are modified, $\Delta_{\rm M}$ will evolve at a different, possibly scale-dependent rate, and hence will be displaced from its GR value. To account for this, $\delta_\Delta = \Delta_{\rm M}/\Delta_{\rm M}^{\rm GR} - 1$ is introduced. In [213] it was shown that this quantity is given by the following integral expression:

$$\delta_\Delta(x,k) = \frac{3}{2}\int_{-\infty}^{x} \Omega_{\rm M}^{\rm GR}(\tilde{x}) I(x,\tilde{x})\, \delta S_f(\tilde{x},k)\, d\tilde{x}. \tag{2.16}$$

The integrand above separates into two parts: $\delta S_f(\tilde{x},k)$, which encapsulates all deviations from GR+ΛCDM, and $\Omega_{\rm M}^{\rm GR}(\tilde{x}) I(x,\, \tilde{x})$, which is a weighting function containing GR+ΛCDM quantities only. It will be useful to present the explicit forms of $\delta S_f(x,k)$ and $I(x,\tilde{x})$ here, derived in [213]:

$$\begin{aligned} \delta S_f(x,k) &= \delta\mu(x,k) - \delta\gamma(x,k) \\ &\quad + \frac{(1-\Omega_{\rm M}^{\rm GR}(x))}{\Omega_{\rm M}^{\rm GR}(x)}\Big[3\,\Omega_{\rm M}^{\rm GR}(x)\;(1+f_{\rm GR}(x))\,u(x) + f_{\rm GR}(x)\beta(x)\Big], & (2.17) \\ I(x,\tilde{x}) &= \int_{\tilde{x}}^{y} dy\, \exp\left[-\int_{\bar{x}}^{y} d\bar{x}\left(2 - \frac{3}{2}\Omega_{\rm M}^{\rm GR}(\bar{x}) + 2f_{\rm GR}(\bar{x})\right)\right], & (2.18) \end{aligned}$$

where $f_{\rm GR}$ is the linear growth rate of structure, as defined in equation 1.44, within GR+ΛCDM.

With these modifications in hand, the parameterised Poisson equation can be written as:

$$\begin{aligned} -2k^2\Phi(x,k) &= 3\mathcal{H}^2(x)\Omega_{\rm M}(x)\Delta_{\rm M}(x,k)\mu(x,k) \\ &= 3\mathcal{H}^2(x)\Omega_{\rm M}(x)\Delta_{\rm M}^{\rm GR}(x,k)\left(1+\delta_\Delta(x,k)\right)\left(1+\delta\mu(x,k)\right). & (2.19) \end{aligned}$$

However, this expressions is not yet complete: the non-GR+ΛCDM perturbations to $\mathcal{H}(x)$ and $\Omega_{\rm M}(x)$ are required. In the case of $\Omega_{\rm M}(x)$, this was given in [213] as:

$$\delta\Omega_{\rm M}(x) = 3u(x)\Omega_{\rm M}^{\rm GR}(x)\left[1-\Omega_{\rm M}^{\rm GR}(x)\right]. \tag{2.20}$$

To obtain the required perturbation around $\mathcal{H}(x)$, the FRW equation is written as

$$\mathcal{H}^2(x) = H_0^2\Omega_{\rm M}(x=0)e^{-x}\left[1 + Re^{3x}e^{-3\int_0^x dx'\,\beta(x')}\right] \tag{2.21}$$

where $R = \Omega_\Lambda(x=0)/\Omega_\mathrm{M}(x=0)$ has been defined. Assuming that $|\beta(x)| \ll 1$ and $|u(x)| \ll 1$, expanding the exponential, and taking a square root leads to:

$$\begin{aligned}
\mathcal{H}(x) &= H_0\sqrt{\Omega_\mathrm{M}(x=0)}e^{-\frac{x}{2}}\left[1 + Re^{3x}(1-3u(x))\right]^{\frac{1}{2}} \\
&\approx H_0\sqrt{\Omega_\mathrm{M}(x=0)}e^{-\frac{x}{2}}\left[1+Re^{3x}\right]^{\frac{1}{2}}\left[1 - \frac{3}{2}\left(\frac{u(x)Re^{3x}}{1+Re^{3x}}\right)\right] \\
&= \mathcal{H}_\mathrm{GR}(x)\left[1 - \frac{3}{2}\left(\frac{u(x)Re^{3x}}{1+Re^{3x}}\right)\right]. \qquad (2.22)
\end{aligned}$$

Substituting back in the definition of R, this can be rewritten to obtain:

$$\delta\mathcal{H}(x) = \mathcal{H}(x) - \mathcal{H}_\mathrm{GR}(x) = -\frac{3}{2}\mathcal{H}_\mathrm{GR}(x)u(x)\left(1 - \Omega_\mathrm{M}^\mathrm{GR}(x)\right). \qquad (2.23)$$

With $\delta\mathcal{H}(x)$ and $\delta\Omega_\mathrm{M}(x)$ then in hand, the combined term of interest can be found:

$$\begin{aligned}
\mathcal{H}(x)^2\Omega_\mathrm{M}(x) &= \left(\mathcal{H}_\mathrm{GR}(x) + \delta\mathcal{H}(x)\right)^2\left(\Omega_\mathrm{M}^\mathrm{GR}(x) + \delta\Omega_\mathrm{M}(x)\right) \qquad (2.24) \\
&\approx \mathcal{H}_\mathrm{GR}(x)^2\Omega_\mathrm{M}^\mathrm{GR}(x)\left(1 + 2\frac{\delta\mathcal{H}(x)}{\mathcal{H}_\mathrm{GR}(x)} + \frac{\delta\Omega_\mathrm{M}(x)}{\Omega_\mathrm{M}^\mathrm{GR}(x)}\right) + \mathcal{O}(\delta\mathcal{H}(x)^2). \qquad (2.25)
\end{aligned}$$

Substituting in equations 2.20 and 2.23, it can be seen that in this combination first order perturbations beyond GR+ΛCDM cancel out such that $\mathcal{H}(x)^2\Omega_\mathrm{M}(x) = \mathcal{H}_\mathrm{GR}(x)^2\Omega_\mathrm{M}^\mathrm{GR}(x)$. Thus, equation 2.19 becomes:

$$-2k^2\Phi(x,k) = 3\mathcal{H}_\mathrm{GR}^2(x)\Omega_\mathrm{M}^\mathrm{GR}(x)\Delta_\mathrm{M}^\mathrm{GR}(x,k)\left(1 + \delta_\Delta(x,k)\right)\left(1 + \delta\mu(x,k)\right). \qquad (2.26)$$

Hence, $\Phi(x,k)$ is given in terms of $\Phi_\mathrm{GR}(x,k)$ by:

$$\Phi(x,k) \simeq \Phi_\mathrm{GR}(x,k)\left(1 + \delta_\Delta(x,k) + \delta\mu(x,k)\right). \qquad (2.27)$$

Combining equations 2.15 and 2.27 provides an expression for $\Phi + \Psi$ in modified gravity in terms of the GR potential plus perturbative correction factors:

$$\Phi(x,k) + \Psi(x,k) \simeq \Phi_\mathrm{GR}(x,k)\Big(2 - \delta\gamma(x,k) + 2\delta_\Delta(x,k) + 2\delta\mu(x,k)\Big). \qquad (2.28)$$

At this stage, it becomes convenient to work directly with the power spectrum of κ_g. This can be computed to linear order in deviations from GR+ΛCDM, in direct analogy to the method outlined for the GR case in Section 2.2.1:

$$\begin{aligned}
C_\ell^{\kappa_\mathrm{g}^i\kappa_\mathrm{g}^j} = \frac{\ell^4}{4}\int_{-\infty}^{0} dx\frac{c}{\mathcal{H}(x)}G_i(\chi(x))G_j(\chi(x))P_\Phi^\mathrm{GR}\left(\frac{\ell}{\chi(x)}, \chi(x)\right) \\
\times\left(1 + 2\delta\mu(x,k) - \delta\gamma(x,k) + 2\delta_\Delta(x,k)\right) \qquad (2.29)
\end{aligned}$$

where $G_i(\chi(x)) = \frac{g_i(\chi(x))}{\chi(x)^3}$ has been defined.

There are still two non-GR effects to account for, both originating from the modified expansion history. First, if $\beta(x) \neq 0$ in equation 2.13, $\chi(x)$ will scale differently with the time variable x. Second, although the above combination of $\mathcal{H}^2(x)\Omega_{\rm M}(x)$ is unaffected by perturbations, the factor of $\mathcal{H}(x)^{-1}$ which is introduced via the definition of dx must be accounted for. Using the expression for $\delta\mathcal{H}(x)$ found in equation 2.23, it is found that:

$$\begin{aligned}\frac{1}{\mathcal{H}(x)} &= \frac{1}{\mathcal{H}_{\rm GR}(x)}\left(1 - \frac{\delta\mathcal{H}(x)}{\mathcal{H}_{\rm GR}(x)}\right) \\ &= \frac{1}{\mathcal{H}_{\rm GR}(x)}\left(1 - \frac{3}{2}u(x)(1-\Omega_{\rm M}^{\rm GR}(x))\right), \end{aligned} \tag{2.30}$$

and hence

$$\begin{aligned}\chi(x) &\approx \int_x^0 \frac{c}{\mathcal{H}_{\rm GR}(x')}\left(1 - \frac{\delta\mathcal{H}(x')}{\mathcal{H}_{\rm GR}(x')}\right) dx' \\ \Rightarrow \delta\chi(x) &\approx \frac{3}{2}\int_x^0 \frac{c}{\mathcal{H}_{\rm GR}(x')}u(x')\left(1-\Omega_{\rm M}^{\rm GR}(x')\right) dx' \end{aligned} \tag{2.31}$$

where $\delta\chi(x) = \chi(x) - \chi_{\rm GR}(x)$.

The deviation of $\chi(x)$ from its GR value will also affect quantities which depend on $\chi(x)$, such as $G(\chi(x))$ and $P_\Phi^{\rm GR}(\ell/\chi(x))$. This is allowed for by expanding these in a Taylor series around $\chi_{\rm GR}(x)$; to first order, this yields:

$$P_\Phi^{\rm GR}\left(\frac{\ell}{\chi_{\rm MG}}\right) \approx P_\Phi^{\rm GR}\left(\frac{\ell}{\chi_{\rm GR}}\right)\left[1 + \left.\frac{\partial\, {\rm ln} P_\Phi}{\partial\, {\rm ln}\chi}\right|_{\chi_{\rm GR}} \frac{\delta\chi}{\chi_{\rm GR}}\right] \tag{2.32}$$

$$G_i(\chi)G_j(\chi) \approx G_i(\chi_{\rm GR})G_j(\chi_{\rm GR})\left[1 + \left.\left(\frac{\partial\, {\rm ln} G_i(\chi)}{\partial\, {\rm ln}\chi} + \frac{\partial\, {\rm ln} G_j(\chi)}{\partial\, {\rm ln}\chi}\right)\right|_{\chi_{\rm GR}} \frac{\delta\chi}{\chi_{\rm GR}}\right] \tag{2.33}$$

where $\delta\chi(x)$ is given by equation 2.31 above and dependence on x has been suppressed for clarity. With this, all modified gravity effects have been accounted for, and these are summarised in Table 2.1.

Finally, it will be more convenient to work in terms of P_δ, the matter power spectrum, instead of P_Φ. This change is accomplished via the following expression, where

Correction	**Equation**
$\Phi(x,k)+\Psi(x,k)\simeq\left(2-\delta\gamma(x,k)\right)\Phi(x,k)$	2.15
$\Phi(x,k)\simeq\Phi_{\rm GR}(x,k)(1+\delta_\Delta(x,k)+\delta\mu(x,k))$	2.27
$\frac{1}{\mathcal{H}(x)}\simeq\frac{1}{\mathcal{H}_{\rm GR}(x)}\left[1-\frac{3}{2}u(x)(1-\Omega_M^{\rm GR}(x))\right]$	2.30
$\chi(x)\simeq\chi_{\rm GR}(x)+\frac{3}{2}\int\frac{c}{\mathcal{H}_{\rm GR}(x)}u(x)\left(1-\Omega_M^{\rm GR}(x)\right)\,dx$	2.31
$G_i(\chi)G_j(\chi)\simeq G_i(\chi_{\rm GR})G_j(\chi_{\rm GR})\left[1+\left(\frac{\partial\ln G_i(\chi)}{\partial\ln\chi}+\frac{\partial\ln G_j(\chi)}{\partial\ln\chi}\right)\Bigg\vert_{\chi_{\rm GR}}\frac{\delta\chi}{\chi_{\rm GR}}\right]$	2.33
$P_\Phi^{\rm GR}\left(\frac{\ell}{\chi}\right)\simeq P_\Phi^{\rm GR}\left(\frac{\ell}{\chi_{\rm GR}}\right)\times\left[1-\frac{\partial\ln(k^{-4}\,P_\delta^{\rm GR}(x=0,k))}{\partial\ln k}\Bigg\vert_{k=\ell/\chi_{\rm GR}}\frac{\delta\chi}{\chi_{\rm GR}}\right]$	2.35

Table 2.1: The corrections to the GR expression for $C_\ell^{\kappa_{\rm g}^i\kappa_{\rm g}^j}$.

for clarity the label ‘GR’ is temporarily omitted on all quantities.:

$$P_\Phi\left(k,x\right)=\frac{1}{k^4}\frac{9}{4}\left(\frac{\mathcal{H}(x)}{c}\right)^4\Omega_{\rm M}^2(x)D(x)^2P_\delta\left(x=0,k\right),\tag{2.34}$$

where $D(x)$ is the growth factor of matter perturbations. Inserting equation 2.34 into equation 2.32, it is found that:

$$P_\Phi^{\rm GR}\left(\frac{\ell}{\chi(x)}\right)\approx P_\Phi^{\rm GR}\left(\frac{\ell}{\chi_{\rm GR}(x)}\right)\quad\left[1-\frac{\partial\ln(k^{-4}\,P_\delta^{\rm GR}(x=0,k))}{\partial\ln k}\Bigg\vert_{k=\ell/\chi_{\rm GR}(x)}\frac{\delta\chi(x)}{\chi_{\rm GR}(x)}\right].\tag{2.35}$$

Drawing together, then, equations 2.29, 2.30, 2.33 and 2.35, and using equation 2.34, the final expression for the convergence power spectrum under modifications to general relativity is obtained:

$$
\begin{aligned}
C_\ell^{\kappa_g^i \kappa_g^j} = \frac{9}{16}\int_{-\infty}^{0} dx\, & \frac{g_i(\chi_{\mathrm{GR}}(x))g_j(\chi_{\mathrm{GR}}(x))}{\chi_{\mathrm{GR}}(x)^2} P_\delta^{\mathrm{GR}}\left(\frac{\ell}{\chi_{\mathrm{GR}}(x)}\right) D_{\mathrm{GR}}^2(x)\frac{\mathcal{H}_{\mathrm{GR}}^3(x)}{c^3}\Omega_{\mathrm{M}}^{\mathrm{GR}}(x)^2 \\
\times & \left[1 + \frac{3}{2}u(x)\left(1-\Omega_{\mathrm{M}}^{\mathrm{GR}}(x)\right) + 2\delta\mu(x,k) - \delta\gamma(x,k) + 2\delta_\Delta(x,k)\right. \\
+ & \left.\left(\frac{\partial \mathrm{ln} G_i(\chi)}{\partial \mathrm{ln}\chi} + \frac{\partial \mathrm{ln} G_j(\chi)}{\partial \mathrm{ln}\chi} - \frac{\partial \mathrm{ln}(P_\delta^{\mathrm{GR}}(x=0,k)/k^4)}{\partial \mathrm{ln} k}\right)\Bigg|_{\chi_{\mathrm{GR}}(x)} \frac{\delta\chi(x)}{\chi_{\mathrm{GR}}(x)}\right]. \qquad (2.36)
\end{aligned}
$$

The major advantage of equation 2.36 is that it neatly separates the convergence power spectrum into the familiar GR expression (the non-bracketed quantity) and a correction factor (the bracketed terms). It is then easy to pick out contributions from:

- the modified clustering properties (described by $\delta\mu(x,k)$ and $\delta\gamma(x,k)$),
- the modified expansion history (described by $\beta(x)$, $u(x)$ and $\delta\chi(x)$), and
- the modified growth rate of matter density perturbations (encapsulated in $\delta_\Delta(x,k)$, see equation 2.16).

Note once again that a flat Universe is assumed in this chapter, which accounts for slight differences in form between the GR part of equation 2.36 and equation 1.35.

It will be useful to write equation 2.36 in a form which explicitly highlights the GR expression and the correction factor:

$$
C_\ell^{\kappa_g^i \kappa_g^j} = \int_{-\infty}^{0} dx\, \mathcal{K}(x,\ell)\big(1+\delta S_{\mathrm{WL}}(x,\ell)\big). \qquad (2.37)
$$

Here the 'kernel' term has been defined as:

$$
\mathcal{K}(x,\ell) = \frac{9}{16}\frac{g_i(\chi_{\mathrm{GR}}(x))g_j(\chi_{\mathrm{GR}}(x))}{\chi_{\mathrm{GR}}(x)^2} P_\delta^{\mathrm{GR}}\left(\frac{\ell}{\chi_{\mathrm{GR}}(x)}\right) D_{\mathrm{GR}}^2(x)\frac{\mathcal{H}_{\mathrm{GR}}^3(x)}{c^3}\Omega_{\mathrm{M}}^{\mathrm{GR}}(x)^2, \qquad (2.38)
$$

and the 'source' term as:

$$
\begin{aligned}
\delta S_{\mathrm{WL}}(x,\ell) = & \frac{3}{2}u(x)\left(1-\Omega_{\mathrm{M}}^{\mathrm{GR}}(x)\right) + 2\delta\mu(x,k) - \delta\gamma(x,k) + 2\delta_\Delta(x,k) \\
+ & \left(\frac{\partial\, \mathrm{ln} G_i(\chi)}{\partial\, \mathrm{ln}\chi} + \frac{\partial\, \mathrm{ln} G_j(\chi)}{\partial\, \mathrm{ln}\chi} - \frac{\partial \mathrm{ln}[P_\delta^{\mathrm{GR}}(x=0,k)/k^4]}{\partial \mathrm{ln} k}\right)\Bigg|_{\chi_{\mathrm{GR}}(x)} \frac{\delta\chi(x)}{\chi_{\mathrm{GR}}(x)}. \qquad (2.39)
\end{aligned}
$$

2.3 Understanding degeneracies with the linear response approach

With the completed derivation of equation 2.36, a new expression is now at hand for $C_\ell^{\kappa_g^i \kappa_g^j}$ under modifications to general relativity. The next objective is to use this expression to understand the degeneracies between gravitational parameters within weak lensing observations. Note that in the interest of simplicity, the discussion of this chapter will be restricted to degeneracies between parameters describing modifications to GR.

In this section, it will be assumed that $\delta\mu$ and $\delta\gamma$ are independent of scale, as the scale-dependence of these functions is expected to be sub-dominant to their time-dependence [92–94]. Their scale-dependence will be investigated briefly in Section 2.4.3, and more thoroughly in Chapter 3. Additionally, in keeping with the quasistatic approximation, all analysis is restricted to the regime of validity of linear cosmological perturbation theory. Various values of $\ell_{\max}$ which ensure this to be true are suggested in the literature (see, for example, [112, 113]). Adopting a conservative approach, $\ell_{\max} = 100$ is selected here and for the remainder of this chapter.

The method for calculating degeneracy directions is first reviewed. Then, using equations 2.17 and 2.36, an investigation is performed as to the effect of the chosen ansatz for $\delta\mu(x)$ and $\delta\gamma(x)$ on the degeneracy direction of weak lensing in the space of the parameters of these functions. Here, and for the remainder of this chapter, the GR+ΛCDM matter power spectrum is computed using the publicly available code CAMB [10] and the best-fit ΛCDM parameters of the 2013 *Planck* release (including *Planck* lensing data) [215]. This constituted the most up-to-date set of cosmological parameters at the time of this work.

2.3.1 Calculating degeneracy directions

Degeneracies exist in the case in which an observation can probe only some combination of the parameters which would ideally be constrained. The expected degeneracy direction is given by the relationship between parameters in the fiducial scenario (here GR+ΛCDM). For example, if this relationship is $a = b$, then the relevant observation is expected to probe only $a - b$, not a or b individually.

In the case of weak lensing, degeneracy directions can be understood in the following schematic way. First, define the fractional difference between $C_\ell^{\kappa_g^i \kappa_g^j}$ in an alternative gravity theory and in GR+ΛCDM:

$$\delta C_\ell^{\kappa_g^i \kappa_g^j} = \frac{C_\ell^{\kappa_g^i \kappa_g^j} - C_{\ell,\mathrm{GR}}^{\kappa_g^i \kappa_g^j}}{C_{\ell,\mathrm{GR}}^{\kappa_g^i \kappa_g^j}}. \tag{2.40}$$

To find the degeneracy direction, one can find the relationship which exists between parameters when $\delta C_\ell^{\kappa_g^i \kappa_g^j} = 0$. Considering a two parameter case (call them a and b), straightforward algebra reveals an expression of the form

$$a = \mathcal{D}(\ell) b \tag{2.41}$$

where $\mathcal{D}(\ell)$ may be a complicated expression, but depends only on GR+ΛCDM quantities. The degeneracy direction, as can be seen, depends on ℓ in the weak lensing case.

In order to calculate $C_\ell^{\kappa_g^i \kappa_g^j}$, it is necessary to specify $W_i(\chi)$, the normalised distribution of source galaxies with comoving distance in the redshift bin i. For this purpose, the source number density, $n(z)$, is assumed to have the following form [216]:

$$n(z) \propto z^\alpha e^{-\left(\frac{z}{z_0}\right)^\beta}, \tag{2.42}$$

with parameter values $\alpha = 2$, $\beta = 1.5$, and $z_0 = z_\mathrm{m}/1.412$, where $z_\mathrm{m} = 0.9$ is the median redshift of the survey, mimicking the number density of a DETF4-type survey [113,114]. Within this section, all galaxies between $z = 0.5$ and $z = 2.0$ will be considered to be in a single redshift bin, with $W(\chi)$ given by multiplying the normalised equation 2.42 by $\frac{dz}{d\chi} = \frac{H(\chi)}{c}$.

In principle, the dependence of the weak lensing degeneracy direction on ℓ could be sufficient to break any parameter degeneracies, but in practice the dependence on ℓ is too weak over the range of ℓ considered here. Instead, a second observable with a different (ideally orthogonal) degeneracy direction must be introduced. The second observable is chosen here to be redshift-space distortions, as it is known to provide nearly orthogonal constraints to weak lensing in the plane of parameters to be considered (see, for example, [69]). Results from [213], which provided a linear response formulation for the redshift-space distortion observable $f\sigma_8$, will therefore often be employed. Particularly, the equation presented in [213] for the deviation of $f\sigma_8(x)$ from its GR value is reproduced here:

$$\delta f\sigma_8(x) = \frac{f\sigma_8(x) - f\sigma_8^{\mathrm{GR}}(x)}{f\sigma_8^{\mathrm{GR}}(x)} = \int_{-\infty}^{x} G_f(x, \tilde{x})\delta S_f(\tilde{x})d\tilde{x} \tag{2.43}$$

where $\delta S_f(x)$ is given as in equation 2.17, and $G_f(x, \tilde{x})$ is a general relativistic kernel. $G_f(x, \tilde{x})$ is given in [213] by

$$G_f(x, \tilde{x}) = \frac{3}{2}\Omega_{\mathrm{M}}^{\mathrm{GR}}(\tilde{x}) \left[\frac{K(x, \tilde{x})}{f_{\mathrm{GR}}(\tilde{x})} + I(x, \tilde{x})\right], \tag{2.44}$$

where $I(x, \tilde{x})$ is given in equation 2.18 and $K(x, \tilde{x})$ is defined as

$$K(x, \tilde{x}) = \exp\left\{-\int_{\tilde{x}}^{x} d\bar{x} \left[f_{\mathrm{GR}}(\bar{x}) + \frac{3}{2}\frac{\Omega_{\mathrm{M}}^{\mathrm{GR}}(\bar{x})}{f_{\mathrm{GR}}(\bar{x})}\right]\right\}. \tag{2.45}$$

Note that $f\sigma_8(x)$ above is independent of k, because it has been assumed in this section that μ and γ are functions of time only.

The degeneracy direction of a measurement of $f\sigma_8(x)$ can be computed in a directly analogous way to that described above for weak lensing. The sole difference is that instead of depending on multipole ℓ, the degeneracy direction is dependent on the time of observation, x.

With this information in hand, the degeneracy directions of weak lensing and redshift-space distortions in the space of the parameters of $\delta\mu(x)$ and $\delta\gamma(x)$ can now be explored.

2.3.2 Degeneracy directions in the $\bar{\mu}_0 - \Sigma_0$ plane

As mentioned above, redshift-space distortions are the preferred choice of an additional observation to break the degeneracy affecting weak lensing in this scenario. Upon closer examination, this statement hinges upon the chosen time-dependent ansatz for the functions which parameterise deviations from GR. As there is no clear front-runner amongst alternative theories of gravity, typically a phenomenological ansatz is chosen, in which deviations from GR become manifest at late times in order to mimic accelerated expansion. It is for this type of phenomenological ansatz that redshift-space distortion and weak lensing observations are known to provide complementary constraints [69].

However, it may also be desirable to constrain the parameters of a specific theory of gravity. The functions which parameterise the deviation of an alternative gravity theory from GR can, in principle, take on a wide range of time-dependencies. Is the combination of weak lensing and redshift-space distortions still an effective way to break degeneracies and constrain the parameters of the theory under consideration? A priori, this is unknown.

To explore this issue, the degeneracy directions of weak lensing and redshift-space distortions are considered under two different ansatzes for the functions which parameterise deviations from GR. Within this section, the simplifying assumption that $\beta(x) = 0$ is made (i.e. the expansion history is assumed to be ΛCDM-like).

First, a simple operation is performed on $\delta\mu(x)$ and $\delta\gamma(x)$ to obtain a more observationally-motivated set of functions. These will be labeled as $\bar{\mu}(x)$ and $\Sigma(x)$, in keeping insofar as possible with the notation used in [69] (see equation A.1). This set of functions allows nearly orthogonal constraints in the $\bar{\mu}_0 - \Sigma_0$ plane for the phenomenological choice of time-dependence. The mapping between the two sets of functions, as shown in Appendix A, is given by:

$$\begin{aligned}\Sigma(x) &= \delta\mu(x) - \frac{1}{2}\delta\gamma(x) \\ \bar{\mu}(x) &= \delta\mu(x) - \delta\gamma(x).\end{aligned} \tag{2.46}$$

The linear response 'source' terms for both weak lensing (equation 2.39) and redshift-space distortions (equation 2.43) can be rewritten in terms of $\bar{\mu}(x)$ and $\Sigma(x)$ (in the $\beta(x) = 0$ case):

$$\begin{aligned}\delta S_{\rm WL}(x) &= 2\Sigma(x) + 3\int_{-\infty}^{x} \Omega_{\rm M}^{\rm GR}(\tilde{x}) I(x,\tilde{x})\, \bar{\mu}(\tilde{x}) d\tilde{x} \\ \delta S_f(x) &= \bar{\mu}(x).\end{aligned} \tag{2.47}$$

As can be seen, $\delta S_f(x)$ depends solely on $\bar{\mu}(x)$.

The expression for $\delta S_{\rm WL}(x)$ requires slightly more pause. It depends on $\Sigma(x)$, but it also contains another term, which comprises an integral over $\bar{\mu}(x)$ and some general-relativistic quantities. By comparing with equation 2.16, this term can be recognised as $2\delta_\Delta(x)$, and quantifies a correction to the degeneracy direction of weak lensing away from $\Sigma_0 = 0$. It is clearly dependent upon the ansatz of time-dependence chosen for $\bar{\mu}(x)$. Particularly, due to the integral nature of the correction term, choices of $\bar{\mu}(x)$ which persist significantly over longer times will result in greater deviations to the degeneracy direction.

Consider then two ansatzes for $\bar{\mu}(x)$ and $\Sigma(x)$. First: a phenomenological ansatz, for which weak lensing and redshift-space distortions are known to be an effective combination in constraining gravity theories. This choice is a specific case of the form proposed in [217] and has been used in, for example, [69]. It is given by:

$$\begin{aligned}\bar{\mu}(x) &= \bar{\mu}_0 \frac{\Omega_\Lambda^{\rm GR}(x)}{\Omega_\Lambda^{\rm GR}(x=0)}\,, \\ \Sigma(x) &= \Sigma_0 \frac{\Omega_\Lambda^{\rm GR}(x)}{\Omega_\Lambda^{\rm GR}(x=0)}\,,\end{aligned} \tag{2.48}$$

where $\Omega_\Lambda^{\rm GR}(x)$ is the time-dependent energy density of dark energy in the fiducial ΛCDM cosmology. This ansatz is chosen in part because it allows $\bar{\mu}$ and Σ to become non-negligible in the era of late-time acceleration, as would be expected if an alternative theory of gravity is to explain this phenomenon.

Inserting $\delta S_{\rm WL}(x)$ (equation 2.47) into equations 2.40 and 2.43 with the chosen $\bar{\mu}(x)$ and $\Sigma(x)$, the procedure sketched in Section 2.3.1 can be followed to find the degeneracy directions of weak lensing and redshift-space distortion in the $\bar{\mu}_0 - \Sigma_0$ plane. In this particular case, the degeneracy direction of redshift-space distortions does not depend on time. This is because $\delta S_f(x)$ is dependent on only one parameter, $\bar{\mu}_0$, and therefore the only degeneracy direction is $\bar{\mu}_0 = 0$.

The degeneracy directions for this ansatz can be seen in Figure 2.1 (left). In the case of weak lensing, the degeneracy direction is plotted for $\ell = 50$; directions for other multipoles $\ell = 10 - 100$ differ only within 5%. It can be seen that the degeneracy directions are nearly orthogonal, with only a slight correction of the weak lensing degeneracy direction away from $\Sigma_0 = 0$. The sensitivity of $C_\ell^{\kappa_g \kappa_g}$ to Σ_0 within this ansatz is demonstrated explicitly in Figure 2.2, where $C_\ell^{\kappa_g \kappa_g}$ is plotted for several values of $\bar{\mu}_0$ and of Σ_0. The greater dependence of the convergence power spectrum on Σ_0, as compared to on $\bar{\mu}_0$, is clearly visible. This is further illustrated in Figure 2.3, which depicts $\frac{\partial C_\ell^{\kappa_g \kappa_g}}{\partial \Sigma_0}$ (left) and $\frac{\partial C_\ell^{\kappa_g \kappa_g}}{\partial \bar{\mu}_0}$ (right). The derivative of the convergence power spectrum with respect to Σ_0 is seen to be considerably larger than that with respect to $\bar{\mu}_0$.

Now, consider selecting an ansatz with a very different time-dependence. To guide this selection, recall that choices of $\bar{\mu}(x)$ which persist over longer times are expected to result in a greater value of the integral term in equation 2.47, and hence a greater deviation of the weak lensing degeneracy direction from $\Sigma_0 = 0$. Therefore, with no attempt to correspond to any particular gravity theory, the simplest possible choice which persists over long times is selected: constant $\bar{\mu}(x)$ and $\Sigma(x)$:

$$\begin{aligned} \Sigma(x) &= \Sigma_0 \\ \bar{\mu}(x) &= \bar{\mu}_0. \end{aligned} \tag{2.49}$$

In reality, step functions which are non-zero from $z = 15$ are employed rather than true constants, to allow for the numerical computation of the degeneracy directions. The degeneracy directions are calculated as before, and are plotted in Figure 2.1 (right). Clearly, they are less orthogonal than in the previous case, as expected from the comments above.

What does this example tell us about the effectiveness of combining weak lensing and redshift-space distortions? The ansatz for $\bar{\mu}(x)$ and $\Sigma(x)$ given by equation 2.49 deviates from GR+ΛCDM at all times after $z = 15$. As mentioned above, most cosmologically-motivated alternative theories of gravity present deviations from GR+ΛCDM at late times only, mimicking accelerated expansion. Therefore, the case of equation 2.49 is treated as a heuristic 'upper bound' on the cumulative effect produced by the integral term of equation 2.47. The effect of this term can be quantified by considering the angle of the weak lensing degeneracy direction with respect to the vertical. It is found that for the range of ℓ which is considered here and for the ansatz given by equation 2.49, the maximum possible value of this angle is $\theta \approx 50°$. Although the degeneracy directions in this case are certainly no longer orthogonal ($\theta = 0°$), they are sufficiently distinct that the resulting constraints are expected to be reasonable (if not ideal). It has thus been shown that the effectiveness of combining weak lensing with redshift-space distortions in the $\beta(x) = 0$ case is relatively robust to the chosen form of $\bar{\mu}(x)$ and $\Sigma(x)$.

2.4 Forecast constraints from future surveys

In addition to providing an understanding of degeneracy directions, the expression for $C_\ell^{\kappa_g^i \kappa_g^j}$ presented in equation 2.36 enables the forecasting of constraints. The straightforward form of this expression renders the calculation of Fisher matrices very simple, and clarifies the interpretation of the resulting forecasts. Taking advantage of these features, constraints are now forecast on gravitational parameters from a DETF4-type survey, as defined in the classification of [218]. As in the previous section, the fo-

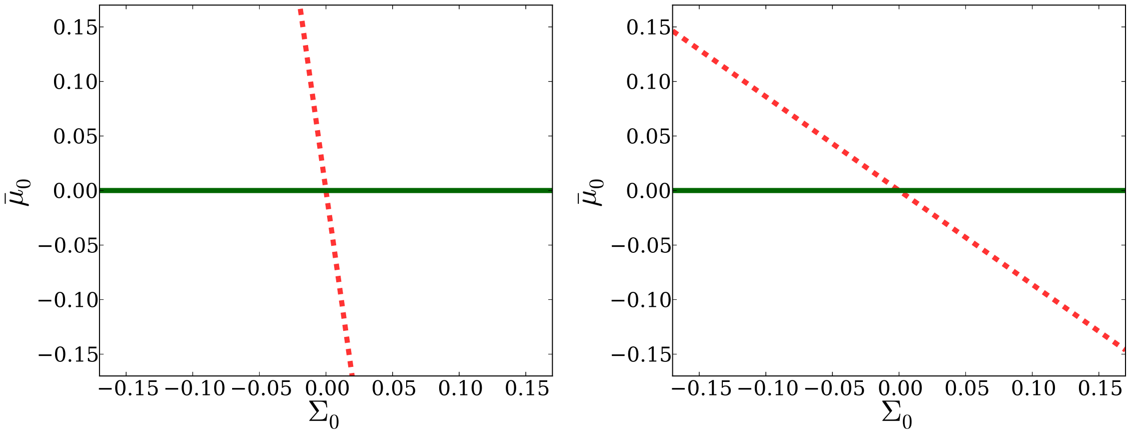

Figure 2.1: Degeneracy directions of weak lensing ($\ell = 50$, red, dashed) and redshift-space distortions (green, solid) in the $\bar{\mu}_0 - \Sigma_0$ plane, where $\bar{\mu}(x)$ and $\Sigma(x)$ scale as $\Omega_\Lambda^{\rm GR}(x)$ (left), and as constants (right).

cus of these forecasts is on combined constraints from weak lensing and redshift-space distortions, with some consideration given also to baryon acoustic oscillations.

The forecasts presented here employ the technique of Fisher forecasting, as introduced in Section 1.3.3. For redshift-space distortions, the results of [213] can be built-upon to construct the appropriate Fisher matrix. It is given by:

$$\mathcal{F}_{ab}^{\rm RSD} = \sum_i \left(\frac{f\sigma_8^{\rm GR}(x_i)}{\sigma_i^{f\sigma_8}} \right)^2 \frac{\partial (\delta f\sigma_8)^i}{\partial p_a} \frac{\partial (\delta f\sigma_8)^i}{\partial p_b} \tag{2.50}$$

where i indicates a quantity averaged in the ith x bin, and $\sigma_i^{f\sigma_8}$, the error in each x bin, is taken from [219].

For weak lensing, the correct expression is that which was introduced in equation 1.48. The required parameter $f_{\rm sky}$ is given by 0.375 for the DETF4-type survey considered here. The observed power spectrum of the convergence, also required to compute the Fisher matrix of weak lensing, is given by equation 1.49, where $\langle \gamma_{\rm int}^2 \rangle^{\frac{1}{2}}$ is equal to 0.22 for a DETF4-type survey.

The number density of source galaxies per steradian in a given redshift bin i, $\bar{n}_i$, is also required to compute the observed power spectrum of the convergence. Computing the appropriate value of $\bar{n}_i$ requires the specification of these source redshift bins. In practice, once in possession of data, the selected bins are those which are maximal in

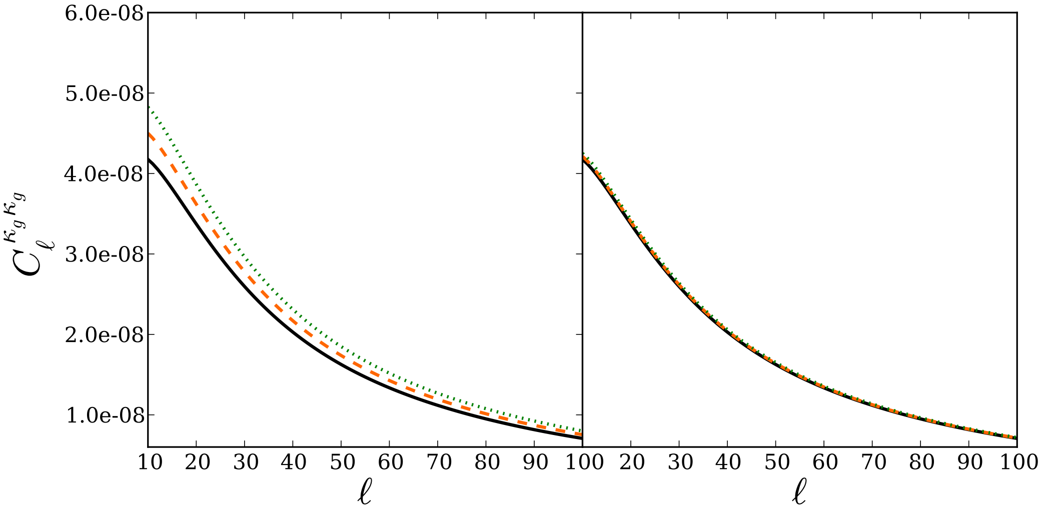

Figure 2.2: $C_\ell^{\kappa_g\kappa_g}$ for variable Σ_0 (left panel) and $\bar{\mu}_0$ (right panel), using the ansatz of equation 2.48. In the left panel, $\bar{\mu}_0 = 0$, and in the right panel, $\Sigma_0 = 0$. Orange dashed lines represent the case in which Σ_0 (left) or $\bar{\mu}_0$ (right) is equal to 0.05, and green dotted lines set Σ_0 or $\bar{\mu}_0$ to 0.1. Black solid lines are the GR case. It is clearly seen that $C_\ell^{\kappa_g\kappa_g}$ depends more strongly on Σ_0 than on $\bar{\mu}_0$, assuming the ansatz of equation 2.48.

number while maintaining a noise level sufficiently below the signal. For the purpose of the forecasts computed in this Chapter, the procedure is instead taken to be that of, for example, [113] and [114]. Redshift bins are selected by subdividing $n(z)$ of equation 2.42 into five sectors, such that the number of galaxies in each bin is equal. The value of the number density of galaxies per steradian for the total redshift range of a DETF4-type survey is given by $\bar{n} = 3.55 \times 10^8$, so the value in each tomographic bin is simply $\bar{n}_i = \bar{n}/5$.

In the following subsections, the Fisher formalism is used to compute forecast constraints in a number of scenarios. In the first instance, constraints are computed on the parameters of $\delta\mu(x)$ and $\delta\gamma(x)$ in the case where the expansion history is fixed to mimic ΛCDM. Expected measurements of w_0 and w_a from baryon acoustic oscillations are then incorporated, to forecast constraints on the parameters of $\delta\mu(x)$ and $\delta\gamma(x)$ in the case in which $\beta(x)$ is allowed to vary. Finally, a brief investigation is made into the directions of best constraint in the parameter space of the scale-dependent ansatz for

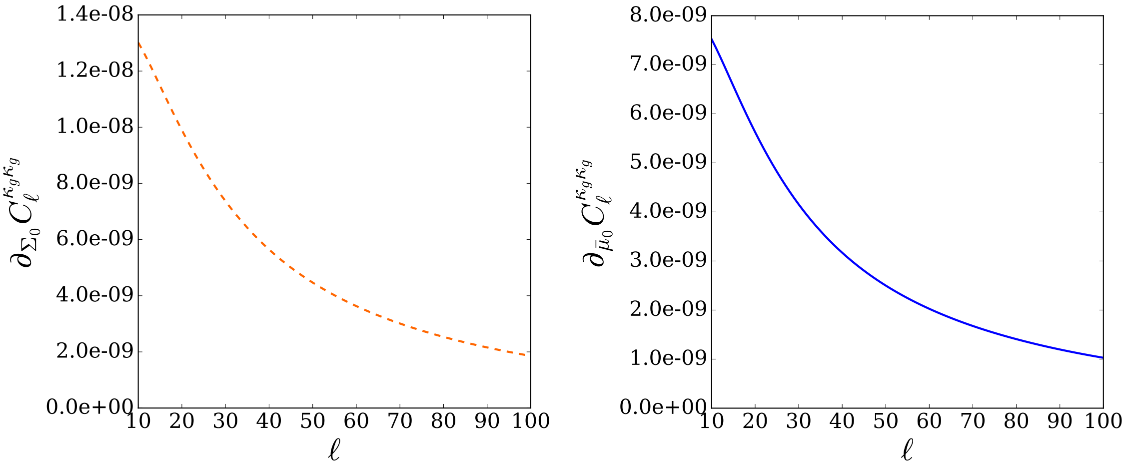

Figure 2.3: Derivatives of $C_\ell^{\kappa_g\kappa_g}$ with respect to Σ_0 (left, orange dashed) and $\bar{\mu}_0$ (right, blue solid), assuming the ansatz of equation 2.48.

$\mu(x, k)$ and $\gamma(x, k)$ put forth in [92].

2.4.1 ΛCDM-like expansion history: $\beta(x) = 0$

First, constraints are forecast on the parameters of $\delta\mu(x)$ and $\delta\gamma(x)$ for the case in which the expansion history is fixed to be ΛCDM-like. $\delta\mu(x)$ and $\delta\gamma(x)$ are once again transformed to $\bar{\mu}(x)$ and $\Sigma(x)$, and their time-dependence is selected to be given by the phenomenological ansatz of equation 2.48. Fisher matrices are calculated for lensing, for redshift-space distortions, and for both observations combined. The straightforward form of equation 2.36 means that the required derivatives (of $\delta f\sigma_8$ and of $C_\ell^{\kappa_{\rm g}^i\kappa_{\rm g}^j}$, with respect to $\bar{\mu}_0$ and Σ_0) can be expressed analytically. These expressions are presented explicitly in Appendix B.

The resulting forecast constraints are illustrated in Figure 2.4. As discussed in Section 2.3, the degeneracy directions of the two observables are nearly orthogonal in this case. Combining them results in promising forecast constraints on $\bar{\mu}_0$ and Σ_0. It is seen that a DETF4-type survey can be expected to provide constraints at a level of approximately 4% in this plane, in the optimistic case where $\beta(x) = 0$ is assumed and other cosmological parameters are held to their ΛCDM best-fit values.

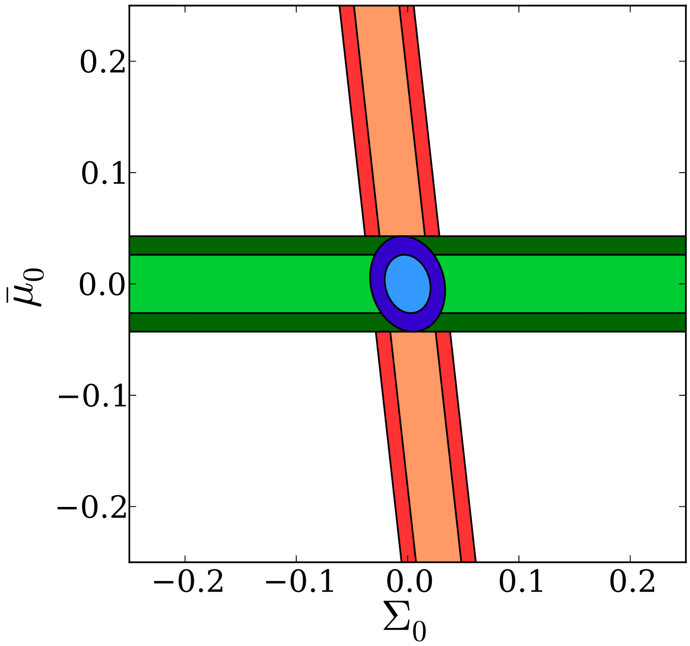

Figure 2.4: Forecast constraints for weak lensing (orange), redshift-space distortions (green) and both observables combined (blue) for a DETF4-type survey, in the $\bar{\mu}_0 - \Sigma_0$ plane with $\beta(x)$ fixed to 0. Contours represent the 68.3% and 95.4% confidence regions.

2.4.2 The effect of marginalising over $\{w_0, w_a\}$

In reality, $\beta(x)$ is not necessarily fixed to zero. Rather, the associated parameters may also be constrained with some non-zero error. While weak lensing and redshift-space distortions provide some constraints in this respect, baryon acoustic oscillation measurements are one observable which is expected to better constrain the expansion history of the Universe.

In this section, a CPL-type ansatz is employed for $\beta(x)$, as introduced in equation 1.32: $\beta(x) = w_0 + 1 + w_a(1 - e^x)$. Forecast BAO constraints on w_0 and w_a are incorporated, and used to obtain expected constraints in the $\bar{\mu}_0 - \Sigma_0$ plane. First, only w_0 is marginalised over, while holding w_a to its fiducial value of 0; then, the effect of allowing w_a to vary is examined.

2.4.2.1 Marginalising over w_0; $w_a = 0$

First, the effect on constraints in the $\bar{\mu}_0 - \Sigma_0$ plane from marginalising over w_0 is investigated, with w_a held fixed to its fiducial value of 0.

Additional derivatives of $C_\ell^{\kappa_{\rm g}^i \kappa_{\rm g}^j}$ and $\delta f\sigma_8(x)$ with respect to w_0 are required; analytic expressions for these are listed in Appendix B. Because transverse measurements of BAO are independent of non-background gravitational effects [220], the Fisher matrix of BAO is non-zero only in the (w_0, w_0) component. The value of this matrix component is equal to $\left(\sigma^2_{w_0,\rm BAO}\right)^{-1}$, where $\sigma_{w_0,\rm BAO}$ is the 1σ error on w_0 from BAO measurements.

To explore the effect of marginalising over w_0, three levels of constraint from BAO are considered:

1. For comparison: the case where w_0 is fixed to its fiducial value. This is identical to the case considered in Section 2.4.1.

2. The case where $\sigma_{w_0,\rm BAO} = 1\%$. This scenario mimics best-case constraints from a DETF4-type survey.

3. The case where $\sigma_{w_0,\rm BAO} = 5\%$. This lies between best constraints from current surveys and scenario 2 above.

The resulting constraints from the combination of weak lensing, BAO, and redshift-space distortions are shown in Figure 2.5 and Figure 2.6. Figure 2.5 shows in the left panel the forecast posterior probability distribution of $\bar{\mu}_0$ for cases $1 - 3$ above when marginalising over w_0 and Σ_0; the right panel displays the same for Σ_0 when marginalising over w_0 and $\bar{\mu}_0$. Figure 2.6 shows the 68.3% forecast joint constraints on $\bar{\mu}_0 - \Sigma_0$ in scenarios $1 - 3$ while marginalising over w_0 only.

In Figure 2.6, it can be seen that the degeneracy direction of the combined constraint in the $\bar{\mu}_0 - \Sigma_0$ plane changes considerably between the three scenarios. $\bar{\mu}_0$ and Σ_0 are mildly negatively correlated in scenario 1, whereas in scenario 2 they are positively correlated, and in scenario 3 even more so. This can be understood by considering the

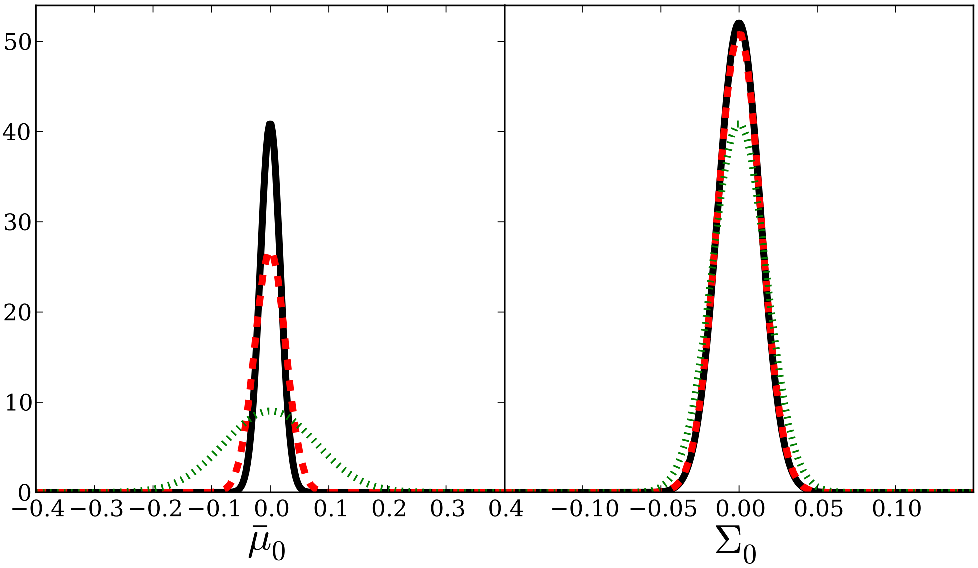

Figure 2.5: Forecast posterior probability distributions from weak lensing, redshift-space distortion, and BAO observations in the case where w_0 has been marginalised over and w_a has been fixed to 0. The left panel shows the distribution of $\bar{\mu}_0$ when Σ_0 is marginalised over, while the right panel shows the distribution of Σ_0 with $\bar{\mu}_0$ marginalised over. Black, solid: w_0 fixed; red, dashed: BAO error on $w_0 = 1\%$ (DETF4); green, dotted: BAO error on $w_0 = 5\%$.

joint forecast constraints in the $w_0 - \bar{\mu}_0$ and $w_0 - \Sigma_0$ planes, marginalised in each case over the other non-w_a parameter. These are displayed at a 68.3% level in Figure 2.7 for scenario 3. Both $\bar{\mu}_0$ and Σ_0 are shown therein to exhibit a positive correlation with w_0. This implies that $\bar{\mu}_0$ and Σ_0 are also positively correlated with each other, except in the case where w_0 is fixed or constrained so tightly that this effect is negated. As the constraint on w_0 is loosened, moving from scenario 1 through scenario 2 to scenario 3, this positive correlation becomes more pronounced.

Figure 2.6 also makes evident the fact that the constraint on Σ_0 is relatively insensitive to the level of BAO constraint on w_0, whereas the constraint on $\bar{\mu}_0$ changes considerably between scenarios $1 - 3$. This is consistent with Figure 2.7, in which it is seen that the degeneracy direction in the $w_0 - \bar{\mu}_0$ plane has a considerably shallower slope than that in the $w_0 - \Sigma_0$ plane, implying that $\bar{\mu}_0$ is more sensitive to changes in w_0. These degeneracy directions, and hence the relative sensitivity of $\bar{\mu}_0$ and Σ_0 con-

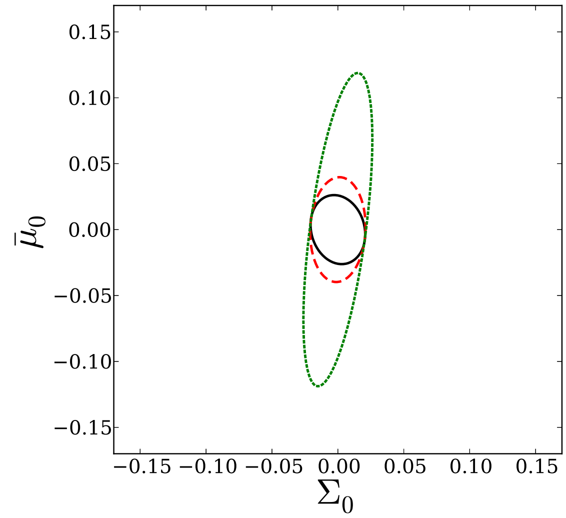

Figure 2.6: Forecast 68.3% confidence regions in the $\bar{\mu}_0 - \Sigma_0$ plane, marginalising over w_0, for the case where $w_a = 0$. Black, solid: w_0 fixed; red, dashed: BAO error on $w_0 = 1\%$ (DETF4); green, dotted: BAO error on $w_0 = 5\%$.

straints to w_0 constraints, can be understood by considering the expressions for $C_\ell^{\kappa_g^i \kappa_g^j}$ (equation 2.36) and $\delta f\sigma_8(x)$ (equations 2.17 and 2.43). Both $C_\ell^{\kappa_g^i \kappa_g^j}$ and $\delta f\sigma_8(x)$ are given by integrals in time over a kernel and a source term. In the case of $\delta f\sigma_8(x)$, the general relativistic kernel $G_f(x, \tilde{x})$ is significant back to $z \simeq 15$, whereas in the weak lensing case, the kernel is non-zero only as far back in redshift as the furthest source galaxies ($z = 2$ in this case). In the current model for $\beta(x)$, deviations from a ΛCDM expansion history are more significant at early times, whereas $\bar{\mu}(x)$ and $\Sigma(x)$ are both chosen to be significant only at late times (below $z \simeq 5$). Therefore, the $\delta f\sigma_8(x)$ integration from $z \simeq 15$ favours sensitivity to the background expansion variable w_0 over $\bar{\mu}_0$, whereas the weak lensing integral, significant only from $z \simeq 2$, results in relatively greater sensitivity to Σ_0. This results in the relative sensitivity of the $\bar{\mu}_0$ constraint to the w_0 constraint level, as seen in Figure 2.6.

Finally, there is clearly a direction in the $\bar{\mu}_0 - \Sigma_0$ plane of Figure 2.6 which is entirely insensitive to the change in the constraint on w_0. This is in fact expected due to the nature of the contours displayed. Given the hypothetical three-dimensional confidence region in the space of $\bar{\mu}_0$, Σ_0 and w_0, the marginalised constraint of scenario 3 is equivalent to projecting this ellipsoid into the $\bar{\mu}_0 - \Sigma_0$ plane. When the error is reduced in only the w_0 direction as in scenario 2 – that is, in the direction orthogonal to the plane of projection – the resulting projection will, by simple geometrical considerations, coincide with the first projection in two locations. The same argument can then be extended to the case of fixed w_0, which involves simply taking a slice of the three-dimensional ellipsoid at the location of the $\bar{\mu}_0 - \Sigma_0$ plane.

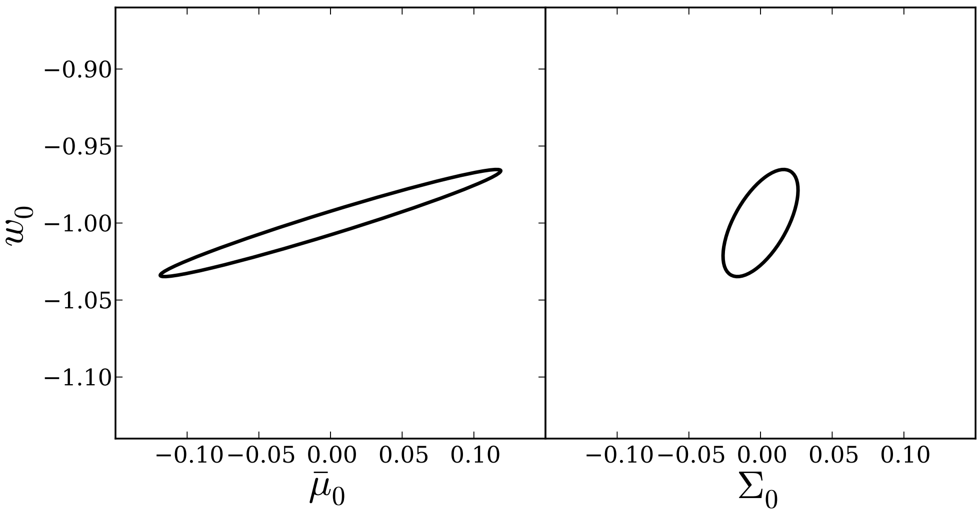

Figure 2.7: Forecast constraints at a 68.3% level from weak lensing, redshift-space distortions and BAO measurements, in the case where $\sigma_{w_0,\mathrm{BAO}} = 5\%$. The left panel displays these joint constraints in the $w_0 - \bar{\mu}_0$ plane, marginalising over Σ_0, while the right panel does the same in the $w_0 - \Sigma_0$ plane, marginalising over $\bar{\mu}_0$. In both cases, w_a is fixed to 0.

2.4.2.2 Marginalising over $\{w_0, w_a\}$

The next case to consider is that in which w_a is not fixed to zero. Derivatives of $C_\ell^{\kappa_\mathrm{g}^i \kappa_\mathrm{g}^j}$ and $\delta f \sigma_8$ with respect to w_a are now required; once again, these are computed analytically from equations 2.36 and 2.43 and listed in Appendix B. In this scenario, the BAO Fisher matrix is slightly more complicated, as the entire 2×2 block related to w_0 and w_a is non-zero.

In analogy to the above, three scenarios are considered:

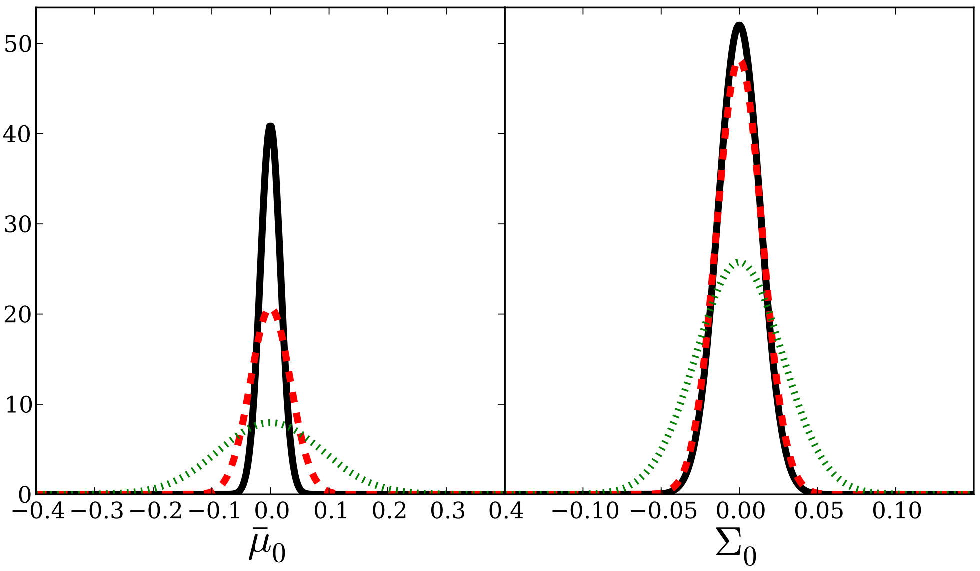

Figure 2.8: Forecast posterior probability distributions from weak lensing, redshift-space distortion, and BAO observations in the case where w_0 and w_a have been marginalised over. The left panel shows the distribution for $\bar{\mu}_0$ when Σ_0 is marginalised over, while the right panel shows the distribution for Σ_0 with $\bar{\mu}_0$ marginalised over. Black, solid: w_0 and w_a fixed; red, dashed: scenario 2 described in Section 2.4.2.2; green, dotted: scenario 3 described in Section 2.4.2.2.

1. The scenario where w_0 and w_a are fixed to their fiducial values. Again, this is for comparison, and is identical to the case considered in Section 2.4.1.

2. The scenario where the BAO Fisher matrix represents the best-case expected constraints from a DETF4-type survey. In this scenario, the components of the BAO-only covariance matrix (the inverse of the Fisher matrix) are given by: $C_{w_0,w_0} = 0.0010$, $C_{w_a,w_0} = -0.0038$, and $C_{w_a,w_a} = 0.016$ [221].

3. The scenario where the BAO-only covariance matrix is obtained by multiplying the covariance matrix listed above in scenario 2 by an overall factor of 8.2^2. This corresponds to the case where the projected 68.3% error on w_0 from BAO is 5% and all other elements of the covariance matrix are scaled up accordingly.

The left panel of Figure 2.8 presents the combined weak lensing, redshift-space distortion and BAO forecast constraints on $\bar{\mu}_0$ while marginalising over w_0, w_a and Σ_0;

the right panel does the same for constraints on Σ_0 while marginalising over w_0, w_a and $\bar{\mu}_0$. Figure 2.9, meanwhile, presents the 68.3% confidence regions in the $\bar{\mu}_0 - \Sigma_0$ plane while marginalising over w_0 and w_a.

It can be seen that the forecast constraint on Σ_0 is now slightly more sensitive to the level of BAO constraint on w_0 and w_a than in the above case where w_a is fixed. This is particularly noticeable in scenario 3, in which the expansion history is the least well-constrained. Turning to $\bar{\mu}_0$, it is clear from Figure 2.8 that the forecast constraint remains sensitive to the level of knowledge about the expansion history in much the same way as in the w_a-fixed case. That is, the constraint in scenario 3 is broadened considerably relative to that in scenario 2, and both are slightly broader than in the above case where w_a fixed. Finally, examining the combined plot in Figure 2.9, it can be seen that the confidence regions therein are slightly larger than those in the corresponding Figure 2.6, where w_a is fixed (other than for scenario 1, which is the same in both figures by design).

In summary, allowing for a time-dependence in the equation of state of the effective dark energy component loosens the expected constraints on $\bar{\mu}_0$ and Σ_0, but not catastrophically so. In fact, the overall level of constraint provided by BAO measurements on the expansion history of the Universe appears to have a greater effect on forecast constraints in the $\bar{\mu}_0 - \Sigma_0$ plane than does the assumed time-dependence of that expansion history.

2.4.3 Scale-dependent $\mu(x, k)$ and $\gamma(x, k)$

Until this point, any scale-dependence of $\mu(x, k)$ and $\gamma(x, k)$ has been neglected, with the focus being exclusively on time-dependence. A scale-dependent ansatz is now considered.

It has been shown that in the quasistatic regime and for Horndeski gravity (that is, any $f(R)$ or scalar-tensor theory with second-order field equations), $\mu(x, k)$ and $\gamma(x, k)$

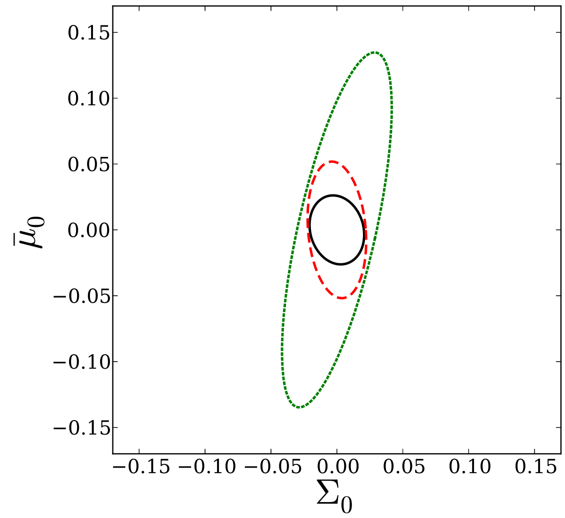

Figure 2.9: Forecast 68.3% confidence regions in the $\bar{\mu}_0 - \Sigma_0$ plane, marginalising over w_0 and w_a. Black, solid: w_0 and w_a fixed; red, dashed: scenario 2 described in Section 2.4.2.2; green, dotted: scenario 3 described in Section 2.4.2.2.

can be expressed as ratios of polynomials in k [92, 222]. They are given by:

$$\begin{aligned}\gamma(x,k) &\simeq \frac{p_1(x)+p_2(x)k^2}{1+p_3(x)k^2} \\ \mu(x,k) &\simeq \frac{p_1(x)+p_2(x)k^2}{p_4(x)+p_5(x)k^2}.\end{aligned} \tag{2.51}$$

This is found by trivially manipulating the equivalent result of [92], in which $\mu(x,k)$ is defined via the Poisson equation with Ψ rather than with Φ. Note that this difference in definition prevents equation 2.51 from taking the typical form, in which the denominator of $\gamma(x,k)$ is equal to the numerator of $\mu(x,k)$.

The form of equation 2.51 which appeared in [92] has recently been considered in [94], in which a Principle Component Analysis was undertaken for a combined future data set including weak lensing and galaxy count measurements from LSST, as well as *Planck* CMB measurements and upcoming supernova data. Here, the Fisher matrix formalism is employed to find the level of forecast constraint from a DETF4-type survey on various parameter space directions. The linear response expression for $C_\ell^{\kappa_g^i \kappa_g^j}$ will then provide an understanding of the related degeneracy structure of the parameter space. Because the goal of this section is only to broadly understand the best-constrained directions of the parameter space, $\beta(x) = 0$ is fixed for simplicity.

In GR+ΛCDM, $p_1(x) = p_4(x) = 1$ and $p_2(x) = p_3(x) = p_5(x) = 0$. Therefore, in keeping with a linear response approach, the following is defined:

$$\begin{aligned} p_1(x) &= 1 + \delta p_1(x) \\ p_2(x) &= \delta p_2(x) \\ p_3(x) &= \delta p_3(x) \\ p_4(x) &= 1 + \delta p_4(x) \\ p_5(x) &= \delta p_5(x). \end{aligned} \tag{2.52}$$

Then, by dropping higher-order terms in $\delta p_i(x)$, expressions are found for $\mu(x,k)$ and $\gamma(x,k)$:

$$\begin{aligned} \mu(x,k) &\simeq 1 + \delta p_1(x) + \delta p_2(x)k^2 - \delta p_4(x) - \delta p_5(x)k^2 \\ \gamma(x,k) &\simeq 1 + \delta p_1(x) + \delta p_2(x)k^2 - \delta p_3(x)k^2. \end{aligned} \tag{2.53}$$

Previous choices for $\delta\mu(x,k)$ and $\delta\gamma(x,k)$ have been consistent with equation 2.53; the assumption has simply been made that $\delta p_2(x)$, $\delta p_3(x)$, and $\delta p_5(x)$ are sub-dominant. Setting then $\delta p_1(x) - \delta p_4(x) = \delta\mu(x)$ and $\delta p_1(x) = \delta\gamma(x)$ recovers the form used in previous sections.

It will be useful to have at hand the equivalent expressions for $\bar{\mu}(x,k)$ and $\Sigma(x,k)$. They can be found using equation 2.46:

$$\begin{aligned} \bar{\mu}(x,k) &\simeq -\delta p_4(x) + k^2\left(\delta p_3(x) - \delta p_5(x)\right) \\ \Sigma(x,k) &\simeq \frac{1}{2}\delta p_1(x) - \delta p_4(x) + k^2\left(\frac{1}{2}\delta p_2(x) + \frac{1}{2}p_3(x) - \delta p_5(x)\right). \end{aligned} \tag{2.54}$$

As usual, in order to forecast constraints, an ansatz must be selected for the functions $\delta p_i(x)$. From equation 2.51, it can be seen that in fact, while $\delta p_1(x)$ and $\delta p_4(x)$ are dimensionless, $\delta p_2(x)$, $\delta p_3(x)$ and $\delta p_5(x)$ must have dimensions of length squared. A form similar to that of equation 2.48 is chosen for both sets of functions, introducing a scale where necessary to account for their different dimensionalities:

$$\begin{aligned} \delta p_{(1,4)}(x) &= p_0^{(1,4)} \frac{\Omega_\Lambda^{\mathrm{GR}}(x)}{\Omega_\Lambda^{\mathrm{GR}}(x=0)} \\ \delta p_{(2,3,5)}(x) &= \frac{p_0^{(2,3,5)} c^2}{(20H_0)^2} \frac{\Omega_\Lambda^{\mathrm{GR}}(x)}{\Omega_\Lambda^{\mathrm{GR}}(x=0)}. \end{aligned} \tag{2.55}$$

Thus, the parameter space is five-dimensional, with parameters $\{p_0^1, p_0^2, p_0^3, p_0^4, p_0^5\}$. The scale $c/20H_0$ has been chosen as it provides sensible numerical eigenvalues. As will be discussed below, the numerical value of this scale will not affect forecasting results.

To compute the necessary Fisher matrices, derivatives of $C_\ell^{\kappa_g^i \kappa_g^j}$ and $\delta f\sigma_8$ with respect to the parameters p_0^i are required. These are computed once again in a straightforward manner from equations 2.36 and 2.43, and are presented in Appendix B. As can be seen there, or as is obvious from equation 2.51, some of these derivative expressions are dependent upon k. In the weak lensing case, this is trivially dealt with, as the Limber approximation sets $k = l/\chi$. However, the derivatives of $\delta f\sigma_8$ with respect to p_0^2, p_0^3 and p_0^5 are truly k-dependent.

In order to treat this case, the usual (general relativistic) assumption of a scale-independent $f\sigma_8$ must be abandoned. Instead, five bins in k are considered. As in [213], these bins are assumed have edges $k = [0.005, 0.02, 0.05, 0.08, 0.12, 0.15]$, stopping short of entering the regime in which nonlinearities dominate. The error on the measurement of $f\sigma_8$ in each k-bin is selected based on the assumption that a DETF4-type survey, which covers a large fraction of the sky, will result in tighter measurements of large-scale modes than of small-scale modes. To model this, the total error budget of each redshift bin, given by [219], is divided into the five k-bins listed above. The first two redshift bins ($k = 0.005 - 0.02$ and $k = 0.02 - 0.05$) receive 36% of the constraining power each, the next two bins ($k = 0.05 - 0.08$ and $k = 0.08 - 0.12$) receive 12% of each, and the final bin ($k = 0.12 - 0.15$) receives 4% of the constraining power.

Fisher matrices can now be constructed for weak lensing and redshift-space distortions, recalling in the redshift-space distortions case to sum over bins of scale as well as of redshift. The total combined Fisher matrix is inverted to obtain the approximate covariance matrix, which is then diagonalised to obtain five eigenvectors with corresponding eigenvalues.

Before examining and interpreting these eigenvalues and eigenvectors, it is helpful to consider more fully the implications of the difference in dimensionality of $\delta p_1(x)$ and $\delta p_4(x)$ versus $\delta p_2(x)$, $\delta p_3(x)$ and $\delta p_5(x)$. In equation 2.55, p_0^2, p_0^3 and p_0^5 have essentially been scaled by $c^2/(20H_0)^2$. This scaling factor is arbitrary, and using a different factor would alter the numerical value of the covariance matrix eigenvalues. Therefore, although all eigenvalues of the covariance matrix are dimensionless, any forecast constraint on p_0^2, p_0^3 or p_0^5, or on any combination thereof, must be multiplied by $c^2/(20H_0)^2$. This provides a physically meaningful value with dimensions length squared, which represents a constraint on the combination $p^0_{(2,3,5)} \times c^2/(20H_0)^2$. Without introducing a prior, it is impossible to meaningfully compare numerical constraints on parameter combinations within two different parameter sub-spaces: that of p_0^1 and p_0^4 and that of p_0^2, p_0^3, and p_0^5.

First, consider those eigenvectors in the subspace of p_0^1 and p_0^4. They are listed here, along with the square root of the associated eigenvalue, σ (which acts as a measure of how well the parameter space is constrained in the direction of the eigenvector):

$$\begin{aligned}\vec{\alpha}_1 &= 0.9\hat{p}_1 - 0.002\hat{p}_2 + 0.002\hat{p}_3 + 0.4\hat{p}_4 - (2\times 10^{-4})\hat{p}_5 \\ &\simeq 0.9\hat{p}_1 + 0.4\hat{p}_4 \qquad (2.56)\end{aligned}$$

with $\sigma \simeq 0.1$, and

$$\begin{aligned}\vec{\alpha}_2 &= -0.4\hat{p}_1 - 0.002\hat{p}_2 + 0.004\hat{p}_3 + 0.9\hat{p}_4 - 0.001\hat{p}_5 \\ &\simeq -0.4\hat{p}_1 + 0.9\hat{p}_4 \qquad (2.57)\end{aligned}$$

with $\sigma \simeq 0.02$. Here, $\hat{p}_i$ is a unit vectors in the parameter space direction of p_0^i. Clearly, due to the numerical nature of the Fisher matrix calculation, some sub-dominant contributions in the directions of $\hat{p}_2$, $\hat{p}_3$ and $\hat{p}_5$ persist; these are ignored.

From the above, it can be seen that the direction $\vec{\alpha}_2$ is better constrained than $\vec{\alpha}_1$. In order to interpret these relative levels of constraint, consider that $\vec{\alpha}_1$ represents a parameter-space direction in which p_0^4 is roughly half as large as p_0^1, and all other p_0^i are negligible. As can be seen in equation 2.54, under these conditions, $\Sigma(x,k)$ is approximately insensitive to modifications to GR. As this is not the case for $\vec{\alpha}_2$, it is clear why this latter parameter space direction is better constrained.

Consider then the eigenvectors in the subspace of p_0^2, p_0^3 and p_0^5. These are given by:

$$\begin{aligned}\vec{\alpha}_3 &= -(7\times 10^{-4})\hat{p}_1 - 0.7\hat{p}_2 + 0.7\hat{p}_3 - 0.005\hat{p}_4 + 0.004\hat{p}_5 \\ &\simeq -0.7\hat{p}_2 + 0.7\hat{p}_3 \qquad (2.58)\end{aligned}$$

with $\sigma \simeq 6\times 10^{-4}$,

$$\begin{aligned}\vec{\alpha}_4 &= -(6\times 10^{-4})\hat{p}_1 - 0.4\hat{p}_2 - 0.4\hat{p}_3 + 0.001\hat{p}_4 + 0.8\hat{p}_5 \\ &\simeq -0.4\hat{p}_2 - 0.4\hat{p}_3 + 0.8\hat{p}_5 \qquad (2.59)\end{aligned}$$

with $\sigma \simeq 2\times 10^{-5}$, and

$$\begin{aligned}\vec{\alpha}_5 &= -(5\times 10^{-4})\hat{p}_1 - 0.6\hat{p}_2 - 0.6\hat{p}_3 - (3\times 10^{-5})\hat{p}_4 - 0.6\hat{p}_5 \\ &\simeq -(0.6\hat{p}_2 + 0.6\hat{p}_3 + 0.6\hat{p}_5) \qquad (2.60)\end{aligned}$$

with $\sigma \simeq 2$. Recall that it is not meaningful to directly compare these σ values with those for eigenvectors $\vec{\alpha}_1$ and $\vec{\alpha}_2$.

In order to understand the relative constraints on the eigenvectors in this subspace, one can first find the relationships between parameter values along the eigenvector directions, as was sketched above for $\vec{\alpha}_1$. Using these relationships in equation 2.54, one can then find simpler expressions for $\Sigma(x,k)$ and $\bar{\mu}(x,k)$:

- In the direction $\vec{\alpha}_3$, $p_0^2 \simeq -p_0^3$ and $p_0^5 \simeq 0$. Therefore, $\Sigma(x,k) \simeq 0$, and $\bar{\mu}(x,k) \simeq \frac{p_0^3 c^2}{(20H_0)^2}\frac{\Omega_\Lambda^{\rm GR}(x)}{\Omega_\Lambda^{\rm GR}(x=0)}k^2$.

- In the direction $\vec{\alpha}_4$, $p_0^2 \simeq p_0^3$ and $p_0^5 \simeq -2p_0^3$. Therefore, $\Sigma(x,k) \simeq 3\frac{p_0^3 c^2}{(20H_0)^2}\frac{\Omega_\Lambda^{\rm GR}(x)}{\Omega_\Lambda^{\rm GR}(x=0)}k^2$, and $\bar{\mu}(x,k) \simeq 3\frac{p_0^3 c^2}{(20H_0)^2}\frac{\Omega_\Lambda^{\rm GR}(x)}{\Omega_\Lambda^{\rm GR}(x=0)}k^2$.
- In the direction $\vec{\alpha}_5$, $p_0^2 \simeq p_0^3 \simeq p_0^5$. Therefore, $\Sigma(x,k) \simeq 0$, and $\bar{\mu}(x,k) \simeq 0$.

With this manipulation, it can be seen why the direction $\vec{\alpha}_4$ is better constrained than $\vec{\alpha}_3$. A small change in the value of p_0^3 along the $\vec{\alpha}_4$ direction produces a larger effect on both $\bar{\mu}(x,k)$ and $\Sigma(x,k)$ than does a similar change in the direction of $\vec{\alpha}_3$. In fact, along direction $\vec{\alpha}_3$, $\Sigma(x,k)$ is totally insensitive to such changes. This greater sensitivity of both $\bar{\mu}(x,k)$ and $\Sigma(x,k)$ to parameter changes along $\vec{\alpha}_4$ accounts for the better-constrained nature of this parameter space direction. It is also plain to see why the direction $\vec{\alpha}_5$ is by far the worst-constrained of this set. As long as $p_2^0 = p_3^0 = p_5^0$, both $\Sigma(x,k)$ and $\bar{\mu}(x,k)$ are entirely insensitive to the value taken by these parameters.

It is tempting to attempt a comparison of the above results directly with those of [94]. However, this would be misleading, as the Principle Component Analysis employed in that work allows the functions $p_i(x)$ to take any time-dependence, whereas the time-dependence is here restricted to that given in equation 2.55. Additionally, the authors of [94] chose to impose a prior upon the variance of each function $p_i(x)$, enabling them to meaningfully discuss constraints on directions which combine the two parameter subspaces which have been considered here. Nevertheless, there is some small comparison we can draw: in [94] it was found that the functions $p_i(x)$ can not be individually constrained, and there is similarly no evidence found in this case of any well-constrained direction corresponding to a single p_0^i.

2.5 Conclusions

The goal of this chapter has been first to develop a new expression for a key weak lensing observable, then to use that expression to understand specifically how weak lensing observations are affected by modifying GR. In this spirit, clarity has been prioritised. Degeneracies between gravitational parameters have been the focus of investigation, while uncertainties in the standard cosmological parameters have not been included at this time.

A new expression for the power spectrum of the galaxy weak lensing convergence under alternative theories of gravity was constructed, and is given in equation 2.36. Derived by considering only small deviations from GR+ΛCDM, this novel expression neatly separates into an integral over two terms: a general relativistic kernel, and a source term which encompasses all deviations from general relativity. The latter is made up of additive terms which are themselves each representative of a different effect due to modifying general relativity. This neat separation, first of the full expression into kernel and source, and then of the source expression into physical effects, allows degeneracies between gravitational parameters to be physically interpreted. The expression is reliable in the ΛCDM-like case of $\beta(x) = 0$, whereas complementary works employing a fluid model have found this limit difficult to constrain [223].

With equation 2.36 in hand, degeneracies were first investigated in the simplified case of a ΛCDM-like expansion history. It was shown how the degeneracy direction of weak lensing in the $\bar{\mu}_0 - \Sigma_0$ plane relies on the time-dependent ansatz for $\bar{\mu}(x)$. However, it was also demonstrated that even for an extreme ansatz, weak lensing and redshift-space distortion measurements remain non-degenerate in this plane, and hence are a viable combination of observables to offer joint constrains on $\bar{\mu}_0$ and Σ_0.

The new expression for $C_\ell^{\kappa_{\rm g}^i \kappa_{\rm g}^j}$ was then employed as a valuable tool in conducting and interpreting Fisher forecasts of weak lensing observations. The linearity of equation 2.36 in the gravitational parameters made the computation of the required Fisher matrices technically easy. Perhaps more importantly, the clarity of the expression provided simple physical interpretations of the degeneracies which presented themselves in the forecast of multi-dimensional constraints. This was first demonstrated by allowing the effective equation of state of the dark energy component to take a CPL form, given in Section 2.4.2. It was found that in the case where $w_a = 0$ and a phenomenological ansatz for $\bar{\mu}(x)$ and $\Sigma(x)$ is assumed, forecast constraints on $\bar{\mu}_0$ from weak lensing and redshift-space distortions are highly sensitive to the level of constraint on w_0 from BAO. Forecast constraints on Σ_0, on the other hand, were found to be nearly unaffected. The separation of the relevant linear-response expressions into source and kernel made evident the stark difference between the redshift dependences of the GR kernels of $C_\ell^{\kappa_g^i \kappa_g^j}$ and $f\sigma_8$. This provided a clear explanation for the higher sensitivity of redshift-space distortions to early time effects, and hence to changes in w_0. Relaxing the requirement that $w_a = 0$, it was then seen that constraints in the $\bar{\mu}_0 - \Sigma_0$ plane were only moderately loosened by marginalising over w_a. This offers the exciting prospect that the analysis of data from a DETF4-type survey may be able to allow for a time-dependent background expansion without sacrificing much constraining power in the $\bar{\mu}_0 - \Sigma_0$ plane.

Finally, the linear response expression for $C_\ell^{\kappa_g^i \kappa_g^j}$, in combination with that for $f\sigma_8$, was used to understand the best-constrained directions in the space of parameters of the scale-dependent ansatz given in [92]. By varying the parameter values along the eigenvectors of the Fisher matrix within the source terms of $C_\ell^{\kappa_g^i \kappa_g^j}$ and of $f\sigma_8$, the differences between directions in the parameter space which were forecast to be well- or poorly-constrained could be understood analytically. This work expands upon the work of [94], both by forecasting for a different survey, and by providing clear explanations for the forecast constraints which were found, something that is non-trivial to do using a Principle Component Analysis method.

The methods developed in this chapter to better understand the effect of modifying gravity on weak lensing could in principle be extended to understanding degeneracies in other scenarios of observational cosmology. Hopefully, the work presented here can provide the groundwork for such developments. As previously noted, in the interest of clarity, uncertainty on standard cosmological parameters has not been included in this chapter. Ideally, these could be included in the future to provide more accurate forecasting and more general conclusions. However, in seeking to include the corresponding additional parameters, the clarity of equation 2.36 is expected to be compromised, and as such it is anticipated that future work in this direction will necessarily involve the sacrifice of the descriptive power shown here. In such future work, forecasting methods involving sampling the posterior of the joint probability distribution of the relevant parameters may be more appropriate.

Chapter 3

Forecast constraints on new physical scales from modified gravity

3.1 Introduction

Modifications to general relativity are thought to result in the novel scale-dependence of certain cosmological observables, as well as in new characteristic physical scales which are not present in GR (see, for example, [117]). In Chapter 2, the possibility of measuring the scale-dependence of functions parameterising modifications to GR was briefly discussed. In this chapter, the detectability of scale-dependence in these functions and of new physical scales is explored more fully.

In order to take advantage of these observational signatures to test or constrain alternative theories of gravity, it is helpful to have a more specific understanding of the nature of the scale-dependence which is expected to be introduced. As mentioned in Chapter 2, the precise form of this scale-dependence has previously been computed for Horndeski gravity [92,222] for the functions μ and γ of the quasistatic parameterisation (defined in equation 1.29). Building upon this result, [93] extended these expressions to incorporate all theories of gravity with second order equations of motion and one new spin-0 degree of freedom. This was achieved without reference to any specific gravitational action or Lagrangian, but rather by appealing to simple physical principles and by working from a set of allowed ‘template’ field equations.

By considering the case in which a hypothetical new physical scale is just slightly within the range of detectability of upcoming surveys, it is possible to derive expressions for the leading order scale-dependent terms of μ and γ in this scenario. Using these expressions, forecasts can be made as to the potential of future surveys to constrain parameters which describe the scale-dependence of μ and γ, including those parameters which characterise potential new physical scales.

The objective of the work presented in this chapter is to explore how well weak gravitational lensing observations, combined with complementary redshift-space distortion measurements, can constrain or detect the novel scale-dependence and new physical scales which are introduced by gravity theories beyond GR. The development of the above-mentioned general expressions for the scale-dependence of μ and γ is first reviewed in Section 3.2, and the equivalent expressions for the more observationally-motivated $\bar{\mu}$ and Σ are introduced. Section 3.3 then describes the survey for which constraints on parameters are forecast and discusses the resulting predicted constraints. Finally, in Section 3.4, conclusions are drawn regarding the potential of next-generation lensing and galaxy surveys to constrain scale-dependence and new physical scales. Note that although the author of this thesis is an author of [93], she was not heavily involved in the derivation of the theoretical results presented in Section 3.2. These results are reviewed here as background information to enable the reader’s understanding of Sections 3.3 and 3.4.

3.2 Theoretical basis

3.2.1 Deriving the scale-dependence of μ and γ

In order to forecast how well upcoming weak gravitational lensing and galaxy observations will constrain the scale-dependence and new scales of alternative theories of gravity, it is necessary to first understand the form that this scale-dependence is predicted to take. To this end, a review is now presented of the derivation of the scale-dependent forms of μ and γ within all theories of gravity which introduce a single new spin-0 degree of freedom.

Consider the set of alternative gravitational theories which introduce a single new spin-0 degree of freedom, and call the perturbations to this degree of freedom χ. In the absence of specific knowledge about χ, an ansatz of $\dot{\chi} = \Gamma_\chi \chi$ is assumed for its rate of change. Γ_χ may correspond to an already-known physical scale (e.g., the Hubble time), or to a new scale introduced by modifying GR.

Assume then the existence of a single such new scale, M. Although M in principle has dimensions of mass, it may be more physically intuitive to think of it as representing an inverse-length $\frac{1}{L}$. L can then be thought of as the transitional length scale above which gravity deviates from GR. Armed with only these new quantities (M, χ, and Γ_χ), two simple physical principles, and the quasistatic approximation, a generic form can be derived for the scale-dependence of μ and γ within theories which introduce a single new spin-0 degree of freedom.

As was discussed in Section 1.2.1, μ and γ are derived from the Poisson equation and from the slip relation respectively, under the quasistatic approximation. To derive the scale-dependence of μ and γ, these two equations, as well as the equation of motion for χ, are first required in their non-quasistatic form. For a given theory, this information is contained within the gravitational field equations. In order to find the correct form of μ and γ not for a particular theory, but more generally, a template can be written down for each of the required equations. These template equations are derived from two principles:

1. The equations of motion must have a gauge-invariant formulation.
2. The equations of motion must be at most second order in derivatives.

In [93], an example is given of the case in which the new degree of freedom is a scalar field ϕ; it is summarised here in order to illustrate how the template equations are derived.

In order to find the template equations required, consider first that the equation of motion for the new degree of freedom must have a gauge-invariant formulation. Recall from equation 1.15 that the line-element of the perturbed FRW metric before gauge fixing can be written as:

$$ds^2 = a(\eta)^2\Big[-(1+2\Psi)d\eta^2 - 2(\vec{\nabla}_i\epsilon)d\eta\, dx^i + (1-2\Phi)\,\gamma_{ij}\, dx^i dx^j + (D_{ij}\nu)\; dx^i dx^j\Big] \tag{3.1}$$

where $D_{ij} = \vec{\nabla}_i\vec{\nabla}_j - \frac{1}{3}\delta_{ij}\vec{\nabla}_k\vec{\nabla}^k$.

It is known that in order to achieve gauge-invariance in the equations of motion, the potentials Φ and Ψ and their derivatives cannot appear in any arbitrary combination (see, for example, [11]), but rather must be grouped into the combination:

$$\dot{\hat{\Phi}} + \mathcal{H}\hat{\Psi} = \dot{\Phi} + \mathcal{H}\Psi + \frac{1}{2}(\dot{\mathcal{H}} - \mathcal{H}^2)(\dot{\nu} + 2\epsilon) \tag{3.2}$$

where the standard Bardeen potentials $\hat{\Phi}$ and $\hat{\Psi}$ have been introduced for clarity [224]. This demonstrates that Ψ must always enter the field equations at one derivative order lower than Φ. Similarly, to ensure gauge-invariance with respect the perturbations of ϕ, the following gauge-invariant combination is introduced:

$$\hat{\delta\phi} = \delta\phi + \frac{\dot{\phi}}{\mathcal{H}}(\Phi + k^2\nu). \tag{3.3}$$

Because the equation of motion for the perturbation of ϕ will necessarily contain $\ddot{\delta\phi}$, it must also contain $\ddot{\Phi}$ in order to allow for gauge-invariance.

Applying these conditions, dimensional consistency, and the fact that the equations of motion should be second order in derivatives, the template for the equation of motion for the perturbations of ϕ can be written as:

$$\begin{aligned} & d_1\ddot{\delta\phi} + d_2[\mathcal{H}, M]\,\dot{\delta\phi} + d_3[\mathcal{H}^2, M^2, \mathcal{H}M]\delta\phi + d_4 k^2\,\delta\phi + b_0\ddot{\Phi} + b_1[\mathcal{H}, M]\dot{\Phi} \\ & \quad + b_2[\mathcal{H}^2, M^2, \mathcal{H}M]\Phi + b_3 k^2\,\Phi + c_1[\mathcal{H}, M]\dot{\Psi} + c_2[\mathcal{H}^2, M^2, \mathcal{H}M]\Psi + c_3 k^2\Psi = 0 \end{aligned} \tag{3.4}$$

where terms such as $[\mathcal{H}^2, M^2, \mathcal{H}M]$ indicate that a function of time has dimensions of, in this case, mass squared (which can be accomplished with any of the three possible bracketed scaling terms), and lowercase letters indicate theory-dependent functions of time. Using the same conditions, the Poisson equation is found to be:

$$\begin{aligned}-2k^2\Phi = 8\pi G a^2\bar{\rho}_{\mathrm{M}}\Delta_{\mathrm{M}} + \Phi\left(h_1k^2 + h_2[\mathcal{H}^2, M^2, \mathcal{H}M]\right) + h_3[\mathcal{H}, M]\dot{\Phi}\\ + m_2[\mathcal{H}^2, M^2, \mathcal{H}M]\Psi + \delta\phi\left(g_1k^2 + g_2[\mathcal{H}^2, M^2, \mathcal{H}M]\right) + g_3[\mathcal{H}, M]\dot{\delta\phi}\end{aligned} \tag{3.5}$$

and the slip relation is

$$\Phi - \Psi = e_0\Phi + j_0\Psi + f_0\delta\phi. \tag{3.6}$$

Through very similar reasoning, it can be shown that this set of equations applies equally to the case where the new degree of freedom represents the fractional energy density of a fluid. A similar set of equations, leading to ultimately the same forms for μ and γ, apply in the case where the new degree of freedom is the spatial spin-0 part of a timelike vector field. Given this generality, $\delta\phi$ will be replaced from now on with the general perturbation χ, introduced above.

With these three template equations in hand, the scale-dependent forms of μ and γ can be found with simple manipulation. The first step is to impose the quasistatic approximation, by setting each of $\ddot{\Phi}$,$\dot{\Phi}$, $\ddot{\Psi}$, and $\dot{\Psi}$ to zero, as well as neglecting all terms which contain factors of $\mathcal{H}$. Setting also $\dot{\chi} = \Gamma_\chi\chi$, the Poisson equation, for example, becomes:

$$-2k^2\Phi = 8\pi G a^2\bar{\rho}_{\mathrm{M}}\Delta_{\mathrm{M}} + \Phi\left[h_1k^2 + h_2M^2\right] + \Psi\left[m_2M^2\right] + \chi\left[g_1k^2 + g_2M^2 + g_3M\Gamma_\chi\right] \tag{3.7}$$

and the two other template equations are similarly simplified.

Because all explicit time derivatives have been eliminated by the introduction of Γ_χ and the use of the quasistatic approximation, Φ, Ψ and χ appear only linearly. Therefore, by making linear combinations of the three equations, it is always possible to obtain forms of the Poisson equation and the slip relation which eliminate χ. The result is a general expression for the scale dependence of μ and of γ in terms of M and

Γ_χ:

$$\gamma = \frac{p_1 + p_2\frac{M^2}{k^2} + p_3\frac{\Gamma_\chi M}{k^2} + p_4\frac{{\Gamma_\chi}^2}{k^2}}{q_1 + q_2\frac{M^2}{k^2} + q_3\frac{\Gamma_\chi M}{k^2} + q_4\frac{{\Gamma_\chi}^2}{k^2}}$$

$$\mu = \left[p_1 + p_2\frac{M^2}{k^2} + p_3\frac{\Gamma_\chi M}{k^2} + p_4\frac{{\Gamma_\chi}^2}{k^2}\right] \times$$

$$\left[t_1 + t_2\frac{M^2}{k^2} + t_3\frac{\Gamma_\chi M}{k^2} + t_4\frac{{\Gamma_\chi}^2}{k^2} + t_5\frac{M^4}{k^4} + t_6\frac{\Gamma_\chi M^3}{k^4} + t_7\frac{{\Gamma_\chi}^2 M^2}{k^4}\right]^{-1}. \qquad (3.8)$$

These two equations can be shown to encompass the known expressions for the scale-dependence of μ and γ within Horndeski gravity, given in equation 2.51. The additional terms not present in that case allow for the possibility of representing theories beyond Horndeski gravity which have a single spin-0 degree of freedom. Note that as with equation 2.55, equation 3.8 takes a slightly different form than that explicitly derived for Horndeski gravity in [92], as μ in this work is defined via the Poisson equation with Φ rather than with Ψ.

3.2.2 The nature of M

Examining the scale-dependent forms of μ and γ presented in equation 3.8, the dependence on the new physical scale M is evident. By making reasonable assumptions about the properties of M, can these expressions be simplified further?

Consider two cases: one in which M is roughly the Hubble scale, $M \approx \mathcal{H}$, and one in which M is much larger than the Hubble scale, and slightly smaller than the maximum wavenumber to be probed by upcoming galaxy and lensing surveys. The first case represents the situation in which the expansion history of the relevant gravity theory has been tuned to reproduce accelerated cosmological expansion, as is the case for many cosmologically-motivated theories. In the interpretation where M is equivalent to an inverse length scale, the latter case is that in which the new physical length scale is just slightly larger than the largest scales to be probed by upcoming surveys.

In the first case, in addition to $M \approx \mathcal{H}$, $\Gamma_\chi \approx \mathcal{H}$ is also required in order to replicate the accelerated expansion of the Universe. Applying the true quasistatic approximation would thus result in μ and γ reducing to fully time-dependent functions, as the quasistatic approximation requires that all terms which go as the Hubble scale be dropped. Considering just first order scale-dependent terms beyond the quasistatic approximation leads to expressions of the form:

$$\gamma = \frac{p_1 + (p_2 + p_3 + p_4)\frac{\mathcal{H}^2}{k^2}}{q_1 + (q_2 + q_3 + q_4)\frac{\mathcal{H}^2}{k^2}} \tag{3.9}$$

$$\mu = \frac{p_1 + (p_2 + p_3 + p_4)\frac{\mathcal{H}^2}{k^2}}{t_1 + (t_2 + t_3 + t_4)\frac{\mathcal{H}^2}{k^2}}. \tag{3.10}$$

Due to the fact that all scale-dependence is encapsulated in ratios of $\mathcal{H}/k$, it would be unexpected to detect scale-dependence in this regime using any survey which does not probe scales approaching the Hubble scale.

Consider then the case in which M is slightly smaller (L slightly larger) than the smallest wavenumber (largest distance) probed by upcoming galaxy and lensing surveys. This more promising scenario will be the focus of the forecasts of Section 3.3, and the remainder of this chapter. In this case, it is in principle necessary to attempt to constrain all functions in equations 3.8. However, this is observationally unrealistic. Instead, one can Taylor-expand about $\frac{M^2}{k^2} = 0$, relying on the fact that for most k within the survey volume, $k \gg M$. This expansion allows expressions to be derived for μ and for γ which include leading order scale-dependent terms:

$$\mu(a,k) \simeq 1 + A_\mu(a)\left[1 + \left(\frac{M_\mu(a)}{k}\right)^2\right] \tag{3.11}$$

$$\gamma(a,k) \simeq 1 + A_\gamma(a)\left[1 + \left(\frac{M_\gamma(a)}{k}\right)^2\right] \tag{3.12}$$

where A_γ, A_μ, M_γ and M_μ are combinations of p_i, q_i, and t_i, and also include dependence on Γ_χ. Γ_χ could be set to either existing scale ($\mathcal{H}$ or M).

Although μ and γ are theoretically useful, it is preferable to employ equivalent functions which are more observationally-motivated. $\bar{\mu}$ and Σ, introduced in Section 2.3, are selected for this purpose. Fortunately, equation 3.12 has an direct analogue in terms of these functions:

$$1 + \bar{\mu}(a,k) \simeq 1 + A_{\bar{\mu}}(a) \left[1 + \left(\frac{M_{\bar{\mu}}(a)}{k} \right)^2 \right] \tag{3.13}$$

$$1 + \Sigma(a,k) \simeq 1 + A_{\Sigma}(a) \left[1 + \left(\frac{M_{\Sigma}(a)}{k} \right)^2 \right] \tag{3.14}$$

where A_Σ, $A_{\bar{\mu}}$, M_Σ and $M_{\bar{\mu}}$ are simply combinations of A_γ, A_μ, M_γ and M_μ. The goal then is to parameterise A_Σ, $A_{\bar{\mu}}$, M_Σ and $M_{\bar{\mu}}$, and to forecast constraints on their parameters. In doing so, the potential for future weak lensing and galaxy surveys to constrain scale-dependence and new gravitational scales can be explored.

3.3 Forecast constraints on new scales

3.3.1 Set-up

Given the theoretical basis reviewed in the previous section, forecasts can now be made for the constraints expected on the parameters of the scale-dependent forms of μ and γ, or equivalently of $\bar{\mu}$ and Σ. This will provide insight into the potential for upcoming galaxy and weak lensing surveys to inform us about scale-dependence sourced by modifications to GR.

The parameters for which constraints will be forecast are those of the functions A_Σ, $A_{\bar{\mu}}$, M_Σ and $M_{\bar{\mu}}$. If tests of a particular theory of gravity were of interest here, it would be possible to derive the exact form of these functions in the relevant theory, and to forecast constraints on the associated parameters. However, the objective of the forecasts presented here is rather to understand how theory-independent constraints may be achieved by future surveys using the general expressions presented in Section 3.2. Therefore, the time-dependence of A_Σ, $A_{\bar{\mu}}$, M_Σ and $M_{\bar{\mu}}$ cannot be directly specified from a theory, and a generic time-dependence must be assumed. This general form should in principle be sufficiently agnostic that signatures of modified gravity would be detectable regardless of the theory to which they correspond. Following therefore in part [69], the ansatz selected for these functions is given by:

$$\begin{aligned}
A_{\bar{\mu}}(a) &= \bar{\mu}_0 \frac{\Omega_\Lambda^{\rm GR}(a)}{\Omega_\Lambda^{\rm GR}(a=1)} \\
A_{\Sigma}(a) &= \Sigma_0 \frac{\Omega_\Lambda^{\rm GR}(a)}{\Omega_\Lambda^{\rm GR}(a=1)} \\
M_{\bar{\mu}} &= m_{\bar{\mu}} \frac{20 H_0}{c} \\
M_{\Sigma} &= m_{\Sigma} \frac{20 H_0}{c}
\end{aligned} \tag{3.15}$$

where $\bar{\mu}_0$, Σ_0, $m_{\bar{\mu}}$, and m_Σ are constants. Note that in an effort to allow $M_{\bar{\mu}}^{-1}$ and M_Σ^{-1} to be interpreted as length scales, an arbitrary subhorizon distance unit of $(c/20H_0)^{-1}$ has been introduced.

Examining equation 3.15 in combination with equations 3.13 and 3.14, it is clear that the parameters available to be constrained independently are $\bar{\mu}_0$, Σ_0, $\bar{\mu}_0 m_{\bar{\mu}}^2$, and $\Sigma_0 m_\Sigma^2$. In the remainder of this chapter, forecast constraints on these parameters are derived for an upcoming survey. In the spirit of considering a next-generation but not unrealistically futuristic observational scenario, a Dark Energy Task Force 4 (DETF4)-type survey [1] is selected, much that like that considered in Chapter 2. This is assumed to combine a weak gravitational lensing survey and a galaxy clustering survey from which redshift-space distortion information can be extracted. Forecasts are conducted using Fisher forecasting methodology, as outlined in Section 1.3.3.

Consider first the weak gravitational lensing set-up. Forecasts are made, as in Chapter 2, with the assumption of a tomographic cosmic shear survey. The cosmic shear observable to be considered is once again the angular power spectrum of the convergence, $C_\ell^{\kappa_{\rm g}^i, \kappa_{\rm g}^j}$, where i and j indicate tomographic bins. The predictions for these spectra are made using the linear response expression of equation 2.36, and analytic expressions for derivatives with respect to the four parameters considered here are given in Appendix B. Source galaxies are assumed to be divided into five redshift bins, with the total distribution of source galaxies, $n(z)$, given as in equation 2.42 (with all parameters the same). $n(z)$ is again divided into five bins between $z = 0.5$ and $z = 2$, each with an equal number of galaxies. Noise is accounted for in the same manner as in

Chapter 2, with the covariance matrix given in equation 1.49. Finally, as in Chapter 2, angular multipoles between $\ell = 10 - 100$ are considered, where the lower limit permits the use of the Limber approximation and the upper limit conservatively ensures that only the regime of validity of linear cosmological perturbation theory is considered.

The angular power spectrum of the weak gravitational lensing convergence incorporates scale-dependence naturally. However, as was discussed in Section 2.4.3, the relevant redshift-space distortion observable $f\sigma_8$ is typically assumed to depend on redshift alone, as is predicted in GR. In order to allow for the possibility of a scale-dependent $f\sigma_8$, errors on this observable are incorporated in bins of scale and redshift, in precisely the same manner as was discussed in Section 2.4.3 [219, 225]. Once again, theoretical predictions are made using the linear response expressions of [213], reviewed in equations 2.17 and 2.43, and analytic expressions for derivatives are given in Appendix B.

It is important to emphasise that the forecasts computed in this section are applicable only for parameter values which preserve the validity of the Taylor expansion of equations 3.13 and 3.14. One way to determine the range of parameter values for which this is true is to require that the next-order term in the Taylor expansion does not exceed a given magnitude. For example, consider the case in which this term is not permitted to exceed 0.01 (a 1% alternation to scale-independence). By making the reasonable assumption that the time-dependence of the next-order term can be parameterised as the square of the time-dependence of the first-order term, it is found that the forecasts are valid when $\{m_{\bar{\mu}}, m_{\Sigma}\} < 0.132$. For given values of $\bar{\mu}_0$ or Σ_0, this translates to a range of validity for the more relevant $\bar{\mu}_0 m_{\bar{\mu}}^2$ and $\Sigma_0 m_{\Sigma}^2$ parameters.

Finally, it is noted that the forecasts presented in this chapter seek only to explore the general characteristics of potential constraints from upcoming surveys on the scale-dependence of $\bar{\mu}$ and Σ. It is not the objective of this work to provide accurate forecasts for a particular future survey. Therefore, in the interest of simplicity, the only parameters which are varied are the gravitational parameters introduced above. All

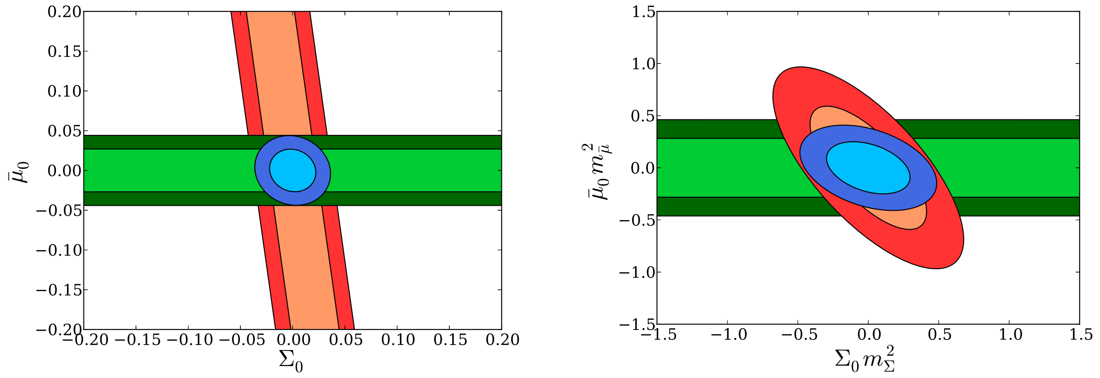

Figure 3.1: Forecast 68.3% and 95.4% constraint contours on the parameters of the scale-dependent expressions for $\bar{\mu}$ and Σ from a DETF4-type survey. Weak gravitational lensing constraints are shown in orange, redshift-space distortion constraints in green, and combined constraints from both observables in blue.

other parameters are fixed to their ΛCDM best-fit values as given in the *Planck* 2013 release [215], the most up-to-date cosmological parameter set at the time of this work. In particular, the expansion history is assumed to precisely match that of ΛCDM. It should therefore be noted that constraints on the four gravitational parameters considered here are expected to be optimistic by nature, as they do not marginalise over auxiliary cosmological parameters. Nevertheless, the forecasts presented can provide an estimate as to the potential for constraining scale-dependence in $\bar{\mu}$ and Σ using weak lensing and galaxy observations, as well as insight into the relevant degeneracies between the four gravitational parameters which are considered.

3.3.2 Results

Performing Fisher forecasting within the above set-up leads to a prediction for the approximate covariance matrix of $\bar{\mu}_0$, Σ_0, $\bar{\mu}_0 m_{\bar{\mu}}^2$, and $\Sigma_0 m_\Sigma^2$. It is given by:

$$\mathbf{C} \simeq \begin{bmatrix} 3.1\times10^{-4} & -2.5\times10^{-5} & -6.2\times10^{-4} & 2.7\times10^{-4} \\ -2.5\times10^{-5} & 2.1\times10^{-4} & -3.2\times10^{-4} & -7.7\times10^{-4} \\ -6.2\times10^{-4} & -3.2\times10^{-4} & 2.7\times10^{-2} & -1.2\times10^{-2} \\ 2.7\times10^{-4} & -7.7\times10^{-4} & -1.2\times10^{-2} & 3.8\times10^{-2} \end{bmatrix}. \tag{3.16}$$

From this 4×4 matrix, predicted parameter constraints can be discerned.

Figure 3.1 displays forecast two-dimensional constraints in the planes of two key parameter pairings. The left panel shows the predicted two-dimensional constraints on those parameters which describe the scale-independent sector, $\bar{\mu}_0$ and Σ_0, while in the right panel, constraints are displayed on the parameters which describe scale-dependence, $\bar{\mu}_0 m_{\bar{\mu}}^2$ and $\Sigma_0 m_{\Sigma}^2$. Forecast constraints from weak gravitational lensing only are shown in orange, those from redshift-space distortions are in green, and those from both observables combined, in blue. In both cases, forecast constraints have been computed with marginalisation over the remaining two parameters.

Consider first the left panel of Figure 3.1. The displayed constraint contours in the plane of $\bar{\mu}_0$ and Σ_0 strongly recall those of Figure 2.4. In fact, the only difference between the result shown here and in Figure 2.4 is marginalisation over $\bar{\mu}_0 m_{\bar{\mu}}^2$ and $\Sigma_0 m_{\Sigma}^2$, which is responsible for the slight loosening of constraints in this case. However the marginalised 1σ constraint on $\bar{\mu}_0$ is in fact degraded by only 2% when compared to the equivalent result from Figure 2.4, while that on Σ_0 is degraded by just 7%. This relative insensitivity to the marginalisation over $\bar{\mu}_0 m_{\bar{\mu}}^2$ and $\Sigma_0 m_{\Sigma}^2$ suggests that it may be worthwhile to consider scale-dependent forms of $\bar{\mu}$ and Σ in the analysis of data from upcoming surveys.

Another similarity between the left panel of Figure 3.1 and Figure 2.4 lies in the orientation of the constraint contour of weak gravitational lensing. The degeneracy direction of this constraint is largely unaffected by marginalisation over $\bar{\mu}_0 m_{\bar{\mu}}^2$, and $\Sigma_0 m_{\Sigma}^2$. This can be explained in part by noting that the time-dependent ansatz selected in equation 3.15 mimics that chosen in equation 2.48. In Chapter 2, it was demonstrated that the time-dependence of $\bar{\mu}$ strongly affects the angle of the weak lensing constraint, therefore it is not unexpected that by choosing a similar ansatz, a similar angle is achieved. It is nevertheless reassuring to note that marginalisation over $\bar{\mu}_0 m_{\bar{\mu}}^2$, and $\Sigma_0 m_{\Sigma}^2$ does not wreak havoc upon the generally-assumed degeneracy-breaking ability of weak lensing and redshift-space distortions in the plane of $\bar{\mu}_0$ and Σ_0.

Turning then to the right panel of Figure 3.1, forecast constraint contours can be seen in the plane of $\bar{\mu}_0 m_{\bar{\mu}}^2$, and $\Sigma_0 m_\Sigma^2$. The absolute value of these constraints is a function of the particular inverse length scale chosen in the ansatz for M_Σ and $M_{\bar{\mu}}$, so their magnitude should not be compared directly with the constraints of the left panel. A feature which can be consistently compared, however, is the degeneracy direction of the weak gravitational lensing constraints. The constraint in this case deviates much further from being exclusively on $\Sigma_0 m_\Sigma^2$. This can be explained by examining the explicit form of $\bar{\mu}$, given the ansatz of equation 3.15:

$$\bar{\mu} \approx 1 + \bar{\mu}_0 \frac{\Omega_\Lambda(a)}{\Omega_\Lambda(a=1)} + \bar{\mu}_0 m_{\bar{\mu}}^2 \frac{\Omega_\Lambda(a)}{\Omega_\Lambda(a=1)} \frac{20^2 H_0^2}{c^2} \frac{\chi(a)^2}{\ell^2} \tag{3.17}$$

where the Limber approximation sets $k = \ell/\chi$. Again, recall from Chapter 2 that the time-dependence of $\bar{\mu}$ is crucial to determining the degeneracy direction of weak lensing: an ansatz for $\bar{\mu}$ which is non-zero at earlier times results in a degeneracy direction which is further from constraining only the parameters of Σ. Equation 3.17 contains a factor of $\chi(a)^2$, which counteracts the effect of $\Omega_\Lambda(a)$ in depressing early-time contributions. Thus, the scale-dependent term in $\bar{\mu}(a, k)$ is non-negligible at earlier times than the scale-independent term, and hence the associated degeneracy direction veers further from vertical. Because the introduction of $\chi(a)^2$ is due entirely to the scale-dependence of the expression, it can be said that the inclusion of scale-dependence itself is the reason that this set of constraints is less orthogonal than those in the scale-independent plane.

Notable also in the right panel of Figure 3.1 is the fact that the forecast constrained region from weak gravitational lensing is visibly closed, indicating that the degeneracy direction of weak lensing must vary with respect to ℓ more strongly in the $\bar{\mu}_0 m_{\bar{\mu}}^2 - \Sigma_0 m_\Sigma^2$ plane than in the $\bar{\mu}_0 - \Sigma_0$ plane. The reason behind this is clear: the scale-dependent terms of $\bar{\mu}$ and Σ, by direct virtue of their scale-dependence, explicitly contain factors of ℓ, as can be seen in equation 3.17. The result is that weak gravitational lensing is arguably more useful as an independent probe in constraining the scale-dependence of $\bar{\mu}$ and Σ than it is in independently constraining the more usual $\bar{\mu}_0$ and Σ_0 parameters. However, the marginalised constraint from weak lensing on $\Sigma_0 m_\Sigma^2$ remains larger than the redshift-space distortion constraint on the complementary $\bar{\mu}_0 m_{\bar{\mu}}^2$, suggesting that redshift-space distortion measurements are the more sensitive probe of scale-dependent gravitational effects.

The forecast constraints displayed in the right panel of Figure 3.1 are complemented by a demonstration, in Figure 3.2, of the effect of varying $\bar{\mu}_0 m_{\bar{\mu}}^2$ and $\Sigma_0 m_{\Sigma}^2$ on the convergence power spectrum. In this figure, the parameter values of $\Sigma_0 m_{\Sigma}^2$ (left panel) and $\bar{\mu}_0 m_{\bar{\mu}}^2$ (right panel) are varied within the range of validity of the present forecasts for the assumed case of $\Sigma_0 = 0.01$ (left panel) and $\bar{\mu}_0 = 0.01$ (right panel). As can be seen, varying these parameters within their regime of validity has very little visible effect on the convergence power spectrum. This is in agreement with the fact that the forecast weak lensing constraints displayed in the right panel of Figure 3.1 are much larger than the parameter values for which the forecasts are valid.

Figure 3.3 further examines the dependence of $C_\ell^{\kappa_g \kappa_g}$ on those parameters related to scale dependence, by depicting $\frac{\partial C_\ell^{\kappa_g \kappa_g}}{\partial (\Sigma_0 m_{\Sigma}^2)}$ (left) and $\frac{\partial C_\ell^{\kappa_g \kappa_g}}{\partial (\bar{\mu}_0 m_{\bar{\mu}}^2)}$ (right), for the illustrative case of a single source redshift bin. It is seen that $\frac{\partial C_\ell^{\kappa_g \kappa_g}}{\partial (\Sigma_0 m_{\Sigma}^2)}$ is larger than $\frac{\partial C_\ell^{\kappa_g \kappa_g}}{\partial (\bar{\mu}_0 m_{\bar{\mu}}^2)}$ at all ℓ considered here. This is consistent with the fact that weak lensing is expected to be more sensitive to Σ than to $\bar{\mu}$, in particular for choices of time-dependence which are non-negligible at late times only. It is also clear from Figure 3.3 that the majority of the constraining power which weak lensing offers with respect to these scale-dependence-related parameters relies on larger-scale (smaller ℓ) measurements.

Finally, although it is not possible to directly predict constraints on m_Σ or $m_{\bar{\mu}}$ using Fisher forecasting, a rough estimate can be made of the expected constraints on these parameters. Consider that:

$$\sigma(m_{\bar{\mu}}^2) \approx \frac{\sigma(\bar{\mu}_0 m_{\bar{\mu}}^2)}{\sigma(\bar{\mu}_0)} \qquad \sigma(m_{\Sigma}^2) \approx \frac{\sigma(\Sigma_0 m_{\Sigma}^2)}{\sigma(\Sigma_0)}, \tag{3.18}$$

an approximation which holds exactly when all parameters are drawn from Gaussian distributions. From this, it is found that $\sigma(m_{\bar{\mu}}^2) \approx 9.3$ and $\sigma(m_{\Sigma}^2) \approx 13.4$. These values can then be used in equation 3.15 to find an approximate upper-bound on new

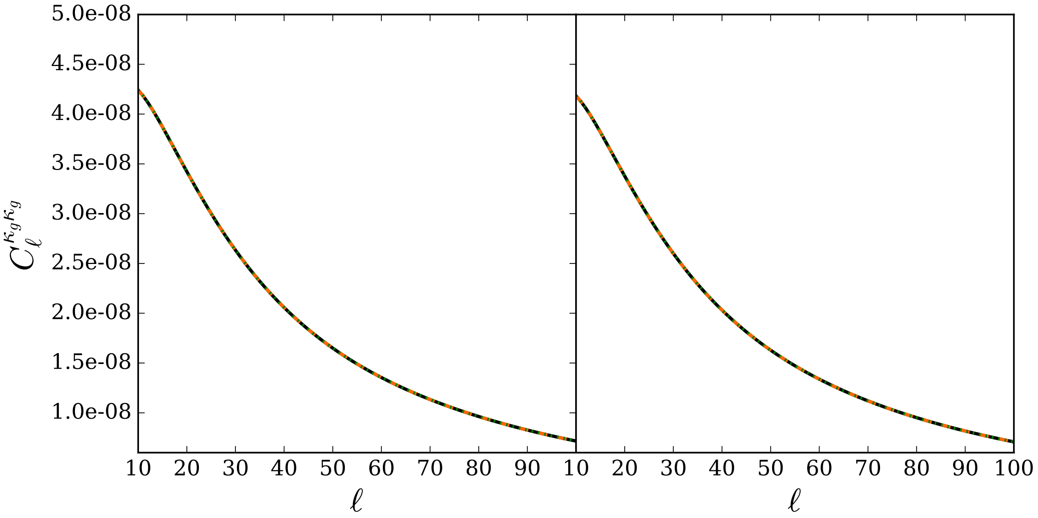

Figure 3.2: $C_\ell^{\kappa_g\kappa_g}$ for variable $\Sigma_0 m_\Sigma^2$ (left) and $\bar{\mu}_0 m_{\bar{\mu}}^2$ (right), for the illustrative case of a single source redshift bin. In the left panel, $\{\bar{\mu}_0, \bar{\mu}_0 m_{\bar{\mu}}^2\} = 0$ and $\Sigma_0 = 0.01$, and in the right panel, $\{\Sigma_0, \Sigma_0 m_\Sigma^2\} = 0$ and $\bar{\mu}_0 = 0.01$. Black solid lines represent the case in which $\Sigma_0 m_\Sigma^2$ (left) or $\bar{\mu}_0 m_{\bar{\mu}}^2$ (right) is equal to 1.3×10^{-4}, orange dashed lines have $\Sigma_0 m_\Sigma^2$ or $\bar{\mu}_0 m_{\bar{\mu}}^2$ equal to 2.0×10^{-4}, and green dotted lines set $\Sigma_0 m_\Sigma^2$ or $\bar{\mu}_0 m_{\bar{\mu}}^2$ to 2.9×10^{-4}. These cases are equivalent to setting m_Σ or $m_{\bar{\mu}}$ equal to 0.08, 0.1, and 0.12 respectively. All three cases produce near-identical power spectra.

length scales which will be detectable in a DETF4-type survey. Expected confidence limits on these length-scale-related parameters are calculated as $\sigma(M_\Sigma^{-1}) \approx 60$ Mpc and $\sigma(M_{\bar{\mu}}^{-1}) \approx 72$ Mpc.

3.4 Conclusions

The objective of this chapter has been to move beyond the introductory treatment of scale-dependence within the quasistatic parameterisation of gravity which was presented in Chapter 2. Here, the observational consequences of this scale-dependence have been explored more fully, and possibilities for constraining the related new physical scale M have also been investigated. This has been accomplished with the help of a general scale-dependent expression for each of the quasistatic parameterising functions $\bar{\mu}$ and Σ, as reviewed in Section 3.2. Using these expressions, first derived in [93], forecast constraints on parameters which describe both the scale-independent and -

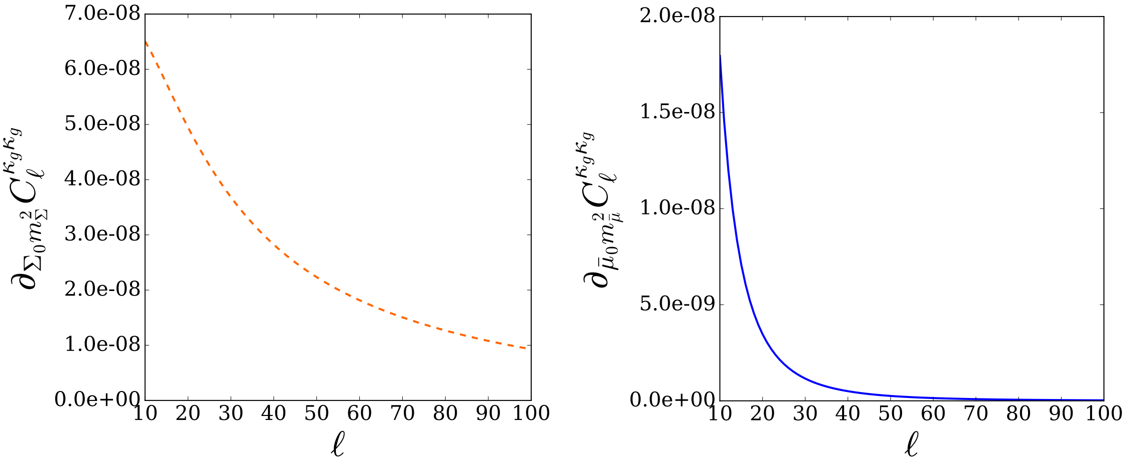

Figure 3.3: Derivatives of $C_\ell^{\kappa_g\kappa_g}$ with respect to $\Sigma_0 m_\Sigma^2$ (left, orange dashed) and $\bar\mu_0 m_{\bar\mu}^2$ (right, blue solid), for the illustrative case of a single source redshift bin.

dependent parts of $\bar\mu$ and Σ have been presented for a DETF4-type survey.

In examining these predicted constraints, it is seen that incorporating the possibility of scale-dependent $\bar\mu$ and Σ will be feasible in upcoming weak lensing and galaxy clustering surveys. The marginalisation over parameters related to scale-dependence did not significantly degrade forecast constraints on the more standard $\bar\mu_0$ and Σ_0 parameters. Furthermore, the near-orthogonality of weak lensing and redshift-space distortion constraints in the plane of $\bar\mu_0$ and Σ_0 was robust to this marginalisation, provided that the same phenomenological time-dependence was selected for $\bar\mu$ and Σ in both cases. This near-orthogonality did not hold to the same extent in the plane of the two scale-dependence-related parameters. Nevertheless, constraints were predicted on parameters related to the new scale M.

It is important to note that while these forecasts have demonstrated that, for example, marginalising over scale-dependence-related parameters does not significantly degrade forecast constraint on $\bar\mu_0$ and Σ_0, this is within the simplified context in which other cosmological parameters are fixed. It is possible that degeneracies exist within the broader set of parameters which may weaken this statement to some extent; a more complex follow-up forecasting study could ascertain this.

Chapter 4

Testing gravity with E_G: Mapping theory onto observations

4.1 Introduction

Although weak gravitational lensing is widely recognised as a powerful probe of gravity, it is subject to degeneracies which affect its ability to independently constrain deviations from GR. For optimal constraints on alternative theories of gravity, multiple cosmological observables must be considered in combination. This was demonstrated in Chapters 2 and 3, where forecasts incorporated weak lensing, redshift-space distortions, and in some cases, BAO observations. Within the Fisher forecasting methodology of those chapters, it was assumed that observables would be combined via standard likelihood methods, as in, for example, [69]. An alternate method of breaking degeneracies is to strategically combine observables into a single statistic. This is the goal behind the statistic E_G.

E_G was first proposed in 2007 [116] as a method of detecting deviations from GR while circumventing potential degeneracies with the galaxy bias. The suggested estimator involved a ratio between $C_{g\kappa_{\rm g}}(l)$, the angular cross-spectrum of galaxy positions and weak lensing convergence (defined in equation 1.40 in the small-scale limit), and $P_{gv}(k)$, the cross-spectrum of velocities with galaxy positions, which could, in principle, be obtained from redshift-space distortion measurements. The same population of galaxies would be used to make both measurements, allowing the galaxy bias to cancel.

Additionally, the required lensing measurement would be from galaxy-galaxy lensing, which is less susceptible to weak lensing systematic effects than is cosmic shear.

The first measurement of E_G was made in 2010 [70], with a second measurement following in 2015 [71]. Both have shown consistency with GR, as well as with other theories of gravity. These two measurements have employed a slightly different definition of E_G, first set out in [70]. This observationally-motivated definition replaces Fourier-space quantities with real-space equivalents, and substitutes the difficult-to-measure $P_{gv}(k)$ with the product of a projected galaxy correlation function and $\beta = f/b$, two galaxy-clustering-related observables described in Section 1.3.2.1. At linear scales, and under the assumption of constant bias, it has been assumed that the new observational definition should agree with the definition of E_G as proposed in [116].

In order to use E_G to constrain or detect deviations from GR, predictions of E_G are required for GR and for alternative theories of gravity. Some such predictions for the original definition of E_G were made in [116], and became the standard choice for comparison with measurement. However, the observational definition of E_G is expected to agree with the original definition only under the above-mentioned assumption of constant bias. Furthermore, as will be discussed, the observational definition contains several additional non-gravitational parameters, which may be degenerate with a departure from GR. It is the difference between the original proposal of [116] and the statistic that is actually used in data analysis which will be explored here.

This chapter is structured as follows. In Section 4.2, both the original and the observational definitions of E_G are reviewed, and an expression is derived for the observational definition in terms of theoretical quantities in general relativity. In Section 4.3, the effect of varying the parameters of the observationally-motivated definition is explored, and the associated uncertainties are compared to the expected level of error on E_G from two possible future measurements. In Section 4.4, the derivation of Section 4.2 is extended to provide a full theoretical expression for E_G under the ($\bar{\mu}$, Σ) parameterisation of modifications to GR. This expression is employed to compute E_G under deviations from GR, and to discuss how well future surveys may constrain alternative theories of gravity using E_G. Finally, conclusions are drawn in Section 4.5.

4.2 Derivation of a theoretical expression for $E_G(R)$

4.2.1 Definitions and review

In this chapter, the original definition of E_G set out in [116] will be referred to as $E_G^0(l)$, and the observationally-motivated definition underlying the statistic used in [70] as $E_G(R)$. The definitions of these quantities are now reproduced here. Note that both $E_G^0(l)$ and $E_G(R)$ are redshift-dependent, but this dependence will typically be suppressed for clarity.

First, $E_G^0(l)$ is defined as the expectation value of

$$\hat{E}_G^0(l, \Delta l) = \frac{C_{g\kappa_{\rm g}}(l, \Delta l)}{3H_0^2 a^{-1} \sum\limits_{\alpha} j_\alpha(l, \Delta l) P_{gv}^{\alpha}}\,, \tag{4.1}$$

where l is the magnitude of the two-dimensional on-sky Fourier-space wavenumber, $C_{g\kappa_{\rm g}}(l, \Delta l)$ is the on-sky cross-spectrum of convergence and galaxy positions in bins of Δl, P_{gv}^{α} is the cross-spectrum of velocities and galaxy positions between k_α and $k_{\alpha+1}$, and $j_\alpha(l, \Delta l)$ is a weighting function which converts P_{gv}^{α} to an angular power spectrum. The expectation value of $\hat{E}_G^0(l, \Delta l)$ is then given by

$$E_G^0(l) = \left[\frac{\nabla^2(\Psi + \Phi)}{3H_0^2 a^{-1} f \Delta_{\rm M}}\right]_{k=l/\bar{\chi}, \bar{z}}\,, \tag{4.2}$$

where f is the linear growth rate of structure, $\Delta_{\rm M}$ is the matter overdensity field, and $\bar{\chi}$ is the comoving distance corresponding to redshift $\bar{z}$. The theoretical value of $E_G^0(l)$ would in fact be expected to be independent of l for any theory of gravity which can be represented by a scale-independent generalised Newtonian constant, with a scale-independent relationship between Φ and Ψ. This is of course the case for GR, where it can be shown that $E_G^0(l) = \frac{\Omega_{\rm M}(z=0)}{f(z)}$ [116].

Next, the observationally-motivated $E_G(R)$ is defined in [70] to be:

$$E_G(R) = \frac{\Upsilon_{gm}(R)}{\beta \Upsilon_{gg}(R)}\,, \tag{4.3}$$

where $\beta = f/b$ (b the galaxy bias as measured on linear scales) and R is the transverse distance from the lens galaxy. $\Upsilon_{gm}(R)$ and $\Upsilon_{gg}(R)$ are annular differential surface densities (ADSDs) [226]: modified versions of standard correlation functions which exclude information on scales below a cut-off threshold denoted R_0.

Equation 4.3 is qualitatively similar to equation 4.1. Both $\Upsilon_{gm}(R)$ and $C_{g\kappa_{\mathrm{g}}}(l, \Delta l)$ represent a cross-correlation between galaxies and matter (with convergence, κ_{g}, mapping matter). Similarly, because $f\Delta_{\mathrm{M}} = v$ on linear scales, $\beta \times \Upsilon_{gg}(R)$ can be interpreted on those scales as a cross-correlation between galaxies and galaxy velocities, much like $P_{gv}(k)$.

Specifically, $\Upsilon_{gm}(R)$ and $\Upsilon_{gg}(R)$ are defined as:

$$\begin{aligned}\Upsilon_{gm}(R) &= \frac{2}{R^2}\int_{R_0}^{R} dR' R' \Sigma_{gm}(R') - \Sigma_{gm}(R) + \left(\frac{R_0}{R}\right)^2 \Sigma_{gm}(R_0) \\ &= \Delta\Sigma_{gm}(R) - \left(\frac{R_0}{R}\right)^2 \Delta\Sigma_{gm}(R_0)\,, \end{aligned} \tag{4.4}$$

$$\Upsilon_{gg}(R) = \rho_{\mathrm{c}}\left[\frac{2}{R^2}\int_{R_0}^{R} dR' R' w_{gg}(R') - w_{gg}(R) + \left(\frac{R_0}{R}\right)^2 w_{gg}(R_0)\right], \tag{4.5}$$

where ρ_{c} is the critical density of the Universe, $\Sigma_{gm}(R)$ is the projected surface mass density at R (see, for example, equation 5 of [226]), and $w_{gg}(R)$ is the projected galaxy autocorrelation function, as defined below in equation 1.42. $\Delta\Sigma_{gm}(R)$ is the excess differential surface mass density, defined in equation 1.39.

4.2.2 Deriving $E_G(R)$ in general relativity

Having now reviewed the definitions of both $E_G^0(l)$ and $E_G(R)$, a full theoretical expression will be developed for $E_G(R)$. In this section, this is undertaken in the context of GR; for an extension to alternative theories of gravity, see Section 4.4.

The first step is to examine equation 4.4 for $\Upsilon_{gm}(R)$. There, $\Upsilon_{gm}(R)$ is seen to be directly dependent upon $\Delta\Sigma_{gm}(R)$, which is in turn related to the tangential shear observed at a transverse distance R from a lens, $\gamma_{\mathrm{t}}^{\mathrm{g}}(R)$. In the case where all lenses are assumed to lie in a thin distribution at $z = z_l$, this relationship is given by:

$$\Delta\Sigma_{gm}(z_l, R) = \langle\gamma_{\rm t}^{\rm g}(R)\rangle \left[\int_{z_l}^{\infty} dz' \frac{n_s(z')}{\Sigma_{\rm c}(z_l, z')}\right]^{-1}, \tag{4.6}$$

where $n_s(z)$ is the normalised redshift distribution of sources and $\Sigma_{\rm c}$ is the critical surface mass density, given by [71]:

$$\Sigma_{\rm c}(z, z') = \frac{c^2\chi(z')}{4\pi G(\chi(z') - \chi(z))\chi(z)(1+z)}. \tag{4.7}$$

It will be convenient to introduce the quantity $\overline{\Sigma_{\rm c}^{-1}}(z_l)$, which is defined as:

$$\overline{\Sigma_{\rm c}^{-1}}(z_l) = \int_{z_l}^{\infty} dz' \frac{n_s(z')}{\Sigma_{\rm c}(z_l, z')}. \tag{4.8}$$

In this chapter, since only hypothetical, apriori-defined source redshift distributions are employed, it is assumed that source redshifts are perfectly known. The result is that for a single lens/source pair:

$$\overline{\Sigma_{\rm c}^{-1}}(z_l, z_s) = \left\{ \begin{array}{cc} \Sigma_{\rm c}^{-1}(z_l, z_s) & , z_s > z_l \\ 0 & , z_s \leq z_l \end{array} \right., \tag{4.9}$$

which results in the following expression for $\Delta\Sigma_{gm}(R, z_l, z_s)$:

$$\Delta\Sigma_{gm}(R, z_l, z_s) = \left\{ \begin{array}{cc} \gamma_{\rm t}^{\rm g}(R, z_l, z_s)\Sigma_{\rm c}(z_l, z_s) & , z_s > z_l \\ 0 & , z_s \leq z_l \end{array} \right.. \tag{4.10}$$

$\langle\gamma_{\rm t}^{\rm g}\rangle$ has become $\gamma_{\rm t}^{\rm g}$ in the limit of a single lens/source pair.

Extending to the full lens and source galaxy populations, the inclusion of redshift information becomes more complex. n_s, which characterises the source galaxy redshift distribution, has already been introduced. For the lenses, the simplifying assumption is made that there exists an effective redshift for the population, which is denoted $\bar{z}_l$. The primary reason for this choice is a reduction in computational difficulty. Throughout this chapter, it is assumed that all lenses are at $\bar{z}_l$, however, for a more general version of these expressions, see Appendix C.

An estimator for $\Delta\Sigma_{gm}(R)$ is obtained by inverse-variance weighting each lens/source pair by a factor of $\overline{\Sigma_{\rm c}^{-1}}^2$ [175], and then by summing over all lens/source pairs. In this case, the source galaxy distribution is treated as continuous, and so summation is replaced with integration. Changing variables from redshift to comoving distance, the resulting expression is

$$\Delta\Sigma_{gm}(R) = \frac{1}{\bar{w}}\int_0^{\chi_H} d\chi_s W_s(\chi_s)\overline{\Sigma_{\rm c}^{-1}}(\bar{\chi}_l,\chi_s)\gamma_{\rm t}^{\rm g}(R,\bar{\chi}_l,\chi_s)\,, \tag{4.11}$$

where $W_s(\chi)$ is the equivalent distribution to $n_s(z)$, and $\bar{w}$ is a normalisation accounting for the weighting factor:

$$\bar{w} = \int_0^{\chi_H} d\chi_s W_s(\chi_s)\left(\overline{\Sigma_{\rm c}^{-1}}(\bar{\chi}_l,\chi_s)\right)^2 . \tag{4.12}$$

An expression is now in hand for $\Delta\Sigma_{gm}(R)$ in terms of the tangential shear. $\gamma_{\rm t}^{\rm g}$ is related to the convergence $\kappa_{\rm g}$ via (see, for example, [227])

$$\gamma_{\rm t}^{\rm g}(R,\chi_s,\bar{\chi}_l) = -\frac{1}{2}\frac{d\bar{\kappa}_{\rm g}(R,\chi_s,\bar{\chi}_l)}{d\ln(R)}\,, \tag{4.13}$$

and the convergence in a direction $\hat{\theta}$ is given by (see, for example, [228]):

$$\bar{\kappa}_{\rm g}(\hat{\theta},\chi_s) = \frac{3}{2}\left(\frac{H_0}{c}\right)^2\Omega_{\rm M}(z=0)\int_0^{\chi_s} d\chi\frac{\chi(\chi_s-\chi)}{\chi_s a(\chi)}\Delta_{\rm M}(r(\chi\hat{\theta},\chi)), \tag{4.14}$$

where χ_s is the comoving distance to the source in question. However, equation 4.13 requires not $\bar{\kappa}_{\rm g}(\hat{\theta},\bar{\chi}_l,\chi_s)$, but $\bar{\kappa}_{\rm g}(R,\bar{\chi}_l,\chi_s)$. To get this, equation 4.14 is first modified to obtain the convergence in direction $\hat{\theta}_2$ given that there is a galaxy in direction $\hat{\theta}_1$ at comoving distance $\bar{\chi}_l$. The small angle approximation is then invoked, and a change of variables is imposed such that the two directions $\hat{\theta}_1$ and $\hat{\theta}_2$ are replaced with the transverse on-sky distance between them, to find:

$$\begin{aligned}\gamma_{\rm t}^{\rm g}(R,\chi_s,\bar{\chi}_l) = &-\frac{3}{2}\left(\frac{H_0}{c}\right)^2\Omega_{\rm M}(z=0)\int_0^{\chi_s} d\chi\frac{\chi(\chi_s-\chi)}{a(\chi)\chi_s}\\ &\times\frac{d}{d\ln R}\left[\int_{S_R}\frac{R'dR'}{R^2}\xi_{gm}(\sqrt{R'^2+(\chi-\bar{\chi}_l)^2},\bar{z}_l,b)\right],\end{aligned} \tag{4.15}$$

where ξ_{gm} is the real-space galaxy-matter cross-correlation function. Inserting equations 4.7 and 4.15 into equation 4.11, it is found that:

$$\begin{aligned}\Delta\Sigma_{gm}(R) = &\frac{-\rho_{\rm c}\Omega_{\rm M}(z=0)}{\bar{w}}\int_0^{\chi_H} d\chi_s W_s(\chi_s)\frac{(4\pi G)}{c^2}\overline{\Sigma_{\rm c}^{-1}}(\bar{\chi}_l,\chi_s)\int_0^{\chi_s} d\chi\frac{\chi(\chi_s-\chi)}{a(\chi)\chi_s}\\ &\times\frac{d}{d\ln R}\left[\int_{S_R}\frac{R'dR'}{R^2}\xi_{gm}(\sqrt{R'^2+(\chi-\bar{\chi}_l)^2},\bar{z}_l,b)\right].\end{aligned} \tag{4.16}$$

It will be convenient to introduce a modified version of the source window function, into which the piecewise nature of $\overline{\Sigma_{\rm c}^{-1}}$ as given in equation 4.9 can be absorbed:

$$\overline{W}_s(\chi_s) = \begin{cases} W_s(\chi_s) & , \chi_s > \bar{\chi}_l \\ 0 & , \chi_s \leq \bar{\chi}_l \end{cases} .$$

Incorporating this, changing the order of integrals, and rewriting $\chi = \bar{\chi}_l + \Delta$ gives:

$$\Delta\Sigma_{gm}(R) = \frac{-\rho_{\rm c}\Omega_{\rm M}(z=0)}{\bar{w}} \int d\Delta \frac{(4\pi G)^2}{c^4} \frac{\bar{\chi}_l(\bar{\chi}_l+\Delta)}{a(\bar{\chi}_l)a(\bar{\chi}_l+\Delta)} \int_{\bar{\chi}_l+\Delta}^{\chi_H} d\chi_s \overline{W}_s(\chi_s) \\ \times (\chi_s - \bar{\chi}_l) \frac{(\chi_s - \bar{\chi}_l - \Delta)}{\chi_s^2} \frac{d}{d\ln R} \left[\int_{S_R} \frac{R' dR'}{R^2} \xi_{gm}(\sqrt{R'^2 + (\Delta)^2}, \bar{z}_l, b) \right] . \tag{4.17}$$

Inserting then equation 4.17 into equation 4.4, it is found that:

$$\Upsilon_{gm}(R) = \frac{\rho_{\rm c}\Omega_{\rm M}(z=0)}{\bar{w}} \int d\Delta \frac{(4\pi G)^2 \bar{\chi}_l(\bar{\chi}_l+\Delta)}{c^4 a(\bar{\chi}_l)a(\bar{\chi}_l+\Delta)} \int_{\bar{\chi}_l+\Delta}^{\chi_H} d\chi_s \overline{W}_s(\chi_s) \frac{(\chi_s - \bar{\chi}_l - \Delta)(\chi_s - \bar{\chi}_l)}{\chi_s^2} \\ \times \left[\frac{2}{R^2} \int_{R_0}^{R} R' dR' \xi_{gm}\left(\sqrt{R'^2+\Delta^2}, \bar{z}_l, b\right) - \xi_{gm}\left(\sqrt{R^2+\Delta^2}, \bar{z}_l, b\right) \right. \\ \left. + \left(\frac{R_0}{R}\right)^2 \xi_{gm}\left(\sqrt{R_0^2+\Delta^2}, \bar{z}_l, b\right) \right], \tag{4.18}$$

where the fact that $R\frac{d}{dR}\left(\frac{2}{R^2}\int_0^R R' dR' F(R')\right) = 2\left(F(R) - \frac{2}{R^2}\int_0^R R' dR' F(R')\right)$ has been used.

Consider now $\Upsilon_{gg}(R)$, the equivalent ADSD for galaxy clustering. Once again, it will be assumed that the galaxy clustering measurement has an effective redshift; this is standard practice in this case. $\Upsilon_{gg}(R)$ depends on $w_{gg}(R)$, the projected galaxy correlation function, which was defined in equation 1.42 for projection in redshift-space. As will be discussed in Section 4.3.2, this can be assumed to be equivalent to projecting over a real-space correlation function when the projection length P is sufficiently large:

$$w_{gg}(R) = \int_{-P}^{P} d\Delta \xi_{gg}\left(\sqrt{\Delta^2 + R^2}\right). \tag{4.19}$$

This expression is inserted into equation 4.5:

$$\Upsilon_{gg}(R) = \rho_{\rm c} \int_{-P}^{P} d\Delta \left[\frac{2}{R^2} \int_{R_0}^{R} R' dR' \xi_{gg}\left(\sqrt{R'^2+\Delta^2}, \bar{z}_l, b^2\right) \right. \\ \left. - \xi_{gg}\left(\sqrt{R^2+\Delta^2}, \bar{z}_l, b^2\right) + \left(\frac{R_0}{R}\right)^2 \xi_{gg}\left(\sqrt{R_0^2+\Delta^2}, \bar{z}_l, b^2\right) \right]. \tag{4.20}$$

The final element which is required to construct $E_G(R)$ is $\beta = f/b$. f is found by solving the following differential equation (where f is given in terms of Δ_M in equation 1.44):

$$\Delta''_{\rm M} + \left(1 + \frac{\mathcal{H}'}{\mathcal{H}}\right)\Delta'_{\rm M} - \frac{3}{2}\Omega_{\rm M}\Delta_{\rm M} = 0, \tag{4.21}$$

where a prime represents a derivative with respect to $\ln(a)$. It is important to note that in $E_G(R)$, b as it appears in β is always scale-independent by definition, due to the fact that β is typically measured on large scales and presumed to be a constant. This is despite the fact that in general the bias may take a scale-dependent form. Because the goal of this chapter is to examine the observational definition of $E_G(R)$ as it is currently applied in practice, this feature is preserved, and β is always taken as a scale-independent quantity.

A full theoretical expression for each of the constituents of $E_G(R)$ has now been developed, summarised in equations 4.18, 4.20, and 4.21. The reader is reminded that the above expressions are for the case where the lens galaxies are assumed to be at an effective redshift $\bar{z}_l$; the more general case is given in Appendix C. It can be seen that these expressions contain several variable quantities which could affect predictions of $E_G(R)$: the distribution of source galaxies W_s, the projection length P, the cut-off scale R_0, and the bias b (particularly if scale-dependent). The effect of varying these quantities on the predictions of $E_G(R)$ in GR is now examined, with the objective of understanding how changes to these parameters may be degenerate with modifications to GR.

4.3 Understanding theoretical uncertainties

Given now the expressions derived in the previous section, predictions of $E_G(R)$ can be computed in GR. An investigation can hence be made as to the uncertainty associated with W_s, P, b and R_0 within the general relativistic prediction.

It is possible that in future measurements of $E_G(R)$, the uncertainty associated with variations to these parameters may be significant. In order to investigate this, these uncertainties are compared to forecast errors from two possible future measurements of $E_G(R)$: one next-generation measurement, and one more futuristic. These measurements are characterised as follows:

1. **DESI + DETF4:** Galaxies for $\Upsilon_{gg}(R)$ and β, as well as the lens galaxies for $\Upsilon_{gm}(R)$, are provided by the Dark Energy Spectroscopic Instrument (DESI) Luminous Red Galaxy sample [202]. Source galaxies for the measurement of $\Upsilon_{gm}(R)$ come from a Dark Energy Task Force 4 (DETF4)-type survey [1], with the same form as equation 2.42 and the same parameters as employed in Chapter 2. For this measurement, $\bar{z}_l = 0.8$, and a sky area of 9000 square degrees is assumed from DESI.

2. **SKA2 + LSST:** Galaxies for $\Upsilon_{gg}(R)$ and β, as well as the lens galaxies for $\Upsilon_{gm}(R)$, are provided by a Phase 2 survey of HI galaxies by the Square Kilometre Array (SKA) [205]. Source galaxies for the measurement of $\Upsilon_{gm}(R)$ come from a survey by the Large Synoptic Survey Telescope (LSST) [208]. The LSST source redshift distribution is given by the same form as equation 2.42, with $\alpha = 2$, $\beta = 1$, and $z_0 = 0.5$ [229]. For this measurement, $\bar{z}_l = 1.0$, and a sky area of 30 000 square degrees from the SKA survey is assumed.

Allowing the lens galaxy population to take an effective redshift has implications for the forecast errors, as all lensing information from any source galaxies situated below this effective redshift must be neglected. The result is that the error bars displayed may be inflated, and should be viewed as an upper bound. For a full explanation of how observational errors are calculated, see Appendix D. Note that all error bars displayed in this chapter are 1σ.

The possible uncertainty which may be introduced by varying W_s, P, b, and R_0 is now considered, and compared with forecast errors. In doing so, a fiducial set of quantities is selected to hold fixed while varying each of these parameters one at a time. Following [70, 71], R_0 is set to 1.5 Mpc/h in order to excise the most non-linear scales. The galaxy bias b is set as constant. P is set to 500 Mpc/h, motivated by the fact that, as will be seen, this is a minimum value for which $E_G(R)$ is insensitive to the specific choice. Finally, W_s is given by equation 4.23 (below) for the DESI+DETF4 measurement, and by the similar form given in [230] for the SKA2+LSST measurement.

The correlation function of matter, ξ_{mm}, is calculated using

$$\xi_{mm}(r) = \frac{1}{2\pi^2} \int_0^\infty dk\, k^2 P_{mm}(k, \bar{z}_l) \frac{\sin(kr)}{kr} e^{-k^2}\,, \tag{4.22}$$

where P_{mm} is the theoretical matter power spectrum (non-linear unless otherwise stated), which is calculated using the publicly available code CAMB [10] with Halofit [14] and the 2015 *Planck* parameters [8]. The notation P_{mm} is employed in this chapter for the matter power spectrum (as opposed to P_δ elsewhere in this thesis) in an attempt to maintain notational consistency with $\Upsilon_{gm}(R)$ and $\Upsilon_{gg}(R)$. Recall that $P_{gg}(k) = b^2 P_{mm}(k)$ and $P_{gm}(k) = bP_{mm}(k)$, and so for constant galaxy bias, equation 4.22 can be trivially adapted to compute ξ_{gm} and ξ_{gg}.

4.3.1 Source galaxy redshift distribution: W_s

First, consider the effect of allowing the shape of the source galaxy distribution, characterised by $W_s(\chi)$, to vary. Three cases are examined, all of which are designed as modifications to the DESI+DETF4 measurement scenario:

- **Case 1:** All sources are assumed to be at a single comoving distance: $W_s(\chi_s) = \delta(\chi_s - \bar{\chi}_s)$. $\bar{\chi}_s$ is set such that all sources are at redshift $z = 0.9$. This is an idealised scenario, which is not suggested to represent reality, but rather to act as a limiting case in which the GR prediction put forth in [116] should be recovered.

- **Case 2:** The source distribution is modelled by a normalised Gaussian in χ, such that the mean of the Gaussian is at $z = 0.9$, and the square root of the variance given by $\sigma_s = 60$ Mpc/h.

- **Case 3:** The source distribution is given by [216]:

  $$W_s(\chi_s) = \frac{z(\chi_s)^\alpha}{N_0} e^{-\left(\frac{z(\chi_s)}{z_0}\right)^\beta} \frac{H(\chi_s)}{c}, \tag{4.23}$$

  where N_0 is a normalisation factor such that $\int d\chi_s W_s(\chi_s) = 1$. This is equivalent to the $n(z)$ presented in equation 2.42. The parameter values are set as $\alpha = 2$, $\beta = 1.5$, and $z_0 = 0.9/1.412$ (see, for example, [113]). The distribution is normalised between $z = 0.5$ and $z = 2$, and $W_s(\chi_s)$ is set to 0 outside of this range.

Calculating $E_G(R)$ for these three cases, it is found that $E_G(R) = \frac{\Omega_{\rm M}(z=0)}{f(z=0.9)}$ within 1%, for the range $R = 2 - 80$ Mpc/h. This suggests that variation in the source galaxy distribution shape has no effect on predictions of $E_G(R)$.

It is useful to pause at this point and consider a key difference between $E_G(R)$ and $E_G^0(l)$, and the related implications of this result. $E_G^0(l)$, defined in Fourier-space, assumes the inclusion of only linear scales. However, $E_G(R)$ is defined in real space, where scales are not so easily separated. It is therefore possible that the mere inclusion of non-linearities in the correlation function would cause $E_G(R)$ to deviate from the expected general relativistic value at small scales. The current result demonstrates that this is not the case, at least for the fiducial parameter set used here. This can be attributed to the fact that nonlinearities enter into $\Upsilon_{gm}(R)$ and $\Upsilon_{gg}(R)$ via the same combination of correlation function terms, as seen in equations 4.18 and 4.20, and therefore effectively cancel out.

4.3.2 Projection length: P

The consequences of varying the projection length P are now considered. There are two related theoretical effects which could alter the value of $E_G(R)$ in this scenario:

- The projection may be over an insufficiently large line-of-sight separation to allow the galaxy-galaxy correlation to become negligible over this distance, thus losing three-dimensional power in the projection.

- Although $w_{gg}(R)$ has been expressed in terms of the real-space correlation function in equation 4.19, in reality the three-dimensional correlation function is measured in redshift-space. If P is insufficiently large, the effect of measuring in redshift-space will be non-negligible, as not all redshift-space effects will cancel along the line-of-sight.

In order to examine these effects, $\xi_{gg}(\sqrt{R^2+\Delta^2})$, in real-space, is replaced with $\xi^s_{gg}(R,\Delta)$, in redshift-space, given by:

$$\xi^s_{gg}(R,\Delta) = \frac{1}{4\pi^2}\int_{-\infty}^{\infty} dk_{||}\cos(k_{||}\Delta)\int_0^{\infty} dk_{\perp}k_{\perp}J_0(k_{\perp}R)P^s_{mm}(k_{||},k_{\perp}). \tag{4.24}$$

Finger-of-God effects [231] and a smoothing scale are additionally incorporated via

$$P^s_{mm}(k_{||},k_{\perp}) = \frac{(1+\beta\mu^2)^2P_{mm}(k)e^{-k^2}}{1+(k\mu\sigma)^2}\,, \tag{4.25}$$

where σ, the Finger-of-God parameter, is set to 400 km/s, or $4/\sqrt{2}$ in units of h/Mpc (see, for example, [232]). k here is $\sqrt{k_{||}^2+k_{\perp}^2}$.

$E_G(R)$ is computed for a range of P values, for both a DESI+DETF4-type measurement, and an SKA2+LSST type measurement. Figure 4.1 shows the results. It can be seen that for both measurement scenarios, when $P = 500$ Mpc/h, $E_G(R)$ is given by the expected $\Omega_{\rm M}(z=0)/f(\bar{z})$. However, as P is reduced, $E_G(R)$ changes in two way: its overall value is reduced, and it is further suppressed at larger R.

The suppression of $E_G(R)$ (or, equivalently, the boosting of $w_{gg}(R)$), can be understood as a result of the two factors mentioned above. First, reducing P within this regime is equivalent to neglecting separations for which the correlation function is negative, and hence the value of the projected correlation function is incorrectly inflated. This effect is enhanced at larger R, where for fixed P, more of the negative region of the correlation function will be neglected than for smaller R. Second, redshift-space distortions result from peculiar velocities, which arise due to increased clustering and hence correspond to a boosted correlation function. Projecting over sufficiently large P induces a cancellation of this effect along the line-of-sight, but as P is reduced, this cancellation is negated and $w_{gg}(R)$ is boosted

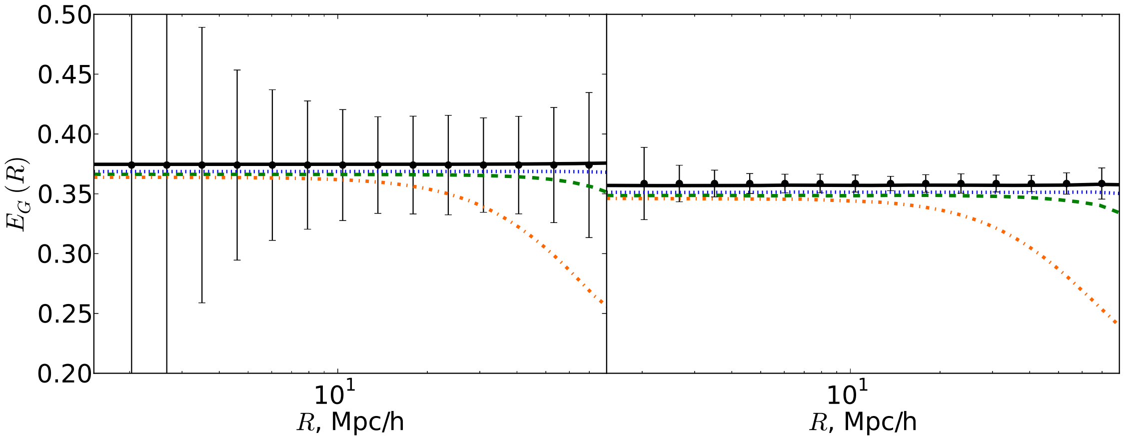

Figure 4.1: The effect on $E_G(R)$ from varying the value of the projection length P. The left panel is for the case of a DESI+DETF4 measurement, with the right panel showing SKA2+LSST. Black, solid: $P = 500$; blue, dotted: $P = 250$; green, dashed: $P = 150$; orange, dot-dashed: $P = 50$. The solid black line also corresponds to the theoretical value of $\Omega_{\mathrm{M}}(z = 0)/f(\bar{z}_l)$. All values of P are in Mpc/h.

As seen in Figure 4.1, for the DESI+DETF4 case, the effect of a reduction in the overall value of $E_G(R)$ at all scales is insignificant compared with the expected errors. The effect of a deviation from the expected value at large R is more worrisome, but only for the smallest P value which is plotted. On the other hand, for the SKA2+LSST case, it can be seen that both effects are significant in comparison with errors and would be important to account for in such a measurement.

Although it may seem from this result that it is optimal to choose the largest possible projection length, note that this may not be the case. In practice, choosing a long projection length may increase the noise of the measurement, by incorporating redundantly large line-of-sight separations at which any structure is uncorrelated [176]. This can be seen explicitly in the expression for the error of $\Upsilon_{gg}(R)$ derived in Appendix D. In reality, the choice of projection length must be balanced between theoretical uncertainty and shot noise.

4.3.3 Scale-dependent bias

The next possible source of theoretical uncertainty to be considered is scale-dependent galaxy bias. In this scenario, ξ_{gg} and ξ_{gm} can no longer be trivially computed from ξ_{mm}. Instead, the following expressions are employed:

$$\begin{aligned} \xi_{gm}(r) &= \frac{1}{2\pi^2}\int_0^\infty dk\, k^2 b(k,\bar{z}_l) P_{mm}(k,\bar{z}_l)\frac{\sin(kr)}{kr}e^{-k^2}\,, \\ \xi_{gg}(r) &= \frac{1}{2\pi^2}\int_0^\infty dk\, k^2 b^2(k,\bar{z}_l) P_{mm}(k,\bar{z}_l)\frac{\sin(kr)}{kr}e^{-k^2}\,, \end{aligned} \tag{4.26}$$

where $b(k,\bar{z}_l)$ is the galaxy bias, and $P_{mm}(k,\bar{z}_l)$ is, for the bias models considered here, the linear power spectrum by definition.

The variation to $E_G(R)$ is investigated under two scale-dependent bias models. The first was introduced as part of the analysis for the 2dF Galaxy Redshift Survey (2dFGRS) [233], and can be written as:

$$b_{\rm 2dF}(k,z) = b_{\rm c}(z)\sqrt{\left[\frac{1+Q(z)k^2}{1+A(z)k}\right]}\,, \tag{4.27}$$

where $b_{\rm c}(z)$, $A(z)$, and $Q(z)$ are constant at a given redshift and can be fit from n-body simulations. The second model features a power law in k, and can be described by [234,235]:

$$b_{\rm PL}(k,z) = b_0(z) + b_1(z)k^n, \tag{4.28}$$

where once again $b_0(z)$ and $b_1(z)$ are z-dependent constants [235], and k is in units of $k_1 = 1$ h/Mpc.

$E_G(R)$ is computed under these scale-dependent bias models, with other parameters fixed to fiducial values. The bias model parameters are taken to have values given in [235] for the case of $\bar{z}_l = 0.8$ (for DESI+DETF4), and $\bar{z}_l = 1.0$ (for SKA2+LSST), with $n = 1.28$ for the power law bias model in both cases. For reference, both choices of bias are displayed as a function of scale in Figure 4.2, for the representative case of $\bar{z}_l = 0.8$. As noted earlier, the factor of the bias which is introduced via $\beta(z) = f(z)/b(z)$ is independent of scale by definition, and should be chosen as $b_{\rm c}(z)$ or $b_0(z)$ as appropriate.

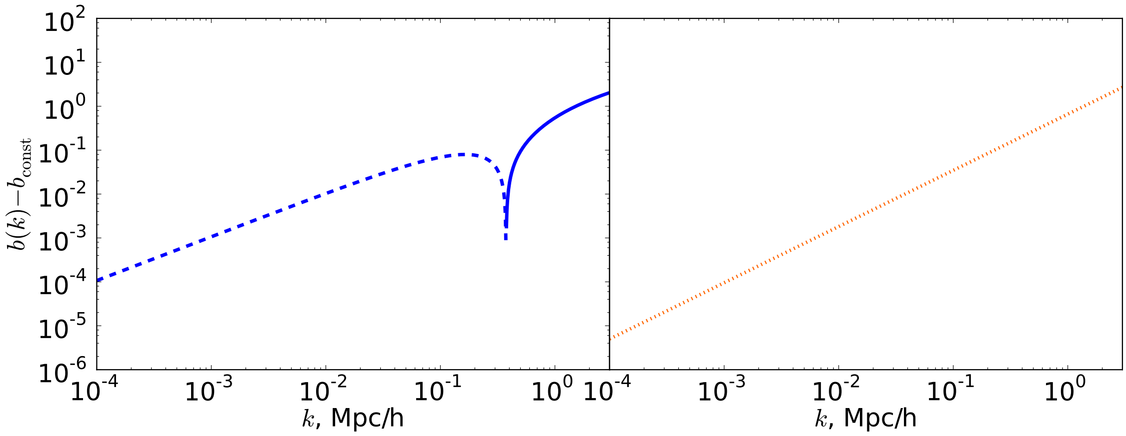

Figure 4.2: The difference between $b(k)$ and the comparable constant bias value for the two scale-dependent bias models in the text (see equations 4.27 and 4.28), for the parameters given in [235] and at $z = 0.8$ (as in a DESI+DETF4 measurement of $E_G(R)$). The left panel shows $b_{\rm 2dF}(k) - b_{\rm c}$, where the dashed portion of the curve is in reality negative, but is displayed in absolute value. The right panel shows $b_{\rm PL}(k) - b_0$.

The resulting predictions are shown in Figure 4.3. It is seen that the inclusion of scale-dependent bias causes $E_G(R)$ to deviate considerably from $\Omega_M(z = 0)/f(\bar{z}_l)$, particularly for small values of R. However, once again, for the DESI+DETF4 case, the effect is largely within the expected 1σ error, while for an SKA2+LSST measurement, this is not the case. The implication is that for a futuristic measurement of this type, scale-dependent bias must be accounted for. Generally, one would expect this to occur via accurate modelling of the scale-dependence. However, in the case of $E_G(R)$, it is possible that an increase to the value of R_0 could sufficiently suppress small-scale deviations from the expected value of $E_G(R)$. This possibility is explored in the next subsection.

Finally, note that the predicted $E_G(R)$ resulting from the 2dFGRS bias model of equation 4.27 approaches $\Omega_{\rm M}(z = 0)/f(\bar{z}_l)$ less closely on this range than does the $E_G(R)$ prediction resulting from the power law bias model of equation 4.28. One reason for this can be seen in Figure 4.2: $b_{\rm 2dF}(k)$ deviates more significantly from constant at larger scales than does $b_{\rm PL}(k)$. This then translates to a more significant large-scale

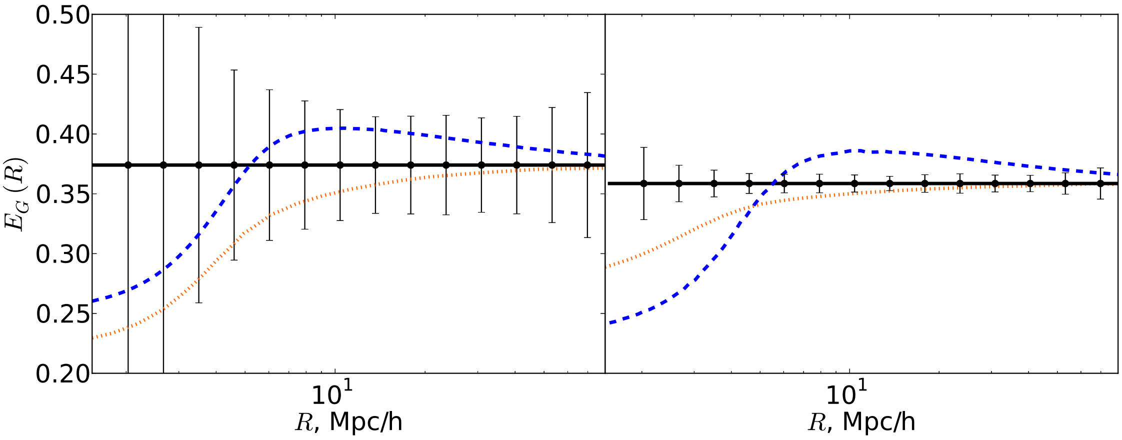

Figure 4.3: $E_G(R)$ for the scale-dependent bias models described in the text. The left panel shows the case of a DESI+DETF4 measurement, and the right shows the case of SKA2+LSST. Black, solid: constant bias; blue, dashed: $b_{\text{2dF}}(k)$ (equation 4.27); orange, dashed: $b_{\text{PL}}(k)$ (equation 4.28).

deviation of the value of $E_G(R)$ away from constant in the $b_{\text{2dF}}(k)$ case.

4.3.4 R_0

The parameter R_0 defines the minimum value of R from below which information is included in $E_G(R)$. In [70] and [71], R_0 was chosen to be 1.5 Mpc/h, with [71] showing their measurement to be unaffected by small variations to R_0. However, with the inclusion of scale-dependent bias, it is possible that the choice of R_0 may strongly influence the degree to which small scale information is removed. $E_G(R)$ is therefore computed while varying R_0 under the scale-dependent bias models outlined in the previous section, as well as in the constant-bias case. Once again, both a DESI+DETF4 and an SKA2+LSST type measurement are considered.

The result in the case of $b_{\text{2dF}}(k)$ (given by equation 4.27) is shown in Figure 4.4, with Figure 4.5 displaying the case of $b_{\text{PL}}(k)$ (equation 4.28). Within each model, $E_G(R)$ is plotted for $R_0 = \{1.5, 5.0, 9.0\}$ Mpc/h. It can be see that for an SKA2+LSST measurement, increasing the value of R_0 will be insufficient to adequately excise information from small scales, particularly in the case of the 2dFGRS bias model. This

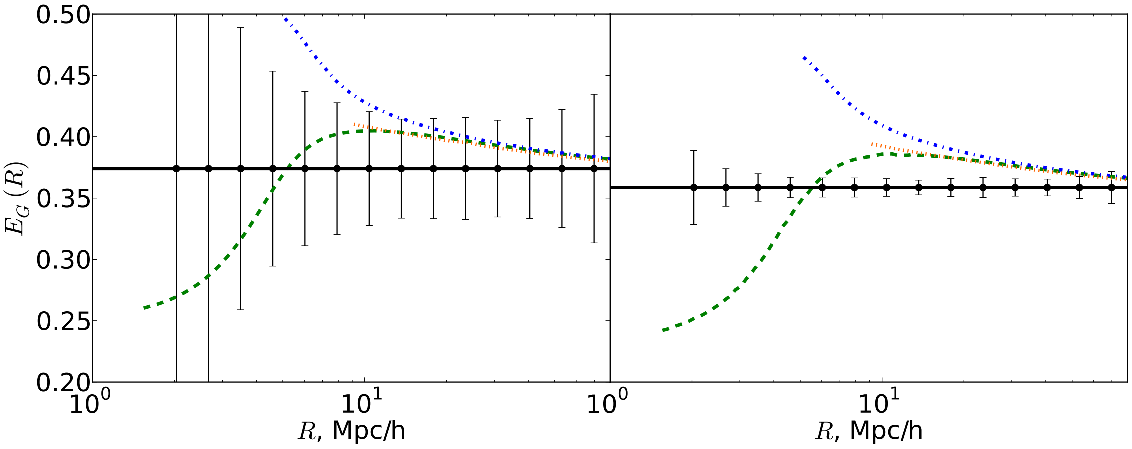

Figure 4.4: $E_G(R)$ with different R_0 values, for the case of $b_{2\mathrm{dF}}(k)$ (equation 4.27). Each curve is displayed at values of R greater than or equal to the relevant R_0. The left panel shows the case of a DESI+DETF4 measurement, and the right shows the case of SKA2+LSST. The curves displayed are for $R_0 = 1.5$ Mpc/h (green, dashed), $R_0 = 5.0$ Mpc/h (blue, dot-dashed), $R_0 = 9.0$ Mpc/h (orange, dotted). The solid black line shows the constant-bias case.

implies that increasing the value of R_0 will likely not prove a viable method of dealing with scale-dependent bias effects in the future, and that scale-dependent bias must be precisely modelled and understood if $E_G(R)$ is to be effectively used to test gravity. Even in the case of a DESI+DETF4 measurement, variation due to a change in R_0 is not fully contained within the 1σ error bars.

The effect of varying R_0 was also tested with the constant galaxy bias model. In this case, all choices of R_0 produced curves in which $E_G(R) \sim \Omega_\mathrm{M}(z=0)/f(\bar{z}_l)$ on the range $R = 2-80$ Mpc/h. For constant bias, the choice of R_0 therefore appears to have no effect on the predicted value of $E_G(R)$, as expected.

4.4 Predictions of E_G with modifications to general relativity

The effect of theoretical uncertainties on the general relativistic prediction for $E_G(R)$ has now been established and compared to forecast errors for future measurements. However, the question has not yet been addressed as to how these forecast errors

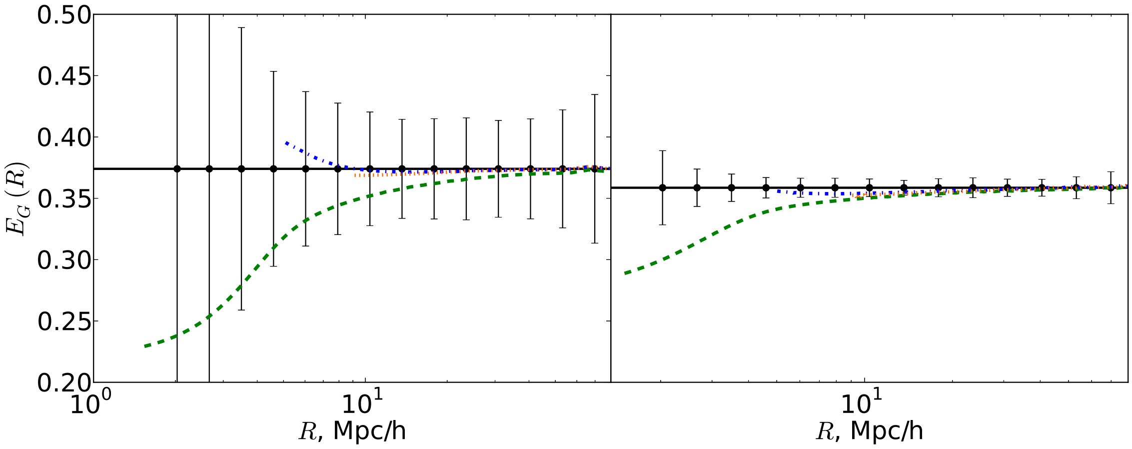

Figure 4.5: $E_G(R)$ with variable R_0, for the case of $b_{\mathrm{PL}}(k)$ (equation 4.28). Each curve is displayed at values of R greater than or equal to the relevant R_0. The left panel shows the case of a DESI+DETF4 measurement, and the right shows the case of SKA2+LSST. The curves displayed are for $R_0 = 1.5$ Mpc/h (green, dashed), $R_0 = 5.0$ Mpc/h (blue, dot-dashed), $R_0 = 9.0$ Mpc/h (orange, dotted). The solid black line shows the constant-bias case.

compare to the expected change in $E_G(R)$ due to signatures of modified gravity. A theoretical expression is now set out for $E_G(R)$ under modifications to GR. This expression is then used, along with the expressions for forecast errors derived in Appendix D, to comment on the level at which $E_G(R)$ might be expected to offer constraints on gravity from the two future measurement scenarios under consideration.

As in Chapters 2 and 3, departures from general relativity are parameterised in this section using the functions μ and γ (or equivalently $\bar{\mu}$ and Σ) of the quasistatic parameterisation of gravity. The modified Poisson equation and slip relation introduced in equation 1.29 are employed to find the relevant expressions for $\Upsilon_{gm}(R)$ and $\Upsilon_{gg}(R)$. Motivated as in Chapter 2 by previous work showing that any scale-dependence is expected to be sub-dominant [92–94], only scale-independent μ and γ are considered. The expression for $\bar{\kappa}_g$, given in equation 4.14 for GR, then becomes:

$$\bar{\kappa}_{\mathrm{g}}(\hat{\theta}) = \frac{3}{4}\left(\frac{H_0}{c}\right)^2 \Omega_{\mathrm{M}}(z=0)\int_0^{\chi_s} d\chi \left(1+\frac{1}{\gamma(\chi)}\right)\mu(\chi)\frac{\chi(\chi_s-\chi)}{\chi_s a(\chi)}\Delta_{\mathrm{M}}(r(\chi\hat{\theta},\chi)). \tag{4.29}$$

Proceeding then in precisely the same manner as in the GR case, $\Upsilon_{gm}(R)$ is obtained:

$$\begin{aligned}\Upsilon_{gm}(R) = {} & \frac{\rho_{\rm c}\Omega_{\rm M}(z=0)b}{2\bar{w}} \int d\Delta \frac{(4\pi G)^2\bar{\chi}_l(\bar{\chi}_l+\Delta)}{c^4 a(\bar{\chi}_l)a(\bar{\chi}_l+\Delta)} \int_{\bar{\chi}_l+\Delta}^{\chi_H} d\chi_s \overline{W}_s(\chi_s) w_s(\chi_s) \\ & \times \left(1+\frac{1}{\gamma(\bar{\chi}_l+\Delta)}\right)\mu(\bar{\chi}_l+\Delta)(\chi_s-\bar{\chi}_l-\Delta)\frac{(\chi_s-\bar{\chi}_l)}{\chi_s^2} \\ & \times \left[\frac{2}{R^2}\int_{R_0}^{R} R'dR' \xi_{gm}^{\rm MG}\left(\sqrt{R'^2+\Delta^2}, \bar{z}_l, b\right) - \xi_{gm}^{\rm MG}\left(\sqrt{R^2+\Delta^2}, \bar{z}_l, b\right)\right. \\ & \left. + \left(\frac{R_0}{R}\right)^2 \xi_{gm}^{\rm MG}\left(\sqrt{R_0^2+\Delta^2}, \bar{z}_l, b\right)\right]. \qquad (4.30)\end{aligned}$$

Υ_{gg} simply becomes:

$$\begin{aligned}\Upsilon_{gg} = \rho_{\rm c} \int_{-P}^{P} d\Delta & \left[\frac{2}{R^2}\int_{R_0}^{R} R'dR' \xi_{gg}^{\rm MG}\left(\sqrt{R'^2+\Delta^2}, \bar{z}_l, b^2\right)\right. \\ & \left. - \xi_{gg}^{\rm MG}\left(\sqrt{R^2+\Delta^2}, \bar{z}_l, b^2\right) + \left(\frac{R_0}{R}\right)^2 \xi_{gg}^{\rm MG}\left(\sqrt{R_0^2+\Delta^2}, \bar{z}_l, b^2\right)\right]. \qquad (4.31)\end{aligned}$$

$\xi_{gm}^{\rm MG}$ and $\xi_{gg}^{\rm MG}$ are computed using equation 4.22 where $P_{mm}(k, \bar{z}_l)$ is taken to be the linear matter power spectrum under the alternative theory in question. Finally, the growth rate f is also required in terms of these quasistatic parameterising functions. It is given by solving an extended version of equation 4.21 [213]:

$$\Delta_{\rm M}'' + \left(1+\frac{(aH)'}{aH}\right)\Delta_{\rm M}' - \frac{3}{2}\Omega_{\rm M}\Delta_{\rm M}\frac{\mu}{\gamma} = 0\,. \qquad (4.32)$$

In principle, $E_G(R)$ could now be computed under specific theories of gravity. However, as in Chapters 2 and 3, in an effort both to enable model-independent tests of gravity and to manage analysis complexity, a phenomenological form is chosen to model deviations from GR. In order to allow for easy comparison with other work, it will once again be preferable to work in terms of the more common observational choice of parameterising functions $\{\bar{\mu}, \Sigma\}$, instead of $\{\mu, \gamma\}$. Under the assumption of small deviations from GR, and letting $\mu = 1+\delta\mu$ and $\gamma = 1+\delta\gamma$ as in Chapter 2, these sets of functions are related by equation 2.46. A phenomenological form for $\bar{\mu}(\chi)$ and $\Sigma(\chi)$

is selected which is equivalent to that introduced in equation 2.48:

$$\bar{\mu}(\chi) = \bar{\mu}_0 \frac{\Omega_\Lambda^{\rm GR}(\chi)}{\Omega_\Lambda^{\rm GR}(\chi=0)}\,,$$
$$\Sigma(\chi) = \Sigma_0 \frac{\Omega_\Lambda^{\rm GR}(\chi)}{\Omega_\Lambda^{\rm GR}(\chi=0)}. \tag{4.33}$$

Given equations 4.30, 4.31 and 4.32 in combination with equation 4.33, $E_G(R)$ can now be computed for a range of $\bar{\mu}_0$ and Σ_0. In doing so, several simplifying assumptions will be made. First, because of the uncertain nature of non-linear structure formation under general modifications to GR, a non-linear power spectrum cannot be computed with confidence, and therefore only linear-level effects are included. For this reason, it would be imprudent to attribute too much weight to these calculations below scales of roughly 10 Mpc/h. Additionally, one could in principle consider modifications to the expansion history as well as perturbative changes. However, due to the fact that the expansion rate has been observationally well-constrained to be near the ΛCDM quantity, and because many theories of interest are designed such that the ΛCDM expansion rate is reproduced, the simplifying case considered here is that in which the expansion history of the Universe matches that of ΛCDM. The fiducial values of the previous section are adopted for the non-gravitational parameters, unless otherwise stated.

The results of computing $E_G(R)$ under modifications to GR are shown in Figures 4.6, 4.7, and 4.8. In Figure 4.6, it can be seen that, given the time-dependent form of $\bar{\mu}(\chi)$ and $\Sigma(\chi)$ that has been chosen, a measurement of $E_G(R)$ from DESI+DETF4 will struggle to distinguish a deviation from GR at a 20% level in $\bar{\mu}_0$ and Σ_0. However, in the case of a measurement from SKA2+LSST, this level of 1σ constraint is feasible. In comparison, it has previously been shown (including in Chapter 2) that for a combination of cosmic shear, growth rate measurements, and baryon acoustic oscillations from a DETF4-type survey, constraints on $\bar{\mu}_0$ and Σ_0 are expected at a 5% level [114]. However, despite the looser constraint expected, $E_G(R)$ remains a valuable cross-checking mechanism, due to the different systematic effects acting on galaxy-galaxy lensing measurements.

In order to compare these forecast errors with currently-available measurements, Figure 4.7 displays $E_G(R)$ at $z = 0.32$ and $z = 0.57$ as measured by the RCSLenS collaboration [71], in addition to the theoretical $E_G(R)$ at several choices of $\bar{\mu}_0$ and Σ_0. In this case, the chosen values of $\bar{\mu}_0$ and Σ_0 are not within the regime of small deviation from GR, so equation 2.46 is not used; rather the equivalent general expression is employed (see, for example, [69]). Fiducial parameters are as described above ($P = 500$ Mpc/h, $R_0 = 1.5$ Mpc/h, and $b(k)$ is a constant), with the exception of W_s, which is given by equation 4.23 with $\alpha = 0.787$, $\beta = 3.436$ and $z_0 = 1.157$ [236]. It can be seen that current 1σ constraints are at approximately at the level of $|\bar{\mu}_0| = |\Sigma_0| = 1.0$. These looser constraints are as expected, since this measurement is intended primarily as a 'consistency check' for general relativity.

Next, the type of degeneracy which may exist between the gravitational parameters described here and the non-gravitational parameters of the previous section is demonstrated. $E_G(R)$ is computed for the case of $\bar{\mu}_0 = \Sigma_0 = 0.2$, this time allowing the galaxy bias to take on scale-dependence as given in equations 4.27 and 4.28. The result is shown in Figure 4.8, where it is clear that the scale-dependence of the bias may dominate over the effect of deviation from GR on all but the largest scales. This reinforces the notion that in order to achieve optimal constraints on gravity using next-generation measurements of $E_G(R)$, accurate modelling of the galaxy bias will be required.

Finally, in order to better understand the dependence of $E_G(R)$ on $\bar{\mu}_0$ and Σ_0, the bias is once again assumed to be constant and R is set to 20 Mpc/h. Then, the evolution of $E_G(R = 20)$ as a function of $\bar{\mu}_0$ and of Σ_0 is examined. The results are seen in Figure 4.9 for the representative case of $\bar{z}_l = 0.8$. The left panel shows $E_G(R = 20)$ as a function of $\bar{\mu}_0$ with $\Sigma_0 = \{0, 0.1\}$, while in the right panel, Σ_0 varies and $\bar{\mu}_0 = \{0, 0.1\}$. It is clear that $E_G(R)$ exhibits a stronger dependence on Σ_0 than

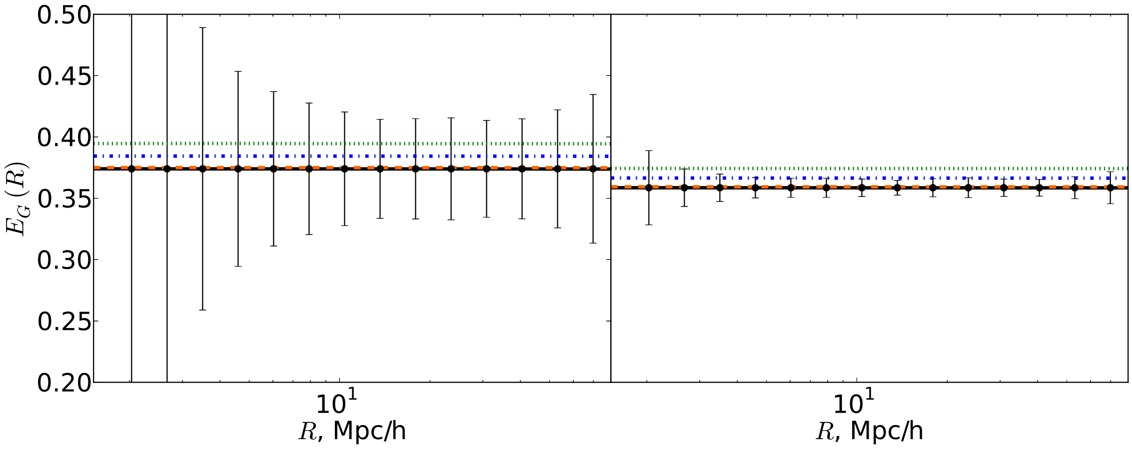

Figure 4.6: $E_G(R)$ as a function of R for different values of $\bar{\mu}_0$ and Σ_0. The left panel shows the case of a DESI+DETF4 measurement, and the right shows the case of SKA2+LSST. Orange, dashed: $\bar{\mu}_0 = \Sigma_0 = 0.01$; blue, dot-dashed: $\bar{\mu}_0 = \Sigma_0 = 0.1$; green, dotted: $\bar{\mu}_0 = \Sigma_0 = 0.2$; black, solid: GR.

on $\bar{\mu}_0$. This can be understood by examining equation 4.30. There, it is seen that $E_G(R)$ is primarily sensitive to the combination $\mu\left(1+\frac{1}{\gamma}\right)$, which, in the case of small deviations from GR, can be written as $2\left(\delta\mu - \frac{1}{2}\delta\gamma\right) = 2\Sigma$, as seen in equation 2.46. $E_G(R)$ is affected by $\bar{\mu}_0$ primarily via the growth rate f (because $\mu/\gamma \sim \delta\mu - \delta\gamma = \bar{\mu}$ in the case of small deviations from GR). However, changes to f as a result of $\bar{\mu}_0$ are small (below 10%) at $z = 0.8$. This relative insensitivity to $\bar{\mu}_0$ may be explained by the fact that the measurement of E_G is here assumed to be taken at the relatively high redshift of $z = 0.8$, where the growth rate of structure has not yet had time to be maximally affected by modifications to gravity. This is an important limitation to bear in mind when selecting a method by which to detect or constrain deviations to GR with the surveys in question. (Note that the results shown in Figure 4.9 are independent of the choice of R.)

4.5 Conclusions

Directly combining observables in order to circumvent potential degeneracies is an attractive prospect for testing gravity on cosmological scales. In this chapter, the

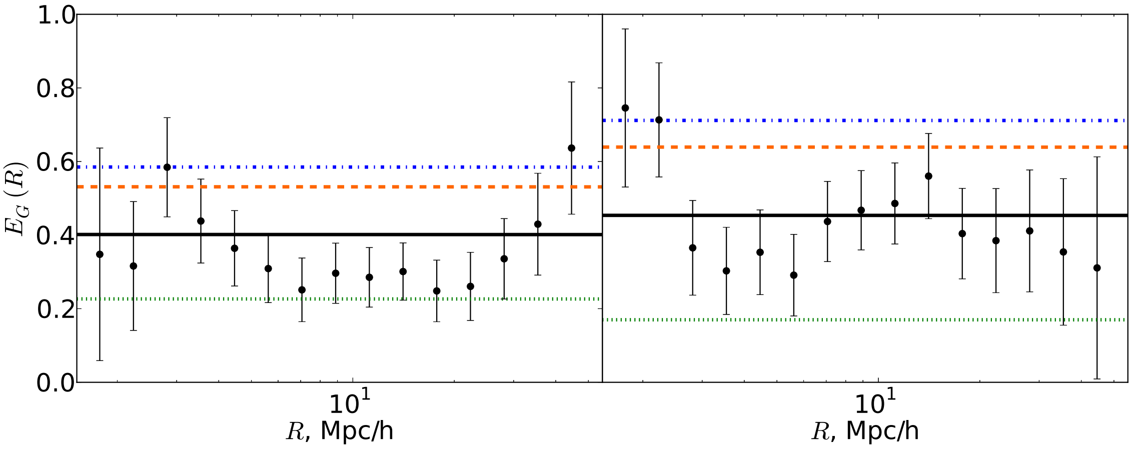

Figure 4.7: $E_G(R)$ predictions as a function of R for modifications to GR, shown with measurements of $E_G(R)$ from the RCSLenS collaboration [71]. The left panel shows the measurement at $z = 0.32$, and the right is at $z = 0.57$. Blue, dot-dashed: $\bar{\mu}_0 = \Sigma_0 = 1.5$; orange, dot-dashed: $\bar{\mu}_0 = \Sigma_0 = 1.0$; green, dotted: $\bar{\mu}_0 = \Sigma_0 = -1.0$; black, solid: GR.

observational definition of one such combination, $E_G(R)$, has been examined in detail. This has been with the goal of understanding how parameters which were not present in the original version of the statistic may introduce theoretical uncertainty, and how this uncertainty may compare to forecast errors from two futuristic measurements.

The investigation of this chapter reveals that of four potential sources of theoretical uncertainty (the distribution of source galaxies W_s, the projection length P, the cut-off scale R_0, and the bias b), only W_s has no effect on the theoretical value of $E_G(R)$. The general relativistic prediction is sensitive to P, to the scale-dependence of the bias $b(k)$, and, under scale-dependent bias, to the value R_0 within which small-scale information is discarded. Until now, these few-percent changes of $E_G(R)$ away from $E_G^0(l)$ have not been critical when compared to statistical error [70, 71]. Similarly, it is found that in comparing theoretical uncertainties with forecast errors from a next-generation measurement combining DESI and a DETF4-type survey, the uncertainties from theory are of the same order of magnitude as, or less than, the predicted errors. However, in a more futuristic measurement, such as that from a combination of SKA2

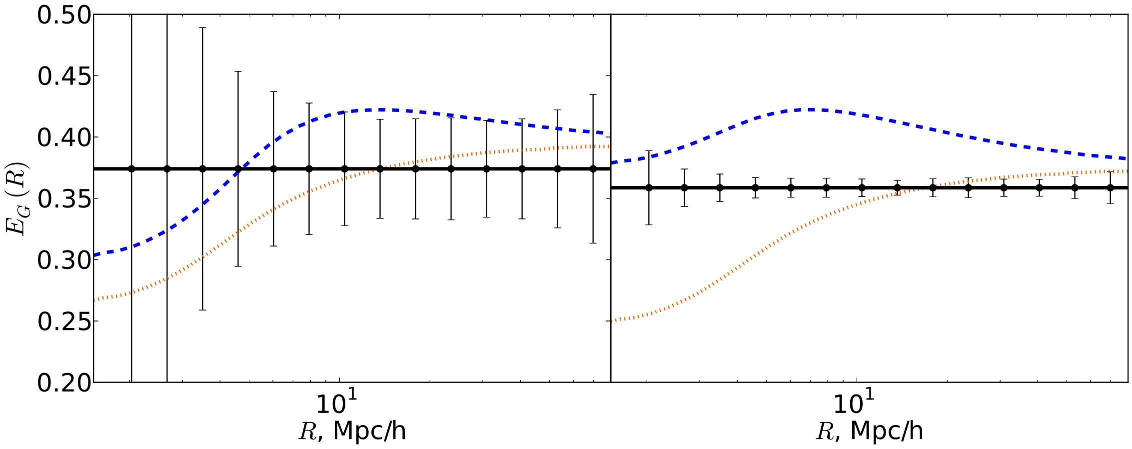

Figure 4.8: $E_G(R)$ as a function of R for $\bar{\mu}_0 = \Sigma_0 = 0.2$, with scale-dependent bias. The left panel shows the case of a DESI+DETF4 measurement, and the right shows the case of SKA2+LSST. Black, solid: constant bias; blue, dashed: $b_{\rm 2dF}$ (equation 4.27); orange, dotted: $b_{\rm PL}$ (equation 4.28).

and LSST, this is not the case. If $E_G(R)$ is to be used as a tool for testing gravity in more futuristic scenarios, it will be essential to take these effects into account.

In the case of the projection length P, one approach would be to compare the measured $E_G(R)$ with a prediction computed using the expression derived in this chapter, with the appropriate P value. For the scale-dependent bias this method would be less practical, as the parameters of the bias models must be known. Thus, accurate modelling of and accounting for $b(k)$ is more likely the solution in this case. In the more futuristic scenario of using $E_G(R)$ not as a consistency check, but as the basis of a Bayesian analysis, this could be accomplished by parameterising $b(k)$ (via a functional form or simply by binning in k), and marginalising over the corresponding bias parameters.

The case of theoretical uncertainty from scale-dependent bias is of particular interest, given that the original objective of E_G was to circumvent degeneracy with the galaxy bias. Note that, as mentioned previously, the definition of $E_G(R)$ assumes that the measured $\beta(z) = f(z)/b(z)$ is scale-independent, which implies that the factor of the galaxy bias which enters via $\beta(z)$ is scale-independent by definition. The result

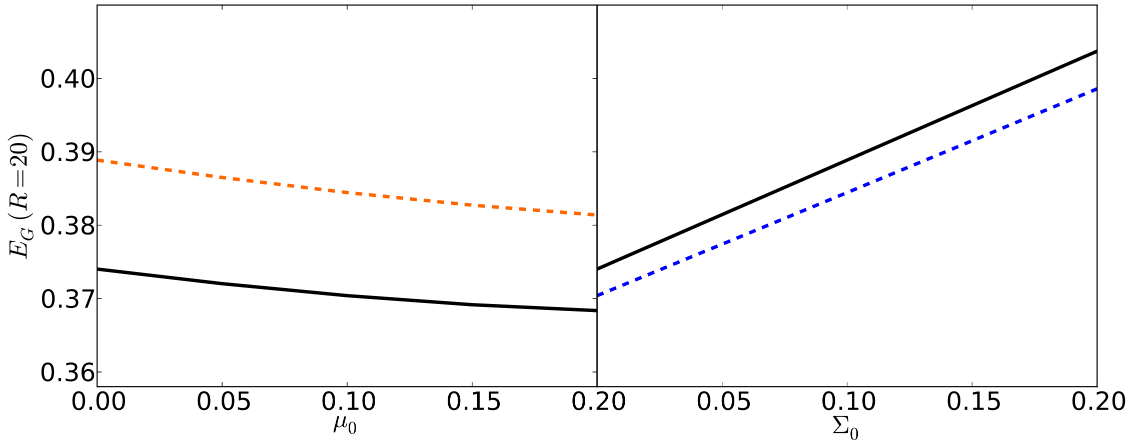

Figure 4.9: E_G at $R = 20$ Mpc/h, as a function of $\bar{\mu}_0$ (left, with $\Sigma_0 = 0$ (black, solid) and $\Sigma_0 = 0.1$ (orange, dashed)) and as a function of Σ_0 (right, with $\bar{\mu}_0 = 0$ (black, solid) and $\bar{\mu}_0 = 0.1$ (blue, dashed)). The curves shown are for $\bar{z}_l = 0.8$, as in the case of a DESI+DETF4 measurement of $E_G(R)$. The dependence of $E_G(R = 20)$ on Σ_0 is clearly greater than that on $\bar{\mu}_0$.

is that any scale-dependent behaviour in the bias will fail to cancel. One potential way to address this would be to measure instead $\beta(z, k) = f(z, k)/b(z, k)$. If possible, this could lead to much less sensitivity of $E_G(R)$ to the galaxy bias. Additionally, the effects of introducing scale-dependent bias are made more problematic by the real-space nature of the observational $E_G(R)$ than they would be in the case of the original Fourier-space statistic, in which case truncation at a particular value of k could eliminate all effects. In light of this, it may be of interest to move towards a Fourier-space observable, as was originally proposed. This idea was explored for the case in which galaxy-galaxy lensing is replaced by CMB lensing in [237, 238].

In addition to the general relativistic expression for $E_G(R)$, an expression for $E_G(R)$ in the quasistatic limit of modified gravity has also been introduced. This has allowed for the comparison of deviations from the GR value of $E_G(R)$ with forecast errors. It is found that, for a measurement from SKA2+LSST, $E_G(R)$ is expected to provide 1σ constraints on modified gravity parameters $\bar{\mu}_0$ and Σ_0 at a level of roughly 20%. This level of constraint is significantly looser than that expected from a combination of cosmic shear tomography and measurements of the growth rate and of baryon acoustic oscillations combined directly from a DETF4-type survey, as was demonstrated in Chapter 2. Bear in mind, however, that in the current chapter, a single source redshift bin has been assumed; by cleverly dividing the data into several redshift bins, it should be possible to increase the statistical power of this method. Furthermore, one primary advantage of $E_G(R)$ is its use of galaxy-galaxy lensing, and the resulting relative insensitivity to cosmic shear systematics. Hence, even a reduced constraint from these different observational techniques will provide a useful cross-check. Recall also that the use of an effective redshift for the lens galaxy population may inflate forecast errors (see Appendix D), and hence this represents an upper bound on the expected error. Finally, it is found that although $E_G(R)$ uses both galaxy-galaxy lensing and galaxy-clustering measurements, $E_G(R)$ is primarily sensitive to Σ_0, with more limited sensitivity to changes in $\bar{\mu}_0$.

$E_G(R)$ as an observable has the potential to provide a powerful test gravity, complementary to constraints using standard likelihood methods. However, in order to benefit from the measurement of $E_G(R)$ from more futuristic surveys, the theoretical uncertainties of the statistic must be modelled and understood. The work presented in this chapter has been a step towards this goal, in providing full theoretical expressions for $E_G(R)$ in GR and in the quasistatic limit of modified gravity, and in studying the theoretical uncertainties which arise in comparison with forecast errors for future surveys.

Chapter 5

Forecast constraints on spatial curvature

5.1 Introduction

Thus far, the focus of this thesis has been on the investigation of degeneracies and theoretical uncertainties as they pertain to the use of weak gravitational lensing as a probe of modifications to general relativity. In this chapter, weak gravitational lensing will once again be considered, but this time as a tool for exploring a different scenario: a Universe with spatial curvature.

Current constraints on the spatial curvature from the combination of *Planck* CMB data and BOSS BAO measurements place a 95.4% confidence limit on $|\Omega_{\rm K}|$ of 5×10^{-3} [8]. With spatial curvature thus constrained to be dynamically negligible at late times, should it be routinely set to zero in cosmological analyses? This is often already done, particularly when examining late-time probes such as, for example, the growth rate of structure. However, assuming a flat Universe in all contexts neglects potentially powerful tests of early Universe physics and large-scale structure effects.

Constraining $\Omega_{\rm K}$ at a $\sim 10^{-4}$ level would provide a useful test of eternal inflation [143, 239]. Slow-roll eternal inflation predicts $|\Omega_{\rm K}| < 10^{-4}$, while false-vacuum eternal inflation would be ruled out by $\Omega_{\rm K} < -10^{-4}$. On the other hand, inflationary models which give rise to bubble collisions or other large-scale anomalies predict non-zero spatial curvature [240, 241]. Tests of standard early Universe cosmology would thus clearly benefit from a high-precision constraint or measurement of $|\Omega_{\mathrm{K}}|$.

In addition to the predictions of inflationary theory, a number of large-scale structure effects result in an observable Ω_{K}. Second-order perturbation terms affecting the distance-redshift relation may shift Ω_{K} at a sub-percent level [242, 243], while local inhomogeneities can result in non-zero Ω_{K} at a level which scales with the depth of the potential well [144, 244]. In large-scale structure surveys, modes with wavelength larger than the survey size can result in an observed non-zero value of Ω_{K}. Subtle general relativistic effects such as the non-commutation of distance and spatial averaging [245] and wide-angle effects [246] could also produce an observable curvature. Finally, certain alternative theories of gravity predict a non-zero observed Ω_{K} [247].

Further incentivising a target $\sim 10^{-4}$ constraint level is the fact that this value represents a floor below which $|\Omega_{\mathrm{K}}|$ cannot be accurately distinguished from primordial fluctuations [74]. Cosmic variance 'noise' due to primordial curvature fluctuations of order the horizon scale precludes constraints on $|\Omega_{\mathrm{K}}|$ below $\sim 1.5 \times 10^{-5}$ [248]. Framing this scenario in the context of Bayesian model selection reveals that, in fact, model confusion occurs between flat and curved models at $|\Omega_{\mathrm{K}}| \sim 10^{-4}$. This higher value is hence adopted as a realistic curvature 'floor', beyond which more precise observations cannot improve constraints.

There thus exist one and a half orders of magnitude between the current curvature constraint level and a well-motivated target measurement, within which a detection of $\Omega_{\mathrm{K}} \neq 0$ could rule out large portions of inflationary model-space or detect novel large-scale structure phenomena. In this chapter, the question is addressed as to how and when Ω_{K} is expected to be constrained at this 10^{-4} level by cosmological observations, including weak gravitational lensing.

Recent efforts have explored future constraints on Ω_{K} within a range of observational scenarios and analysis frameworks [74, 75, 148, 149, 229, 246, 249–254]. These works have focussed largely on geometric observables, with some probes of the growth of structure also having been considered. The work presented in this chapter expands upon these efforts by considering constraints from weak gravitational lensing in combination with CMB and BAO observations. Weak lensing is of particular interest as a probe of curvature at high precision, due to the fact that its position as a key observable of several upcoming surveys has instigated an ongoing and intensive study of relevant systematic errors (see, for example, [255–257]). Similarly, CMB and BAO are included because they are arguably the 'purest' precision observables, in that they are likely to offer the best control over systematic effects and biases.

There are two principle ways in which the work presented in this chapter seeks to improve upon previous forecasts. First, the forecasts here are guided by a broadly conservative approach. Parameters are incorporated which may exhibit significant degeneracies with $\Omega_{\rm K}$ (e.g. the neutrino mass, M_ν, and the time-evolution of dark energy), and the effect of varying or fixing these parameters is examined. Uncertainties due to observational nuisance parameters are accounted for, and several possible additional sources of systematic bias are discussed. In contrast, most previous work has focused upon single or limited extensions beyond a non-flat ΛCDM model. Second, the forecasts presented here investigate a suite of current and upcoming surveys in combination, whereas previous work has generally focused upon a single set or very limited sets of future surveys. In this way, the aim of this chapter is to answer the question of how and when one might first achieve the target constraint of 10^{-4}, rather than to examine the properties of a particular survey or surveys of interest.

The remainder of this chapter is structured as follows. In Section 5.2, relevant aspects of the observational probes to be considered are briefly reviewed, and the forecasting methodology is described. Section 5.3 puts forward forecast constraints on the spatial curvature from three generations of ongoing and upcoming surveys, and describes the systematic biases which could affect these forecasts. Conclusions are drawn in Section 5.4.

5.2 Forecasting setup

5.2.1 Observational probes

The three observational probes from which constraints on spatial curvature are forecast in this chapter are weak gravitational lensing, the cosmic microwave background, and baryon acoustic oscillations.

From the CMB, the angular power spectra of the temperature and polarization anisotropies are included. Information is also employed from the CMB lensing convergence power spectrum, the theoretical form of which is given below in equation 5.3.

Baryon acoustic oscillations are assumed to be measured in the context of a model for the redshift-space galaxy power spectrum put forward in [258]:

$$P^s_{gg}(k,\mu) = b^2\left(1+\frac{f}{b}\mu^2\right)^2 P_{\rm sm}(k)\left[1+f_{\rm BAO}(k)\right]e^{-\frac{k^2}{2}\left([1-\mu^2]\Sigma_\perp^2+\mu^2\Sigma_\parallel^2\right)}, \tag{5.1}$$

where f is the linear growth rate of structure, b is the galaxy bias, $P_{\rm sm}$ is the galaxy power spectrum with BAO effects removed, and $f_{\rm BAO}$ is a function which contains all BAO scale information. In order to extract information which depends only on BAO effects, the argument of $f_{\rm BAO}$ is relabelled as k'. Then, in the Fisher forecasting procedure, derivatives are taken only with respect to this BAO scale. k' is given by:

$$(k')^2 = \alpha_s^2\left[(\alpha_\perp k_\perp)^2 + (\alpha_\parallel k_\parallel)^2\right], \tag{5.2}$$

where $k_\perp = k\sqrt{1-\mu^2}$ and $k_\parallel = k\mu$. $(\alpha_\parallel, \alpha_\perp)$ represent shifts with respect to a fiducial cosmology, with $\alpha_\parallel$ scaling as the ratio of fiducial-to-true Hubble parameter, and $\alpha_\perp$ scaling as the ratio of true-to-fiducial angular diameter distance. α_s accounts for uncertainty in modelling shifts of the BAO scale due to non-linearities. In computing forecast constraints, f and b will be allowed to vary, but $(\Sigma_\perp, \Sigma_\parallel)$ are fixed, under the assumption that BAO smoothing is perfectly known.

The third and final observable of interest is weak gravitational lensing. The angular power spectrum of the convergence for galaxy weak lensing (in general relativity) has already been given in equation 1.35. A more general version of this expression is now presented, which is valid for the angular power spectra of the convergence in the case of galaxy weak lensing, CMB lensing, and their cross-correlation:

$$C_\ell^{A^iB^j} = \frac{9}{16}\int_0^{\chi_\infty} d\chi \frac{g^{A^i}(\chi)g^{B^j}(\chi)}{f_K(\chi)^2c^3}\mathcal{H}(\chi)^4\Omega_{\rm M}(\chi)^2 P_\delta\left(\frac{\ell}{f_K(\chi)},\chi\right). \tag{5.3}$$

A and B indicate galaxy or CMB convergence, while i and j refer to the source galaxy redshift bin (relevant only in the galaxy case). The Limber approximation is employed, and as such a minimum multipole of $\ell_{\rm min} = 10$ is assumed for all lensing spectra in this chapter.

In equation 5.3, $g^{A^i}(\chi)$ (the lensing kernel, given by equation 1.36) depends on the source distribution function $W^{A^i}(\chi)$. In the case of CMB lensing, $W^{\kappa_{\rm c}}(\chi) = \delta(\chi - \chi_*)$, where χ_* is the comoving distance to last scattering. For galaxy lensing, $W^{\kappa_{\rm g}^i}(\chi)$ is the distribution of source galaxies in each redshift bin i. In previous chapters, the simplifying assumption has been made that $W^{\kappa_{\rm g}^i}(\chi)$ is given without regard for photometric redshift effects. However, the forecasts undertaken in this chapter seek primarily to be conservative, and hence photometric redshift effects are incorporated. This is modelled using (see, for example, [259]):

$$W^{\kappa_{\rm g}^i}(z) = \frac{n(z)\int_{z_{i-1}}^{z_i} dz_{\rm ph}p(z_{\rm ph},z)}{\int_0^{z_{\rm max}} dz' n(z')\int_{z_{i-1}}^{z_i} dz_{\rm ph}p(z_{\rm ph},z')}, \tag{5.4}$$

where $p(z_{\rm ph}, z)$ describes the spread of photometric redshifts around the true redshift value. It is given by a Gaussian with mean z and variance σ_z (where σ_z is the photometric redshift uncertainty). To obtain $W^{\kappa_{\rm g}^i}(\chi)$ from $W^{\kappa_{\rm g}^i}(z)$, the right side of equation 5.4 is simply multiplied by $\frac{dz}{d\chi} = \frac{H(\chi)}{c}$. The true redshift distribution of the total population of source galaxies, $n(z)$, is modelled using the form of equation 2.42. The photometric redshift uncertainty σ_z is used to determine the number of tomographic redshift bins, requiring that each bin has a width $\Delta z = 3\sigma_z(1 + z)$.

In the spirit of conducting conservative and realistic forecasts which include possible signal contaminants, the effect of intrinsic galaxy alignments on weak gravitational lensing spectra is also incorporated. Instrinsic alignments were discussed in Section

1.3.1.2, and their effect on galaxy lensing spectra is accounted for here using equation 1.38. For the cross-correlation between galaxy and CMB lensing, there is a similar adjustment, which is computed as described in [260]: $C_\ell^{\epsilon^i \kappa_\mathrm{c}} = C_\ell^{\kappa_\mathrm{g}^i \kappa_\mathrm{c}} + C_\ell^{I^i \kappa_\mathrm{c}}$. This accounts for the potential anti-correlation between the weak lensing of the CMB and the alignment of galaxies which are physically associated with a lensing mass.

Within the intrinsic alignment model employed in this work, the simplifying assumption is made that the fraction of red galaxies f_red is constant over the redshifts to be considered. The result is that each of the final three terms of equation 1.37 depends on an amplitude parameter f_c, where $f_c = C_1 \rho_\mathrm{c} f_\mathrm{red}$, and C_1 is the standard amplitude parameter for intrinsic alignments. The combined parameter f_c is then marginalised over to account for uncertainty in the intrinsic alignment amplitude.

Finally, some minor cross-correlations are also expected between CMB temperature and CMB lensing via the Integrated Sachs-Wolfe effect (see, for example, [261]). These are comparatively negligible.

5.2.2 Fisher forecasting methodology

The forecasts in this chapter are conducted using Fisher forecasting methodology, introduced in Section 1.3.3.

The Fisher matrix is computed for each observable with respect to the parameters: Ω_K, $\Omega_\mathrm{b} h^2$, $\Omega_\mathrm{c} h^2$, h, n_s, A_s, τ, M_ν, w_0, w_a, $\{f_i\}$, $\{b_i\}$, and f_c. As can be seen from this parameter list, a general-relativistic growth of structure is assumed, but a non-ΛCDM expansion history is permitted. The possibility of a consistent model exhibiting a non-ΛCDM expansion history as well as spatial curvature was considered in, for example, [262, 263]. Fiducial values of the ΛCDM model parameters are taken as reported by *Planck* in 2015 [8], while $\{w_0, w_a\}$ are taken as -1 and 0, respectively. The fiducial linear bias in each redshift bin, b_i, is survey-specific, and f_i is the linear growth rate per bin. f_c is fiducially taken as 0.0067, following the standard convention in which $C_1 \rho_\mathrm{c} = 0.0134$ [171] and setting f_red fiducially to 0.5.

Fisher matrices containing independent information can be directly summed in order to obtain a combined Fisher matrix. Here, three independent Fisher matrices are considered: one for CMB temperature and polarization, one for BAO, and one for CMB lensing and galaxy lensing. By computing the Fisher matrices in this manner, any covariance between CMB temperature and lensing, and between CMB E-mode polarization and lensing, is assumed to be negligible.

The single Fisher matrix describing both the temperature and polarization of the CMB takes the form

$$\mathcal{F}_{ab}^{\mathrm{CMB}} = \sum_{\ell} f_{\mathrm{sky}} \left(\frac{\partial C_\ell}{\partial p_a}\right)^T \Sigma_\ell^{-1} \left(\frac{\partial C_\ell}{\partial p_b}\right), \tag{5.5}$$

where f_{sky} is the fractional sky coverage, and Σ_ℓ is the covariance matrix between angular power spectra at a given ℓ. Σ_ℓ has dimensions $N \times N$ where N is equal to the number of spectra considered. $\frac{\partial C_\ell}{\partial p_a}$ is a vector of length N, containing derivatives of each spectrum at multipole ℓ with respect to parameter p_a.

Similarly, the weak gravitational lensing of galaxies and of the CMB are described in a single Fisher matrix. This is given by the expression presented in equation 1.48. However, the matrices C_ℓ which describe the observed power spectra are now of dimension $(N_{\mathrm{L}} + 1) \times (N_{\mathrm{L}} + 1)$, where N_{L} is the number of source galaxy tomographic redshift bins. The one additional dimension accounts for the inclusion of CMB lensing. Note that the noise term of the observed power spectrum takes a different form than that given in equation 1.49 for the case of the CMB lensing autocorrelation. It depends on the CMB temperature and polarization spectra, and is computed using the method of [264]. The noise term for cross-correlation between CMB lensing and cosmic shear is assumed to be zero.

Finally, the Fisher matrix of BAO is related to that for galaxy clustering. In the distant observer approximation,

$$\mathcal{F}_{ab}^{\mathrm{Gal}} = \int_{-1}^{+1} d\mu \int_{k_{\mathrm{min}}}^{k_{\mathrm{max}}} \frac{dk}{(2\pi)^2} k^2 V_{\mathrm{sur}} \left(\frac{P_{gg}^s(k,\mu)}{P_{gg}^s(k,\mu) + 1/n}\right)^2 \frac{\partial \log P_{gg}^s(k,\mu)}{\partial p_a} \frac{\partial \log P_{gg}^s(k,\mu)}{\partial p_b}, \tag{5.6}$$

	α	β	z_0	σ_z	$n_{\rm gal}$	$\langle\gamma_{\rm int}^2\rangle^{\frac{1}{2}}$	$f_{\rm sky}$
DES	2	1.5	0.425	0.07	12	0.32	0.12
Euclid	2	1.5	0.637	0.05	30	0.22	0.375
LSST	2	1	0.5	0.03	40	0.18	0.485

Table 5.1: Survey parameters for the three generations of weak gravitational lensing surveys considered. $n_{\rm gal}$ is given in units of galaxies per square arcminute.

where n is the number density of detected galaxies. In order to extract information only from BAO, derivatives are considered only with respect to the BAO scale k' described above, i.e.: $\frac{\partial P^s_{gg}}{\partial p_a} \propto \frac{\partial f_{\rm BAO}(k')}{\partial k'}\frac{\partial k'}{\partial p_a}$. The desired Fisher matrix, $\mathcal{F}^{\rm BAO}_{ab}$, then follows directly.

5.2.3 Numerical issues and non-linear scales

The public code CAMB [10] is employed to output the required CMB temperature and polarization spectra, as well as the matter power spectra necessary to compute BAO and lensing observables using the expressions above. Unlike in Chapters 2 and 3, the derivatives required for the Fisher matrices are then computed numerically.

When employing numerical derivatives, it is crucial to select a step size in the differentiation parameter which lies within the regime of convergence – too small a step can yield numerical errors, while too large will depart from the regime of validity. In the case of the weak gravitational lensing of galaxies, ensuring convergence proved non-trivial. This was due to the prescription for computing the non-linear matter power spectrum. In the case where non-linearities were included, derivative convergence was not uniformly achievable at higher multipoles, but when predictions were artificially restricted to linear theory, convergence was easily achieved. Therefore, in order to be certain of robust results, forecast constraints from galaxy weak lensing are reported using $\ell_{\rm max} = 300$. This maximum multipole is selected because it provides agreement of better than 5% between the problematic non-linear case and the well-behaved linear case. Note that this conservative $\ell_{\rm max}$ cut is made only for galaxy lensing and for the cross-correlation between galaxy and CMB lensing; the CMB lensing auto-correlation is less affected due to its sensitivity to higher redshifts, where non-linear effects are less important.

Although this cut is made to deal with numerical problems, it also serves the overall goal of providing conservative forecasts, as it naturally excises multipoles at which non-linearities become important. Regardless of numerical issues, at smaller scales uncertainties arise in non-linear modelling and baryonic physics which currently affect the matter power spectrum at around the 10% level. To illustrate the potential of including higher multipoles were this problem to be solved in the future, forecast constraints are also presented with $\ell_{\max} = 2000$ (and, in the case of the hypothetical cosmic-variance-limited lensing survey explored below, with $\ell_{\max} = 5000$). However, these constraints may be subject to errors due to the numerical issues discussed above, so should be treated with care.

5.2.4 Cosmological surveys

Fisher matrices are computed for experiments representing three generations of cosmological surveys for weak gravitational lensing, CMB, and BAO observations:

- **Stage II (current):** *Planck* [8], the Dark Energy Survey (DES) [198], and the Baryon Oscillation Spectroscopic Survey (BOSS) [201].
- **Stage III (next-generation):** Advanced ACTPol (Atacama Cosmology Telescope) [211], and Euclid [265] (for both galaxy weak lensing and BAO).
- **Stage IV (future):** A Stage IV CMB survey [212], the Large Synoptic Survey Telescope (LSST) [2], and Phase 2 of the Square Kilometre Array (SKA2) [266].

SKA2 is selected as the Stage IV BAO experiment due to the fact that it is expected to out-perform non-radio counterparts in this observable out to $z = 1.4$ [267]. Note that Euclid is technically a Stage IV experiment, but it is included here in Stage III due to its earlier operating timeframe than SKA2.

The required survey parameters are given in Table 5.1 for weak lensing surveys, while those pertaining to BAO were given in [268–270] for BOSS, Euclid, and SKA2 respectively. The specifications employed here for Advanced ACTPol are the same as those given in Table I of [271] for the Stage III (wide) experiment, while the CMB Stage IV survey considered here employs the specifications of the Stage IV CMB survey described in the same work. Both CMB surveys are assumed to be conducted over 40% of the sky, with information from *Planck* included at low ℓ in both cases. Note that, in all cases, forecast constraints from CMB experiments include CMB lensing as well as polarization.

5.3 Results

Constraints are forecast on $\Omega_{\rm K}$ for each generation of surveys. At each generation, forecast constraints from the CMB survey are first considered independently. They are then combined separately with galaxy weak lensing (WL) observations, and with BAO measurements. Finally, all three surveys are combined. This presentation of results is chosen because CMB observations at a given generation independently offer the best constraint on $\Omega_{\rm K}$ of the three observables considered.

5.3.1 Forecast constraints for each generation of surveys

For each combination of surveys, forecast constraints at the 95.4% CL (2σ) level are given in Table 5.2. Note that all constraint values have been divided by 10^{-4} for clarity.

The first column of Table 5.2 (labelled 'uninformative priors') provides forecast constraints on $\Omega_{\rm K}$ for the case in which all other parameters are marginalised over, without reference to any prior information. In this pessimistic case, the expected constraint from *Planck* + BOSS is approximately eight times worse than the published result of 5×10^{-3} [8]. This is due to the fact that a time-evolving w is highly degenerate with $\Omega_{\rm K}$, in what is commonly referred to as the geometric degeneracy [145–147]. The published constraint from *Planck* + BOSS fixes w to its ΛCDM value. If the relevant 'fixed w' column is examined for this combination of surveys, a result that is much closer to the published constraint is found.

Experiments	Uninformative priors	Mild priors	Fixed w	Fixed α_s	Fixed M_ν	Fixed τ	Fixed f_c	Fixed b_i	$\ell_{\rm max} =$ 2000	Fixed all
Planck CMB	393.4	280.7	239.3	280.7	258.4	267.9	280.7	280.7	280.7	4.6
+BOSS BAO	382.0	144.2	59.5	144.1	138.1	142.7	144.2	144.2	144.2	4.6
+DES WL	312.9	240.4	228.6	240.4	219.6	232.8	220.4	240.4	188.8	4.6
+both	305.9	118.0	56.4	117.8	114.1	116.7	118.0	118.0	105.8	4.6
Adv. ACTPol CMB	164.1	128.7	116.1	128.7	76.3	123.7	128.7	128.7	128.7	1.2
+Euclid BAO	153.6	44.1	18.8	43.4	29.1	41.0	44.1	44.1	44.1	1.2
+Euclid WL	97.9	83.4	70.2	83.4	43.0	80.7	74.4	83.4	42.7	1.2
+both	87.7	25.3	18.3	23.2	23.3	23.5	24.0	25.3	19.7	1.2
S4 CMB	94.1	74.9	63.6	74.9	39.2	73.4	74.9	74.9	74.9	0.9
+SKA2 BAO	68.2	31.4	13.9	30.6	21.7	28.5	31.4	31.4	31.4	0.9
+LSST WL	56.6	51.8	31.2	51.8	23.6	51.2	45.0	51.8	24.7	0.9
+both	47.8	22.2	12.7	19.4	17.3	21.3	21.1	22.2	15.0	0.9
CV-limited	3.6	3.5	3.3	2.2	3.5	1.9	3.4	3.5	—	0.4

Table 5.2: Forecast marginal constraints on $\Omega_{\rm K}$ at a 95.4% confidence level, divided by 10^{-4}. Each column provides the marginalised constraint for a different set of priors or with a particular parameter fixed (see text for details). In columns $3-9$, the mild priors of column 2 are assumed for the non-fixed parameters. Note that there is no result for the CV-limited combination of surveys in the $\ell_{\rm max} = 2000$ column because $\ell_{\rm max} = 5000$ is assumed for weak lensing in this case.

Even in the case without informative priors, there is significant improvement with each successive generation of experiments. This is driven primarily by the CMB surveys. However, at each generation, galaxy weak lensing and BAO observations do improve the forecast constraint over CMB alone, by up to 49%. The best forecast constraint for the 'uninformative priors' case is from all three Stage IV surveys combined. At 4.8×10^{-3}, this is still significantly off the $\sim 10^{-4}$ mark.

In the next column of Table 5.2 (labelled 'mild priors'), a weak Gaussian prior is applied to a select group of parameters, while remaining parameters are treated the same as in the 'uninformative priors' case. This still-conservative set-up is selected with the intention of breaking only the worst degeneracies. Gaussian priors are applied as follows, corresponding to 95.4% CL (2σ) external constraints: $\sigma(\alpha_s) = 0.01$, $\sigma(b_i) = 1$, $\sigma(M_\nu) = 0.4$, $\sigma(f_c) = 0.05$, $\sigma(w_0) = 1$, $\sigma(w_a) = 2$, and $\sigma(\tau) = 0.1$. These priors are chosen such that they might be provided by external datasets. For example, 21 cm observations have the potential to constrain τ [272], while Type 1a supernovae can provide information about w_0 and w_a. Imposing these mild priors results in varying levels of improvement over the case of uninformative priors. The most dramatic gain is for the Advanced ACTPol + Euclid BAO combination of surveys, where the constraint is tightened by approximately a factor of 3.5. For the remaining columns of Table 5.2, this set of weak priors should be assumed to be applied unless otherwise specified.

Following this, in each of columns $3 - 9$, a single parameter is fixed to its fiducial value in an attempt to understand its individual effect on the spatial curvature constraint. First, in column 3 ('fixed w'), the parameters describing the equation of state of dark energy are fixed. The effect on forecast constraints is considerable, due to the fact that this explicitly removes the above-mentioned geometric degeneracy. In particular, it is seen that fixing w offers a significant improvement for the combination of BAO and CMB experiments at each generation. In the best case scenario in which all three Stage IV surveys are combined, fixing the equation of state of dark energy provides a constraint of 1.3×10^{-3} on $\Omega_{\rm K}$, a significant improvement over the ‘mild priors’ case. However, this is not particularly realistic, as several of the surveys considered here have as an explicit goal the measurement of $w(z)$.

Fixing the neutrino mass, M_ν, is shown to be only mildly helpful in increasing the combined constraining power of all three observables. Fixing τ has a similarly small effect, with improvements reflecting the breaking of the degeneracy between the optical depth and A_s, which is itself degenerate with Ω_K.

Examining column 4, it can be seen that fixing the BAO parameter α_s produces only a small improvement over the ‘mild priors’ case. Similarly, columns 7 and 8 demonstrate that fixing either the galaxy bias b_i or intrinsic alignments parameter f_c has a negligible effect on the forecast constraint values. These parameters are of more relevance as sources of potential bias in inferred parameters values, as will be discussed in Section 5.3.2. Allowing the galaxy weak lensing power spectra to contribute out to a multipole of 2000 rather than 300 (‘$\ell_\mathrm{max} = 2000$’) results in a more noticeable effect: for Stage IV, the improvement over the ‘mild priors’ scenario in the three-observable case exceeds the 30% level, reaching a constraint on Ω_K of 1.5×10^{-3}.

In the rightmost column of Table 5.2, a highly optimistic case is considered, in which all parameters except for Ω_K are fixed to their fiducial values. In this scenario, there is no benefit from the addition of galaxy weak lensing or BAO observations: the best constraint comes from the CMB alone at each generation, and hence the best overall constraint comes from the Stage IV CMB experiment. For this experiment, a constraint at the 10^{-4} level is achievable, while the constraint from a Stage III Advanced ACTPol survey comes close to the target. However, it is not realistic to assume external constraints on all other parameters to this high degree. Therefore, the conclusion must be drawn that constraints on spatial curvature at the 10^{-4} level are not realistically reachable by Stage IV weak lensing, CMB, and BAO surveys. $\sim 10^{-3}$ is a more realistic prediction for the constraint on Ω_K from these experiments.

Finally, in the bottom row of Table 5.2, the forecast constraint in each scenario from a hypothetical cosmic-variance-limited combination of CMB, BAO and galaxy weak lensing observations is presented. It is interesting to note that even in this extremely futuristic case, only by once again fixing all parameters other than Ω_{K} can the 10^{-4} curvature floor be reached.

5.3.2 Systematic errors, biases, and degeneracies

The goal of the research presented in this chapter is to establish how, when, and whether spatial curvature will be constrained at the 10^{-4} level. This target measurement presents not only the statistical challenge of reaching sufficiently high signal-to-noise in various observables, but also the more subtle difficulty of being sure that such a result, if achieved, can be believed. There are various systematic errors or biases which may cause an offset to any measured value of Ω_{K} at this high precision, as well as degeneracies which could prevent the objective from being reached. Some examples of these issues and potential solutions are discussed here.

Shifts in the BAO peak: The BAO distance scale can be shifted from its predicted value due to non-linear effects, or because of scale- and redshift-dependent galaxy bias. The former can in principle be dealt with via calibration from simulations and correction for coherent peculiar velocities via the ‘reconstruction’ technique [273]. The latter galaxy bias-related effects have been shown in simulations to shift the BAO peak by $(0.300 \pm 0.015)\%$ [274]. It is possible to then mitigate this potential bias by marginalising over α_s with a prior of 0.015% (although a more conservative prior was imposed within the ‘mild priors’ of the previous subsection).

Non-linearities in the matter power spectrum: Theoretical predictions of the power spectra of weak gravitational lensing observables are highly sensitive to the behaviour of the non-linear matter power spectrum. Because of the complicated dependency of weak lensing statistics on the matter power spectrum, it is not possible to perform a ‘reconstruction-like’ procedure, as with BAO. The usual strategy is instead to model the matter power spectrum on non-linear scales as accurately as possible.

Because the current best simulation-based models of non-linear and baryonic effects on the matter power spectrum are only accurate at about the 10% level [275], often the chosen approach is to restrict multipoles to linear-dominated scales, as has been done here. As previously alluded to, extending ℓ_{max} for galaxy weak lensing to 2000 via better modelling of the non-linear power spectrum could improve the constraint on Ω_{K} by greater than 30% for the combination of Stage IV CMB, BAO, and weak lensing observations.

Massive neutrinos: The mass of neutrinos is correlated with Ω_{K} in CMB observations because both it and the spatial curvature are correlated with the amplitude of the CMB lensing power spectrum (see Figure 9 of [271]). An increased neutrino mass results in increased gravitational collapse and growth of structure, and a corresponding boost in lensing. Increasing the spatial curvature parameter, on the other hand, causes a decrease in the overall matter density for a fixed CMB acoustic scale, thereby decreasing lensing. The conclusion is that it is not necessarily prudent to fix the mass of neutrinos when constraining curvature, as a biased measurement of Ω_{K} could follow.

Time-evolution of dark energy: A sufficiently general time-evolution of the equation of state of dark energy, $w(z)$, can absorb the redshift-dependence of any non-zero curvature component, thus leading in part to the geometric degeneracy mentioned above. One possible solution is to impose theoretical priors such that only those models for $w(z)$ which stem from stable and physically-motivated dark energy scenarios are considered [276–278]. Imposing such theoretical priors on $w(z)$ can significantly reduce the viable dark energy parameter space and hence reduce the effect of the geometric degeneracy.

Intrinsic alignments: The intrinsic alignment of galaxies contributes to the observed galaxy lensing power spectrum, as well as to the observed cross-spectrum between galaxy lensing and CMB lensing. The choice of prior for the amplitude of the intrinsic alignment contribution has a small effect on the spatial curvature constraint, as described above. It is also found that increasing the fiducial value of the amplitude parameter f_c leads to a tighter constraint on $\Omega_{\rm K}$. For example, for the combination of all three Stage III experiments, $\sigma(\Omega_{\rm K})$ decreases by $\sim 6\%$ when the fiducial value for $f_{\rm red}$ is increased from 0.1 to 1 (with fixed fiducial C_1). This result is somewhat surprising, as it might be expected that adding more 'contaminant' to the lensing signal in the form of intrinsic alignments would loosen cosmological constraints. Intrinsic alignments are sensitive to cosmological parameters in their own right though, and so it is entirely plausible that an increase in their amplitude would render the lensing signal more sensitive to spatial curvature – essentially, the intrinsic alignment contribution contains extra information about $\Omega_{\rm K}$.

Super-sample modes: Modes of large wavelength which lie outside of the given survey volume can couple to modes within the survey, altering cosmological observations and hence parameter inferences. This is of particular relevance for weak gravitational lensing surveys, where effects on parameter constraints can be significant [279,280]. One promising option for mitigating this effect is to calibrate from simulations [281, 282].

Local inhomogeneities: Local inhomogeneities, such as, for example, the potential well of the local supercluster of galaxies [283], can alter the observed value of the spatial curvature. This could occur, for example, via changes to the distance-redshift relation. Thus, it is important that to prevent biases to the measured value of $\Omega_{\rm K}$, the local structure is well-modelled. Another option to reduce the effect of this issue is to perform precise measurements of CMB spectral distortions [144].

Higher-order perturbations: Because of the precise level at which a constraint on $\Omega_{\rm K}$ is sought, second-order (or higher) effects in perturbation theory are not necessarily negligible. For example, second-order lensing effects can alter the angular diameter distance at $z \sim 1$ at a 8×10^{-4} level – sufficient to cause a significant $\Omega_{\rm K}$ bias. Fortunately, for a given observable, these higher-order perturbations can be computed exactly [284].

CMB systematic effects: While systematic effects affecting space-based CMB experiments, and in particular their temperature maps, have been impressively well-studied (see, for example, [285–287]), there still exist some CMB-related systematics which could bias parameter inferences. For example, systematic effects relevant to lensing reconstruction and polarization still require further study, as do atmospheric fluctuations (for ground-based surveys) and polarized foregrounds. As polarization and lensing become a main focus of CMB observations, it is expected that these systematic effects will become well-characterised.

5.4 Conclusions

It has been shown in this chapter that planned weak gravitational lensing, CMB, and BAO surveys are together unlikely to constrain Ω_{K} down to the curvature floor of $\sim 10^{-4}$. Even the combination of Stage IV CMB, BAO and galaxy weak lensing experiments is realistically only likely to constrain Ω_{K} at the $\sim 10^{-3}$ level, an order of magnitude away from the target accuracy.

This conclusion may seem to be incongruous with certain other forecasts in the literature, which claim that constraints at a $\sim 10^{-4}$ level may be reachable by a single experiment alone, or in combination with only *Planck* CMB observations (see, for example, [74, 254]). There are two crucial differences between these approaches and the method presented here. First, the forecasts in this chapter have considered a conservative combination of CMB, BAO, and weak gravitational lensing surveys, ignoring other observables which may be more prone to systematics (or for which systematics are not being actively and aggressively investigated). For example, forecast constraints from supernova observations have not been included here, due in part to the ongoing tensions between supernova and CMB measurements of H_0 [8]. In addition, the forecasts presented have included marginalisation over a broad range of relevant parameters, including nuisance parameters. However, even the chosen set of parameters does not account for all potential sources of systematic bias or degeneracies, as described in Section 5.3.2. For an even more realistic scenario, effects such as super-sample modes and higher-order perturbations could be included.

This is not to say that the curvature floor can never be reached in principle. The forecasts presented in this chapter have included only weak lensing, CMB, and BAO observations. Other observables could improve upon constraints, should their systematics be controlled. Experiments such as Euclid and SKA2 could employ measurements of redshift-space distortions, as well as of the shape of the galaxy power spectrum, to improve constraining power. The SKA will also allow for 21 cm observations, which could significantly improve constraints on τ. Type 1a supernovae samples are expected to increase in size in the near future, while observations of the weak lensing of radio galaxies could improve upon our current understanding of intrinsic alignments. However, at present these observables are generally prone to poorly characterised systematic errors, which could engender doubt as to the validity of any precise measurement of Ω_{K} dependent upon them.

The study of systematic errors and of sources of bias is at present a key issue more generally in cosmology, as is evidenced in part by the work presented in this thesis. Given that statistical errors are expected to vastly decrease on many observables with the next-generation of surveys, can our understanding of systematic effects and of theoretical uncertainties keep pace? Measuring or constraining Ω_{K} at the 10^{-4} level – and agreeing on the interpretation of this result – would not only provide exciting information about inflationary models and about novel effects in large-scale structure; it would also serve as a litmus test for the understanding of systematic effects in cosmological observations at a high-precision level.

Chapter 6

Conclusions

Weak gravitational lensing is a remarkably promising cosmological observable, the potential of which is only beginning to be explored. Observations of weak lensing have matured dramatically since the first detection of cosmic shear in the year 2000 [3], with the 2012 CFHTLenS data providing the current state-of-the-art weak lensing constraints on cosmological parameters [150, 151]. Some first weak lensing constraints have also been found on aspects of cosmology beyond the standard paradigm, including constraints on alternative gravitational theories [69–71].

With cosmological observations of weak gravitational lensing continuing to improve, numerous systematics and data analysis issues must be characterised. Current surveys such as DES [198], KiDS [288], and the Hyper Suprime-Cam (HSC) survey [289] possess expected final observational areas of at least ten times that of CFHTLenS. These experiments must tackle corresponding new analysis challenges, in order to achieve the best possible cosmological parameter constraints from their datasets. Even more demanding, though, will be the level of care required for the next generation of surveys, including Euclid and LSST. These surveys will revolutionise the field of weak gravitational lensing by providing a wealth of source galaxy images over vast portions of the sky. A significant effort is already underway to prepare for the novel difficulties in data analysis and systematics which will accompany these radically improved surveys.

As a result of this incredible effort, weak gravitational lensing observations will soon have the potential to provide precision cosmological constraints, both on ΛCDM parameters and beyond the standard cosmological model. However, in order to maximally exploit the next generation of weak lensing surveys to learn about the Universe, it is crucial that an equivalent effort is made towards understanding theoretical uncertainties and degeneracies. Otherwise, there is risk that the constraining power of these future experiments will be limited not by statistics or systematics, but by a lack of theoretical clarity. The research presented in this thesis has been a step towards exploring degeneracies and theoretical uncertainties which may affect weak gravitational lensing tests of cosmology beyond the standard paradigm.

First, in Chapters 2 and 3, new theoretical tools were developed and utilised to explore degeneracies affecting weak lensing tests of gravity beyond GR. Beginning in Chapter 2, a new expression was derived for the angular power spectrum of the convergence under small deviations from GR+ΛCDM. This expression was employed to investigate degeneracies between gravitational parameters using the quasistatic parameterisation of modifications to GR. It was found that a known degeneracy-breaking effect, which occurs when combining weak lensing and redshift-space distortion observations to test gravity, is reliant upon the ansatz selected for the quasistatic parameterising function $\bar{\mu}$. Fortunately, for most viable choices of the time-dependence of $\bar{\mu}$, this combination of observables is still expected to provide reasonably good constraints. The newly-derived expression for $C^{\ell}_{\kappa_{\rm g}\kappa_{\rm g}}$ also permitted Fisher forecasts to be performed using analytic derivatives. Taking advantage of this feature, predicted constraints on gravity from weak gravitational lensing, redshift-space distortions, and BAO observations were explored. It was found that the precision of BAO measurements had a greater effect on constraints than did the assumed time-dependence of the expansion history of the Universe.

The potential for detecting scale-dependence in the parameterising functions of gravity was also briefly investigated in Chapter 2, and was considered more thoroughly in Chapter 3. Taking advantage of a generic form for the scale-dependence of the quasistatic parameterising functions, predicted constraints were explored for a Dark Energy

Task Force 4 (DETF4)-type survey. Constraints were forecast on the standard $\bar{\mu}_0$ and Σ_0 parameters, as well as on parameters which characterise novel scale-dependence and new physical scales. It was shown that the inclusion of these scale-dependence-related parameters did not significantly degrade constraints on $\bar{\mu}_0$ and Σ_0 in the case in which a ΛCDM expansion history was assumed, nor did it alter the near-orthogonality of weak lensing and redshift-space distortion constraints. This suggested that incorporating this potential scale-dependence within the analysis of a DETF4-type survey is a realistic possibility. On the other hand, constraints from weak lensing and redshift-space distortions were demonstrated to be much less orthogonal in the plane of those parameters related to scale-dependence.

Following this, in Chapter 4, a different method of testing gravity was examined: the galaxy-galaxy lensing-based statistic $E_G(R)$. A new theoretical expression for this quantity was derived using the standard observational definition, both in GR and for the quasistatic parameterisation of modified gravity. This allowed for an investigation of the theoretical uncertainty introduced to $E_G(R)$ via the survey- and model-related parameters of the observational definition. It was shown that the projection length, the scale-dependence of the galaxy bias, and, in the case of scale-dependent bias, the minimum length scale included, all affected the prediction of $E_G(R)$ in GR. These effects were within the tolerance of a potential future measurement of $E_G(R)$ from a DETF4-type survey combined with DESI, but were found to be significant in the case of a more futuristic measurement from LSST and SKA2. Predictions of $E_G(R)$ under modifications to GR demonstrated that for next-generation surveys, tests of gravity using this statistic would not be competitive with those which employ more standard likelihood methods. However, $E_G(R)$ is still useful as a valuable cross-check, because its use of galaxy-galaxy lensing incorporates different weak lensing systematics than are present in cosmic shear measurements.

Finally, in Chapter 5, possibilities were considered for the use of weak lensing in combination with complementary CMB and BAO measurements to constrain the spatial curvature of the Universe at a high precision. A conservative set of forecasts was performed for a suite of ongoing and upcoming surveys, in which numerous beyond-ΛCDM parameters and potential systematic effects were considered. The resulting forecasts demonstrated that, even for Stage IV surveys in all three observables, a target 2σ constraint of $|\Omega_\mathrm{K}| < 10^{-4}$ could only be reached by fixing all other cosmological parameters. This included fixing not only deviations to the standard model such as w_0 and w_a, but also the ΛCDM parameters. A more likely outcome from future weak lensing, CMB, and BAO surveys is a constraint on Ω_K at the 10^{-3} level, five times better than current best constraints from *Planck* and BOSS.

The research presented in this thesis has explored the potential of weak gravitational lensing as a test of cosmology beyond the standard paradigm. However, as mentioned above, the field of weak lensing is relatively young, and there remains considerable work to be done in order to take full advantage of future surveys. Each of the projects presented above suggests natural avenues of further study, which will now be discussed.

First, a common theme of this work was the use of the quasistatic parameterisation for alternative theories of gravity. As was partially investigated, forecasts, and ultimately real cosmological constraints, naturally rely on the ansatz selected for the parameterising functions of this framework. A more careful study of the robustness of constraints to this choice would be of interest, particularly in the case where scale-dependence is included. Furthermore, the quasistatic parameterisation itself may not be an ideal framework in some future observational scenarios, depending on the range of scales to be examined. In some cases, it may be preferable to work with a more complex parameterisation of gravity, such as the parameterised post-Friedmann framework [63] or an effective field theory parameterisation [99, 107–109].

Throughout Chapters 2, 3, and 4, only a small number of parameters of interest were varied, while the majority of cosmological parameters were held fixed. However, as was seen in Chapter 5 for the case of spatial curvature constraints, other cosmological parameters, including the ΛCDM parameters, can contribute important degeneracies.

This is particularly relevant to the work of Chapters 2 and 3, where Fisher forecasts were also performed. An exciting project would be to extend the forecasts of Chapters 2 and 3 to include variation in other standard cosmological parameters, and hence to more fully explore the degeneracy space. Either Fisher forecasting or MCMC-based forecasting methods could be used for this.

The research presented in Chapter 4, exploring the theoretical uncertainties affecting $E_G(R)$, illuminates some potential areas in which this statistic could be improved. As was suggested in that chapter, developing a modified definition of $E_G(R)$ which incorporates tomographic weak lensing is an intriguing prospect. Another interesting possibility would be that of measuring a scale-dependent $\beta(z, k) = f(z, k)/b(z, k)$ in order to mitigate degeneracies with the galaxy bias.

Finally, the issue of uncertainties in non-linear structure formation, either within the GR context or in alternative theories of gravity, was relevant to every project presented in this thesis. Understanding how to reduce theoretical uncertainty in the non-linear growth of structure as well as in baryonic physics is currently a key problem in cosmology. Avenues of exploration range from n-body simulations within alternative theories of gravity (see, for example, [104, 105, 290–292]) to clever marginalisation over baryonic effects [293]. Improving our knowledge of these issues could allow weak gravitational lensing measurements to be exploited for cosmology at much smaller scales, which could result in significant improvements in parameter constraints [294].

Weak gravitational lensing will soon have the potential to provide precision cosmological constraints. Preparations are underway for next-generation surveys, including intensive investigations into the associated new observational and systematic challenges. At the same time, there are looming theoretical issues which must be solved in order to take full advantage of the upcoming influx of data. This thesis has presented work towards answering these crucial questions, with a study of the degeneracies and theoretical uncertainties which may affect weak gravitational lensing tests of cosmology beyond the standard paradigm.

Appendix A

Converting between $\{\delta\mu, \delta\gamma\}$ and $\{\bar{\mu}, \Sigma\}$

Often in this thesis, a conversion is made between two sets of functions which parameterise alternative theories of gravity within the quasistatic regime: $\{\mu, \gamma\}$ (or $\{\delta\mu, \delta\gamma\}$ near GR+ΛCDM) and $\{\bar{\mu}, \Sigma\}$. In this appendix, a derivation of the near-GR+ΛCDM relationship between these two sets of functions is presented, as given in equation 2.46.

Equations 4 and 5 of [69] will be of use in this derivation, and so for reference they are reproduced here. The time variable $x = \ln(a)$ is employed, and some minor notational alterations are made in order to maintain the conventions of Chapter 2:

$$\begin{aligned}\Psi(x,k) &= [1+\bar{\mu}(x,k)]\Psi^{\mathrm{S}}_{\mathrm{GR}}(x,k)\\ \Psi(x,k)+\Phi(x,k) &= [1+\Sigma(x,k)](\Psi^{\mathrm{S}}_{\mathrm{GR}}(x,k)+\Phi^{\mathrm{S}}_{\mathrm{GR}}(x,k)).\end{aligned} \tag{A.1}$$

The general relativistic potentials are labeled with an S due to the fact that they are slightly different from $\Psi_{\mathrm{GR}}(x,k)$ and $\Phi_{\mathrm{GR}}(x,k)$ as denoted in this work. $\Psi^{\mathrm{S}}_{\mathrm{GR}}(x,k)$ and $\Phi^{\mathrm{S}}_{GR}(x,k)$ follow a general relativistic Poisson equation and slip relation, but they may generally still have a different value than $\Psi_{\mathrm{GR}}(x,k)$ and $\Phi_{\mathrm{GR}}(x,k)$, due to any difference in the history of the growth of overdensities.

Now, from equation 2.19 it can be seen that:

$$\Phi(x,k) = (1+\delta\mu(x,k))(1+\delta_{\Delta}(x,k))\Phi_{\mathrm{GR}}(x,k). \tag{A.2}$$

In fact, $\Phi^{\mathrm{S}}_{\mathrm{GR}}(x,k) = (1+\delta_{\Delta}(x,k))\Phi_{\mathrm{GR}}(x,k)$, such that:

$$\Phi(x,k) = (1+\delta\mu(x,k))\Phi^{\mathrm{S}}_{\mathrm{GR}}(x,k). \tag{A.3}$$

From equations 1.29 and 2.12, it is seen that in the quasistatic regime, $\Phi(x,k) = (1+\delta\gamma(x,k))\Psi(x,k)$. Therefore:

$$\begin{aligned}
\Psi(x,k) &= \frac{1+\delta\mu(x,k)}{1+\delta\gamma(x,k)}\Phi^{\rm S}_{\rm GR}(x,k) \\
&= \frac{1+\delta\mu(x,k)}{1+\delta\gamma(x,k)}\Psi^{\rm S}_{\rm GR}(x,k) \\
&\simeq (1+\delta\mu(x,k)-\delta\gamma(x,k))\Psi^{\rm S}_{\rm GR}(x,k) \qquad \text{(A.4)}
\end{aligned}$$

where the second line is a result of the fact that $\Phi^{\rm S}_{\rm GR}(x,k) = \Psi^{\rm S}_{\rm GR}(x,k)$. Referring to equation A.1, it is seen that:

$$\bar{\mu}(x,k) = \delta\mu(x,k) - \delta\gamma(x,k), \qquad \text{(A.5)}$$

as in equation 2.46.

From here, equations A.3 and A.4 can be used to write (suppressing time- and scale-dependence for brevity):

$$\begin{aligned}
\Psi + \Phi &= \frac{1+\delta\mu}{1+\delta\gamma}\Psi^{\rm S}_{\rm GR} + (1+\delta\mu)\Phi^{\rm S}_{\rm GR} \\
&= \frac{1+\delta\mu}{1+\delta\gamma}\Phi^{\rm S}_{\rm GR} + (1+\delta\mu)\Phi^{\rm S}_{\rm GR} \\
&= \frac{1}{2}\left[\frac{1+\delta\mu}{1+\delta\gamma} + (1+\delta\mu)\right](\Phi^{\rm S}_{\rm GR} + \Psi^{\rm S}_{\rm GR}) \\
&\simeq \left(1+\delta\mu - \frac{1}{2}\delta\gamma\right)(\Phi^{\rm S}_{\rm GR} + \Psi^{\rm S}_{\rm GR}) \qquad \text{(A.6)}
\end{aligned}$$

and by comparison with equation A.1, it is shown that

$$\Sigma(x,k) = \delta\mu(x,k) - \frac{1}{2}\delta\gamma(x,k) \qquad \text{(A.7)}$$

as in equation 2.46.

Appendix B

Analytic derivative expressions

Chapters 2 and 3 make use of analytic derivatives of $C_\ell^{\kappa_{\rm g}^i\kappa_{\rm g}^j}$ (equation 2.36) and $\delta f\sigma_8$ (equation 2.43) to perform Fisher forecasts. These derivatives are presented explicitly here. $\mathcal{K}(x,\ell)$ is defined in equation 2.38, and $G_f(x,x')$ in equation 34 of [213].

Derivatives with respect to $\bar{\mu}_0$ and Σ_0:

$$\begin{aligned}
\frac{\partial C_\ell^{\kappa_{\rm g}^i\kappa_{\rm g}^j}}{\partial\bar{\mu}_0} &= \int_{-\infty}^{0} dx\,\mathcal{K}(x,\ell)\left[3\int_{-\infty}^{x} d\bar{x}\,\Omega_{\rm M}^{\rm GR}(\bar{x})I(x,\bar{x})\frac{\Omega_\Lambda^{\rm GR}(\bar{x})}{\Omega_\Lambda^{\rm GR}(\bar{x}=0)}\right]\\
\frac{\partial C_\ell^{\kappa_{\rm g}^i\kappa_{\rm g}^j}}{\partial\Sigma_0} &= 2\int_{-\infty}^{0} dx\,\mathcal{K}(x,\ell)\frac{\Omega_\Lambda^{\rm GR}(x)}{\Omega_\Lambda^{\rm GR}(x=0)}\\
\frac{\partial(\delta f\sigma_8(x))}{\partial\bar{\mu}_0} &= \int_{-\infty}^{x} G_f(x,x')\frac{\Omega_\Lambda^{\rm GR}(x')}{\Omega_\Lambda^{\rm GR}(x'=0)}dx'\\
\frac{\partial(\delta f\sigma_8(x))}{\partial\Sigma_0} &= 0.
\end{aligned}\tag{B.1}$$

Derivatives with respect to w_0 and w_a:

$$\begin{aligned}
\frac{\partial C_\ell^{\kappa_{\rm g}^i\kappa_{\rm g}^j}}{\partial w_0} = &\int_{-\infty}^{0} dx\,\mathcal{K}(x,\ell)\Bigg\{\frac{3}{2}\int_{-\infty}^{x} d\bar{x}\,\Big(I(x,\bar{x})(1-\Omega_{\rm M}^{\rm GR}(\bar{x}))\\
&\times\left[3\Omega_{\rm M}^{\rm GR}(\bar{x})(1+f_{\rm GR}(\bar{x}))\bar{x}+f_{\rm GR}(\bar{x})\right]\Big)+\frac{3x}{2}(1-\Omega_{\rm M}^{\rm GR}(x))\\
&+\Bigg[\left(\frac{\partial\ln G_j(x)}{\partial\ln\chi}+\frac{\partial\ln G_i(x)}{\partial\ln\chi}-\frac{\partial\ln(P_\delta^{\rm GR}(x=0,k)/k^4)}{\partial\ln k}\right)\Bigg|_{\chi_{\rm GR}}\\
&\times\frac{3}{2\chi_{\rm GR}(x)}\int_{\infty}^{x} d\bar{x}\frac{\bar{x}}{\mathcal{H}_{\rm GR}(\bar{x})}(1-\Omega_{\rm M}^{\rm GR}(\bar{x}))\Bigg]\Bigg\}
\end{aligned}$$

$$
\begin{aligned}
\frac{\partial C_\ell^{\kappa_{\rm g}^i\kappa_{\rm g}^j}}{\partial w_a} &= \int_{-\infty}^{0} dx\,\mathcal{K}(x,\ell)\Bigg(\frac{3}{2}[x-(e^x-1)](1-\Omega_{\rm M}^{\rm GR}(x)) \\
&+\frac{3}{2}\int_{-\infty}^{x} d\bar{x}\,\Big(I(x,\bar{x})(1-\Omega_{\rm M}^{\rm GR}(\bar{x})) \\
&\times\left\{3\Omega_{\rm M}^{\rm GR}(\bar{x})(1+f_{\rm GR}(\bar{x}))[\bar{x}-(e^{\bar{x}}-1)]+f_{\rm GR}(\bar{x})(1-e^{\bar{x}})\right\}\Big) \\
&+\Bigg[\left(\frac{\partial\ln G_j(x)}{\partial\ln\chi}+\frac{\partial\ln G_i(x)}{\partial\ln\chi}-\frac{\partial\ln(P_\delta^{\rm GR}(x=0,k)/k^4)}{\partial\ln k}\right)\Bigg|_{\chi_{\rm GR}} \\
&\times\frac{3}{2}\int_{\infty}^{x} d\bar{x}\frac{\bar{x}-(e^{\bar{x}}-1)}{\mathcal{H}_{\rm GR}(\bar{x})}(1-\Omega_{\rm M}^{\rm GR}(\bar{x}))\Bigg]\Bigg) \\
\frac{\partial(\delta f\sigma_8(x))}{\partial w_0} &= \int_{-\infty}^{x} G_f(x,x')\left[\frac{(1-\Omega_{\rm M}^{\rm GR}(x'))}{\Omega_{\rm M}^{\rm GR}(x')}3\Omega_{\rm M}^{\rm GR}(x')(1+f_{\rm GR}(x'))x'+f_{\rm GR}(x')\right]dx' \\
\frac{\partial(\delta f\sigma_8(x))}{\partial w_a} &= \int_{-\infty}^{x} G_f(x,x')\Bigg\{\frac{(1-\Omega_{\rm M}^{\rm GR}(x'))}{\Omega_{\rm M}^{\rm GR}(x')}3\Omega_{\rm M}^{\rm GR}(x')(1+f_{\rm GR}(x'))[x'-(e^{x'}-1)] \\
&+f_{\rm GR}(x')(1-e^{x'})\Bigg\}dx'.
\end{aligned}
\tag{B.2}
$$

Derivatives with respect to $\{p_0^i\}$:

$$
\begin{aligned}
\frac{\partial C_\ell^{\kappa_{\rm g}^i\kappa_{\rm g}^j}}{\partial p_0^1} &= \int_{-\infty}^{0} dx\,\mathcal{K}(x,\ell)\frac{\Omega_\Lambda^{\rm GR}(x)}{\Omega_\Lambda^{\rm GR}(x=0)} \\
\frac{\partial C_\ell^{\kappa_{\rm g}^i\kappa_{\rm g}^j}}{\partial p_0^2} &= \int_{-\infty}^{0} dx\,\mathcal{K}(x,\ell)\frac{\Omega_\Lambda^{\rm GR}(x)}{\Omega_\Lambda^{\rm GR}(x=0)}\frac{\ell^2c^2}{\chi_{\rm GR}^2(x)(20H_0)^2} \\
\frac{\partial C_\ell^{\kappa_{\rm g}^i\kappa_{\rm g}^j}}{\partial p_0^3} &= \int_{-\infty}^{0} dx\,\mathcal{K}(x,\ell)\Bigg[\frac{\Omega_\Lambda^{\rm GR}(x)}{\Omega_\Lambda^{\rm GR}(x=0)}\frac{\ell^2c^2}{\chi_{\rm GR}^2(x)(20H_0)^2} \\
&\qquad+3\int_{-\infty}^{x} d\bar{x}\,I(x,\bar{x})\Omega_{\rm M}^{\rm GR}(\bar{x})\frac{\Omega_\Lambda^{\rm GR}(\bar{x})}{\Omega_\Lambda^{\rm GR}(\bar{x}=0)}\frac{\ell^2c^2}{\chi_{\rm GR}^2(\bar{x})(20H_0)^2}\Bigg] \\
\frac{\partial C_\ell^{\kappa_{\rm g}^i\kappa_{\rm g}^j}}{\partial p_0^4} &= -\int_{-\infty}^{0} dx\,\mathcal{K}(x,\ell)\left[2\frac{\Omega_\Lambda^{\rm GR}(x)}{\Omega_\Lambda^{\rm GR}(x=0)}+3\int_{-\infty}^{x} d\bar{x}\,I(x,\bar{x})\Omega_{\rm M}^{\rm GR}(\bar{x})\frac{\Omega_\Lambda^{\rm GR}(\bar{x})}{\Omega_\Lambda^{\rm GR}(\bar{x}=0)}\right] \\
\frac{\partial C_\ell^{\kappa_{\rm g}^i\kappa_{\rm g}^j}}{\partial p_0^5} &= -\int_{-\infty}^{0} dx\,\mathcal{K}(x,\ell)\Bigg[2\frac{\Omega_\Lambda^{\rm GR}(x)}{\Omega_\Lambda^{\rm GR}(x=0)}\frac{\ell^2c^2}{\chi_{\rm GR}^2(x)(20H_0)^2} \\
&\qquad+3\int_{-\infty}^{x} d\bar{x}\,I(x,\bar{x})\Omega_{\rm M}^{\rm GR}(\bar{x})\frac{\Omega_\Lambda^{\rm GR}(\bar{x})}{\Omega_\Lambda^{\rm GR}(\bar{x}=0)}\frac{\ell^2c^2}{\chi_{\rm GR}^2(\bar{x})(20H_0)^2}\Bigg]
\end{aligned}
\tag{B.3}
$$

$$
\begin{aligned}
\frac{\partial(\delta f\sigma_8(x,k))}{\partial p_0^1} &= 0\\
\frac{\partial(\delta f\sigma_8(x,k))}{\partial p_0^2} &= 0\\
\frac{\partial(\delta f\sigma_8(x,k))}{\partial p_0^3} &= \int_{-\infty}^{x} G_f(x,x')\frac{\Omega_\Lambda^{\mathrm{GR}}(x')}{\Omega_\Lambda^{\mathrm{GR}}(x'=0)}\frac{c^2k^2}{(20H_0)^2}dx'\\
\frac{\partial(\delta f\sigma_8(x,k))}{\partial p_0^4} &= -\int_{-\infty}^{x} G_f(x,x')\frac{\Omega_\Lambda^{\mathrm{GR}}(x')}{\Omega_\Lambda^{\mathrm{GR}}(x'=0)}dx'\\
\frac{\partial(\delta f\sigma_8(x,k))}{\partial p_0^5} &= -\int_{-\infty}^{x} G_f(x,x')\frac{\Omega_\Lambda^{\mathrm{GR}}(x')}{\Omega_\Lambda^{\mathrm{GR}}(x'=0)}\frac{c^2k^2}{(20H_0)^2}dx'.
\end{aligned}
\tag{B.4}
$$

Derivatives with respect to $\bar{\mu}_0 m_\mu^2$ and $\Sigma_0 m_\Sigma^2$:

$$
\begin{aligned}
\frac{\partial C_\ell^{\kappa_{\mathrm{g}}^i\kappa_{\mathrm{g}}^j}}{\partial\left(\bar{\mu}_0 m_\mu^2\right)} &= \int_{-\infty}^{0} dx\,\mathcal{K}(x,\ell)\left[3\int_{-\infty}^{x} d\bar{x}\,\Omega_{\mathrm{M}}^{\mathrm{GR}}(\bar{x})I(x,\bar{x})\frac{\Omega_\Lambda^{\mathrm{GR}}(\bar{x})}{\Omega_\Lambda^{\mathrm{GR}}(\bar{x}=0)}\frac{\chi(\bar{x})^2}{\ell^2}\right]\left(\frac{20H_0}{c^2}\right)^2\\
\frac{\partial C_\ell^{\kappa_{\mathrm{g}}^i\kappa_{\mathrm{g}}^j}}{\partial\left(\Sigma_0 m_\Sigma^2\right)} &= 2\int_{-\infty}^{0} dx\,\mathcal{K}(x,\ell)\frac{\Omega_\Lambda^{\mathrm{GR}}(x)}{\Omega_\Lambda^{\mathrm{GR}}(x=0)}\frac{\chi(x)^2}{\ell^2}\left(\frac{20H_0}{c^2}\right)^2\\
\frac{\partial(\delta f\sigma_8(x,k))}{\partial\left(\bar{\mu}_0 m_\mu^2\right)} &= \int_{-\infty}^{x} G_f(x,x')\frac{\Omega_\Lambda^{\mathrm{GR}}(x')}{\Omega_\Lambda^{\mathrm{GR}}(x'=0)}\left(\frac{20H_0}{kc^2}\right)^2dx'\\
\frac{\partial(\delta f\sigma_8(x,k))}{\partial\left(\Sigma_0 m_\Sigma^2\right)} &= 0.
\end{aligned}
\tag{B.5}
$$

Appendix C

The general form of $\Upsilon_{gm}(R)$

In the main text of Chapter 4, $\Upsilon_{gm}(R)$ is derived under the assumption of an effective redshift for the lens galaxies. Here, the expression for $\Upsilon_{gm}(R)$ is presented without this assumption.

A function to characterise the lens galaxy redshift distribution, $W_l(\chi)$, is introduced, and normalised over the integration range. Equation 4.11 becomes:

$$\Delta\Sigma_{gm}(R) = \frac{1}{\bar{w}} \int_0^{\chi_H} d\chi_s W_s(\chi_s) \int_0^{\chi_H} d\chi_l W_l(\chi_l) \overline{\Sigma_c^{-1}}(\chi_l, \chi_s) \gamma_{\rm t}^{\rm g}(R, \chi_l, \chi_s) \tag{C.1}$$

with $\bar{w}$ becoming:

$$\bar{w} = \int_0^{\chi_H} d\chi_s W_s(\chi_s) \int_0^{\chi_H} d\chi_l W_l(\chi_l) \left(\overline{\Sigma_c^{-1}}(\chi_l, \chi_s) \right)^2 . \tag{C.2}$$

Equation 4.14 is then extended analogously to in the main text to obtain an expression for the convergence in direction $\hat{\theta}_2$ and at χ_l given a galaxy in direction $\hat{\theta}_1$ and at χ_s, in terms of two comoving distances and the angle θ between directions $\hat{\theta}_1$ and $\hat{\theta}_2$. It can be found that:

$$\bar{\kappa}_{\rm g}(\theta, \chi_l, \chi_s) = \frac{3}{2} \left(\frac{H_0}{c} \right)^2 \Omega_{\rm M}(z=0) \int_0^{\chi_H} d\chi_l W_l(\chi_l) \int_0^{\chi_s} d\chi \frac{g(\chi, \chi_s)}{a(\chi)} [\xi(\chi_l, \chi, \theta)]. \tag{C.3}$$

In order to convert this to a function of R, the expression $\theta = \frac{R}{\chi_l}$ is employed, such that the value of θ depends on χ_l at each point in the lens distribution. Propagating through to the expression for $\Upsilon_{gm}(R)$, this results in:

$$\begin{aligned}\Upsilon_{gm}(R) = {} & \frac{\rho_{\rm c}\Omega_{\rm M}(z=0)}{\bar{w}} \int_0^{\chi_H} d\chi_l W_l(\chi_l) \int d\Delta \frac{(4\pi G)^2 \chi_l(\chi_l+\Delta)}{c^4 a(\chi_l) a(\chi_l+\Delta)} \int_{\chi_l+\Delta}^{\chi_H} d\chi_s \overline{W}_s(\chi_s) \\ & \times \frac{(\chi_s-\chi_l-\Delta)(\chi_s-\chi_l)}{\chi_s^2} \left[\frac{2}{R^2} \int_0^R R' dR' \xi_{gm}\left(\chi_l, \chi_s, \frac{R'}{\chi_l}, b\right) \right. \\ & \left. - \xi_{gm}\left(\chi_l, \chi_s, \frac{R}{\chi_l}, b\right) + \left(\frac{R_0}{R}\right)^2 \xi_{gm}\left(\chi_l, \chi_s, \frac{R_0}{\chi_l}, b\right) \right]. \end{aligned} \qquad \text{(C.4)}$$

Appendix D

Forecast errors on E_G

Here the derivation of forecast errors on $E_G(R)$ is presented. For each bin R_i, the variance of E_G^i is given by:

$$\sigma^2(E_G^i) = (E_G^i)^2 \left(\left(\frac{\sigma(\Upsilon_{gm}^i)}{\Upsilon_{gm}^i} \right)^2 + \left(\frac{\sigma(\Upsilon_{gg}^i)}{\Upsilon_{gg}^i} \right)^2 + \left(\frac{\sigma(\beta)}{\beta} \right)^2 \right). \tag{D.1}$$

The error of Υ_{gm}^i, Υ_{gg}^i and β are therefore calculated in turn. All practical error calculations assume the fiducial choices of R_0, W_s, and b (given in Chapter 4), while for P the more realistic choice of 300 Mpc/h is assumed.

D.1 Forecast errors on Υ_{gm}

In order to calculate the forecast error of $\Upsilon_{gm}(R)$ in bin R_i (which will be denoted $\sigma(\Upsilon_{gm}^i)$) the method of [295] is followed, where a similar calculation is made for the tangential shear. Consider $\Upsilon_{gm}(R)$ as written in the form:

$$\Upsilon_{gm}(R) = \Delta\Sigma_{gm}(R) - \left(\frac{R_0}{R} \right)^2 \Delta\Sigma_{gm}(R_0). \tag{D.2}$$

The variance of $\Delta\Sigma_{gm}$ is first calculated, and this result is then extended to Υ_{gm}. $\Delta\Sigma_{gm}$ is given by:

$$\Delta\Sigma_{gm}(\vec{R}) = \frac{1}{\bar{w}} \int_0^{\chi_\infty} d\chi_s W_s(\chi_s) \overline{\Sigma_{\rm c}^{-1}}(\bar{\chi}_l, \chi_s) \gamma_{\rm t}^{\rm g}(\bar{\chi}_l, \chi_s, \vec{R}) \tag{D.3}$$

where $\vec{R} = (R\cos\phi, R\sin\phi)$ has not yet been azimuthally averaged over. Note that $\gamma_{\rm t}^{g}$ here is the tangential shear *about a lens galaxy.*

The variance of $\Delta\Sigma_{gm}$ is given by:

$$\langle \Delta\Sigma_{gm}(R)\Delta\Sigma_{gm}(R')\rangle - \langle \Delta\Sigma_{gm}(R)\rangle\langle \Delta\Sigma_{gm}(R')\rangle. \tag{D.4}$$

$\langle \Delta\Sigma_{gm}(\vec{R})\Delta\Sigma_{gm}(\vec{R}')\rangle - \langle \Delta\Sigma_{gm}(\vec{R})\rangle\langle \Delta\Sigma_{gm}(\vec{R}')\rangle$ will first be computed, and then azimuthal averaging will be performed to obtain the desired expression.

Consider the first term in equation D.4. Following equation B.1 of [295], this can be written as:

$$\langle \Delta\Sigma_{gm}(\vec{R})\Delta\Sigma_{gm}(\vec{R}')\rangle = \frac{1}{\bar{w}^2}\int_0^{\chi_\infty} d\chi_s W_s(\chi_s)\int_0^{\chi_\infty} d\chi'_s W_s(\chi'_s)\frac{1}{n_{\mathrm{L}}^2}\sum_{i,j}^{n_{\mathrm{L}}}\int d^2\hat{n}\int d^2\hat{n}'$$
$$\times \langle \delta(\hat{n}-\hat{n}^i)\delta(\hat{n'}-\hat{n'}^j)\overline{\Sigma_{\mathrm{c}}^{-1}}(\bar{\chi}_l,\chi_s)\overline{\Sigma_{\mathrm{c}}^{-1}}(\bar{\chi}_l,\chi'_s)\gamma_{\mathrm{t}}^{\mathrm{g}}(\hat{n},\bar{\chi}_l,\chi_s,\vec{R})\gamma_{\mathrm{t}}^{\mathrm{g}}(\hat{n'},\bar{\chi}_l,\chi'_s,\vec{R}')\rangle \tag{D.5}$$

where $\hat{n}$ represents the direction on the sky at which the lens galaxy is situated, and n_{L} is the total number of lens galaxies. The sum above separates into two cases: $i = j$ and $i \neq j$. This results in two terms, representing the case where two shears are measured relative to the same galaxy and the case where they are measured relative to different galaxies:

$$\langle \Delta\Sigma_{gm}(\vec{R})\Delta\Sigma_{gm}(\vec{R}')\rangle = \frac{1}{\bar{w}^2}\int_0^{\chi_\infty} d\chi_s W_s(\chi_s)\int_0^{\chi_\infty} d\chi'_s W_s(\chi'_s)\frac{1}{n_{\mathrm{L}}^2}\sum_{i,j}^{n_{\mathrm{L}}}\int d^2\hat{n}\int d^2\hat{n}'$$
$$\times \Bigg[\delta(\hat{n}-\hat{n'})\langle n_{\mathrm{L}}(\hat{n},\bar{\chi}_l)\overline{\Sigma_{\mathrm{c}}^{-1}}(\bar{\chi}_l,\chi_s)\overline{\Sigma_{\mathrm{c}}^{-1}}(\bar{\chi}_l,\chi'_s)\gamma_{\mathrm{t}}(\hat{n},\chi_s,\vec{R})\gamma_{\mathrm{t}}(\hat{n'},\chi'_s,\vec{R}')\rangle$$
$$+ \langle n_{\mathrm{L}}(\hat{n},\bar{\chi}_l)n_{\mathrm{L}}(\hat{n}',\bar{\chi}_l)\overline{\Sigma_{\mathrm{c}}^{-1}}(\bar{\chi}_l,\chi_s)\overline{\Sigma_{\mathrm{c}}^{-1}}(\bar{\chi}_l,\chi'_s)\gamma_{\mathrm{t}}(\hat{n},\chi_s,\vec{R})\gamma_{\mathrm{t}}(\hat{n'},\chi'_s,\vec{R}')\rangle\Bigg]. \tag{D.6}$$

$n_{\mathrm{L}}(\hat{n})$ is the surface density of lens galaxies at direction $\hat{n}$. Note that here the dependence of the tangential shear on $\bar{\chi}_l$ has vanished because γ_{t} is not the tangential shear about a galaxy, but just the tangential shear. $n_{\mathrm{L}}(\hat{n})$ is expanded as $n_{\mathrm{L}}(\hat{n}) = \bar{n}_{\mathrm{L}}(1+\delta_g(\hat{n},\bar{\chi}_l))$, and then $N_{\mathrm{L}} = \bar{n}_{\mathrm{L}}4\pi f_{\mathrm{sky}}$ is used to obtain:

$$\langle \Delta\Sigma_{gm}(\vec{R})\Delta\Sigma_{gm}(\vec{R}')\rangle = \frac{1}{4\pi f_{\mathrm{sky}}N_{\mathrm{L}}\bar{w}^2}\int_0^{\chi_\infty} d\chi_s W_s(\chi_s)\int_0^{\chi_\infty} d\chi'_s W_s(\chi'_s)$$
$$\times \int d^2\hat{n}\overline{\Sigma_{\mathrm{c}}^{-1}}(\bar{\chi}_l,\chi_s)\overline{\Sigma_{\mathrm{c}}^{-1}}(\bar{\chi}_l,\chi'_s)\langle\gamma_{\mathrm{t}}(\hat{n},\chi_s,\vec{R})\gamma_{\mathrm{t}}(\hat{n},\chi'_s,\vec{R}')\rangle$$
$$+ \frac{1}{f_{\mathrm{sky}}^2 16\pi^2\bar{w}^2}\int_0^{\chi_\infty} d\chi_s W_s(\chi_s)\int_0^{\chi_\infty} d\chi'_s W_s(\chi'_s)\int d^2\hat{n}\int d^2\hat{n}'\overline{\Sigma_{\mathrm{c}}^{-1}}(\bar{\chi}_l,\chi_s)\overline{\Sigma_{\mathrm{c}}^{-1}}(\bar{\chi}_l,\chi'_s)$$
$$\times \Big[\langle\gamma_{\mathrm{t}}(\hat{n},\chi_s,\vec{R})\gamma_{\mathrm{t}}(\hat{n'},\chi'_s,\vec{R}')\rangle + \langle\delta_g(\hat{n},\bar{\chi}_l)\delta_g(\hat{n}',\bar{\chi}_l)\gamma_{\mathrm{t}}(\hat{n},\chi_s,\vec{R})\gamma_{\mathrm{t}}(\hat{n'},\chi'_s,\vec{R}')\rangle\Big]. \tag{D.7}$$

As in [295], it is assumed that $\langle\delta_g\gamma_{\rm t}\gamma_{\rm t}\rangle = 0$.

Consider first the one galaxy term (the first term of equation D.7). The quantities inside angle brackets are Fourier-expanded to get:

$$\begin{aligned}&\frac{1}{\bar{w}^2}\int_0^{\chi_\infty} d\chi_s W_s(\chi_s)\int_0^{\chi_\infty} d\chi_s' W_s(\chi_s')\overline{\Sigma_{\rm c}^{-1}}(\bar{\chi}_l,\chi_s)\overline{\Sigma_{\rm c}^{-1}}(\bar{\chi}_l,\chi_s')\\ &\times\left[\frac{1}{n_{\rm L}}\int\frac{d^2\vec{l}}{(2\pi)^2}P_{\kappa\kappa}(l,\chi_s,\chi_s')\cos[2(\phi-\varphi)]\cos[2(\phi'-\varphi)]e^{i\vec{l}(\vec{R}-\vec{R}')}+\frac{\langle\gamma_{\rm int}^2\rangle\delta(\vec{R}-\vec{R}')}{n_{\rm L}n_{\rm s}}\right]\end{aligned} \tag{D.8}$$

where $\vec{l} = (l\cos\varphi, l\sin\varphi)$, $P_{\kappa\kappa}$ is the two-dimensional power spectrum of the convergence , and $n_{\rm s}$ is the average source galaxy surface density.

Now consider the two-galaxy contribution. The first part of the two-galaxy term is zero, being just two averages of tangential shear over the sky. The second part can be expanded using Wick's theorem. This leads to:

$$\begin{aligned}&\langle\Delta\Sigma_{gm}(\vec{R})\rangle\langle\Delta\Sigma_{gm}(\vec{R}')\rangle+\frac{1}{4\pi f_{\rm sky}\bar{w}^2}\int_0^{\chi_\infty} d\chi_s W_s(\chi_s)\int_0^{\chi_\infty} d\chi_s' W_s(\chi_s')\int d^2\hat{n}\int d^2\hat{n}'\\ &\times\overline{\Sigma_{\rm c}^{-1}}(\bar{\chi}_l,\chi_s)\overline{\Sigma_{\rm c}^{-1}}(\bar{\chi}_l,\chi_s')\int\frac{d^2\vec{l}}{(2\pi)^2}\cos[2(\phi-\varphi)]\cos[2(\phi'-\varphi)]e^{i\vec{l}(\vec{R}-\vec{R}')}\\ &\times\left[P_{g\kappa}(l,\bar{\chi}_l,\chi_s')P_{g\kappa}(l,\bar{\chi}_l,\chi_s)+P_{gg}(l,\bar{\chi}_l)\left[P_{\kappa\kappa}(l,\chi_s,\chi_S')+\frac{\langle\gamma_{\rm int}^2\rangle}{n_{\rm s}}\right]\right].\end{aligned} \tag{D.9}$$

It can be seen that the first part of this term cancels with $\langle\Delta\Sigma_{gm}(\vec{R})\rangle\langle\Delta\Sigma_{gm}(\vec{R}')\rangle$ in equation D.4.

Adding together equations D.9 and D.8 gives $\langle\Delta\Sigma_{gm}(\vec{R})\Delta\Sigma_{gm}(\vec{R}')\rangle$. Subtracting then $\langle\Delta\Sigma(\vec{R})\rangle\langle\Delta\Sigma(\vec{R}')\rangle$ to get the variance of $\Delta\Sigma_{gm}(\vec{R})$, and azimuthally averaging, results in:

$$\begin{aligned}&\langle\Delta\Sigma_{gm}(R)\Delta\Sigma_{gm}(R')\rangle-\langle\Delta\Sigma_{gm}(R)\rangle\langle\Delta\Sigma_{gm}(R')\rangle=\\ &\frac{1}{4\pi f_{\rm sky}\bar{w}^2}\int_0^{\chi_\infty} d\chi_s W_s(\chi_s)\int_0^{\chi_\infty} d\chi_s' W_s(\chi_s')\overline{\Sigma_{\rm c}^{-1}}(\bar{\chi}_l,\chi_s)\overline{\Sigma_{\rm c}^{-1}}(\bar{\chi}_l,\chi_s')\int\frac{ldl}{2\pi}J_2(lR)J_2(lR')\\ &\times\left[P_{g\kappa}(l,\bar{\chi}_l,\chi_s')P_{g\kappa}(l,\bar{\chi}_l,\chi_s)+\left(P_{gg}(l,\bar{\chi}_l,)+\frac{1}{\bar{n}_{\rm L}}\right)\left[P_{\kappa\kappa}(l,\chi_s,\chi_s')+\frac{\langle\gamma_{\rm int}^2\rangle}{n_{\rm s}}\right]\right]\end{aligned} \tag{D.10}$$

where $n_{\mathrm{L}} = \bar{n}_{\mathrm{L}} 4\pi f_{\mathrm{sky}}$ has been used to incorporate the one-halo term. Averaging in R bins, it is found that:

$$\begin{aligned}\sigma^2\left(\Delta\Sigma^i_{gm}\right) = & \frac{1}{4\pi \bar{w}^2 f_{\mathrm{sky}}(R^{i+1}-R^i)(R^{i+1}-R^i)} \int_0^{\chi_\infty} d\chi_s W_s(\chi_s) \int_0^{\chi_\infty} d\chi_s' W_s(\chi_s') \\ & \overline{\Sigma_{\mathrm{c}}^{-1}}(\bar{\chi}_l, \chi_s)\overline{\Sigma_{\mathrm{c}}^{-1}}(\bar{\chi}_l, \chi_s') \int_{R_i}^{R_{i+1}} dR \int_{R_i}^{R_{i+1}} dR' \int \frac{ldl}{2\pi} J_2(lR) J_2(lR') \\ & \times \left[P_{g\kappa}(l, \bar{\chi}_l, \chi_s') P_{g\kappa}(l, \bar{\chi}_l, \chi_s) + \left(P_{gg}(l, \bar{\chi}_l) + \frac{1}{\bar{n}_{\mathrm{L}}}\right) \left[P_{\kappa\kappa}(l, \chi_s, \chi_s') + \frac{\langle \gamma^2_{\mathrm{int}} \rangle}{n_{\mathrm{s}}} \right]\right].\end{aligned} \tag{D.11}$$

Finally, the error on the second term in equation D.2 is approximated by computing the variance of $\Delta\Sigma_{gm}(R)$ in a small (extent $R_0/5$) bin around R_0, and then averaging the full term in R bins. The total squared 1σ error of $\Upsilon_{gm}(R)$ in bin R_i is the sum of this result and equation D.11.

Note that, as in Chapter 4, it has been assumed that an effective redshift $\bar{z}_l$ exists for the lens population, corresponding to an effective comoving distance $\bar{\chi}_l$. However, in computing forecast errors, the fact that some source galaxies may be at lower redshift than $\bar{z}_l$ must be accounted for. In a real observational scenario, these galaxies would be lensed by low redshift lens galaxies, and hence would still contribute to the signal. However, in this case, they cannot be considered. The fraction of galaxies from the source galaxy distribution that are at higher redshift than $\bar{z}_l$ is computed, and n_{s} is multiplied by this fraction before computing errors. Thus, error bars are likely somewhat inflated and should be treated as an upper bound.

D.2 Forecast errors on Υ_{gg}

$\Upsilon_{gg}(R)$ as given in equation 4.5 consists of three terms, all related to the projected correlation function $w_{gg}(R)$. A measurement of $w_{gg}(R)$ is made by first measuring the redshift-space correlation function $\xi^s_{gg}(R, \Delta)$. When calculating expected errors, it is assumed that as long as the projection length is long, it will be equivalent to use the real-space correlation function, $\xi_{gg}(R, \Delta)$. It can then be found that the variance of this correlation function is given by:

$$\sigma^2(\xi_{gg}(R_1,\Delta_1,R_2,\Delta_2)) = \frac{1}{\pi^2 V}\int_0^\infty dk_{||}\cos(k_{||}\Delta_1)\cos(k_{||}\Delta_2) \times \int_0^\infty dk_\perp k_\perp J_0(k_\perp R_1) J_0(k_\perp R_2)\left(P_{gg}(k_{||},k_\perp)+\frac{1}{n_{\rm g}}\right)^2, \tag{D.12}$$

where $n_{\rm g}$ is the volume density of galaxies and V is the volume of the survey. Δ_1 and Δ_2 are projected over $\{-P,\ P\}$, and the expressions is averaged over bin R_i, to find:

$$\sigma^2(w^i_{gg}) = \frac{4}{(\Delta R_i)^2\pi^2 V}\int_{R^i}^{R^{i+1}} dR_1 \int_{R^i}^{R^{i+1}} dR_2 \int_0^\infty dk_{||}\frac{\sin^2(k_{||}P)}{k_{||}^2} \times \int_0^\infty dk_\perp k_\perp J_0(k_\perp R_1) J_0(k_\perp R_2)\left(P_{gg}(k_{||},k_\perp)+\frac{1}{n_{\rm g}}\right)^2. \tag{D.13}$$

It is numerically difficult to compute this quantity directly in the above form. This is as a result of the $\frac{1}{n_{\rm g}^2}$ term: performing the integrals in $k_\perp$ over the oscillatory Bessel functions is unfeasible without the damping effect of the smoothed power spectrum at high $k_\perp$. Fortunately, the bracketed term can be expanded in order to allow the $\frac{1}{n_{\rm g}^2}$ portion to be evaluated analytically. The result is:

$$\sigma^2(w^i_{gg}) = \frac{4}{(\Delta R_i)^2\pi^2 V}\int_{R^i}^{R^{i+1}} dR_1 \int_{R^i}^{R^{i+1}} dR_2 \int_0^\infty dk_{||}\frac{\sin^2(k_{||}P)}{k_{||}^2} \int_0^\infty dk_\perp k_\perp J_0(k_\perp R_1) \times J_0(k_\perp R_2)\left(P_{gg}(k_{||},k_\perp)^2 + 2P_{gg}(k_{||},k_\perp)/n_{\rm g}\right) + \frac{2|P|\ln\left(\frac{R^{i+1}}{R^i}\right)}{\pi V \Delta R_i n_{\rm g}^2} \tag{D.14}$$

where ΔR_i is the extent of the given R bin. The variance of the middle term of equation 4.5 is trivially the above times $\rho_{\rm c}^2$.

To find the squared error associated with the first term of equation 4.5, the same strategy is employed, with the result:

$$\sigma^2 = \frac{16}{(\Delta R_i)^2\pi^2 V}\int_{R^i}^{R^{i+1}} dR_1 \int_{R^i}^{R^{i+1}} dR_2 \frac{1}{R_1^2 R_2^2} \times \int_{R_0}^{R_1} dR_1' \int_{R_0}^{R_2} dR_2' \int_0^\infty dk_{||}\frac{\sin^2(k_{||}P)}{k_{||}^2} \times \int_0^\infty dk_\perp k_\perp J_0(k_\perp R_1') J_0(k_\perp R_2')\left(P_{gg}(k_{||},k_\perp)^2 + \frac{2P_{gg}(k_{||},k_\perp)}{n_{\rm g}}\right) + \frac{4|P|}{(\Delta R_i)^2\pi n_{\rm g}^2 V}\left(\frac{1}{R^i}-\frac{1}{R^{i+1}}\right)\left(R^{i+1}-R^i+\frac{R_0^2}{2}\left(\frac{1}{R^{i+1}}-\frac{1}{R^i}\right)\right). \tag{D.15}$$

The error is estimated on the third term of equation 4.5, $\frac{R_0^2}{R^2}w_{gg}(R_0)$, by approximating the variance of $w_{gg}(R_0)$ as the variance in a small bin around $w_{gg}(R_0)$ (with extent $R_0/5$).

D.3 Forecast errors on β

In computing the error on β, the formula developed in [296] is used:

$$\sigma(\beta) = \beta \frac{Cb^{0.7}}{V^{0.5}} e^{\frac{n_0}{b^2 n_{\rm g}}} \tag{D.16}$$

where $C = 4.5 \times 10^2 \,(\mathrm{Mpc/h})^{\frac{3}{2}}$ and $n_0 = 1.7 \times 10^4 \,(\mathrm{h/Mpc})^3$. b is the constant galaxy bias.

Bibliography

[1] European Space Agency, *Euclid definition study report (Red Book).* (ESA/SRE, 2011), arXiv: 1110.3193.

[2] LSST Dark Energy Science Collaboration, arXiv e-prints (2012), arXiv: 1211.0310.

[3] L. Van Waerbeke *et al.*, Astronomy and Astrophysics **358**, 30 (2000), arXiv: astro-ph/0002500.

[4] A. Einstein, Annalen der Physik **49**, 769822 (1916).

[5] F. W. Dyson, A. S. Eddington, and C. Davidson, Philosophical Transactions of the Royal Society of London A: Mathematical, Physical and Engineering Sciences **220**, 291 (1920).

[6] G. W. Richter and R. A. Matzner, Physical Review D **26**, 1219 (1982).

[7] A. Friedmann, Zeitschrift für Physik A Hadrons and Nuclei **21**, 326 (1924).

[8] Planck Collaboration, arXiv e-prints (2015), arXiv: 1502.01589.

[9] S. Dodelson, *Modern Cosmology*, First ed. (Elsevier, 2003).

[10] A. Lewis, A. Challinor, and A. Lasenby, The Astrophysical Journal **538**, 473 (2000), arXiv: astro-ph/9911177.

[11] C.-P. Ma and E. Bertschinger, The Astrophysical Journal **455**, 7 (1995), arXiv: astro-ph/9506072.

[12] P. Callin, arXiv e-prints (2006), arXiv: astro-ph/0606683.

[13] J. Lesgourgues, arXiv e-print (2011), arXiv: 1104.2932.

[14] R. E. Smith *et al.*, Monthly Notices of the Royal Astronomical Society **341** (2003), arXiv: astro-ph/0207664.

[15] R. Takahashi, M. Sato, T. Nishimichi, A. Taruya, and M. Oguri, The Astrophysical Journal **761**, 152 (2012), arXiv: 1208.2701.

[16] A. H. Guth, Physical Review D **23**, 347 (1981).

[17] A. D. Linde, Physics Letters B **108**, 389 (1982).

[18] S. W. Hawking, I. Moss, and J. Stewart, Physical Review D **26**, 2681 (1982).

[19] A. H. Guth and E. J. Weinberg, Nuclear Physics B **212**, 321 (1983).

[20] S. W. Hawking, Physics Letters B **115**, 295 (1982).

[21] A. A. Starobinsky, Physics Letters B **117**, 175 (1982).

[22] A. H. Guth and S.-Y. Pi, Physical Review Letters **49**, 1110 (1982).

[23] J. M. Bardeen, P. J. Steinhardt, and M. S. Turner, Physical Review D **28**, 679 (1983).

[24] J. Martin, C. Ringeval, and V. Vennin, Physics of the Dark Universe **5**, 75 (2014), arXiv: 1303.3787.

[25] J. H. Oort, Bulletin of the Astronomical Institutes of the Netherlands **6**, 249 (1932).

[26] F. Zwicky, Helv. Phys. Acta **6**, 15 (1933).

[27] V. C. Rubin and W. K. Ford Jr, The Astrophysical Journal **159**, 379 (1970).

[28] J. P. Ostriker and P. J. Peebles, The Astrophysical Journal **186**, 467 (1973).

[29] J. Einasto, A. Kaasik, and E. Saar, Nature **250**, 309 (1974).

[30] J. Ostriker, P. Peebles, and A. Yahil, The Astrophysical Journal **193**, L1 (1974).

[31] M. Roberts, The rotation curves of galaxies, in *Symposium-International Astronomical Union* Vol. 69, pp. 331–340, Cambridge Univ Press, 1975.

[32] V. C. Rubin, W. K. Ford Jr, and N. Thonnard, The Astrophysical Journal **238**, 471 (1980).

[33] W. G. Mathews, The Astrophysical Journal **219**, 413 (1978).

[34] P. Peebles, The Astrophysical Journal **263**, L1 (1982).

[35] J. R. Bond, A. S. Szalay, and M. S. Turner, Physical Review Letters **48**, 1636 (1982).

[36] G. R. Blumenthal, H. Pagels, and J. R. Primack, Nature **299**, 37 (1982).

[37] G. R. Blumenthal, J. R. Primack, M. J. Rees, and S. Faber, Nature **311**, 517 (1984).

[38] D. Clowe *et al.*, The Astrophysical Journal Letters **648**, L109 (2006), arXiv: astro-ph/0608407.

[39] G. Steigman and M. S. Turner, Nuclear Physics B **253**, 375 (1985).

[40] R. Hlozek, D. Grin, D. J. Marsh, and P. G. Ferreira, Physical Review D **91**, 103512 (2015), arXiv: 1410.2896.

[41] S. Dodelson and L. M. Widrow, Physical Review Letters **72**, 17 (1994), arXiv: hep-ph/9303287.

[42] A. H. Peter, arXiv e-prints (2012), arXiv: 1201.3942.

[43] J. F. Navarro, C. S. Frenk, and S. D. White, The Astrophysical Journal **490**, 493 (1997), arXiv: astro-ph/9611107.

[44] A. J. S. Hamilton, P. Kumar, E. Lu, and A. Matthews, The Astrophysical Journal **374** (1991).

[45] W. De Blok, Advances in Astronomy **2010** (2010), arXiv: 0910.3538.

[46] G. Kauffmann, S. D. White, and B. Guiderdoni, Monthly Notices of the Royal Astronomical Society **264**, 201 (1993).

[47] X. Fan, C. L. Carilli, and B. Keating, Annual Review of Astronomy & Astrophysics **44**, 415 (2006), arXiv: astro-ph/0602375.

[48] D. Fixsen *et al.*, The Astrophysical Journal **473**, 576 (1996), arXiv: astro-ph/9605054.

[49] J. A. Peacock *et al.*, Nature **410**, 169 (2001), arXiv: astro-ph/0103143.

[50] A. N. Taylor and M. Rowan-Robinson, Nature **359**, 396 (1992).

[51] J. P. Ostriker and P. J. Steinhardt, Nature **377**, 600 (1995).

[52] A. G. Riess *et al.*, The Astronomical Journal **116**, 1009 (1998), arXiv: astro-ph/9805201.

[53] S. Perlmutter *et al.*, The Astrophysical Journal **517**, 565 (1999), arXiv: astro-ph/9812133.

[54] D. J. Eisenstein *et al.*, The Astrophysical Journal **633**, 560 (2005), arXiv: astro-ph/0501171.

[55] S. Naess *et al.*, Journal of Cosmology and Astroparticle Physics **2014**, 007 (2014), arXiv: 1405.5524.

[56] S. Weinberg, Reviews of Modern Physics **61**, 1 (1989).

[57] I. Zlatev, L. Wang, and P. J. Steinhardt, Physical Review Letters **82**, 896 (1999), arXiv: astro-ph/9807002.

[58] S. M. Carroll, Physical Review Letters **81**, 3067 (1998), arXiv: astro-ph/9806099.

[59] C. Armendariz-Picon, V. Mukhanov, and P. J. Steinhardt, Physical Review D **63**, 103510 (2001), arXiv: astro-ph/0006373.

[60] E. Babichev, V. Mukhanov, and A. Vikman, Journal of High Energy Physics **2008**, 101 (2008), arXiv: 0708.0561.

[61] T. Clifton, P. Ferreira, A. Padilla, and C. Skordis, Physics Reports **513** (2012), arXiv: 1106.2476.

[62] A. A. Starobinsky, JETP Letters **86**, 157 (2007), arXiv: 0706.2041.

[63] T. Baker, P. G. Ferreira, and C. Skordis, Physical Review D **87**, 024015 (2013), arXiv: 1209.2117.

[64] D. Huterer and E. V. Linder, Physical Review D **75** (2007), arXiv: astro-ph/0608681.

[65] J. Khoury and A. Weltman, Physical Review Letters **93**, 171104 (2004), arXiv: astro-ph/0309300.

[66] G. R. Dvali, G. Gabadadze, and M. Porrati, Physics Letters B **B485**, 208 (2000), arXiv: hep-th/0005016.

[67] T. P. Sotiriou and V. Faraoni, Reviews of Modern Physics. **82**, 451 (2010), arXiv: 0805.1726.

[68] P. Hořava, Physical Review D **79**, 084008 (2009), arXiv: 0901.3775.

[69] F. Simpson *et al.*, Monthly Notices of the Royal Astronomical Society **429**, 2249 (2013), arXiv: 1212.3339.

[70] R. Reyes *et al.*, Nature **464**, 256 (2010), arXiv: 1003.2185.

[71] C. Blake *et al.*, Monthly Notices of the Royal Astronomical Society **456**, 2806 (2016), arXiv: 1507.03086.

[72] Planck Collaboration, arXiv e-prints (2015), arXiv: 1502.01590.

[73] M.-N. Célérier, arXiv e-prints (2007), arXiv: astro-ph/0702416.

[74] M. Vardanyan, R. Trotta, and J. Silk, Monthly Notices of the Royal Astronomical Society **397**, 431 (2009), arXiv: 0901.3354.

[75] M. Vardanyan, R. Trotta, and J. Silk, Monthly Notices of the Royal Astronomical Society: Letters **413**, L91 (2011), arXiv: 1101.5476.

[76] S. M. Carroll, V. Duvvuri, M. Trodden, and M. S. Turner, Physical Review D **70**, 043528 (2004), arXiv: astro-ph/0306438.

[77] S. Capozziello, S. Carloni, and A. Troisi, arXiv e-prints (2003), arXiv: astro-ph/0303041.

[78] D. Lovelock, Journal of Mathematical Physics **12**, 498 (1971).

[79] H. A. Buchdahl, Monthly Notices of the Royal Astronomical Society **150**, 1 (1970).

[80] T. Chiba, Physics Letters B **575**, 1 (2003), arXiv: astro-ph/0307338.

[81] T. P. Sotiriou, Classical and Quantum Gravity **23**, 5117 (2006), arXiv: gr-qc/0604028.

[82] Y.-S. Song, W. Hu, and I. Sawicki, Physical Review D **75**, 044004 (2007), arXiv: astro-ph/0610532.

[83] L. Lombriser, A. Slosar, U. Seljak, and W. Hu, Physical Review D **85**, 124038 (2012), arXiv: 1003.3009.

[84] H. Burton and R. B. Mann, Physical Review D **57**, 4754 (1998), arXiv: gr-qc/9711003.

[85] G. W. Horndeski, International Journal of Theoretical Physics **10**, 363 (1974).

[86] C. Charmousis, E. J. Copeland, A. Padilla, and P. M. Saffin, Physical Review Letters **108**, 051101 (2012), arXiv: 1106.2000.

[87] J. Gleyzes, D. Langlois, F. Piazza, and F. Vernizzi, Physical Review Letters **114**, 211101 (2015), arXiv: 1404.6495.

[88] J. Gleyzes, D. Langlois, F. Piazza, and F. Vernizzi, Journal of Cosmology and Astroparticle Physics **2015**, 018 (2015), arXiv: 1408.1952.

[89] J. D. Bekenstein, Physical Review D **70**, 083509 (2004), arXiv: astro-ph/0403694.

[90] M. von Strauss, A. Schmidt-May, J. Enander, E. Mörtsell, and S. F. Hassan, Journal of Cosmology and Astroparticle Physics **2012**, 042 (2012), arXiv: 1111.1655.

[91] J. Moffat, Journal of Cosmology and Astroparticle Physics **2006**, 004 (2006), arXiv: gr-qc/0506021.

[92] A. Silvestri, L. Pogosian, and R. V. Buniy, Physical Review D **87**, 104015 (2013), arXiv: 1302.1193.

[93] T. Baker, P. G. Ferreira, C. D. Leonard, and M. Motta, Physical Review D **90**, 124030 (2014), arXiv: 1409.8284.

[94] A. Hojjati, L. Pogosian, A. Silvestri, and G.-B. Zhao, Physical Review D **89**, 083505 (2014), arXiv: 1312.5309.

[95] P. Creminelli, G. D'Amico, J. Norena, and F. Vernizzi, Journal of Cosmology and Astroparticle Physics **0902**, 018 (2009), arXiv: 0811.0827.

[96] T. Baker, P. G. Ferreira, C. Skordis, and J. Zuntz, Physical Review D **84**, 124018 (2011), arXiv: 1107.0491.

[97] R. A. Battye and J. A. Pearson, Journal of Cosmology and Astroparticle Physics **1207**, 019 (2012), arXiv: 1203.0398.

[98] J. Gleyzes, D. Langlois, F. Piazza, and F. Vernizzi, Journal of Cosmology and Astroparticle Physics **8**, 25 (2013), arXiv: 1304.4840.

[99] J. K. Bloomfield and É. É. Flanagan, Journal of Cosmology and Astroparticle Physics **2012** (2012), arXiv: 1112.0303.

[100] L. Amendola, S. Fogli, A. Guarnizo, M. Kunz, and A. Vollmer, Physical Review D **89**, 063538 (2014), arXiv: 1311.4765.

[101] A. Hojjati, Journal of Cosmology and Astroparticle Physics **1**, 9 (2013), arXiv: 1210.3903.

[102] J. Noller, F. von Braun-Bates, and P. G. Ferreira, Physical Review D **89**, 023521 (2014), arXiv: 1310.3266.

[103] F. Schmidt, Physical Review D **80**, 043001 (2009), arXiv: 0905.0858.

[104] G.-B. Zhao, B. Li, and K. Koyama, Physical Review D **83**, 044007 (2011), arXiv: 1011.1257.

[105] A. Barreira, B. Li, W. A. Hellwing, C. M. Baugh, and S. Pascoli, Journal of Cosmology and Astroparticle Physics **2013**, 027 (2013), arXiv: 1306.3219.

[106] B. Li *et al.*, Journal of Cosmology and Astroparticle Physics **2013**, 012 (2013), arXiv: 1308.3491.

[107] M. Park, K. M. Zurek, and S. Watson, Physical Review D **81**, 124008 (2010), arXiv: 1003.1722.

[108] J. K. Bloomfield, É. É. Flanagan, M. Park, and S. Watson, Journal of Cosmology and Astroparticle Physics **1308**, 010 (2013), arXiv: 1211.7054.

[109] L. Lombriser and A. Taylor, Physical Review Letters **114**, 031101 (2015), arXiv: 1405.2896.

[110] B. Hu, M. Raveri, N. Frusciante, and A. Silvestri, Physical Review D **89**, 103530 (2014), arXiv: 1312.5742.

[111] P. E. Dewdney, P. J. Hall, R. T. Schilizzi, and T. J. L. Lazio, Proceedings of the IEEE **97**, 1482 (2009).

[112] F. Schmidt, Physical Review D **78**, 043002 (2008), arXiv: 0805.4812.

[113] S. A. Thomas, F. B. Abdalla, and J. Weller, Monthly Notices of the Royal Astronomical Society **395**, 197 (2009), arXiv: 0810.4863.

[114] L. Amendola, M. Kunz, and D. Sapone, Journal of Cosmology and Astroparticle Physics **2008**, 013 (2008), arXiv: 0704.2421.

[115] S. Tsujikawa and T. Tatekawa, Physics Letters B **665**, 325 (2008), arXiv: 0804.4343.

[116] P. Zhang, M. Liguori, R. Bean, and S. Dodelson, Phys. Rev. Lett. **99**, 141302 (2007), arXiv: 0704.1932.

[117] E. Bertschinger and P. Zukin, Physical Review D **78**, 024015 (2008), arXiv: 0801.2431.

[118] L. Knox, Y.-S. Song, and J. A. Tyson, Physical Review D **74**, 023512 (2006), arXiv: astro-ph/0503644.

[119] M. Ishak, A. Upadhye, and D. N. Spergel, Physical Review D **74**, 043513 (2006), arXiv: astro-ph/0507184.

[120] M. Amarzguioui, Ø. Elgarøy, D. F. Mota, and T. Multamäki, Astronomy & Astrophysics **454**, 707 (2006), arXiv: astro-ph/0510519.

[121] M. S. Movahed, M. Farhang, and S. Rahvar, International Journal of Theoretical Physics **48**, 1203 (2009), arXiv: astro-ph/0701339.

[122] M. Martinelli, A. Melchiorri, and L. Amendola, Physical Review D **79**, 123516 (2009), arXiv: 0906.2350.

[123] B. Hu, M. Liguori, N. Bartolo, and S. Matarrese, Physical Review D **88**, 123514 (2013), arXiv: 1307.5276.

[124] B. Jain, V. Vikram, and J. Sakstein, The Astrophysical Journal **779**, 39 (2013), arXiv: 1204.6044.

[125] P. Brax, C. Burrage, and A.-C. Davis, Journal of Cosmology and Astroparticle Physics **9**, 020 (2011), arXiv: 1106.1573.

[126] R. R. Caldwell, R. Dave, and P. J. Steinhardt, Physical Review Letters **80**, 1582 (1998), arXiv: astro-ph/9708069.

[127] B. Ratra and P. J. Peebles, Physical Review D **37**, 3406 (1988).

[128] A. Kamenshchik, U. Moschella, and V. Pasquier, Physics Letters B **511**, 265 (2001), arXiv: gr-qc/0103004.

[129] L. Amendola, Physical Review D **62**, 043511 (2000), arXiv: astro-ph/9908023.

[130] T. Chiba, T. Okabe, and M. Yamaguchi, Physical Review D **62**, 023511 (2000), arXiv: astro-ph/9912463.

[131] P. G. Ferreira and M. Joyce, Physical Review Letters **79**, 4740 (1997), arXiv: astro-ph/9711102.

[132] R. R. Caldwell, Physics Letters B **545**, 23 (2002), arXiv: astro-ph/9908168.

[133] E. J. Copeland, M. Sami, and S. Tsujikawa, International Journal of Modern Physics D **15**, 1753 (2006), arXiv: hep-th/0603057.

[134] M. Chevallier and D. Polarski, International Journal of Modern Physics D **10**, 213 (2001), arXiv: gr-qc/0009008.

[135] E. V. Linder, Phys. Rev. Lett. **90**, 091301 (2003), arXiv: astro-ph/0208512.

[136] A. Hojjati, E. V. Linder, and J. Samsing, Physical Review Letters **111**, 041301 (2013), arXiv: 1304.3724.

[137] N. Said, C. Baccigalupi, M. Martinelli, A. Melchiorri, and A. Silvestri, Physical Review D **88**, 043515 (2013), arXiv: 1303.4353.

[138] M. Oguri *et al.*, The Astronomical Journal **135**, 512 (2008), arXiv: 0708.0825.

[139] J.-Q. Xia, H. Li, and X. Zhang, Physical Review D **88**, 063501 (2013), arXiv: 1308.0188.

[140] O. Farooq and B. Ratra, The Astrophysical Journal Letters **766**, L7 (2013), arXiv: 1301.5243.

[141] V. Salvatelli, A. Marchini, L. Lopez-Honorez, and O. Mena, Physical Review D **88**, 023531 (2013), arXiv: 1304.7119.

[142] M. Sullivan *et al.*, The Astrophysical Journal **737**, 102 (2011), arXiv: 1104.1444.

[143] M. Kleban and M. Schillo, Journal of Cosmology and Astroparticle Physics **2012**, 029 (2012), arXiv: 1202.5037.

[144] P. Bull and M. Kamionkowski, Physical Review D **87**, 081301 (2013), arXiv: 1302.1617.

[145] K. Ichikawa and T. Takahashi, Journal of Cosmology and Astroparticle Physics **2**, 001 (2007), arXiv: astro-ph/0612739.

[146] C. Clarkson, M. Cortês, and B. Bassett, Journal of Cosmology and Astroparticle Physics **8**, 011 (2007), arXiv: astro-ph/0702670.

[147] Y. Wang and P. Mukherjee, Physical Review D **76**, 103533 (2007), arXiv: astro-ph/0703780.

[148] Y. Chen, B. Ratra, M. Biesiada, S. Li, and Z.-H. Zhu, arXiv e-prints (2016), arXiv: 1603.07115.

[149] A. Smith *et al.*, Physical Review D **85**, 123521 (2012), arXiv: 1112.3006.

[150] M. Kilbinger *et al.*, Monthly Notices of the Royal Astronomical Society **430**, 2200 (2013), arXiv: 1212.3338.

[151] C. Heymans *et al.*, Monthly Notices of the Royal Astronomical Society **432**, 2433 (2013), arXiv: 1303.1808.

[152] M. Bartelmann and P. Schneider, Physics Reports **340**, 291 (2001), arXiv: astro-ph/9912508.

[153] P. Schneider, arXiv e-prints (2005), arXiv: astro-ph/0509252.

[154] B. R. Gillis and A. N. Taylor, Monthly Notices of the Royal Astronomical Society **456**, 2518 (2016), arXiv: 1507.01858.

[155] B. Casaponsa *et al.*, Monthly Notices of the Royal Astronomical Society **430**, 2844 (2013), arXiv: 1209.1646.

[156] J. Alsing, D. Kirk, A. Heavens, and A. H. Jaffe, Monthly Notices of the Royal Astronomical Society **452**, 1202 (2015), arXiv: 1410.7839.

[157] L. Miller *et al.*, Monthly Notices of the Royal Astronomical Society **429**, 2858 (2013), arXiv: 1210.8201.

[158] M. Kilbinger, Reports on Progress in Physics **78**, 086901 (2015), arXiv: 1411.0115.

[159] Planck Collaboration, arXiv e-prints (2015), arXiv: 1502.01591.

[160] Planck Collaboration, Astronomy & Astrophysics **571**, A17 (2014), arXiv: 1303.5077.

[161] S. Das *et al.*, Journal of Cosmology and Astroparticle Physics **4**, 014 (2014), arXiv: 1301.1037.

[162] M. Becker *et al.*, arXiv e-prints (2015), arXiv: 1507.0559.

[163] K. Kuijken *et al.*, Monthly Notices of the Royal Astronomical Society **454**, 3500 (2015), arXiv: 1507.00738.

[164] D. N. Limber, The Astrophysical Journal **117** (1953).

[165] P. Simon, Astronomy & Astrophysics **473**, 711 (2007), arXiv: astro-ph/0609165.

[166] M. L. Brown, A. N. Taylor, N. C. Hambly, and S. Dye, Monthly Notices of the Royal Astronomical Society **333**, 501 (2002), arXiv: astro-ph/0009499.

[167] R. Mandelbaum *et al.*, Monthly Notices of the Royal Astronomical Society **410**, 844 (2011), arXiv: 0911.5347.

[168] C. M. Hirata and U. Seljak, Physical Review D **70**, 063526 (2004), arXiv: astro-ph/0406275.

[169] M. D. Schneider and S. Bridle, Monthly Notices of the Royal Astronomical Society **402**, 2127 (2010), arXiv: 1001.3787.

[170] D. Kirk, A. Rassat, O. Host, and S. Bridle, Monthly Notices of the Royal Astronomical Society **424**, 1647 (2012), arXiv: 1112.4752.

[171] N. E. Chisari, J. Dunkley, L. Miller, and R. Allison, Monthly Notices of the Royal Astronomical Society **453**, 682 (2015), arXiv: 1507.03906.

[172] R. Mandelbaum, U. Seljak, G. Kauffmann, C. M. Hirata, and J. Brinkmann, Monthly Notices of the Royal Astronomical Society **368**, 715 (2006), arXiv: astro-ph/0511164.

[173] M. Velander *et al.*, Monthly Notices of the Royal Astronomical Society **437**, 2111 (2014), arXiv: 1304.4265.

[174] J. Clampitt *et al.*, arXiv e-prints (2016), arXiv: 1603.05790.

[175] R. Mandelbaum *et al.*, Monthly Notices of the Royal Astronomical Society **361** (2005), arXiv: astro-ph/0501201.

[176] I. Zehavi *et al.*, The Astrophysical Journal **608**, 16 (2004), arXiv: astro-ph/0301280.

[177] N. Kaiser, Monthly Notices of the Royal Astronomical Society **227**, 1 (1987).

[178] D. J. Eisenstein and W. Hu, The Astrophysical Journal **496**, 605 (1998), arXiv: astro-ph/9709112.

[179] D. J. Eisenstein, W. Hu, J. Silk, and A. S. Szalay, The Astrophysical Journal Letters **494**, L1 (1998), arXiv: astro-ph/9710303.

[180] L. Anderson *et al.*, Monthly Notices of the Royal Astronomical Society **441**, 24 (2014), arXiv: 1312.4877.

[181] F. Beutler *et al.*, Monthly Notices of the Royal Astronomical Society **416**, 3017 (2011).

[182] C. Blake *et al.*, Monthly Notices of the Royal Astronomical Society **418**, 1707 (2011), arXiv: 1108.2635.

[183] A. A. Penzias and R. W. Wilson, The Astrophysical Journal **142**, 419 (1965).

[184] D. Fixsen, The Astrophysical Journal **707**, 916 (2009), arXiv: 0911.1955.

[185] Planck Collaboration, arXiv e-prints (2015), arXiv: 1502.01582.

[186] G. Hinshaw *et al.*, The Astrophysical Journal **208**, 19 (2013), arXiv: 1212.5226.

[187] A. Kosowsky, New Astronomy Reviews **47**, 939 (2003), arXiv: astro-ph/0402234.

[188] A. Kosowsky, New Astronomy Reviews **50**, 969 (2006), astro-ph/0608549.

[189] J. Ruhl *et al.*, The south pole telescope, in *SPIE Astronomical Telescopes+ Instrumentation*, pp. 11–29, International Society for Optics and Photonics, 2004, arXiv: astro-ph/0411122.

[190] P. Ade *et al.*, Physical Review Letters **112**, 241101 (2014), arXiv: 1403.3985.

[191] BICEP2/Keck and Planck Collaborations, Physical Review Letters **114**, 101301 (2015), arXiv: 1502.00612.

[192] M. Remazeilles, C. Dickinson, H. Eriksen, and I. Wehus, Monthly Notices of the Royal Astronomical Society **458**, 2032 (2016), arXiv: 1509.04714.

[193] R. A. Fisher, *The design of experiments* (Oliver & Boyd, 1935).

[194] H. L. Van Trees, Detection, estimation and modulation, Part I, 1968.

[195] M. Tegmark, A. N. Taylor, and A. F. Heavens, The Astrophysical Journal **480**, 22 (1997), arXiv: astro-ph/9603021.

[196] B. A. Bassett, Y. Fantaye, R. Hlozek, and J. Kotze, International Journal of Modern Physics D **20**, 2559 (2011), arXiv: 0906.0993.

[197] W. Hu, The Astrophysical Journal Letters **522**, L21 (1999), arXiv: astro-ph/9904153.

[198] Dark Energy Survey Collaboration, arXiv e-prints (2005), astro-ph/0510346.

[199] T. Abbott *et al.*, arXiv e-prints (2015), arXiv: 1507.05552.

[200] T. Kacprzak *et al.*, arXiv e-print (2016), arXiv: 1603.05040.

[201] K. S. Dawson *et al.*, The Astronomical Journal **145**, 10 (2012), arXiv: 1208.0022.

[202] M. Levi *et al.*, arXiv e-prints (2013), arXiv: 1308.0847.

[203] M. Santos *et al.*, Advancing Astrophysics with the Square Kilometre Array (AASKA14) , 19 (2015), arXiv: 1501.03989.

[204] P. Bull, P. G. Ferreira, P. Patel, and M. G. Santos, The Astrophysical Journal **803**, 21 (2015), arXiv: 1405.1452.

[205] M. Santos, D. Alonso, P. Bull, M. B. Silva, and S. Yahya, Advancing Astrophysics with the Square Kilometre Array (AASKA14) , 21 (2015), arXiv: 1501.03990.

[206] I. Harrison, S. Camera, J. Zuntz, and M. L. Brown, arXiv e-prints (2016), arXiv: 1601.03947.

[207] M. Brown *et al.*, Advancing Astrophysics with the Square Kilometre Array (AASKA14) , 23 (2015), 1501.03828.

[208] Z. Ivezic, J. A. Tyson, and the LSST Collaboration, arXiv e-prints (2008), arXiv: 0805.2366.

[209] J. Fowler *et al.*, The Astrophysical Journal **722**, 1148 (2010), arXiv: 1001.2934.

[210] M. Niemack *et al.*, ACTPol: a polarization-sensitive receiver for the Atacama Cosmology Telescope, in *SPIE Astronomical Telescopes+ Instrumentation*, pp. 77411S–77411S, International Society for Optics and Photonics, 2010, arXiv: 1006.5049.

[211] S. W. Henderson *et al.*, Journal of Low Temperature Physics (2016), arXiv: 1510.02809.

[212] W. Wu *et al.*, The Astrophysical Journal **788**, 138 (2014), arXiv: 1402.4108.

[213] T. Baker, P. Ferreira, and C. Skordis, Physical Review D **89**, 024026 (2014), arXiv: 1310.1086.

[214] W. Hu, Physical Review D **62**, 043007 (2000), arXiv: astro-ph/0001303.

[215] Planck Collaboration, Astronomy & Astrophysics **571**, A16 (2014), arXiv: 1303.5076.

[216] I. Smail, R. S. Ellis, and M. J. Fitchett, Monthly Notices of the Royal Astronomical Society **270**, 245 (1994), arXiv: astro-ph/9402049.

[217] P. G. Ferreira and C. Skordis, Physical Review D **81**, 104020 (2010), arXiv: 1003.4231.

[218] A. Albrecht *et al.*, arXiv e-prints (2006), arXiv: astro-ph/0609591.

[219] E. Majerotto *et al.*, Monthly Notices of the Royal Astronomical Society **424**, 1392 (2012), arXiv: 1205.6215.

[220] B. Bassett and R. Hlozek, *Baryon acoustic oscillations* (Cambridge University Press, 2010), p. 246, arXiv: 0910.5224.

[221] P. Bull, Private communication.

[222] A. De Felice, T. Kobayashi, and S. Tsujikawa, Physics Letters B **706**, 123 (2011), arXiv: 1108.4242.

[223] R. A. Battye, A. Moss, and J. A. Pearson, Journal of Cosmology and Astroparticle Physics **4**, 048 (2015), arXiv: 1409.4650.

[224] J. M. Bardeen, Physical Review D **22**, 1882 (1980).

[225] A. Johnson *et al.*, Monthly Notices of the Royal Astronomical Society **444**, 3926 (2014), arXiv: 1404.3799.

[226] T. Baldauf, R. E. Smith, U. Seljak, and R. Mandelbaum, Physical Review D **81** (2010), arXiv: 0911.4973.

[227] J. Miralda-Escudé, The mass distribution in clusters of galaxies from weak and strong lensing, in *Astrophysical Applications of Gravitational Lensing*, edited by

C. S. Kochanek, , Proceedings of the symposium of the international astronomical union No. 173, 1995.

[228] J. Guzik and U. Seljak, Monthly Notices of the Royal Astronomical Society **321** (2002), arXiv: astro-ph/0007067.

[229] H. Zhan, L. Knox, and J. A. Tyson, The Astrophysical Journal **690**, 923 (2008), arXiv: 0806.0937.

[230] A. Hojjati *et al.*, Physical Review D **85**, 043508 (2012), arXiv: 1111.3960.

[231] R. Scoccimarro, Physical Review D **70**, 083007 (2004), arXiv: astro-ph/0407214.

[232] A. Cabré and E. Gaztañaga, Monthly Notices of the Royal Astronomical Society **396**, 1119 (2009), arXiv: 0807.2461.

[233] S. Cole *et al.*, Monthly Notices of the Royal Astronomical Society **362**, 505 (2005), arXiv: astro-ph/0501174.

[234] J. N. Fry and E. Gaztanaga, The Astrophysical Journal **413**, 447 (1993), arXiv: astro-ph/9302009.

[235] L. Amendola, E. Menegoni, C. Di Porto, M. Corsi, and E. Branchini, arXiv e-prints (2015), arXiv: 1502.03994.

[236] J. Benjamin *et al.*, Monthly Notices of the Royal Astronomical Society **381**, 702 (2007), arXiv: astro-ph/0703570.

[237] A. R. Pullen, S. Alam, and S. Ho, Monthly Notices of the Royal Astronomical Society **449**, 4326 (2015), arXiv: 1412.4454.

[238] A. R. Pullen, S. Alam, S. He, and S. Ho, arXiv preprint (2015), arXiv: 1511.04457.

[239] A. H. Guth, D. I. Kaiser, and Y. Nomura, Physics Letters B **733**, 112 (2014), arXiv: 1312.7619.

[240] G. Aslanyan and R. Easther, Physical Review D **91**, 123523 (2015), arXiv: 1504.03682.

[241] M. C. Johnson and W. Lin, Journal of Cosmology and Astroparticle Physics **3**, 051 (2016), arXiv: 1508.03786.

[242] C. Bonvin, C. Clarkson, R. Durrer, R. Maartens, and O. Umeh, Journal of Cosmology and Astroparticle Physics **6**, 050 (2015), arXiv: 1503.07831.

[243] N. Kaiser and J. A. Peacock, Monthly Notices of the Royal Astronomical Society **455**, 4518 (2016), arXiv: 1503.08506.

[244] R. Wojtak, T. M. Davis, and J. Wiis, Journal of Cosmology and Astroparticle Physics **7**, 025 (2015), arXiv: 1504.00718.

[245] C. Bonvin, C. Clarkson, R. Durrer, R. Maartens, and O. Umeh, Journal of Cosmology and Astroparticle Physics **7**, 040 (2015), 1504.01676.

[246] E. Di Dio *et al.*, arXiv e-prints (2016), arXiv: 1603.09073.

[247] J. D. Barrow and D. J. Shaw, Physical Review Letters **106**, 101302 (2011), arXiv: 1007.3086.

[248] T. P. Waterhouse and J. P. Zibin, arXiv e-prints (2008), arXiv: 0804.1771.

[249] L. Knox, Y.-S. Song, and H. Zhan, The Astrophysical Journal **652**, 857 (2006), arXiv: astro-ph/0605536.

[250] L. Knox, Physical Review D **73**, 023503 (2006), arXiv: astro-ph/0503405.

[251] M. J. Mortonson, Physical Review D **80**, 123504 (2009), arXiv: 0908.0346.

[252] G. Barenboim, E. F. Martínez, O. Mena, and L. Verde, Journal of Cosmology and Astroparticle Physics **2010**, 008 (2010), arXiv: 0910.0252.

[253] D. Sapone, E. Majerotto, and S. Nesseris, Physical Review D **90**, 023012 (2014), arXiv: 1402.2236.

[254] M. Takada and O. Doré, Physical Review D **92**, 123518 (2015), arXiv: 1508.02469.

[255] A. Hall and A. Taylor, arXiv e-prints (2016), arXiv:1603.08431.

[256] T. D. Kitching *et al.*, MNRAS **455**, 3319 (2016), 1507.05334.

[257] S. Joudaki *et al.*, arXiv e-prints (2016), arXiv: 1601.05786.

[258] H.-J. Seo and D. J. Eisenstein, The Astrophysical Journal **665**, 14 (2007), arXiv: astro-ph/0701079.

[259] B. Joachimi and P. Schneider, Astronomy & Astrophysics **507**, 105 (2009), arXiv: 0905.0393.

[260] A. Hall and A. Taylor, Monthly Notices of the Royal Astronomical Society **443**, L119 (2014), arXiv: 1401.6018.

[261] T. Giannantonio *et al.*, Physical Review D **77**, 123520 (2008), arXiv:0801.4380.

[262] A. Pavlov, S. Westmoreland, K. Saaidi, and B. Ratra, Physical Review D **88**, 123513 (2013), arXiv: 1307.7399.

[263] O. Farooq, D. Mania, and B. Ratra, Astrophysics and Space Science **357**, 11 (2015), arXiv: 1308.0834.

[264] W. Hu and T. Okamoto, The Astrophysical Journal **574**, 566 (2002), arXiv: astro-ph/0111606.

[265] A. Refregier *et al.*, arXiv e-prints (2010), arXiv: 1001.0061.

[266] R. Maartens, F. B. Abdalla, M. Jarvis, and M. G. Santos, Advancing Astrophysics with the Square Kilometre Array (AASKA14) , 016 (2015), arXiv: 1501.04076.

[267] P. Bull *et al.*, Advancing Astrophysics with the Square Kilometre Array (AASKA14) , 24 (2015), 1501.04088.

[268] A. Font-Ribera *et al.*, Journal of Cosmology and Astroparticle Physics **5**, 023 (2014), arXiv: 1308.4164.

[269] L. Amendola *et al.*, Living Reviews in Relativity **16** (2013), arXiv: 1206.1225.

[270] P. Bull, The Astrophysical Journal **817**, 26 (2016), arXiv: 1509.07562.

[271] R. Allison, P. Caucal, E. Calabrese, J. Dunkley, and T. Louis, Physical Review D **92**, 123535 (2015), arXiv: 1509.07471.

[272] A. Liu *et al.*, Physical Review D **93**, 043013 (2016), arXiv: 1509.08463.

[273] D. J. Eisenstein, H.-J. Seo, E. Sirko, and D. N. Spergel, The Astrophysical Journal **664**, 675 (2007), arXiv: astro-ph/0604362.

[274] H.-J. Seo *et al.*, The Astrophysical Journal **720**, 1650 (2010), arXiv: 0910.5005.

[275] A. Schneider and R. Teyssier, Journal of Cosmology and Astroparticle Physics **12**, 049 (2015), arXiv: 1510.06034.

[276] D. J. E. Marsh, P. Bull, P. G. Ferreira, and A. Pontzen, Physical Review D **90**, 105023 (2014), arXiv: 1406.2301.

[277] L. Pèrenon, F. Piazza, C. Marinoni, and L. Hui, Journal of Cosmology and Astroparticle Physics **11**, 029 (2015), arXiv: 1506.03047.

[278] V. Salvatelli, F. Piazza, and C. Marinoni, arXiv e-prints (2016), arXiv: 1602.08283.

[279] M. Sato *et al.*, The Astrophysical Journal **701**, 945 (2009), arXiv: 0906.2237.

[280] M. Takada, Statistical challenges in weak lensing cosmology, in *Statistical Challenges in 21st Century Cosmology*, edited by A. Heavens, J.-L. Starck, and A. Krone-Martins, , IAU Symposium Vol. 306, pp. 78–89, 2014, arXiv: 1407.3330.

[281] Y. Li, W. Hu, and M. Takada, Physical Review D **89**, 083519 (2014), arXiv: 1401.0385.

[282] T. Baldauf, U. Seljak, L. Senatore, and M. Zaldarriaga, arXiv e-prints (2015), arXiv: 1511.01465.

[283] R. B. Tully, H. Courtois, Y. Hoffman, and D. Pomarède, Nature **513**, 71 (2014), arXiv: 1409.0880.

[284] O. Umeh, C. Clarkson, and R. Maartens, Classical and Quantum Gravity **31**, 202001 (2014), arXiv: 1207.2109.

[285] N. Jarosik *et al.*, The Astrophysical Journal Supplement Series **192**, 14 (2011), arXiv: 1001.4744.

[286] Planck Collaboration, Astronomy & Astrophysics **571**, A3 (2014), arXiv: 1303.5064.

[287] Planck Collaboration, arXiv e-prints (2015), arXiv: 1507.08853.

[288] J. T. A. de Jong, G. A. Verdoes Kleijn, K. H. Kuijken, and E. A. Valentijn, Experimental Astronomy **35**, 25 (2013), arXiv: 1206.1254.

[289] M. Takada, Subaru Hyper Suprime-Cam Project, in *American Institute of Physics Conference Series*, edited by N. Kawai and S. Nagataki, , American Institute of Physics Conference Series Vol. 1279, pp. 120–127, 2010.

[290] J. Khoury and M. Wyman, Physical Review D **80**, 064023 (2009), arXiv: 0903.1292.

[291] P. Brax, A.-C. Davis, B. Li, H. A. Winther, and G.-B. Zhao, Journal of Cosmology and Astroparticle Physics **2012**, 002 (2012), arXiv: 1206.3568.

[292] P. Brax, A.-C. Davis, B. Li, H. A. Winther, and G.-B. Zhao, Journal of Cosmology and Astroparticle Physics **2013**, 029 (2013), arXiv: 1303.0007.

[293] A. R. Zentner *et al.*, Physical Review D **87**, 043509 (2013), arXiv: 1212.1177.

[294] T. D. Kitching and A. N. Taylor, Monthly Notices of the Royal Astronomical Society **416**, 1717 (2011), arXiv: 1012.3479.

[295] D. Jeong, E. Komatsu, and B. Jain, Physical Review D **80**, 123527 (2009), arXiv: 0910.1361.

[296] D. Bianchi *et al.*, Monthly Notices of the Royal Astronomical Society **427**, 2420 (2012), arXiv: 1203.1545.